



NASA/ OHIO SPACE GRANT CONSORTIUM

2018-2019 ANNUAL STUDENT RESEARCH SYMPOSIUM PROCEEDINGS XXVII



April 5, 2019
Held at the Ohio Aerospace Institute
Cleveland, Ohio



Follow OSGC on:



*Just click on any Section or Student Name,
and it will link you to the page immediately!*

TABLE OF CONTENTS

	<u>Page(s)</u>
Table of Contents	2-7
Foreword	8
Member Institutions	9
Acknowledgments	10
Agenda	11-17
Symposium Photographs	18-28

<i>Student Name</i>	<i>College/University</i>	<i>Page(s)</i>
Arthurs, Samantha K.	Columbus State Community College	29-30
Analysis of Using Ozone to Treat Extracellular Cyanotoxins in Drinking Water Treatment Plants		
Brittman, Dazjuan M. D.	Central State University	31-32
Zero Gravity Gardenia		
Brooks, Brian M.	Cincinnati State Technical and Community College	33-34
Rehabilitating a Historical Building		
Buchman, Zachary J.	The University of Toledo	35-36
Investigating the Role of Commercial-of-the-Shelf Products in CubeSat Development		
Burks, Destonee S.	Wilberforce University	37-39
Interaction of 5G Waves with the Human Body		
Cain, Andrew D.	Columbus State Community College	40-41
Improving Upon Current Mid- & High-Rise Structures with Hybrid Floor Systems		
Cintron, Eleana	Lorain County Community College	42-45
Evaluating Ceramic Electrolyte Morphology Composed of Several Compositions via the Phase Inversion Method		
Collins, Brooke A.	Kent State University	46-48
Changes in Season (What Is Happening to Our School's Trees and Its Leaves?)		
Crouch, Michaela M.	Cedarville University	49-52
Quality Assessment of 3D Printed PLA Scaffolds for Tissue Engineering of Bone Restoration Implants		

<i>Student Name</i>	<i>College/University</i>	<i>Page(s)</i>
Curtis, Monica L.	Marietta College	53-54
Phases of the Moon		
Custer, Erica M.	Ohio University	55-58
Cortical Bone Mechanics Technology (CBMT) and Quasi-Static Mechanical Testing (QMT) Sensitivity to Bone Collagen Degradation		
Deibel, Angela M.	Kent State University	59-62
What Does It Take to Generate One Megawatt of Power from Fuel Cells?		
Demus, Justin C.	Miami University	63-65
MOSFET Junction Temperature Measurements Based on Conducted Electromagnetic Emissions		
Evans, Rachel E.	Wright State University	66-69
The Effect of Scan Strategy in Additive Manufacturing		
Flack, Curtis A.	Cleveland State University	70-72
Wake Flow Structure of a Seal-Whisker-Inspired Low-Pressure Turbine Blade		
Frisco, Lynnae S.	Central State University	73-77
Solar Tracker		
Ghrist, Miranda L.	Lorain County Community College	78-79
Numerical Solutions of Heat Transfer Models to Determine Thermal Properties of Novel Insulating Materials for Hypersonic Aerospace Applications		
Gibboney, Kristopher A.	Cedarville University	80-81
Understanding and Responding to the Physical and Economic Impact of Natural Disasters on Communities and Agriculture		
Gomez, Andrea	Wright State University	82-91
Mathematical Modeling for Release Kinetic Prediction of LENVIMA		
Hauerwas, Joel A.	Case Western Reserve University	92-93
Development of Control Systems for Flapping Winged Micro Air Vehicles		
Innes, Ashley E.	Lorain County Community College	94
A Novel Mutation Located In the C-terminal Cytoplasmic Domain of the CCR5 Gene With Potential Effects on HIV Infectivity		
Innocenzi, Steven H.	The University of Akron	95-96
Octaworm: Semi-Rigid Robotics		

<i>Student Name</i>	<i>College/University</i>	<i>Page(s)</i>
Jeske, Madelyn P.	The University of Akron	97-105
Increasing Mechanical Toughness of a Double Network Hydrogel from Agar, Polyacrylamide and Methylenabisacrylamide		
Jewell, Madison M.	Wright State University.....	106-110
Effect of DNA Methyltransferase Inhibition in Hypoxic and Normoxic Conditions on Cellular Proliferation and Potential Growth Regulators in Human Diffuse Intrinsic Pontine Gliomas		
Joy, Lindsay S.	Marietta College.....	111-113
Importance of Our Sun		
Kavaras, Joel R.	Baldwin Wallace University	114-117
Mathematical Modeling of Beech Leaf Disease Spread		
Kirwin, Roan M.	Miami University.....	118-124
Modification of Existing Wire-EDM Wire Lag Models to Include Surface Feed Rate		
Klimek, Jared I.	Cedarville University.....	125-128
Fabrication Methods and Testing of 3D Printed PLA Scaffolds for Tissue Engineering of Bone Restoration Implants		
Kosir, Shane T.	University of Dayton.....	129-134
Improvement in Jet Aircraft Operation with the Use of High-Performance Drop-in Fuels		
Krieg, Derek L.	Marietta College.....	135-137
Electric Generation Potential in the Upstream Oil and Gas Industry		
Kungle, Jonathan L.	Marietta College.....	138-139
Alternatives to Decommissioning Offshore Infrastructure		
Licht, Kathleen M.	Cincinnati State Technical and Community College.....	140-141
Self-Sufficient Medical Devices		
Love, André L.	Central State University	142-143
The Neighborhood Youth Activities Project		
Manning, Nicholas B.	Kent State University	144-149
Water Quality Assessment of Euclid Creek Using Remote Sensing and VPCA Analysis		
Mast, Malia R.	Columbus State Community College	150-153
Will BIM, VR, & AI Utilization Bring Actual Solves for Construction's Top Issues		

<i>Student Name</i>	<i>College/University</i>	<i>Page(s)</i>
Mazursky, Alex J.	Miami University.....	154-160
A Compact and Compliant Electrorheological Actuator for Mobile Haptic Feedback		
McCue, Garrett S.	Baldwin Wallace University	161-164
FTY720 Fails to Increase Protein Phosphatase 2A Activity in a <i>Caenorhabditis elegans</i> Model of Tauopathy		
McMullen, Nya A.	Central State University	165-166
What's the Weather?		
Messer, Derek K.	The University of Toledo.....	167-170
Quantifying Defects from High Throughput Continuous Production of Graphene		
Miller, Amanda M.	University of Cincinnati.....	171-174
Development of a Sensor Frame Harness Gait Assessment Device for Occupational Health in Nursing		
Omer, Liam M.	The University of Akron	175-177
Hyaluronan Drug Delivery Systems		
O'Neill, Collin J.	The Ohio State University.....	178-181
Active Flow Control in an Aggressively Offset High-Speed Inlet/Diffuser Model		
Opacich, Katherine C.	University of Dayton	182-194
Analyzing the Relative Impact of Spray and Volatile Fuel Properties on Gas Turbine Combustor Ignition in Multiple Rig Geometries		
Payne, Kylon J.	Central State University	195-199
Solar Tracker		
Payne, Nathaniel M.	Ohio Northern University	200-203
Cant Angle Effect on Winglet Performance		
Peters, Nicole A.	Cedarville University.....	204-207
Sizing the Solar System		
Pickering, Lynn K.	University of Cincinnati.....	208-209
Fuzzy Logic Based 2-Player Tetris		
Prigg, David B.	Case Western Reserve University.....	210-212
Robot to Clean Fresh Water Pipes		

<i>Student Name</i>	<i>College/University</i>	<i>Page(s)</i>
Rose, Evan N.	Case Western Reserve University.....	213-218
Effects of Fuel Oscillation on Flame Spread in Microgravity		
Rymarz, Reannah N.	Marietta College.....	219-220
The Future of Geothermal Energy		
Sauder, Rachel E.	Ohio Northern University.....	221
Extraterrestrial Geology		
Scott, Christina E.	University of Dayton.....	222-226
Fabrication of Periodic Poled Lithium Niobate for Three-wave Mixing		
Shapley, Sarah M.	Baldwin Wallace University.....	227-228
Role of PADI2 on Actin in Myelination		
Steiner, Joshua B.	The University of Toledo.....	229-234
Dual Functional Materials for CO₂ Conversion		
Taylor, Mallory L.	Ohio Northern University.....	235-239
How Camber and Angle of Attack Impact Drag, Lift and Pressure Coefficients of NACA 4-digit Airfoils		
Tesny, Erin M.	Cleveland State University.....	240-246
Design of Heat Exchanger for Intense Cooling of Inlet Bleed Air at High Mach Numbers		
True, Timothy M.	Cedarville University.....	247-250
Signal Analysis and Decomposition of Musical Instruments		
Wagner, Grant A.	Youngstown State University.....	251-252
Calibration of Optical Paints for Aerodynamic Testing		
Warnock, Sarah M.	Ohio University.....	253-256
Cortical Bone Mechanics Technology (CBMT) and Dual X-Ray Absorptiometry (DXA) Sensitivity to Bone Collagen Degradation in Human Ulna Bone		
Watkins, Barbara L.	Columbus State Community College.....	257-258
Mass Timber as a Sustainable Alternative for the Construction Industry		
Waugh, Carly G.	Ohio Northern University.....	259-269
Observing the Effects of Airfoil Alteration on Flight Parameters		

Weaver, Kyle A.	Miami University.....	270-273
Controllable Stiffness “Smart” Skins Based on Magneto-Rheological Elastomers: Characterization and Application		

Weisfeld, Matthias S.	Case Western Reserve University.....	274-279
Biomimicry of <i>Manduca sexta</i> Hawkmoth Wings for Use in a Flapping Wing Micro Air Vehicle		

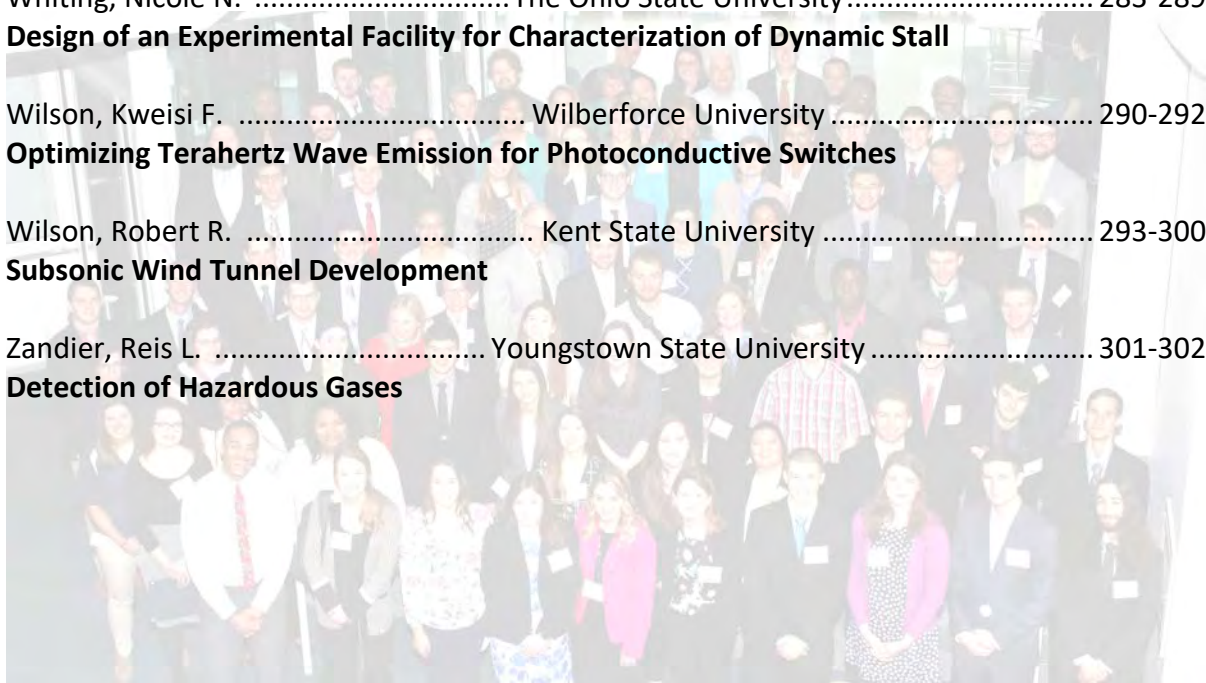
Wessels, Austin M.	University of Cincinnati.....	280-282
VertiCat: Custom VTOL Platform		

Whiting, Nicole N.	The Ohio State University.....	283-289
Design of an Experimental Facility for Characterization of Dynamic Stall		

Wilson, Kweisi F.	Wilberforce University.....	290-292
Optimizing Terahertz Wave Emission for Photoconductive Switches		

Wilson, Robert R.	Kent State University.....	293-300
Subsonic Wind Tunnel Development		

Zandier, Reis L.	Youngstown State University.....	301-302
Detection of Hazardous Gases		



FOREWORD

The Ohio Space Grant Consortium (OSGC), a member of the NASA National Space Grant College and Fellowship Program, awards graduate fellowships and undergraduate scholarships to students working toward degrees in Science, Technology, Engineering and Mathematics (STEM) disciplines at OSGC-member universities. The awards are made to United States citizens, and the students are competitively selected. Since the inception of the program in 1989, over 1,265 undergraduate scholarships and 175 graduate fellowships have been awarded.

Matching funds are provided by the 24 member universities/community colleges, the Ohio Aerospace Institute (OAI), Choose Ohio First, the Nord Family Foundation, the Nordson Corporation Foundation, and private industry. Note that this year ~ \$500,000 will be directed to scholarships and fellowships representing contributions from NASA, the Ohio Aerospace Institute, member universities, foundations, and industry.

By helping more students to graduate with STEM-related degrees, OSGC provides more qualified technical employees to industry. The research conducted for the Master's fellowship must be of interest to NASA. A prime aspect of the scholarship program is the undergraduate research project that the student performs under the mentorship of a faculty member. This research experience is effective in encouraging U. S. undergraduate students to attend graduate school in STEM. The Education scholarship recipients are required to attend a workshop conducted by NASA personnel where they are exposed to NASA educational materials and create a lesson plan for use in their future classrooms.

On Friday, April 5, 2019, all OSGC Scholars and Fellows reported on these projects at the Twenty Seventh Annual Student Research Symposium held at the Ohio Aerospace Institute in Cleveland, Ohio. In multiple sessions, Fellows and Senior Scholars offered 15-minute oral presentations on their research projects and fielded questions from an audience of their peers and faculty, and received written critiques from a panel of evaluators. Junior, Community College, and Education Scholars presented posters of their research and entertained questions from all attendees during the poster session. The University of Akron Lunabotics Team and their Robot, R.O.C.K.E.E., and also Professor Marlin Linger's Unmanned Aerial Systems (UAS) display. All students were awarded Certificates of Recognition for participating.

Research reports of students from the following schools are contained in this publication:

Affiliate Members

- The University of Akron
- Baldwin Wallace University
- Case Western Reserve University
- Cedarville University
- Central State University
- Cleveland State University
- University of Dayton
- Kent State University
- Marietta College
- Miami University
- Ohio Northern University
- The Ohio State University
- Ohio University
- University of Cincinnati
- The University of Toledo
- Wilberforce University
- Wright State University
- Youngstown State University

Community Colleges

- Cincinnati State Technical and Community College
- Columbus State Community College
- Lorain County Community College

MEMBER INSTITUTIONS

Affiliate Members

- Baldwin Wallace University..... James W. McCargar, Ph.D.
- Case Western Reserve University Roger D. Quinn, Ph. D.
- Cedarville University Robert Chasnov, Ph.D., P.E.
- Central State University Augustus Morris, Jr., Ph.D., P.E.
- Cleveland State University Ms. Rose Begalla, M.A.
- Kent State University..... Joseph D. Ortiz, Ph.D.
- Marietta College..... Prof. Craig Rabatin, P.E.
- Miami University James Moller, Ph.D., P.E.
- Ohio Northern University..... Jed E. Marquart, Ph.D., P.E.*
- The Ohio State University Dr. Mo Samimy
- Ohio University..... Dr. Shawn Ostermann
- The University of Akron.....Dr. Craig C. Menzemer
- University of Cincinnati Dr. Kelly Cohen
- University of Dayton..... Dr. Robert J. Wilkens
- The University of ToledoDr. Lesley M. Berhan
- Wilberforce University Jennifer N. Williams, Ph.D.
- Wright State University Mitch Wolff, Ph.D.
- Youngstown State University Kevin J. Disotell, Ph.D.

Campus Representative

Community Colleges

- Cincinnati State Technical and Community College Professor Abigail Yee
- Columbus State Community College..... Professor Jeffery M. Woodson, M.S., I.E.
- Cuyahoga Community College Prof. Michelle S. Davis
- Lakeland Community College..... Professor Tom Ciferno
- Lorain County Community College..... Regan L. Silvestri, Ph.D.
- Sinclair Community College Eric C. Dunn

Campus Representative

NASA Glenn Research Center - Representatives

- Dr. M. David Kankam
- Ms. Susan M. Kohler
- Mr. Robert F. LaSalvia



Lead Institution

- Ohio Aerospace InstituteMs. Ann O. Heyward

Representative



*Dr. Marquart also serves as Director of the Ohio Space Grant Consortium

ACKNOWLEDGMENTS

Thank you to all who helped with the OSGC's 27th Annual Research Symposium!

STEM Panel:

- ★ Joshua E. Allen, NASA Glenn Research Center
- ★ Charles W. Barbour, II, Raytheon
- ★ Collin E. Mikol, Swagelok
- ★ Gretchen M. Morales-Valle, NASA Glenn Research Center
- ★ Brian E. Neiss, Lockheed Martin

Campus Representatives – 4-Year Universities

- Dr. James W. McCargar, Baldwin Wallace University
- Dr. Roger Quinn, Case Western Reserve University
- Robert Chasnov, Ph.D., P.E., Cedarville University
- Augustus Morris, Jr., Ph.D., P.E., Central State University
- Ms. Rose Begalla, M.A., Cleveland State University
- Dr. Joseph D. Ortiz, Kent State University
- Professor Craig Rabatin, P.E., Marietta College
- James Moller, Ph.D., P.E., Miami University
- Jed E. Marquart, Ph.D., P.E., Ohio Northern University*
- Dr. Mo Samimy, The Ohio State University
- Dr. Shawn Ostermann, Ohio University
- Dr. Craig C. Menzemer, The University of Akron
- Dr. Kelly Cohen, University of Cincinnati
- Dr. Robert J. Wilkens, University of Dayton
- Dr. Lesley M. Berhan, The University of Toledo
- Jennifer N. Williams, Ph.D., Wilberforce University
- Mitch Wolff, Ph.D., Wright State University
- Kevin J. Disotell, Ph.D., Youngstown State University

Campus Representatives - Community Colleges

- Professor Abigail Yee, Cincinnati State Technical and Community College
- Professor Jeffery M. Woodson, M.S., I.E., Columbus State Community College
- Professor Michelle S. Davis, Cuyahoga Community College
- Professor Tom Ciferno, Lakeland Community College
- Regan L. Silvestri, Ph.D., Lorain County Community College
- Eric C. Dunn, Sinclair Community College

Special thanks go out to the following:

- Dr. John Sankovic and OAI for hosting the event
- Ohio Aerospace Institute staff whose assistance made the event a huge success!
- Everyone who served as a facilitator during the PowerPoint Sessions
- NASA Glenn Research Center – Human Resources – Christina Koleno
- Industry Attendees
- Novotny Catering (Del Novotny)
- Sharon Mitchell Photography

*Dr. Marquart also serves as Director of the Ohio Space Grant Consortium



2019 OSGC STUDENT RESEARCH SYMPOSIUM
Hosted By: Ohio Aerospace Institute (OAI)
22800 Cedar Point Road • Cleveland, OH 44142
• (440) 962-3000
Friday, April 5, 2019

AGENDA

8:00 AM – 8:30 AM	Sign-In / Continental Breakfast / Student Portraits (30 minutes).....Lobby
8:30 AM – 8:35 AM	Welcome and Introductions (5 minutes) Forum (Lobby Level) <i>Jed E. Marquart</i> Director, Ohio Space Grant Consortium (OSGC) and Professor of Mechanical Engineering, Ohio Northern University
8:35 AM – 8:40 AM	Symposium Logistics (5 minutes) <i>Laura A. Stacko</i> Program Manager, OSGC
8:40 AM – 8:50 AM	Group Photograph (10 minutes).....Lobby / Atrium Stairwell
9:00 AM – 11:00AM	Student Oral Presentations – Senior Scholars and Fellows (120 minutes) •Group 1 Forum (Lobby Level) •Group 2Presidents’ Room (Lower Level) •Group 3 Industry Room A (2nd Floor) •Group 4 Industry Room B (2nd Floor) •Group 5.....Board Room
11:00 AM – 12:15 PM	Various Displays (75 minutes) •Student Poster Presentations.....Lobby Junior, Community College, and Pre-Service Teacher (Education) Scholars •NASA and Industry Displays Lobby •Team DisplaysAtrium (Lower Level)
12:15 PM – 1:15 PM	Luncheon Buffet (60 minutes).....Atrium / Sunroom (Lower Level)
1:15 PM – 2:30 PM	Panel Discussion and Q&A (75 minutes)..... Forum (Lobby Level) <i>“Launching a STEM Career”</i> <i>Panel Members:</i> ★Joshua E. Allen, NASA Glenn Research Center ★Charles W. Barbour, II, Raytheon ★Collin E. Mikol, Swagelok ★Gretchen M. Morales-Valle, NASA Glenn Research Center ★Brian E. Neiss, Lockheed Martin
2:30 PM	Symposium Adjourns



STUDENT ORAL PRESENTATIONS

9:00 AM to 11:00 AM (120 minutes)

Group 1 – Mechanical Engineering / Aerospace Engineering / Aeronautical & Astronautical Engineering	
FORUM (AUDITORIUM – LOBBY LEVEL)	
Facilitator: Andrew H. Work	
9:00	Matthias S. Weisfeld, Senior, Mechanical Engineering/Aerospace Engineering, Case Western Reserve <i>Manufacturing of Artificial Moth Wings for use in a Flapping Wing Micro Aerial Vehicle</i>
9:15	Collin J. O'Neill, Senior, Aerospace Engineering, The Ohio State University <i>Active Flow Control in a Compact High-Speed Inlet/Diffuser Model</i>
9:30	Austin M. Wessels, Senior, Aerospace Engineering, University of Cincinnati <i>VertiCat: Custom VTOL Platform</i>
9:45	Robert R. Wilson, Senior, Aerospace Engineering, Kent State University <i>Subsonic Wind Tunnel Development</i>
10:00	Nicole N. Whiting, MS1, Aeronautical & Astronautical Engineering, The Ohio State University <i>Design of an Experimental Facility for Characterization of Dynamic Stall</i>
10:15	Evan N. Rose, MS1, Mechanical Engineering, Case Western Reserve University <i>Effects of Fuel Oscillation on Flame Spread in Microgravity</i>

Group 2 – Neuroscience / Biology / Biological Sciences / Biomedical Engineering / Exercise Physiology / Geology / Mathematics / Physics	
PRESIDENTS' ROOM (LOWER LEVEL)	
Facilitator: Jay N. Reynolds	
9:00	Garrett S. McCue, Senior, Neuroscience / Biology, Baldwin Wallace University <i>FTY720 Fails to Increase Protein Phosphatase 2A Activity in a Caenorhabditis Elegans Model of Tauopathy</i>
9:15	Erica M. Custer, Senior, Exercise Physiology, Ohio University <i>Cortical Bone Mechanics Technology and Quasi-Static Mechanical Testing Sensitivity to Bone Collagen Degradation</i>
9:30	Sarah M. Warnock, Senior, Biological Sciences, Ohio University <i>CBMT and DXA Sensitivity to Bone Collagen Degradation</i>
9:45	Liam M. Omer, Senior, Biomedical Engineering, The University of Akron <i>Hyaluronan Drug Delivery Systems</i>
10:00	Nicholas B. Manning, Senior, Geology, Kent State University <i>Water Quality Assessment of Euclid Creek Using Remote Sensing and VPCA Analysis</i>
10:15	Joel R. Kavaras, Senior, Mathematics, Baldwin Wallace University <i>Mathematical Modeling of Beech Leaf Disease Spread</i>
10:30	Timothy M. True, Senior, Physics, Cedarville University <i>Analysis and Decomposition of Signal from Musical Instruments</i>



STUDENT ORAL PRESENTATIONS (Continued)

9:00 AM to 11:00 AM (120 minutes)

Group 3 – Mechanical Engineering 1	
INDUSTRY ROOM A (SECOND FLOOR)	
Facilitator: Nathaniel A. Orndorf	
9:00	Michaela M. Crouch, Senior, Mechanical Engineering, Cedarville University <i>Quality Assessment of 3D Printed PLA Scaffolds for Tissue Engineering of Bone Restoration Implants</i>
9:15	Angela M. Deibel, Senior, Mechanical Engineering, Kent State University <i>What Does It Take to Generate 1 Megawatt from Fuel Cells?</i>
9:30	Rachel E. Evans, Senior, Mechanical Engineering, Wright State University <i>The Effects of Scan Strategy in Additive Manufacturing</i>
9:45	Jared I. Klimek, Senior, Mechanical Engineering, Cedarville University <i>Fabrication Methods and Testing of 3D Printed PLA Scaffolds for Tissue Engineering of Bone Restoration Implants</i>
10:00	Shane T. Kosir, Senior, Mechanical Engineering, University of Dayton <i>Improvement in Jet Aircraft Operation with the Use of High-Performance Drop-in Fuels</i>
10:15	Derek K. Messer, Senior, Mechanical Engineering, The University of Toledo <i>Quantifying Defects from High Throughput Continuous Production of Graphene</i>
10:30	Erin M. Tesny, MS1, Mechanical Engineering, Cleveland State University <i>Design of Heat Exchanger for Intense Cooling of Inlet Bleed Air at High Mach Numbers</i>

Group 4 – Mechanical Engineering 2	
INDUSTRY ROOM B (SECOND FLOOR)	
Facilitator: Tadas P. Bartkus	
9:00	Amanda M. Miller, Senior, Mechanical Engineering, University of Cincinnati <i>Development of a Sensor Frame Harness Gait Assessment Device for Occupational Health in Nursing</i>
9:15	Katherine C. Opacich, Senior, Mechanical Engineering, University of Dayton <i>Analyzing the Relative Impact of Spray and Volatile Fuel Properties on Gas Turbine Combustor Ignition in Multiple Rig Geometries</i>
9:30	Nathaniel M. Payne, Senior, Mechanical Engineering, Ohio Northern University <i>Cant Angle Effect on Winglet Performance</i>
9:45	David B. Prigg, Senior, Mechanical Engineering, Case Western Reserve University <i>Water Pipe Cleaning Robot</i>
10:00	Carly G. Waugh, Senior, Mechanical Engineering, Ohio Northern University <i>Observing the Effects of Airfoil Alteration on Flight Parameters</i>
10:15	Roan M. Kirwin, MS1, Mechanical Engineering, Miami University <i>Modification of Existing Wire-EDM Wire Lag Models to Include Surface Feed Rate</i>
10:30	Alex J. Mazursky, MS1, Mechanical Engineering, Miami University <i>A Compact and Compliant Electrorheological Actuator for Mobile Haptic Feedback</i>

**Group 5 – Chemical Engineering / Electrical Engineering / Petroleum Engineering /
Manufacturing Engineering**

BOARD ROOM (SECOND FLOOR)

Facilitator: Valerie M. Hale

9:00	Madelyn P. Jeske, Senior, Chemical Engineering, The University of Akron <i>Increasing Mechanical Properties of a Double Network Hydrogel from Agar and Polyacrylamide with Methylenebisacrylamide</i>
9:15	Joshua B. Steiner, Senior, Chemical Engineering, The University of Toledo <i>Dual Functional Materials for CO₂ Conversion</i>
9:30	Kyle A. Weaver, Senior, Chemical Engineering/Biochemistry, Miami University <i>Characterization of the Indentation and Pulse Properties of Vein-Inserted Magnetorheological Elastomers for use as Skin Models</i>
9:45	Kweisi F. Wilson, Senior, Electrical Engineering, Wilberforce University <i>Terahertz Technology</i>
10:00	DerekAllen L. Krieg, Senior, Petroleum Engineering, Marietta College <i>Electric Generation Potential in Upstream Oil and Gas</i>
10:15	Reannah N. Rymarz, Senior, Petroleum Engineering, Marietta College <i>The Future of Geothermal Energy</i>
10:30	Lynnae S. Frisco and Kylon J. Payne, Seniors, Manufacturing Engineering, Central State University <i>Solar Concentrator</i>

STUDENT POSTER PRESENTATIONS
LOBBY (MAIN FLOOR)
11:00 AM to 12:15 PM (75 minutes)

Junior Science, Technology, Engineering, and Mathematics (STEM) Scholarship Recipients
Zachary J. Buchman, Junior, Electrical Engineering, The University of Toledo <i>Effect of COTS Hardware on Cubesat Development</i>
Destonee S. Burks, Senior, Biology, Wilberforce University <i>Interaction of 5G Waves with the Human Body</i>
Cyaira K. Cook, Junior, Mechanical Engineering, Wilberforce University <i>Optomechanic Analysis of Micro Mirror Systems</i>
Justin C. Demus, Junior, Electrical Engineering, Miami University <i>MOSFET Junction Temperature Measurements based on Conducted Electromagnetic Emissions</i>
Curtis A. Flack, Junior, Mechanical Engineering, Cleveland State University <i>Wake Flow Structure of a Seal-Whisker-Inspired Low-Pressure Turbine Blade</i>
Andrea Gomez-Carrillo, Junior, Biomedical Engineering, Wright State University <i>Drug Delivery LENVIMA Mathematical Model</i>
Joel A. Hauerwas, Junior, Mechanical Engineering, Case Western Reserve University <i>Control Systems of Flapping Winged Robots</i>
Steven H. Innocenzi, Junior, Biomedical Engineering, The University of Akron <i>OctaWorm: Semi-Rigid Robotics</i>
Madison M. Jewell, Junior, Neuroscience, Wright State University <i>Effect of DNA Methyltransferase Inhibition in Restoration of H3.3K27M-induced p16 Repression in Human DIPG Cell Lines</i>
Johnathan L. Kungle, Junior, Petroleum Engineering, Marietta College <i>Alternatives to Decommissioning Offshore Infrastructure</i>
André L. Love, Senior, Computer Science, Central State University <i>The Neighborhood Youth Activities Project (NYAP)</i>
Sarah M. Shapley, Junior, Neuroscience/Biology, Baldwin Wallace University <i>Role of PAD2 on Actin in Myelination</i>
Mallory L. Taylor, Junior, Mechanical Engineering, Ohio Northern University <i>How Camber and Angle of Attack Impact Drag, Lift and Pressure Coefficients of NACA 4-digit Airfoils</i>
Grant A. Wagner, Junior, Mechanical Engineering, Youngstown State University <i>The Calibration of Optical Paints for Aerodynamic Testing</i>
Reis L. Zandier, Junior, Chemical Engineering, Youngstown State University <i>Detection of Hazardous Gases Using Carbon Nanotubes</i>

STUDENT POSTER PRESENTATIONS
LOBBY (MAIN FLOOR)
11:00 AM to 12:15 PM (75 minutes)

Sophomore Community College STEM Scholarship Recipients
Samantha K. Arthurs, Soph., Environmental Science, Safety, & Health, Columbus State Community College <i>Cost-benefit Analysis of Using Ozone to Treat Extracellular Cyanotoxins in Drinking Water Treatment Plants</i>
Brian M. Brooks, Soph., Civil Engineering Technology, Cincinnati State Technical and Community College <i>Restoring Historical Buildings</i>
Andrew D. Cain, Sophomore, Mechanical Engineering Technology, Columbus State Community College <i>Improving Upon Current Mid- & High-Rise Structures with Hybrid Floor Systems</i>
Sarah T. Closson, Soph., Electro-Mechanical Engineering, Cincinnati State Technical and Community College <i>Solar Technology Applications</i>
Miranda Ghrist, Sophomore, Computer Information Systems, Lorain County Community College <i>Numerical Solutions of Heat Transfer Models to Determine Thermal Properties of Insulating Material for Hypersonic Aerospace Applications</i>
Ashley E. Innes, Sophomore, Biology, Lorain County Community College <i>A Novel Mutation Located in the C-terminal Cytoplasmic Domain of the CCR5 Gene with Potential Effects on HIV Infectivity</i>
Kathleen M. Licht, Soph., Electrical Engineering Technologies, Cincinnati State Technical & Community College <i>Self-Sufficient Medical Devices</i>
Malia R. Mast, Sophomore, Construction Management, Columbus State Community College <i>BIM,VR,AI Technology Impacts on the Construction Industry</i>
Barbara L. Watkins, Sophomore, Construction Management, Columbus State Community College <i>Mass Timber as a Sustainable Alternative for the Construction Industry</i>

Pre-Service Teacher (Education) Scholarship Recipients
Dazjuan M. D. Brittman, Sophomore, Middle Childhood Education, Agriculture, Central State University <i>Zero Gravity Gardening</i>
Monica L. Curtis, Senior, Early Childhood Education, Marietta College <i>Phases of the Moon</i>
Kristopher A. Gibboney, Sophomore, Adolescent to Young Adult (AYA), Science, Cedarville University <i>Understanding and Responding to the Physical and Economic Impact of Natural Disasters on Communities and Agriculture</i>
Lindsay S. Joy, Senior, Early Childhood Education, Marietta College <i>Importance of Our Sun</i>
Nya McMullen, Sophomore, Middle Childhood Education, Mathematics, Central State University <i>What's the Weather?</i>
Nicole A. Peters, Senior, Middle Childhood Education, Science and Mathematics, Cedarville University <i>Sizing the Solar System</i>
Rachel E. Sauder, Senior, Adolescent to Young Adult (AYA), Integrated Science, Ohio Northern University <i>Extraterrestrial Geology</i>

STUDENT TEAMS
ATRIUM (OUTSIDE PRESIDENT'S ROOM/LOWER LEVEL)
11:00 AM to 12:15 (75 minutes)

Case Western Reserve University Unmanned Aircraft Systems (UAS)
•Professor Marlin Linger

The University of Akron (UA) NASA Robotics Mining Competition Team
<i>Team Members:</i> •Seth Carpenter •Kelly O'Neill •Sly Robakowski <i>Advisor:</i> Dr. Michael French

Ohio Space Grant Consortium



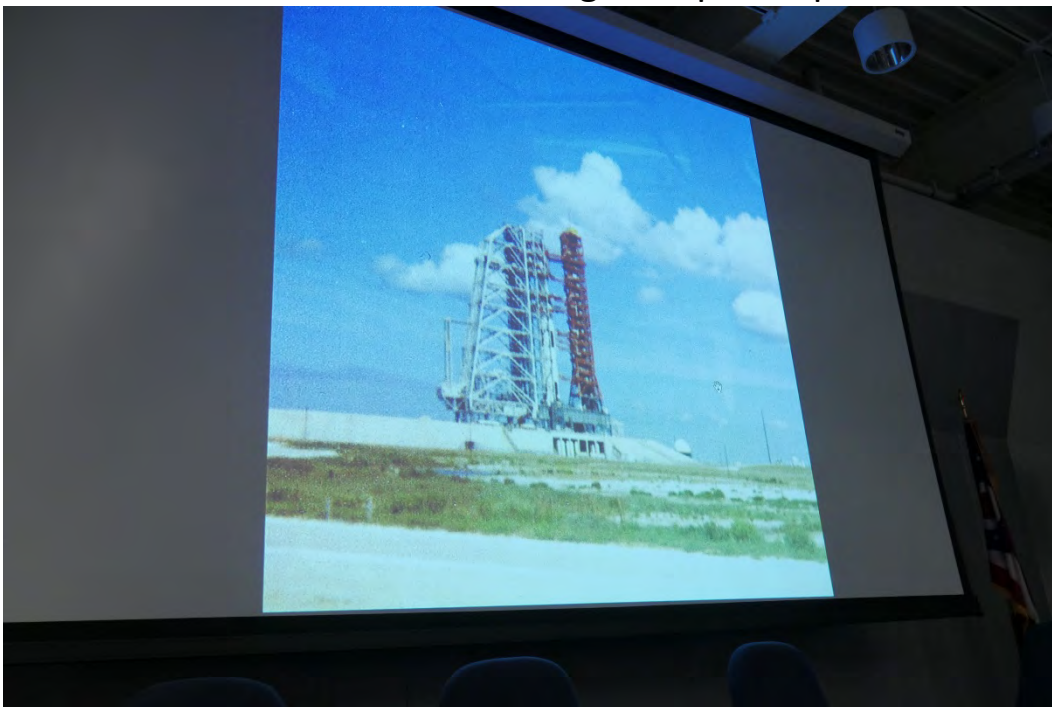
27th Annual OSGC Student Research Symposium

**Friday, April 5, 2019
Ohio Aerospace Institute
Cleveland, Ohio**

Welcome Session



Dr. Jed Marquart, Director of the Ohio Space Grant Consortium, started off bidding everyone good morning. He shared an anecdote from his youth where he and his family vacationed to Florida and visited Kennedy Space Center (when it was called Cape Canaveral). He lucked out and witnessed the original Apollo Space Mission.



Senior and Fellow Presentations



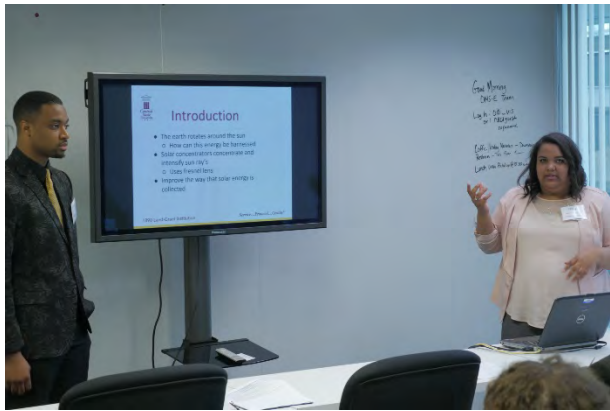
Michaela Crouch (Cedarville University) explains “Quality Assessment of 3D Printed PLA Scaffolds for Tissue Engineering of Bone Restoration Implants.”



Joel Kavaras (Baldwin Wallace University) shares the results of his work on “Mathematical Modeling of the Spread of Beech Leaf Disease.”



Amanda Miller (University of Cincinnati) describes the “Development of a Sensor Frame Based Gait Assessment Device for the Sit-to-Stand Transition.”



Kylon Payne and Lynnae Frisco (Central State University) explain the methodology behind their “Solar Concentrator” research project.



Jared Klimek (Cedarville University) elaborates on the “Design and Testing of 3D Printed Scaffolds for Large Bone Defects.”



Katherine Opacich (University of Dayton) enlightens the audience on “Analyzing the Relative Impact of Spray and Volatile Fuel Properties on Gas Turbine Combustor Ignition in Multiple Rig Geometries.”

Senior and Fellow Presentations



Garrett McCue (Baldwin Wallace University) on the complexities of "FTY720 and the Effect on Neurofibrillary Tangles Within *Caenorhabditis elegans*."



Angela Deibel (Kent State University) asks, "What Does it Take to Produce 1MW of Power?"



Erica Custer (Ohio University) immerses us in "Cortical Bone Mechanics Technology and Quasi-Static Mechanical Testing Sensitivity to Bone Collagen Degradation."



Kweisi Wilson (Wilberforce University) delves into "Optimizing Terahertz Wave Emission for Photoconductive Switches."



Madelyn Jeske (The University of Akron) explains the "Increasing Mechanical Properties of a Double-Network Hydrogel From Agar and N-Hydroxyethyl Acrylamide."



Rachel Evans (Wright State University) describes the "Effects of Scan Strategy in Additive Manufacturing."

Senior and Fellow Presentations



Reannah Rymarz (Marietta College) explores the “The Future of Geothermal Energy.”

Matthias Weisfeld (Case Western Reserve University) gives the final conclusions on his last year of working on the “Manufacturing of Artificial Moth Wings for Use in a Flapping Wing Micro Aerial Vehicle.”



Collin O’Neill (The Ohio State University) describes the “Active Flow Control in Compact Inlet/Diffuser Model of Next Generation Tactical Aircraft.”



Nicole Whiting (The Ohio State University) discusses “Active Control of Dynamic Stall Over a NACA 0012 Using NS-DBD Plasma Actuators.”



Student Teams

The University of Akron Robotics Team represented by Seth Carpenter, Kelly O'Neill, and their robot, R.O.C.K.E.E.



Professor Marlin Linger of Case Western Reserve University showing off an RC plane and drone. Professor Linger organizes UAV (Unmanned Aerial Vehicle) classes and competitions throughout the State of Ohio.



NASA Glenn HR



Christina Koleno
NASA Glenn Research Center Human Resources

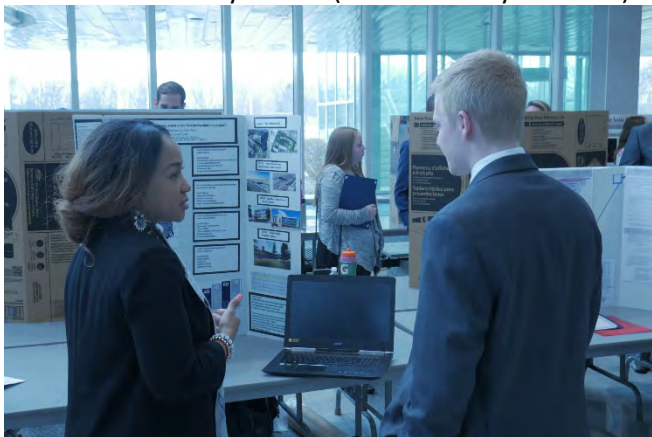
Poster Session



Samantha Arthurs (Columbus State Community College) explains the “Cost-benefit Analysis of Using Ozone to Treat Extracellular Cyanotoxins in Drinking Water Treatment Plants” to Madelyn Jeske (The University of Akron).



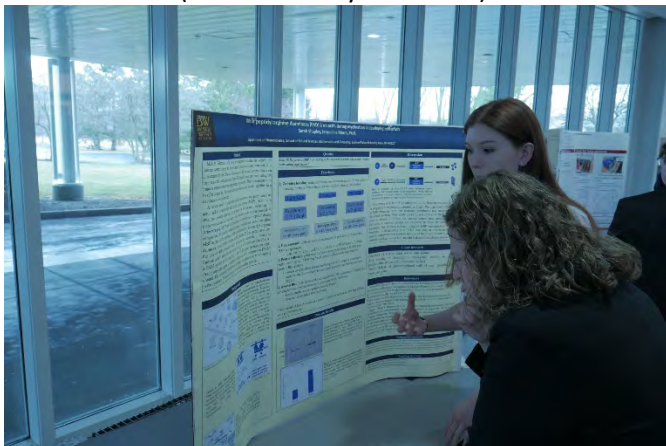
Steven Innocenzi (The University of Akron) showing off the biomimicry involved in the Octaworm (Semi-Rigid Robotics) to Angela Deibel (Kent State University).



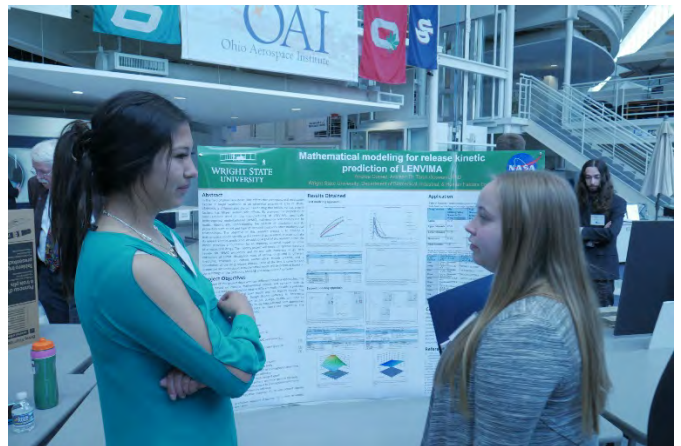
Malia Mast (Columbus State Community College) speculates on the ability of “BIM, VR, & AI Utilization to Solve Construction’s Top Issues” to Derek Messer (The University of Toledo).



Wilberforce University represented by Cyaira Cook, Dr. Jennifer Williams, Kweisi Wilson, alum Joshua Allen (NASA Glenn Research Center), Dr. Nkorni Katte, and Destonee Burks.



Carly Waugh (Ohio Northern University) learns about “Role of PAD2 on Actin in Myelination” from Sarah Shapley (Baldwin Wallace University).



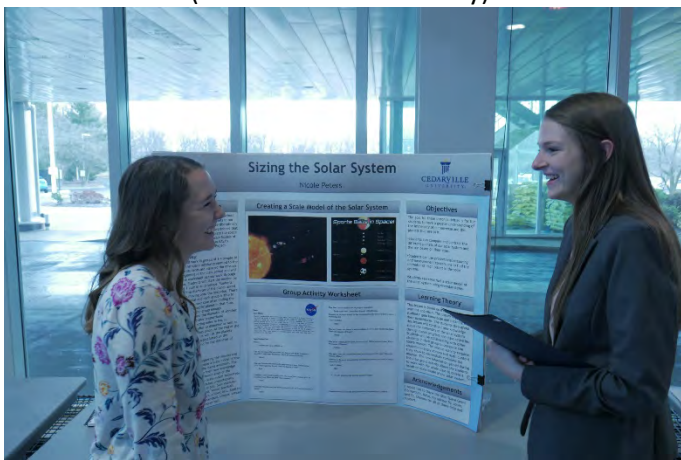
Andrea Gomez-Carrillo (Wright State University) elaborates on “Mathematical Modeling for Release Kinetic Prediction of LENVIMA” to Rachel Evans (Wright State University).



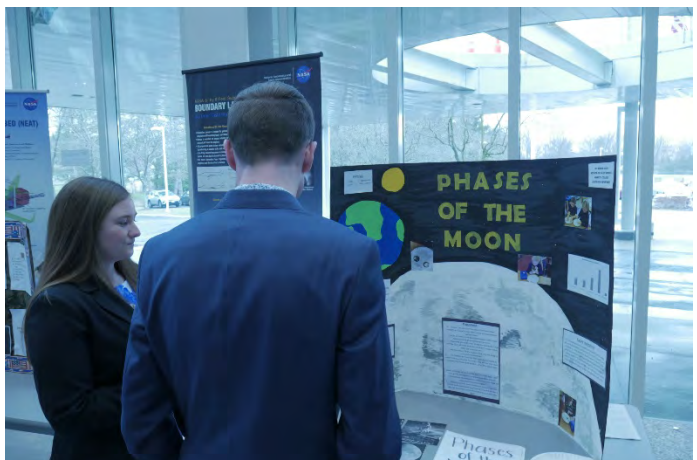
Lindsay Joy (Marietta College) shares her lesson plan on the “Importance of Our Sun” with Nya McMullen (Central State University).



Dazjuan Brittman (Central State University) hypothesizes on “Zero Gravity Gardening” with Colin Mikol (Swagelok).



Nicole Peters (Cedarville University) extrapolates on “Sizing the Solar System” with Michaela Crouch (Cedarville University).



Monica Curtis (Marietta College) asks Derek Krieg (Marietta College) “What Can You See in the Sky?”



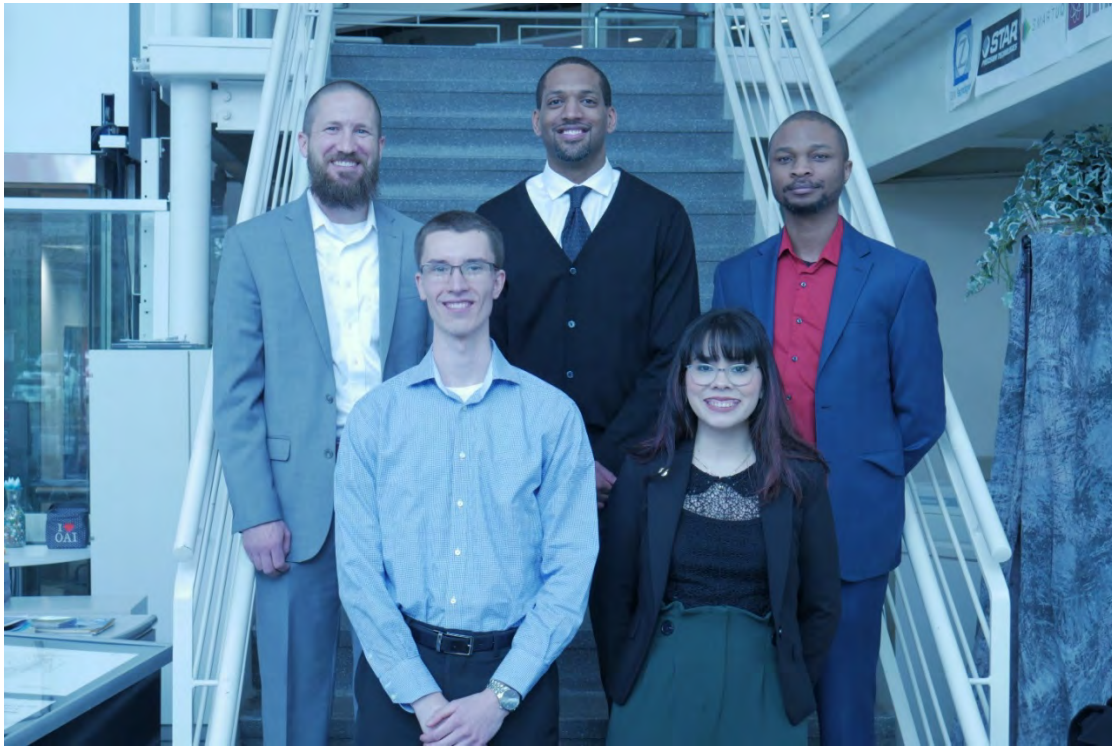
Zachary Buchman (The University of Toledo) discusses “Investigating the Role of Commercial-of-the-Shelf Products in CubeSat Development” with Professor Abigail Yee (Cincinnati State Technical and Community College.)



Madison Jewell (Wright State University) delves into the “Effect of a DNA Methyltransferase Inhibitor in Restoration of H3.3K27M-Induced p16 Repression in Human DIPG Cell Lines” with Andre Love (Central State University.)

Launching A STEM (Science, Technology, Engineering, and Math) Career

Replacing a keynote speaker with a panel of professionals, some being OSGC alumni, to discuss the job search and give real-life tips has been a great addition to the Symposium. So, behold, our lineup from this year!



This year's STEM Panel members (from left to right): Brian Neiss (Lockheed Martin); Colin Mikol (Swagelok); Joshua Allen (NASA Glenn Research Center); Gretchen Morales-Valle (NASA Glenn Research Center); and Charles Barbour, II (Raytheon).



Analysis of Using Ozone to Treat Extracellular Cyanotoxins in Drinking Water Treatment Plants

Student Researcher: Samantha K. Arthurs

Advisor: Dr. Jeff Bates

Columbus State Community College
Environmental Science, Safety, and Health

Abstract

Warmer than usual temperatures and increased nutrient pollution from runoff have increased the likelihood and severity of harmful algal blooms (HABs) in surface water around the world. HABs are large colonies of blue-green algae, known as Cyanobacteria, which can produce cyanotoxins with symptoms that can range in severity from skin irritation to liver failure. In water treatment, they are a problem for plants that use surface water sources, such as Lake Erie, because typical treatment techniques can break open the cells and release the cyanotoxins into the drinking water. Once the cyanotoxins are released from their cells, or lysed, they are considered extracellular toxins and must be treated differently than intact blooms that may be dealt with in the coagulation/flocculation stage of treatment. A memorable example of how extracellular cyanotoxins can affect drinking water occurred in 2014 when Toledo, Ohio residents were unable to drink their tap water for four days due to unsafe levels of microcystins [3]. Existing research suggests that ozone can be effective in treating the most common and dangerous classes of cyanotoxins: microcystins, anatoxin-a, and cylindrospermopsin. This project considers the costs and benefits of utilizing ozone in the drinking water treatment process in Ohio.

Methodology

The research for this project was conducted solely through existing documents on the topic, including scientific journals and the EPA official website. Effectiveness in treating extracellular cyanotoxins, usability other than treating cyanotoxins, potential byproducts, and approximate cost of the process were all considered.

Results

Ozone is useful for treating extracellular cyanotoxins because it specifically targets the double bonds, activated aromatic systems, and neutral amines of the toxins [2]. Microcystin-LR is considered one of the most toxic types of cyanotoxin as well as one of the most common [4]. Compared to two other common oxidants found in typical water treatment plants (chlorine and permanganate), ozone is more effective in treating microcystin-LR, more effective in treating cylindrospermopsin, and effective in treating anatoxin-a though slightly less effective than permanganate [2]. According to one paper, 95% oxidation of extracellular cyanotoxins was achieved for microcystin-LR by using 0.25 mg/L of ozone, for cylindrospermopsin at 0.38 mg/L of ozone, and for anatoxin-a at 0.75 mg/L of ozone [2].

A treatment plant may not be able to justify incorporating ozone for the sole purpose of treating extracellular cyanotoxins which are only a threat in the summer months, so they may also consider ozone's effectiveness as a disinfectant. Ozone is considered the second most powerful oxidant for disinfection in water treatment plants by the EPA [6]. It is considered very effective in the inactivation of cryptosporidium, a common threat to drinking water, at mean levels of 1.78, 2.75, and 3.91 mg/L [6]. It does have limitations in its effectiveness by water quality factors, including pH, temperature, and levels of iron and manganese [6].

With disinfection, there is the need to consider disinfection byproducts. Ozone does not produce the same byproducts that chlorine does, namely trihalomethanes [3]. However, ozone does react with natural levels of bromide in raw water to create the harmful disinfection byproduct of bromate [6]. Formation of bromate was detected at doses much higher than necessary to treat extracellular cyanotoxins [2]. Even 2 mg/L of ozone is below the World Health Organization guideline value of 10 µg/L of bromate [2]. Bromate formation can also be controlled by lowering the pH if necessary [6].

The costs for ozone treatment systems are directly related to the dose of ozone applied for treatment, but other factors to consider are operator training costs, ozone generator installation, in-line pumping, electrical costs for running the process, off-gas destruction facilities, and more [6]. Another cost consideration is the need to add a chemical feed for lowering pH in an effort to avoid bromate formation [6]. However, ozone uses smaller doses than other oxidants, and the need for pH adjustment is on a case-by-case basis [6].

Conclusion

Based on the results of this research paper, ozone appears to be worth the initial costs of installation and adjusting current operations. Ozone can be used as a very effective disinfectant with a manageable risk of disinfection byproducts. This not only solves the problem of extracellular cyanotoxins in the treatment plant but also assists the plant in meeting EPA rules for disinfection byproducts. Water treatment plants in Ohio may all benefit from using ozone as a primary disinfectant; however, plants that rely on surface water sources should strongly consider the use of ozone. These plants should be mindful of the levels of bromide in their source water and of the presence of extracellular cyanotoxins in their plant to ensure pH adjustments can be made if necessary.

References

1. Collins Park Water Treatment Plant. (2018). A Watertight Plan. Retrieved from <http://toledoh2o.com/the-plan>
2. Rodríguez, E. et al. (2007). Oxidative elimination of cyanotoxins: Comparison of ozone, chlorine, chlorine dioxide and permanganate. *Water Research*, 41 (15) 3381-3393. <https://doi.org/10.1016/j.watres.2007.03.033>
3. Stanford, B. D. et al. (2016). CyanoTOX: Tools for Managing Cyanotoxins in Drinking Water Treatment With Chemical Oxidants. *Journal: American Water Works Association*, 108(12), 41-46. <https://doi.org/10.5942/jawwa.2016.108.0197>
4. U.S. Environmental Protection Agency. (2014). Cyanobacteria and Cyanotoxins: Information for Drinking Water Systems. Retrieved from https://www.epa.gov/sites/production/files/2014-08/documents/cyanobacteria_factsheet.pdf
5. U.S. Environmental Protection Agency Office of Water. (2005). Technologies and Costs Document for the Final Long Term 2 Enhanced Surface Water Treatment Rule and Final Stage 2 Disinfectants and Disinfection Byproducts Rule. Retrieved from <https://nepis.epa.gov/Exe/ZyPDF.cgi?Dockkey=P100LZ09.txt>

Zero Gravity Gardenina

Student Researcher: Dazjuan M. D. Brittman

Advisor: Dr. Rajeev Swami

Central State University
College of Education

Abstract

This experimental lesson will use information NASA's data bases on the importance of plants in space, and also from the page on growing plants and vegetables in a space garden. All of this with their previous knowledge and experience with plants will co-exist when students' try to become **zero gravity gardeners**. Students will gain first-hand experience in planting plants in an unconventional manner making them think outside the box and build space knowledge.

Lesson

The idea for this experimental lesson came from an interest in plants, and the effects of gravity on them. Students will be observing and assessing the differences between normal root growth and "zero gravity" root growth, and students will partake in critical thinking.

Objectives

Communicate investigations
Critically Explain

Underlying Theory

This lesson is a great approach to independent learning and analyzation student experience, as first-hand experience students will put their prior knowledge to use and understand their new experiences. The teacher will be present to facilitate the experiments and guide students to get the most out of the experiment time. The students will have already have gained prior plan knowledge and vocabulary, as well as put it to use.

Student Engagement

The students' knowledge from the beginning of the unit will be put to the test with this hands-on activity students are responsible for their groups plants.

Resources

- Each group will need:
- 1-2 large bean seeds
- Resealable sandwich bag
- [folded] Piece of Paper
- [wet] towel
- Piece of Cardboard

Procedure

Each group will need 1-2 large bean seeds, and a resealable sandwich bag which they will open, and place a dampened folded paper in the bag.

They will then place the seeds in the middle and top of the wet towel.
The bag should then be sealed
Put the baggie in the center of their piece of cardboard, and make sure the ends are secured with tape to help hold the seeds in place.
Also make sure the bag is stretched to avoid sagging.
The cardboard should be stood upright on its side and leaned against the wall.
Students' should observe their seeds and record data over the next three days.
Once root growth is shown one to three centimeters, turn the cardboard ninety degrees.
Finally continue to observe root growth over the next several days.

Conclusion

This project will give students an opportunity to dive into the world of space, while bringing plants along for the ride. After observing the roots students will potentially have varying results, and in that they will be able to assess and identify the differences in normal root growth versus "zero gravity" root growth.

Rehabilitating a Historical Building

Student Researcher: Brian M. Brooks

Advisor: Carol Morman

Cincinnati State Technical and Community College
Civil Engineering; Construction Management

Abstract

There are a few differences in remodeling a normal building and a historical one. I have had the pleasure of working on a historical site. The steps taken before the actual work starts is different and some of the work requirements are as well. I will be discussing some of the differences in the two types of remodel.

Project Objectives

My objectives in this research are to explain some of the differences between a standard remodel and the remodeling of a Historical building. The project I used for my research is the old School of Creative and Performing Arts building in Cincinnati, Ohio, now called Alumni Lofts.

Project Breakdown

Remodeling a Historic building is a slightly different process than a normal building. For example, in a normal rehab you could cover or replace the damaged walls in the building and move forward but not so with a Historical marked building. Once the building owner has a permit to remodel, they must contact the local Historical Society in order for them to come out and inspect the building and determine what must remain intact and visible from the building's original structure in order to maintain its Historical designation. That means any of the building's original walls and floors had to be repaired not covered as in a normal building. In the example that I am using Alumni Lofts, we converted an old high school building into loft style apartments. The walls in this building were made of plaster and were severely damaged due to years of water damage. Plaster repair is a lengthy process, first you must scrape the damaged plaster off the walls. Once that is done you can get a better idea of how much damage needs repair. Plaster must be applied in layers, the first must be allowed to set before applying the next layer. It may take several layers to repair depending on the extent of the damage. The walls in the building must be kept at a minimum of 65 degrees in order for it to set right, so the winter months posed as a problem, because the walls being repaired were exterior. On several occasions the plaster would freeze, thaw and crack or fall out of the wall so the process took extremely long. It is because of this many owners as well as contractors prefer the more modern method of drywall. With a Historical building this is not an option which is the biggest difference in remodeling a normal building and a Historical one. After the plaster is done you may move forward with running your electric plumbing and ventilation systems. Fire and smoke alarms will also be installed. The interior partitions can be constructed in the more conventional drywall method.

The next step that differs in a Historical building is the floors. The floors are under the same standard as the walls, the original floor must be preserved and exposed. The hallway flooring consisted of tile, so we used grout to fill in the bigger holes then a floor machine was brought in to scrub and polish. The wood floors in the building were stripped and stained back to the original color and then buffed and waxed. In traditional remodels you generally go for the "new" look. New flooring is installed and new drywall hung and painted. In the Historic building the look is more nostalgic. You get the feel of being in an old building that looks to be kept in excellent condition. On the job site we called the imperfection

“character” which is the look you are seeking. It should look slightly damaged in order to highlight the fact that it is Historical.

Conclusion

The remodeling of a Historical building is not about repairing a building that is old and falling apart, but bring back the classic buildings of the past. The purpose is not to improve on the structure of the building which is why the original structure must be fixed and exposed, to be considered Historical. It is more about beautifying and appreciating the construction of our past. We have made many improvements in the way we build and the materials used as we moved onward in the 21 Century. I think it is important to revisit some of the classic methods of construction to compare the differences in our modern buildings and the buildings of yester year. Although it may be painstaking restoring the classic buildings and not destroying them can be useful in helping to continue the way we build in the future. Although it may be a burden remodeling the Historical building is a value to us because it allows us to revisit the past and admire how we constructed the old buildings. Construction methods have greatly improved over the years we have more tools more machines and more knowhow, but we can still appreciate the buildings of the past. More and more people are getting involved in the remodeling of the Historical buildings. It is kind of like when you buy an old car and bring it back to its glory days.

Investigating the Role of Commercial-of-the-Shelf Products in CubeSat Development

Student Researcher: Zachary J. Buchman

Advisor: Dr. Richard Molyet

The University of Toledo
Electrical Engineering and Computer Science

Abstract

Commercial-off-the-shelf (COTS) technologies have become trendy options in the world of CubeSat development. These technologies are gaining popularity because of their readiness and cost-effectiveness. Because CubeSats are often developed by students, an already-existing option is favorable as it minimizes design time. Although COTS technology is usually regarded as a quick, cheap solution, they often present issues in the areas of ease of use and reliability.

Project Objectives

The objective of this project is to research the impact of commercial off-the-shelf products in the development of CubeSats. According to United States law, a commercial off-the-shelf product (or commercially available off-the-shelf item) is a product that is a commercial item, is sold in substantial quantities in the commercial marketplace, and is offered to the Federal Government, without modification, in the same form in which it is sold in the commercial marketplace ("41 U.S. Code § 104 - Commercially Available off-the-Shelf Item.") CubeSats derive their name from their standardized cube shape. The cube shape is defined by the dimensions 10cm x 10cm x 10cm for a 1U CubeSat. CubeSat packages also include 2U, 3U, 4U, and 6U, which consists of "x" number of 1U dimensions (Loff 2017.)

Methodology Used

To evaluate the impact of COTS technologies on CubeSat developments, three specific areas were investigated: cost-effectiveness, ease of use, and reliability. For this project, cost-effectiveness is considered by comparing the price of the technology to its non-COTS counterpart, in addition to the impact its price has on the overall mission. Ease of use concerns how easily a given technology can be implemented into a larger overall system. Reliability is concerned with the dependability of the technology, specifically in a space environment.

Results Obtained

CubeSats have emerged because of their cheap entry price to accessing space. The main drivers in keeping their price low is their size and utilization of cheaper COTS components (Alanazi & Straub.) The alternative to COTS components is military approved, space certified products, which are typically too expensive for CubeSats (Bedi 2017.) While COTS components aren't as reliable as their alternatives, NASA has been utilizing COTS products for their cost effectiveness for several decades and has outlined proper use and screening for the space environment ("The NESC 2014 Technical Update," 10.)

COTS components are available in a short notice. Because timelines can be short for CubeSat launches, utilization of COTS components is imperative (Bedi 2017.) Though readily available, COTS components have documentation geared towards the product's target market. Due to this, a gray area is revealed in specifications, requiring additional research and testing to be done to determine if the product will work in system ("The NESC 2014 Technical Update," 10.) Additionally, some products have poor, misleading documentation further emphasizing the need for additional research and testing (Venturini 2017, 61.)

COTS products have a higher rate of failure due to lack of radiation-hardened components. Forty percent of CubeSats launched since 2000 were categorized as launch fail, DOA, or early loss. One common attributable cause was the utilization of COTS products (Bannatyne 2017.) Because of the inherent, accepted risk in using COTS product, the degree of pre-flight testing has increased as well as levels of redundancy (Venturini 2017, 60 & 75.)

Significance and Interpretation of Results

COTS are a fundamental aspect of CubeSat development. In order to keep mission costs low, COTS components may be depended upon. Because of the nature of COTS components, testing must be done to verify that a product will operate as intended, although the degree of testing may vary depending upon the accepted risk of the mission. Redundancy in design and of components on hand will help to mitigate the risks of utilizing COTS products.

References

1. "41 U.S. Code § 104 - Commercially Available off-the-Shelf Item." *Legal Information Institute*, Cornell Law School, www.law.cornell.edu/uscode/text/41/104.
2. Alanazi, Abdulaziz, and Jeremy Straub. "Statistical Analysis of CubeSat Mission Failure." Florida Space Grant.
3. Bannatyne, Ross. "The Challenges and Evolution of CubeSat Electronics." *Embedded*, 23 Jan. 2017, www.embedded.com/electronics-blogs/say-what-/4443299/The-challenges-and-evolution-of-CubeSat-electronics.
4. Bedi, Rajan. "Using and Selecting COTS Components for Space Applications." *Out of This World Design*, EDN Network, 13 Apr. 2017, www.edn.com/electronics-blogs/out-of-this-world-design/4458274/Using-and-selecting-COTS-components-for-space-applications.
5. Loff, Sarah. *CubeSats Overview*. National Aeronautics and Space Administration, 22 July 2015, www.nasa.gov/mission_pages/cubesats/overview.
6. "The NESC 2014 Technical Update." NASA Engineering and Safety Center.
7. Venturini, Catherine C. "Improving Mission Success of CubeSats." National Aeronautics and Space Administration, 12 June 2017.

Interaction of 5G Waves with the Human Body

Student Researchers: Destonee Burks and Brittney Gibbs

Advisors: Jennifer N. Williams, Ph.D. and Nkorni Katte, Ph.D.

Wilberforce University

Departments of Biology and Electrical Engineering

Abstract

The evolution of cellular phone devices, in the past decade, has raised serious health concerns over the level of radiofrequency (RF) waves these devices emit. This study seeks to review updated research associated with many of the health concerns raised from the specific interaction of electromagnetic waves that are absorbed in human body tissue. Energy absorption mechanisms and near-field body-antenna interactions were studied at frequencies of relevance for the next generation of mobile communication networks, 5G. The use of COSMOL software and the finite element method (FEM) technique are also analyzed to show the propagation of RF waves through human tissue. Based on simulations using COMSOL, correlations have been made between the frequencies emitted by cellular phone use and the measurement of Specific Absorption Rates (SAR), or the amount of radiation absorbed per mass of tissue within a specific time.

Project Objectives

Cellphones typically operate in the 0.4GHz-2.5GHz range. In order to analyze how much radiation is absorbed by a tissue we have to define some technical terms. The primary term used to describe the amount of radiation absorbed by a tissue is called the specific absorption rate (SAR).¹ SAR values are dependent on the separation distance of the body and the mobile phones. As the distance between the body and mobile phones decreases, the SAR values will increase, and visa-versa. This is the amount of radiation absorbed per mass of tissue, within a specific time. If the electrical conductivity of a body is σ , the magnitude of the electric field of a wave is $|\mathbf{E}|$, and the mass density of the body is ρ , the SAR is given by the formula below:

Figure 1. SAR (Specific Absorption Rate) equation in units of [W/kg].

$$SAR = \frac{\sigma |\mathbf{E}|^2}{\rho}$$

The energy absorbed in the tissues of the living body causes an increase in temperature, especially in the higher frequency regions. These waves have been reported to also affect living tissues at the cellular level, changing the modifying structures of building blocks such as the DNA.³

Methodology Used

It is of interest to analyze a typical case, where the propagation of RF energy from a device such as cell phone goes through the tissues of the human body, using realistic data. Values of the dielectric constant of the different body tissue were obtained by entering a desired frequency value into the above webpage, which then generated the real part of the dielectric constant at the frequency and the electrical conductivity, which was then used to calculate the imaginary part of the dielectric constant.⁵ The dielectric constant values for body fat used in this work were calculated based on the complex dielectric constant, expressed as: $\epsilon_r = \epsilon_r' - j\epsilon_r''$. The dielectric constant of the fabric layer is assumed to be 4, for all

frequency values considered, in the calculations. A spline function was used to extract data values not provided in the table. COMSOL multiphysics was used, to design the model and to solve the associated partial differential equations with the finite element method (FEM) technique; along with other techniques such as the finite difference time domain (FDTD), to study these models, using Maxwell's equations as the equations of interest.³

The simple model in our initial analysis was based on a cell phone situated on the pant pocket of a male. We will consider the shortest distance from the antenna of the phone to the testis of the human male, which is typically referred to as the path length. This distance comprises layers of clothing, skin, fat, muscle, and bone. Let us assume that the wave penetrates the various layers in the sequence shown in Table 1.

Table 1. Schematic representation of layers of various tissues and their assumed thicknesses

Cell phone	Clothing	Skin	Fat	Muscle	Bone	Muscle	Fat	Testicular tissue
	3mm	4mm	6cm	5cm	3cm	5cm	6cm	= 1.5cm

It is assumed that the distribution of fat and muscle layers about a central bone is symmetrical, that is why those layers are repeated, as seen in Table 1. The source of electromagnetic wave is assumed to be a cell phone. The frequency of the cell phone is varied from 0.5 GHz to about 3.5 GHz, and the following results of the field penetration and the transmission (fraction of transmitted power to incident power) were observed. After initial calculations, the peak incident electric field is assumed to be about 28V/m, which corresponds to a power density of about 1W/m², a realistic value for cell phones. The second model focuses on interaction of the cell phone with the head/brain, as seen in Figure 2.

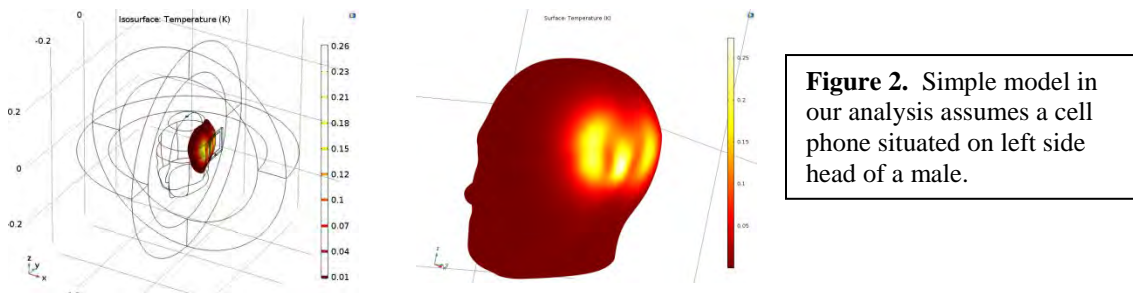


Figure 2. Simple model in our analysis assumes a cell phone situated on left side head of a male.

Results Obtained

As the frequency increases from 0.4 GHz to 3.5 GHz, the transmission of electromagnetic power drops significantly as seen in Figure 3 below. This suggest that higher frequency devices are preferred to lower frequency ones. However higher frequency fields above 1.95 GHz have been shown to attack cellular proteins (Hamada, Singh and Agarwal, 2011). This happens because the cells of our body get polarized and oscillate in sync with very high frequency fields. Hence many smart phones in the US operate at frequencies from 0.9 to 1.9 GHz.⁴

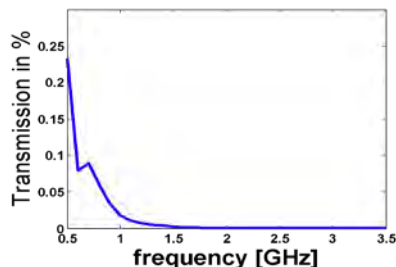


Figure 3. The Transmission of RF energy as function of frequency

The propagation of electromagnetic waves through these various tissue layers was simulated, in order to determine the electric field levels when the waves reach the testes where sperm is produced. SAR values can be very high, at about 58.9W/kg, even when the penetrated power density is seemingly small, at about 0.025mW/m². Such a high SAR could be responsible for serious biological effects like nervousness, weakness, fatigue, limb pain, joint pain and digestive problems, at this power density value.³

Conclusion

5G millimeter waves (MMW) are extremely high-frequency (30–300GHz) electromagnetic radiation. In general, the longer the wavelength the longer it travels and the farther apart broadcast stations are placed. The 5G short higher frequency millimeter wavelengths travel shorter distances (a few hundred meters). Thus to achieve a seamless integrated wireless system the “small cell” antennas are proposed to be placed about every 250m. With this information, the new 5G towers would be placed roughly two and a half football fields apart from each other, eventually resulting in higher amounts of RF energy generated at astounding rates. With these towers placed in rural communities, there are high concerns with higher radiation absorption rates within these populations. Despite simulations created with COMSOL software, studies remain inconclusive without lifetime exposure studies that adequately simulate RF wave exposure.

References

1. A. Wdowiak; et al. “Effect of electromagnetic waves on human reproduction”. *Annals of Agricultural and Environmental Medicine* 2017 Vol 24, No1 p13-18.
2. C. L. Russel “5 G wireless communications expansion: Public health and environmental implications” *Environmental Research* 165 (2018) 484-495.
3. La Vignera, S., et al. “Effects of the Exposure to Mobile Phones on Male Reproduction:” A Review of the Literature. *Journal of Andrology*, 2012, 33: 350–356.
4. V. Kumar, et al. “Interaction of Mobile Phone Waves with Tissues of Skeletal Muscles and Bone of Human Beings” *IOSR Journal of Phar. & Bio. Sciences*; V1, Issue 6 (July t 2012), P 06.
5. D. Basandraia and A. K. Dhamia. “Study of penetration depth and SAR of skin tissue exposed to cell-phone radiation” *Journal of Chemical and Pharmaceutical Research*, 2016, 8(3):917-920.

Improving Upon Current Mid- & High-Rise Structures with Hybrid Floor Systems

Student Researcher: Andrew D. Cain

Advisor: Dr. Adele Wright

Columbus State Community College
Mechanical Engineering Technology

Abstract

In recent years the field of construction science and rapid development of material science related to the construction industry has bloomed. In several studies of CLT (cross laminated timber) being used in conjunction with current concrete flooring designs, results achieved included the ability to make longer spans, have less mass, and allow for more floor deflection. An added benefit to the replacement of some of the regular use for concrete with timber is the partial reduction of CO₂ emissions from typical concrete construction.

While the research into using timber as a building material for larger and larger structures, the development of integrating timber to complement the strengths of concrete and steel construction is a step to a more sustainable building future.

Projective Objective

The objective of my research is to prove a positive correlation between using timber as a reinforcement material in a concrete system. From there, the objective is to find what common or uncommon reinforcement materials for concrete best compliment a timber reinforcement.

Methodology

Two sets of concrete samples 90mm x 508mm were poured, one set was used as a baseline at 38.00mm thick the other was 25.4mm used in conjunction with 12.7mm plywood representing a scaled down CLT system. Reinforcement materials added to the concrete samples included: fiberglass, steel fiber, hemp fiber, prestressed steel cable, as well as a non-reinforced sample. A sample of the plywood alone, as well as a 38.00mm thick plywood sample, was made to compare.

One set of the 38.00mm samples and two sets of the 25.4mm samples were poured, cure time for both sets was 24 hours in a temperature-controlled environment at 19 C. Once removed from the forms; samples cured in open air for 120 hours. 25.4mm samples were then adhered to prepared plywood using Titebond wood to the hard surface adhesive; curing for an additional 48 hours.

A digitally controlled breaking rig was designed and built to be able to repeatedly apply even pressure across the width of the samples, while at the same time recording the force data applied and sample deflection.

Each sample was set with the breaker armature in the middle, crosswise to the sample, held with steel tubing 30mm from either end. The dial indicator for deflection was set halfway between the center and 30mm from the end of the sample.

Each sample was individually loaded, until ultimate failure.

Results

The results from this testing determine if there is a benefit of using timber as a reinforcement, and if so, what concrete reinforcement best complements a benefit from timber. These findings help to narrow down a direction to focus on more in-depth research into the specifics of using timber in conjunction with concrete and steel structures. Besides just strength benefits that these systems have, reduction of CO₂ from concrete production, and sequestration of CO₂ in the growth of timber are environmental benefits as well.

Significance of the Results

The research I conducted did prove a positive correlation between using less concrete and adding a CLT foundation to the samples. An important finding was that between all the reinforcement materials for concrete- steel fiber, fiberglass, and cable, the least common material, hemp fiber, was very consistent, not only did it allow the concrete to deflect more with an applied load, it held the concrete together even after failure. I find this to be one of the most significant aspects because as a renewable, and biodegradable material it has excellent properties as a reinforcement alone, as well as with a CLT reinforcement in combination.

With ongoing, and future studies, I look forward to a future of stronger, longer-lasting buildings, that can be net zero CO₂. As well as be able to apply some of these newer technologies and advancements in residential building design.

References

1. 2013, Ongoing Research Since. "Timber Tower Research Project." *SOM*, www.som.com/ideas/research/timber_tower_research_project
2. Author, No. "awc_final." *American Wood Council*, www.awc.org/sustainability
3. "Cross-Laminated Timber (CLT)." *Cross-Laminated Timber (CLT) - APA – The Engineered Wood Association*, www.apawood.org/cross-laminated-timber.
4. Evans, Layne. "ReThinkMag." *ReThinkMag*, www.awc.org/pdf/education/mat/ReThinkMag-MAT240A-CLT-131022.pdf
5. Yeh, Borjen, and T G Williamson. *Creep and Creep-Rupture Behavior of Structural Composite Lumber Evaluated in Accordance with ASTM D 6815*, www.apawood.org/Data/Sites/1/documents/technicalresearch/paper-2007-cib-w18---creep-with-astm-d6815.pdf

Evaluating Ceramic Electrolyte Morphology Composed of Several Compositions via the Phase Inversion Method

Student Researcher: Eleana Cintron

Advisors: Frederick Dynys, Ph.D., Regan Silvestri Ph.D.

Lorain County Community College
Science and Mathematics Division

Abstract

The use of different polymer additives can be utilized to fabricate a 3D ceramic electrolyte morphology solid oxide fuel cells and solid-state batteries. In this study, the fabrication of the ceramic electrolyte is investigated via polymer phase inversion technique. To control the process, chemical additives, e.g., polyvinylpyrrolidone & polyethylene glycol, are investigated to alter the 3D structure.

Multiple slurries with different additives and polyethersulfone concentrations were casted into planar sheets at constant temperature and humidity. The ratio of polymer to ceramic was kept low to maintain a high ceramic content. The casted ceramic sheets will be analyzed through scanning electron microscopy to study the pore morphology. X-Ray powder diffraction may be used to look at possible crystalline structures.

Project Objectives

The purpose of this project is to identify chemical composition process space to create 3D ceramic electrolyte. This will be done by polymer phase inversion utilizing solvents, temperature and additives to modify the pore geometry. This process will help to develop a three-dimensional electrolyte with desired pore and channel size energy related applications.

Background and Approach

The technique of phase inversion is commonly in fabrication filtration membranes. The reaction involves a polymer, solvent, and a non-solvent. The polymer is usually one that is hydrophobic and is soluble within an organic solvent, with water acting as the non-solvent. The mixture is first prepared with the organic solvent and polymer along with the additives, and then casted and placed within a coagulant bath. Within the coagulant bath, a process of liquid-liquid demixing occurs and there is an exchange between solvent and non-solvent due to thermodynamic instability which leads to a polymer-rich phase (2004). This demixing process is utilized to create a porous membrane.

Methodology

The preparation of the slurry plays a tremendous role in affecting the morphology of the casted sheet. The viscosity of the slurry will change based on the amount of PES added as well as additives or dispersants. The viscosity will most likely increase with a higher concentration of PES within the solution and decrease with a lower concentration of PES. Based off of previous research, for the purpose of this experiment the concentration of PES in the solution will be maintained between 2.5 (w/w%) and 10 (w/w%). The desired amount of PES polymer is first measured out to be placed within a dry oven at 60 degrees Celsius to get rid of excess humidity within the granules. The organic solvent (N-N Dimethylformamide) is measured and the granules are dissolved within the solvent for several hours and stirred until fully homogenous. Then the addition of Al₂O₃ powder along with additive

(polyvinylpyrrolidone) is added to the mixture and stirred until homogenous. This mixture is then ball milled for approximately 24hrs, and then ball milled on a slower speed in order to avoid the formation of air bubbles. The slurry is then casted via doctor blade method and then placed either within a coagulant bath or sprayed with the coagulant from a spray bottle with the coagulant being either tap water or deionized water. After reacting for several hours, the sheet is then placed to dry for several hours to remove solvent and water. After drying, the casted slurry is taken for scanning electron microscopy analysis. The composition will then be evaluated based off the formation of the pores and will be modified to induced to different pore morphologies. This process will be repeated several times with different compositions made up of different organic solvents, polymer concentration, and additives such as polyethylene glycol etc. After this process is complete, different variables can be manipulated such as the temperature in which the slurries are made and then the morphology will be looked at once again. Shown below in Figure 1 and Figure 2 are two compositions that were test casted and sprayed via spray bottle to look under SEM.

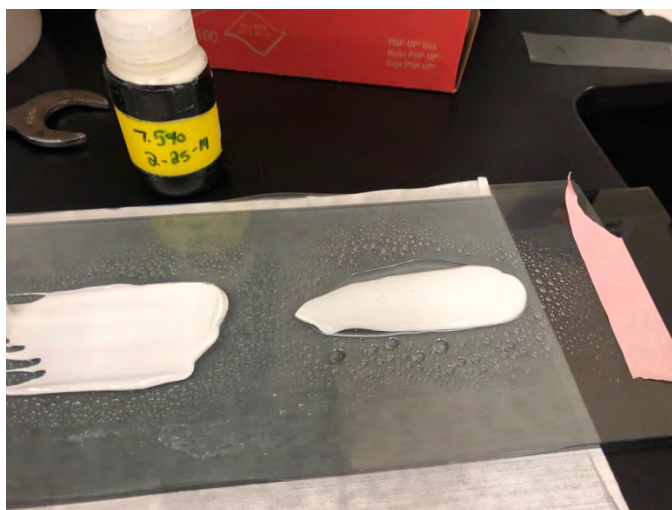


Figure 1. 7.5% PES Solution.



Figure 2. 5% PES Solution.

Results Obtained and Modifications

Currently, there are several modifications that can be made to allow for the experimental process to ensure that will allow for pore modification. The composition process needs to be perfected along with the casting process. Binders other than the PES may be used to assist in the casting process. Shown below are SEM images that show the surfaces of one of the solutions. For future runs, the samples will be coated before SEM to have better conductivity and allow for clearer images. The pictures below show a fine pore formation.

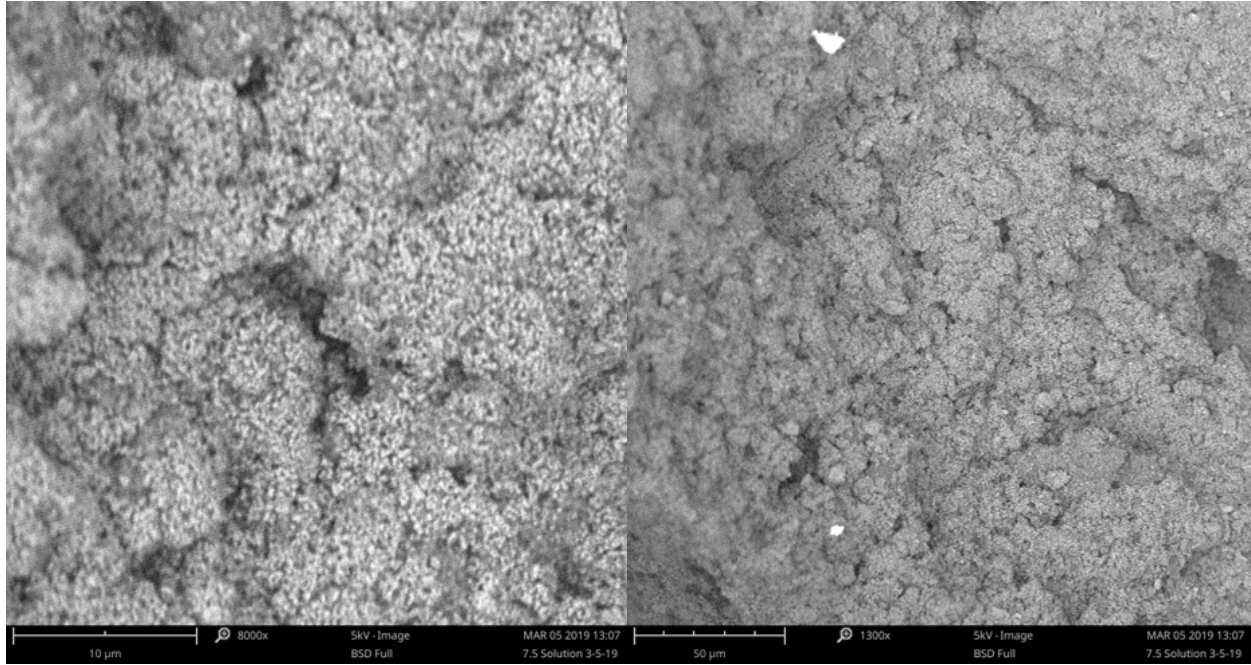


Figure 3. 7.5% PES Solution SEM Topside (left), 7.5% PES Solution Bottom Side (right).

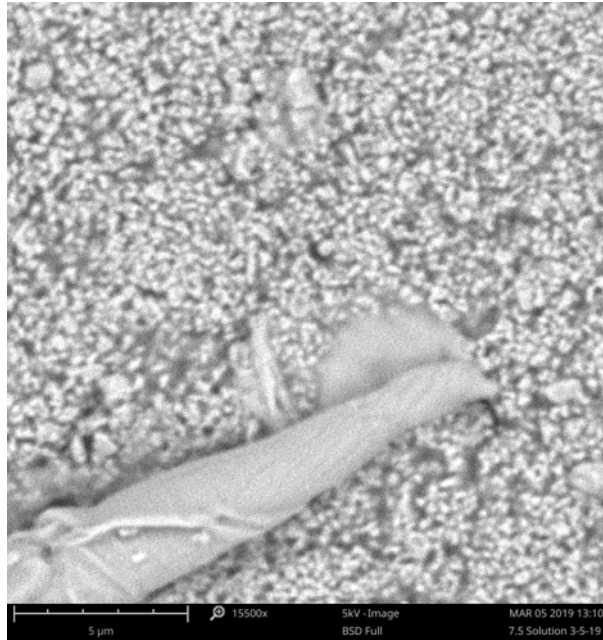


Figure 4. 7.5% PES Solution SEM (side view).

References

1. Jong, Judith & Benes, Nieck & Koops, Geert & Wessling, Matthias. (2004). Towards Single Step Production of Multi-Layer Inorganic Hollow Fibers. *Journal of membrane science*. 239. 265-269. 10.1016/j.memsci.2004.02.039.

Changes in Season (What Is Happening to Our School’s Trees and Its Leaves?)

Student Researcher: Brooke A. Collins

Advisors: Dr. Joseph D. Ortiz and Dr. Bridget K. Mulvey

Kent State University
College of Education

Abstract

In describing the series of lessons I planned, I chose to make the focus localized and personal to directly influence the first-grade students that were a part of this learning segment. I planned my learning experiences around a 5E inquiry cycle, centered around how to engage my students, provide them with an opportunity to explore concepts that need more clarification, and extend their learning to become applicable to knowledge outside of this unit, all the while using formal and informal types of assessments to help guide the decisions I would make. The lesson is concentrated on the students using their discoveries to drive this lesson; in understanding and searching for the reason as to why the leaves of the trees near their playground are changing color and falling, and will be presenting their findings to the class and other administrators at the end of the unit. In order to conduct this study, the students will be using resources provided by NASA, along with Nature of Science concepts to think about throughout this overall investigation.

Lesson

Prior to the initial start of the learning segment, students will take home a chart to complete with the support of their families in noting what times it becomes dark and light at their homes, in order for them to begin making the connection that the amount of daylight becomes shorter as we move into the season of winter, which then affects the trees’ leaves.

Engage (Day 1)	Explore (Day 2)	Explain (Day 3)	Extend (Day 4)
Students will use their written and drawn observations over what they initially notice in looking at the trees over several weeks as they share their observations and we will collect our findings on one large anchor chart.	Students will be separated into small groups and offered a printed photograph taken from NASA’s “Globe Visualization System” interactive website that will express what and how a different country’s season of fall looks like around the world.	Students will use their individually collected data to explore our findings on the changes in daylight. We will also read a short article that will encourage them to think about why adaptations and why specific environments help living things survive, such as our trees, and how they must adapt in order to continue living.	Students will be encouraged to think back to all of our findings over these past three days and to create posters with partners to showcase what they learned was happening to their schools’ trees.

Project Objectives and Alignment to Content Standards

Life Science, Basic Needs of Living Things, 2. Living things survive only in environments that meet their needs. *Effects of seasonal changes within the local environment directly impact the availability of resources.*

Throughout this learning segment, students will be able to:

- **Observe** and **describe** at least two physical changes in their local environment over a short-period of time and of a certain quality.
- **Explain**, using evidence, how certain things survive only in environments that meet their needs.
- **Compare** how the season of their own environment is different from other areas of the world in at least two ways.
- **Use** the Nature of Science character of background knowledge and experiences, as well as their own observations, to study and make sense of science in many different ways in at least one statement.

Methodology Used

In describing how this science unit specifically relates with events I have observed that focus on the children and their interests overall, the children have displayed a curiosity in our tree's changing leaf color as they have stated, "Look, the trees are changing color!" The children portray a limited understanding over the changing of seasons, so I wanted to offer my students more personal experiences in seeing this knowledge directly impact their own life and thinking. Because we were currently in the season of fall during the implementation of this learning segment, I chose to focus this unit of study on making the learning personal, hands-on, and localized to the environment in which this group of children live, while also connecting their discoveries to their own lives and experiences as aligned in theorist John Dewey's philosophies on child-centered instructional approaches. The students were active participants as "scientists" in conducting their own investigations and creation of knowledge as they noticed how their local environment was changing around them during this short period of time and in how they built upon their previous knowledge and experiences. I used the Nature of Science's elements of observation and inference to motivate the study along, by emphasizing the importance that their own collection of data matters. In wanting to connect my students' school learning environment with aspects from their individual homes and communities in this investigation, I facilitated activities where families could have conversations with their children to these topics as a result of my handout's prompts.

Results Obtained

Students' expression of knowledge will be gathered in several different ways. In order to pre-assess the understanding students have before beginning our learning segment, I will use their "Engage" observation handouts and their family "Sunrise/Sunset" chart as a preassessment to see what they know during the prior weeks before the targeted unit's lesson. While gauging the children's knowledge after presenting the instructional materials and experiences, I will use formative assessments of students' stated explanations during small and whole group discussions using an observational checklist and exit slip illustrations and prompts in order to inform where my instruction should go throughout the course of the week. In gathering their overall understanding, I will use the posters that they created during our "Extend" learning experience to present their findings from our unit's investigation over the course of this week as a summative form of assessment.

Significance and Interpretation of Results

In reflecting upon this project, the students gained much knowledge about Ohio's seasons of weather and adaptations of living things to the different environments in which they live. Students began portraying their understanding of how certain trees in warm and cool areas adapt and change the way they are in order to live in that specific environment. They appeared to enjoy exploring the NASA website as we found different places around the United States, as well as the world while we looked at the photographs they recently updated of their natural environment and its vegetation. Overall, the

majority of the students grasped the standard that trees have to adapt to the changing environment and with the trees losing their leaves, it helps them stay alive throughout winter and the rest of the year. I liked that this learning segment incorporated an interdisciplinary approach to the first-grades' subjects, but I would have liked to further spend even more time analyzing and uploading our own data and findings to the GLOBE website and get into contact with other schools. In this way, the children themselves could really see themselves as more of scientists and the importance of gathering and analyzing data in order for others to learn from.

Resources and References

- Created Materials: "Sunlight/Sunset" charts, observation charts
- Materials: paper, pencils, large chart paper, markers, poster paper
- The GLOBE Program: Global Learning and Observations to Benefit the Environment. (2018). Globe visualization system. Retrieved from <https://vis.globe.gov/GLOBE/>
- Time for Kids. (2017). A time of changes. *Time for Kids: K-1*. Retrieved from <https://www.timeforkids.com/k1/seasons/>

Quality Assessment of 3D Printed PLA Scaffolds for Tissue Engineering of Bone Restoration Implants

Student Researcher: Michaela M. Crouch

Advisor: Dr. Timothy Norman

Cedarville University

Department of Engineering and Computer Science

Abstract

The ability to repair and initiate the healing of large bone defects is a major challenge being faced by the medical field today. Small bone defects will typically heal unaided, but large bone defects require medical intervention. Current solutions are to replace the missing bone tissue with biocompatible and readily customizable materials such as 3D Printed PLA (Polylactic Acid).

This work builds on previous research that investigated the use of biodegradable scaffolds to stimulate the healing of large bone defects. The scaffolds were created using a desktop 3D printer and PLA filament and were seeded with cells to assess viability of approach. The current work investigates assessing the precision of the 3D printed scaffolds by microscopic examination methods for quantifying the effects of multiple printing parameters. Microscopic measurements (e.g. print diameter) were used to test the effects of 3D printing parameters including nozzle size, extrusion temperature, print speed, travel speed, and layer thickness. The results from this work will be used to conduct high precision production of 3D printed PLA scaffolds for the study of their use to promote bone growth.

Project Objectives

The overall goal of this research is to develop a method to create biodegradable 3D printed scaffolds that support bone growth to heal large defects. Previous research developed a unit cell based scaffold structure with compatible stiffness for being implanted in bone defects. It was demonstrated that these scaffolds were capable of hosting cell growth. The goal of this research was to determine the factors that lead to higher print quality. The first objective in accomplishing this goal was to develop a method for assessing the quality of the print. Using this method, the second objective was to evaluate the effects of various print parameters on print quality.

Methodology

Thirty-six PLA scaffolds, each 4 unit cells x 4 unit cells x 4 unit cells as shown in Figure 1a, were printed with varying printing parameters. The parameters vary were print speed, travel speed, layer thickness, extruder temperature, and extruder size.

To develop the method of assessment, measurable physical indicators of the quality were chosen. These indicators included the extraneous filament existing in the cavities of the unit cells, appearing as strings across the openings, and the measurement of the angle θ of the internal rods in the unit cell (Figure 1b). The other characteristics measured were the change in diameter d in the unit cell shown in Figure 1b, the change in diameter d across the width of the whole scaffold specimen, and the precision of the edges of the scaffold.

One face of each scaffold was selected for viewing under a microscope by visually estimating which face was representative of the overall quality of the scaffold specimen. The top and bottom faces were excluded from this selection. One row of unit cells, parallel to the printed layers, on this face was

randomly selected. The extraneous filament strings visible (Figure 2a) were counted for each unit cell in this row, and an average was taken. The angle θ projected onto the observed face was measured using the angle measurement tool in Lumenera ANALYZE software (Figure 2d). The angle was measured for each of the four unit cells in the row, and an average was taken. Next, the changes in diameter of the rods was measured. One of the rods that ran parallel to the print layer was chosen, and the maximum and minimum diameters was measured in each unit cell in the row using the Lumenera software (Figure 2b). The difference between each maximum and minimum was calculated, and an average for the row was found. The difference between the ultimate maximum and minimum for the entire row was also calculated as a measurement of the change in diameter across the width of the whole specimen. The final measurement to be made was the precision of the edges. This was found by selecting one of the edge columns, perpendicular to print layer, on the face and measuring the difference in endpoints of each print layer using Lumenera ANALYZE (Figure 2c). This was done for each unit cell in the column, and an average was taken.

In order to more easily compare the quality of the various specimens, an equation was developed to get one numerical value from the multiple measured values. The angle measurements were imprecise due to the measurement method and did not vary significantly, so these measurements were not included in the equation. The equation was developed by calculating the averages for the number of strings per unit cell, the change in rod diameter across the unit cell, the change in rod diameter across the whole specimen, and the change in endpoint position. These averages were used to weight each of these variables equally which resulted in the following equation:

$$Q = 33.86s + 1.82d + D + 1.67p$$

where s is the number of strings per unit cell, d is the change in diameter in a unit cell in micrometers, D is the change in diameter across the whole specimen in micrometers, and p is the change in endpoint position in micrometers. Using this equation, lower numbers mean higher quality, while higher numbers indicate lower quality. Analysis of variance was performed to determine if the results were significant ($p < 0.05$).

Results Obtained

The results showed that Q varied with all parameters (Figure 4). When the data was pooled by averaging the Q values of specimens with the same print parameters, the results showed that the smaller extruder sizes resulted in lower Q values, meaning they produced higher quality specimens in almost every case (Figure 3e). Using the smallest extruder size (0.25 mm) significantly ($p < 0.05$) affected the quality of the specimens. Increasing the extruder temperature and increasing the layer thickness appeared to increase the quality slightly as well, but these differences were not statistically significant.

These parameters can be used to print high quality scaffolds for further mechanical testing and cell culturing. Ongoing research is examining how the scaffolds degrade over time in the cell culturing process and how this degradation affects the stiffness of the scaffolds. Future research will be done to verify the cell growth can result in the complete healing of large bone defects, given enough time.

Figures and Tables

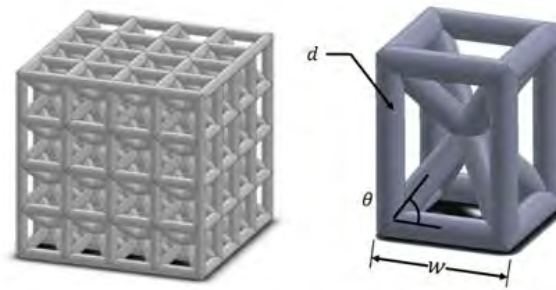


Figure 1a-b. Scaffold specimen 3D model (left) and unit cell with parameters d , w , and θ labeled (right).

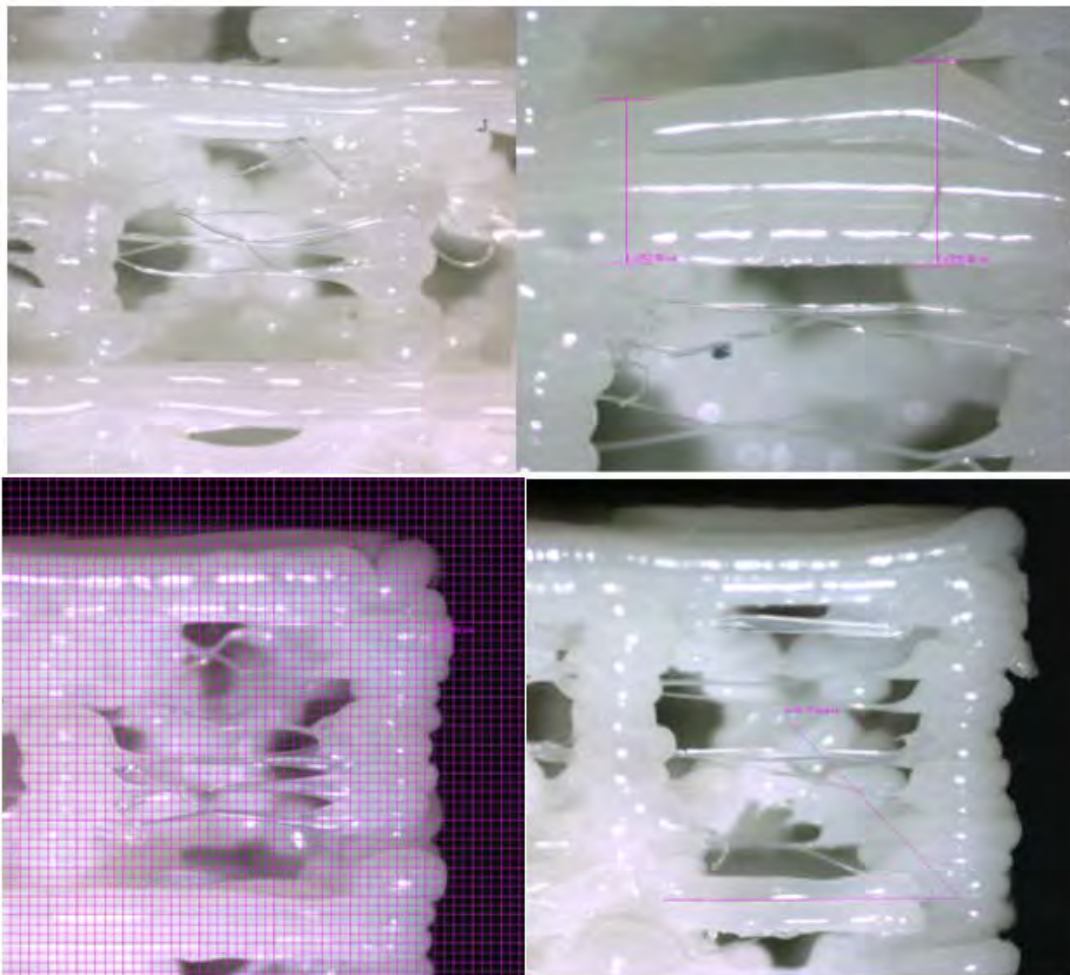


Figure 2a-d. Unit cell with several strings across opening (*top left*), maximum and minimum diameter of rod being measured (*top right*), change in endpoint position being measured using a grid (*bottom left*), and angle of internal rod being measured (*bottom right*).

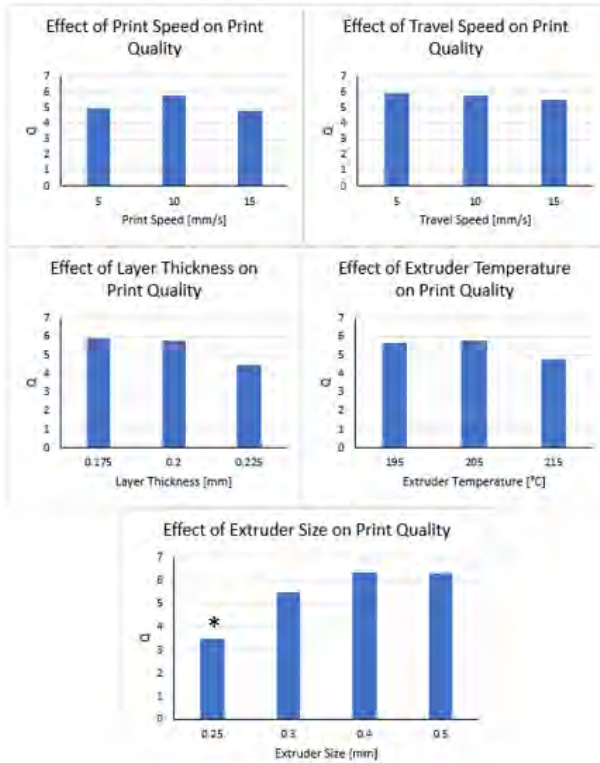


Figure 3a-e. Effects of the printing parameters: print speed, travel speed, layer thickness, extruder temperature, and extruder size, on the quality value obtained. (Lower Q values indicate higher quality.) The 0.25 nozzle had significantly better quality ($p < 0.05$) than the other nozzles.

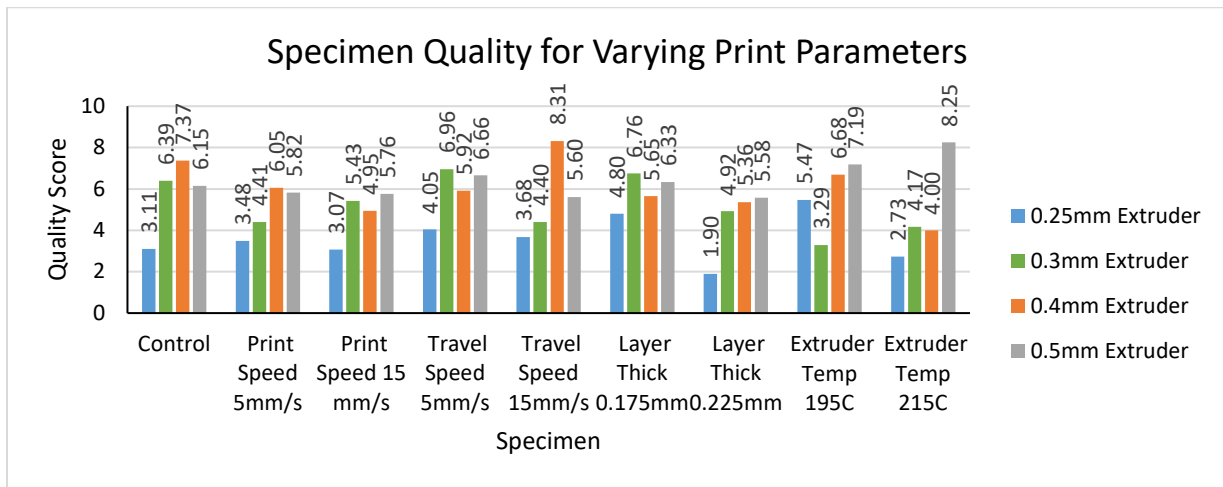


Figure 4. Quality values for each specimen.

Acknowledgments

The author of this paper would like to thank Dr. Timothy Norman, School of Engineering and Computer Science and Biomechanics Laboratory, and Dr. Rocco Rotello, School of Pharmacy, for their guidance and input in the project. They would also like to thank Sarah Seman, Jared Klimek, and Luke Schwan for their continuing research. The author would also like to thank the Ohio Space Grant Consortium for their support.

Phases of the Moon

Student Researcher: Monica L. Curtis

Advisor: Dr. Cathy Mowrer

Marietta College
Education Department

Abstract

This lesson will be geared toward kindergarten as they explore the phases of the moon and when they can see them. The Moon Phase Oreos lesson plan will be used as a reference when doing this with students. I will also use the NASA Space Place photos of the moon at the beginning of the lesson for inquiry. The students will talk about the moon compared to the sun to understand how it goes through phases. The students will have a “Night Journal” to draw pictures of what they observe. Students will work independently to create their moon phase, along with drawing the moon phase and writing what it is after doing it.

Lesson

Students will start off by observing pictures of the moon from NASA Space Place. These photos include a crescent moon, a full moon, a quarter moon, a gibbous moon, and an astronaut on the moon. They will tell what they observe to write down and if they have any questions about the pictures. If there are questions, they will be written on the board to answer by the end of the lesson.

We will then look at an anchor chart that has each phase of the moon drawn on it around the sun. This will show the students what each looks like in comparison to where the Earth and the sun are. It will show them the important phases and how the moon reflects the light from the sun to see it on Earth. It will also help them learn the names of the phases (crescent, full moon, new moon, gibbous, and quarter) and will be a reference for the students when they create their phases with Oreos.

After discussing the anchor chart, it will be modeled for the students how they will make a moon phase with their Oreo. They will be shown how to use their spoon to scrape off the crème and then draw their phase on their paper plate. The students will be able to choose any phase they choose. When they have finished making their phase and drawing it, each student will be able to explain what their phase is and what it looks like.

If time allows when the students finish their creations and drawings, they may get into groups of three to create the moon with their arms, legs, and bodies. The students will then be “sculptures” of their moon phase for their classmates to see.

Objectives

The students will be able to create the phases of the moon.

The students will be able to describe the phases of the moon.

Alignment

Kindergarten Ohio State Standard ESS.K.2. *The observable shape of the moon changes in size very slowly throughout each day of every month.*

Underlying Theory

This lesson includes a variety of ways to learn so that it can help students gain knowledge in the best way that they learn. There are many different learning styles and visual, kinesthetic, and auditory learning are three of the most important ones that students learn by within this classroom. The pictures at the beginning of the lesson lend to the visual aspect of learning, while the questions and discussion lend to the auditory aspect of learning. Using the Oreos to create a phase of the moon is a kinesthetic way for the students to learn because they are able to touch and manipulate to create and then see what they have done after. Using their own bodies to create a phase of the moon also helps with kinesthetic learning because students are able to move around and use more than just a visual to show different phases. Using all three ways of learning gives students different perspectives throughout the lesson to learn it in many different ways.

Student Engagement

The students are engaged at the beginning of the lesson when they are seeing real photographs of the moon because they are observing something that is interesting, or they may not have seen before and also asking questions. Discussing the anchor chart is more passive during the lesson before they do the Oreo phases and the sculpture phases. The Oreos are a more hands-on approach that engages students during the work because they are able to create the phase themselves instead of just looking at it. The sculpture phases are also more active, so the students are moving and engaged in this part of the learning segment since they get to move their bodies and create the phases of the moon.

Results

Twenty-one out of twenty-one of the students knew what phase they had created by the end of the lesson. Three students created a full moon, three students created a new moon, nine students created a crescent moon, five students created a quarter moon, and one student created a gibbous moon. While not all of them knew at the beginning of the lesson more than a full moon and a crescent moon, by the end, seventy-five percent (sixteen) of the students knew all of the basic phases of the moon.

Assessment

The students will be assessed on whether or not they can create a phase of the moon out of their Oreo and then out of their bodies. They will also be assessed on if they can explain what phase they created and something about the phase they chose to do.

Conclusion

This project gave students a hands-on experience and a new and interesting way to learn the phases of the moon. They had a concrete example of their moon phase and also a picture example to take home and explain. The students were able to learn with a variety of learning styles to understand about the phases. By the end of the lesson, the students were able to grasp the concept of the different phases that the moon can go through.

Cortical Bone Mechanics Technology (CBMT) and Quasi-Static Mechanical Testing (QMT) Sensitivity to Bone Collagen Degradation

Student Researcher: Erica M. Custer

Advisor: Dr. Anne B. Loucks

Ohio University

Honors Tutorial College – Translational Health Degree

Abstract

Currently, there is no way to measure bone strength in living people. In the absence of such a measure, bone mineral density (BMD) by dual energy x-ray absorptiometry (DXA) has become the standard used to assess bone health. DXA does not measure bone mechanics and BMD does not predict fracture risk well [1]. The purpose of this study was to determine the accuracy of Cortical Bone Mechanics Technology (CBMT) in measuring excised human ulna flexural rigidity (EI) and estimating cortical bending strength with potassium hydroxide (KOH) induced collagen degradation by comparing measurements made by quasi-static mechanical testing (QMT). A randomized experimental design was used in which eight pairs of ulna bones excised from cadaveric human arms were immersed in 1M KOH solution or a 0.9% calcium-buffered saline solution. For each pair of arms, the saline solution served as the control for the KOH solution. DXA measurements 1/3 region of the ulna and CBMT and QMT measurement of ulna EI (Nm^2) were made before and after immersion. QMT measurements of bone bending strength are destructive and could only be made after immersion. The maximum moment (M_{max} , Nm) was used to indicate bone strength. Effect of KOH on bone strength was detected by comparison to the contralateral ulna immersed in saline. The average percent change in nondestructive EI of the eight saline immersed specimens measured with QMT displayed no decrease in EI ($p=0.47$) but EI declined by $27.2 \pm 3.2\%$ after 39 hours of immersion in 1 M KOH ($p<0.0001$). Percent change in KOH immersed specimen EIs measured by CBMT was not statistically different from the EI change measured by QMT ($p=0.21$). KOH immersion was found to decrease measures of EI by QMT and CBMT while saline immersed specimens did not change over the immersion period. CBMT accurately detected collagen-mediated effects of KOH on the bending stiffness of whole human ulna bones.

Project Objectives

It is projected that there will be over three million incidents of fracture in the year 2025 paired with a projected financial burden of \$25 billion in the United States [2]. Alarming, the current standard of diagnosing increase fracture risk, bone mineral density (BMD), is not an accurate predictor of bone strength. One study of 261,000 post-menopausal American women found that 81% of fractures occurred in women not diagnosed with increased fracture risk [1]. Bone strength depends on more than just bone mineral. One of those properties is bone collagen [3].

The gold standard for measuring bone strength, quasi-static mechanical testing (QMT), quantifies bone strength and bone stiffness through the assessment of maximum load and bending tests. Bending stiffness (K_b) does not take the size or geometry of the bone into account so the flexural rigidity (EI) is calculated using K_b and the length (L) between the supports using equation 1. [Eqn 1: $EI = K_b \cdot L^3 / 48$]. EI has been shown to be an accurate predictor of bone strength [4–6]. Unfortunately, QMT can only test bones that have been removed from the body and therefore cannot be used in a clinical population. Cortical Bone Mechanics Technology (CBMT) is a device being developed at Ohio University that is

capable of measuring Kb and EI in the ulnas of living people. EI from CBMT has been shown to be accurate [6].

One goal of this study was to test the ability of altering collagen and mechanical properties with immersion of the whole human ulna bone in 1M potassium hydroxide (KOH). An additional goal was to determine CBMT's accuracy in measuring excised human ulna flexural rigidity and estimating cortical bending strength with KOH induced collagen degradation by comparing to measurements made by QMT. The final goal was to further prove CBMT's value by exhibiting DXA's inability to detect changes in cortical bone strength in bones with degraded protein. This goal, as well as the DXA data, was analyzed by my colleague, Sarah Warnock.

Methodology Used

A randomized experimental design was used in which eight pairs of ulna bones excised from cadaveric human arms were immersed in 1M potassium hydroxide (KOH) solution or a calcium-buffered 09% saline solution. For each pair of arms, the saline solution served as the control for the KOH solution. DXA measurements at the 1/3 region of the ulna and CBMT and QMT measurement of ulna EI (Nm²) were made before and after immersion. QMT measurements of bone bending strength are destructive and could only be made after immersion. The maximum moment (Mmax, Nm) was used to indicate bone strength. Effect of KOH on bone strength was detected by comparison to the contralateral ulna immersed in saline.

We procured eight pairs of fresh frozen cadaveric arms for a total of 16 arms from a human tissue bank (Science Care, Phoenix, AZ). Donors were restricted to males over 79.5 kg. The reason for selecting large males was to avoid getting extremely frail bones. Specimens were required to be frozen within 10 days of the donor's death to avoid altered bone stiffness [7].

A specimen was removed from the freezer and thawed before the tissue was removed. The specimens required tissue and radius removal to test in a 3-point bending testing using QMT and CBMT and for the immersion. The elbow joint was left intact because the humerus acts as a natural support for the proximal end of the ulna. After tissue removal, the 1/3 region of the ulna was scanned with DXA by Sarah Warnock after the ulna and humerus were sealed in plastic mounted in a plastic fixture and placed in a plastic container with saline. Saline simulated the *in vivo* soft tissue surrounding bones. Testing with CBMT followed and consisted of repeated measures of varying loads (15-20 N) at 50% of the ulna's length over CBMT's systematic range of frequencies (40-1200 Hz). Next, QMT was used to measure cortical bending stiffness (Kb) by repeated nondestructive 3-point bending tests to a maximum load of 100 N and EI was calculated. Then the specimens were immersed in their predetermined solution, 1 M KOH or calcium buffered 0.9% saline, for 39 hours. During the immersion, the solution was stirred periodically.

Day 2 of testing began with the removal of the bone from the immersion solution. The KOH specimen removal was more involved because the caustic solution would be dangerous if spilled. The KOH specimen was rinsed with water to avoid further collagen degradation in the bone throughout the day of testing, damage to the testing equipment or injury to lab personnel. After the rinse, another QMT nondestructive Kb test was performed to determine if the KOH immersion time was long enough to show a detectable change in EI. All KOH specimens demonstrated decreases in EI from the 39-hour immersion. The procedure for Day 2 of the saline-immersed specimen was identical to the procedure for the KOH-immersed specimen after the first round of QMT. The specimens were DXA scanned, measured with CBMT, measured with a nondestructive Kb with QMT, and then fractured with QMT. The QMT

fracture test was performed to measure the strength of the bone and concluded the testing on that specimen. After specimens were fractured, they were immediately deconstructed. Deconstruction consisted of cutting through the tissue of the elbow joint to separate the bones from each other and to separate the ulna in distal and proximal halves at the fracture site. Tissue was removed from each bone segment. The distal ulna length was measured and recorded to note where the fracture occurred along the length of the ulna. The proximal and distal ends of the ulna were weighed.

Results Obtained

The mean (\pm SD) of the age and BMI of the eight donors were 68.9 ± 8.4 years and 28.2 ± 4.7 kg/m², respectively. The mean (\pm SE) EI before immersion of all the specimens was 46.3 ± 4.1 Nm² measured by QMT and 45.2 ± 4.3 Nm² by CBMT. A paired t-test found these values to not be different from each other ($p=0.13$).

One aim of this study was to show the change in mechanical properties of the specimens due to immersion. The mean percent change in nondestructive EI of the eight saline immersed specimens measured with QMT displayed no decrease in EI ($p=0.47$) but EI declined by $27.2 \pm 3.2\%$ after 39 hours of immersion in 1 M KOH ($p<0.0001$) as shown in Figure 1.

Another aim of this study was to compare CBMT’s detection of change in mechanical properties to QMT’s detection. The mean percent change in EI of the eight saline immersed specimens measured with CBMT was not statistically different from zero change ($p=0.8$) but the KOH immersion resulting in a $20.6 \pm 6.1\%$ decline in EI ($p=0.01$) as shown in Figure 1. Percent change in KOH immersed specimen EIs measured by CBMT was not statistically different than EI change measured by QMT ($p=0.2$).

Change in Mmax was calculated by subtracting the saline Mmax from its paired KOH Mmax (Fig 2). The mean (\pm SE) percent change for these pairs was $-29.2 \pm 6.4\%$. This difference was significantly different than zero ($p=0.003$).

Significance and Interpretation of Results

These findings demonstrate the ability of CBMT to detect the collagen-mediated effects of KOH on the bending stiffness of whole human ulna bones.

Figures/ Charts

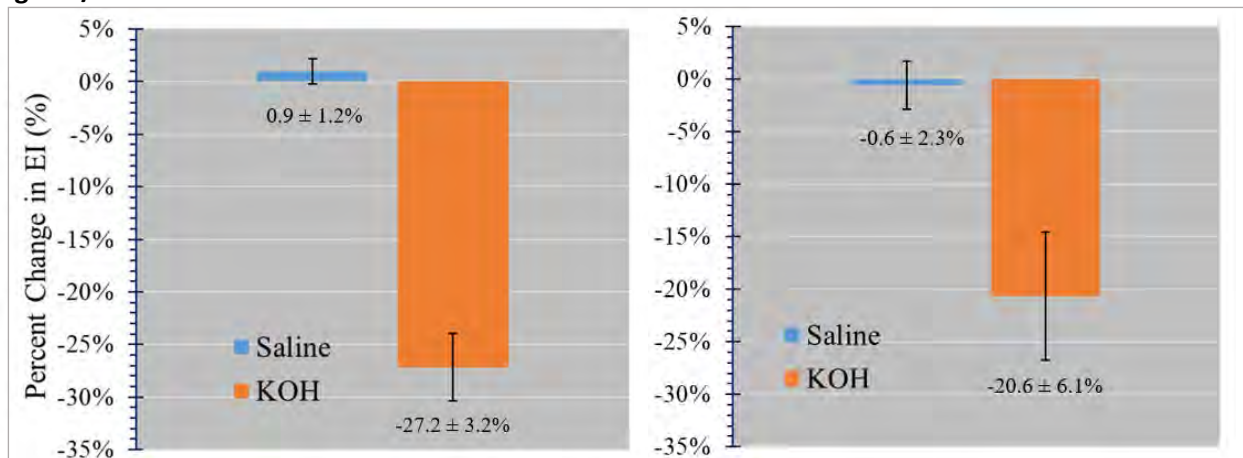


Figure 1. Mean percent change (\pm SE) in EI by QMT (left) and CBMT (right) from pre- to post-immersion.

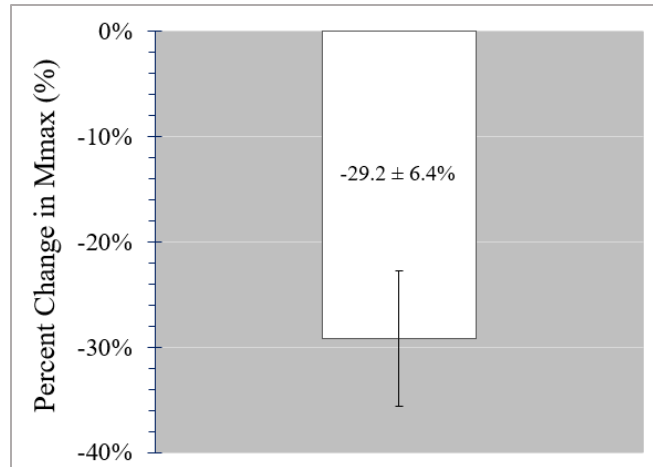


Figure 2. Immersion effect on paired (KOH-saline) mean percent change (\pm SE) in Mmax.

Acknowledgments

Research described in this report was supported by the National Institute on Aging of the National Institutes of Health under Award Number R43AG058312. The author would like to thank Dr. Betty Sindelar of the Ohio University Division of Physical Therapy for the use of her QMT device. Additionally, the author would like to thank Dr. Anne Loucks and Mr. Lyn Bowman for their guidance on the project. Finally, the author would like to thank her colleague, Ms. Sarah Warnock, for her collaboration and the lab assistants for their contribution.

References

1. Siris, E. S., Miller, P. D., Barrett-Connor, E., Faulkner, K. G., Wehren, L. E., Abbott, T. A., Berger, M. L., Santora, A. C., Sherwood, L. M.: Identification and fracture outcomes of undiagnosed low bone mineral density in postmenopausal women: results from the national osteoporosis risk assessment. *JAMA*. 286, 2815–2822 (2001). doi:10.1001/jama.286.22.2815
2. Burge, R., Dawson-Hughes, B., Solomon, D.H., Wong, J.B., King, A., Tosteson, A.: Incidence and economic burden of osteoporosis-related fractures in the united states, 2005–2025. *J. Bone Miner. Res.* 22, 465–475 (2007). doi:10.1359/jbmr.061113
3. Viguet-Carrin, S., Garnero, P., Delmas, P.D.: The role of collagen in bone strength. *Osteoporos. Int.* 17, 319–336 (2006). doi:10.1007/s00198-005-2035-9
4. Borders, S., Petersen, K.R., Orne, D.: Prediction of bending strength of long bones from measurements of bending stiffness and bone mineral content. *J. Biomech. Eng.* 40–44 (1977). doi:10.1115/1.3426267
5. Jurist, J. M., Foltz, A. S.: Human ulnar bending stiffness, mineral content, geometry and strength. *J. Biomech.* 10, 455–459 (1977). doi:10.1016/0021-9290(77)90099-9
6. Bowman, L., Ellerbrock, E. R., Hausfeld, G. C., Neumeyer, J. M., Loucks, A. B.: A new noninvasive mechanical bending test accurately predicts ulna bending strength in cadaveric human arms. *Bone*. 120, 336–346 (2019). doi:10.1016/j.bone.2018.11.018
7. Tennyson, R. C., Ewert, R., Niranjana, V.: Dynamic viscoelastic response of bone. *Exp. Mech.* 12, 502–507 (1972). doi:10.1007/BF02320746
8. Nyman, J. S., Roy, A., Shen, X., Acuna, R. L., Tyler, J. H., Wang, X.: The influence of water removal on the strength and toughness of cortical bone. *J. Biomech.* 39, 931–938 (2006). doi:10.1016/j.jbiomech.2005.01.012

What Does It Take to Generate One Megawatt of Power from Fuel Cells?

Student Researcher: Angela M. Deibel

Advisor: Dr. Yanhai Du

Kent State University

College of Aeronautics and Engineering

College of Businesses Administration

Abstract

Many people of the population will continue to remain blissfully unaware- as they do now, of where their energy comes from. Consumers do not think of energy in terms of its source, or impact, but rather in terms of its availability- whether it is there for their use or not.

At the end of the day, a person often does not care where that particular megawatt of power come from, only that refrigerator runs or the dishwasher starts. Whether it comes from coal, wind energy or natural gas does not matter-as long as they have power. Luckily, energy is a fungible asset. One megawatt of non-renewable sourced power can be replaced with one megawatt of renewable power without consumers' noticing.

A one megawatt fuel cell generator was created by two companies using a series of nine Proton Exchange Membrane Fuel Cells (PEMFC). Three of these commercial PEMFCs were donated to Kent State's Clean Energy and Sustainability lab. A fuel cell is a device that converts fuel into electricity. If using hydrogen as the fuel, it produces no emissions. Among the three donated, one was disassembled and put back together.

Project Objectives

Successfully disassemble and reassemble a Fuel Cell Module (FCM); Understand the fuel cell module from the smallest atomic level, to the general systems level; Analyze energy as a product from a consumer's point of view, and explore the applications of a fuel cell system.

Methodology Used (Disassembly)

Note: Disassembly occurred in stages using FCM13. To ensure that the module could be properly reassembled, it was partially dissembled, put back together, and partially dissembled again, a little further each time.

- 1.) The five faces of FCM13 were taken off to expose the inside.
- 2.) The cage of the FCM had to be removed to access the inner components.
- 3.) Tubes were disconnected first. A system of numbers and letters were used to pair the tubes with their fittings so they could be replaced exactly as found.
- 4.) Following the removal of the tubes was the removal of the extensive water filtration unit
- 5.) The hydrogen cast was removed after, and the manifold to the fuel cell stack was finally exposed
- 6.) Removal of one single stack was achievable after being given access to the manifold.
- 7.) The fuel cell stack was opened using a small handsaw.
- 8.) A single cell was removed from the stack, exposing the gas distribution channels
- 9.) The FCM was reassembled, with the exception of one stack. The stack, no longer being under tension, will not be able to be replaced back into the cell.

Results Obtained

The FCM has three major flows in its system: water, hydrogen, and oxygen. Hydrogen entered the FCM and was sent to the hydrogen cast. The cast's role was to bring the gas up to temperature and to humidify the fuel so that the cells would not dry out. The air cast played a similar role, bringing oxygen up to temperature and humidifying it before it entered the fuel cell stack.

The flow of water in the fuel cell module was the most extensive part of the system, occupying most of the physical space inside the module. The role water played was also the most confounding, as every pipe, fitting and tube connection was waterlogged during disassembly. The company who manufactured the FCM sent a representative to answer questions per the researcher's request.

The flow of water in the system regulated the temperature of the fuel cell. The water produced by the cell's electricity generation was added to this flow, and used to humidify the air and hydrogen before they entered the manifold. The extensive water filtration unit ensured that the water did not become accidentally conductive. As water flows through the module's pipes and fittings, small metallic particles can come loose and join the flow. If the water is conductive, electricity can be carried out of the fuel cell stack, which is undesirable.

Significance and Interpretation of Results

The FCM13 has undergone a disassembly which will cause it to never work again. However, due to the size of the module, and the amount of hydrogen required to run it, it far surpasses most university's capabilities.

The Fuel Cell Modules in Kent State's Clean Energy and Sustainability lab have found a higher purpose as a method for teaching and learning, as well as public education on fuel cell technologies. A number of undergraduate students, faculty, graduate students, post-docs, and high school students assisted in its disassembly. When visitors come to Kent State University's Clean Energy and Sustainability lab, the module exists as a prime example of engineering, passion and science.

Acknowledgments and References

The author of this paper would like to thank Dr. Yanhai Du, for providing the opportunity, mentorship, guidance, and inspiration. Other people to be acknowledged in this project are as follows: Kyle W. Angermeier (undergraduate), Edward "Wayne" St. James (lab technician), Joseph Hughes (High school student / Intern), Donna Payravi (Final Editor), Tejas Dudhade (Graduate/Lab Assistant), Hai Feng (Graduate/Lab Assistant), Dr. Dhruva Panthi (Post-Doc), and Dr. Nader Hedayat (Post-Doc).

Figures/Charts



Figure 1 (above). FCM13. Front face. Weight: 720 lbs

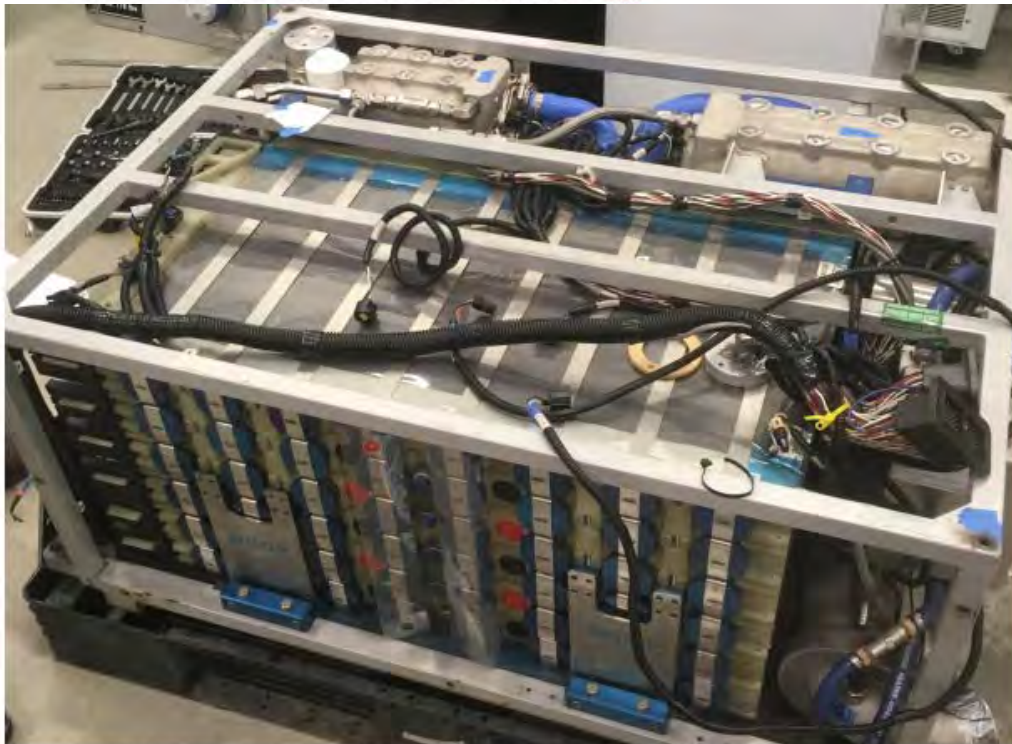


Figure 2 (above). FCM 13, exposed. Alternating red and black dots on the side represent the fuel cell stacks



Figure 3 (above). One fuel cell stack removed.

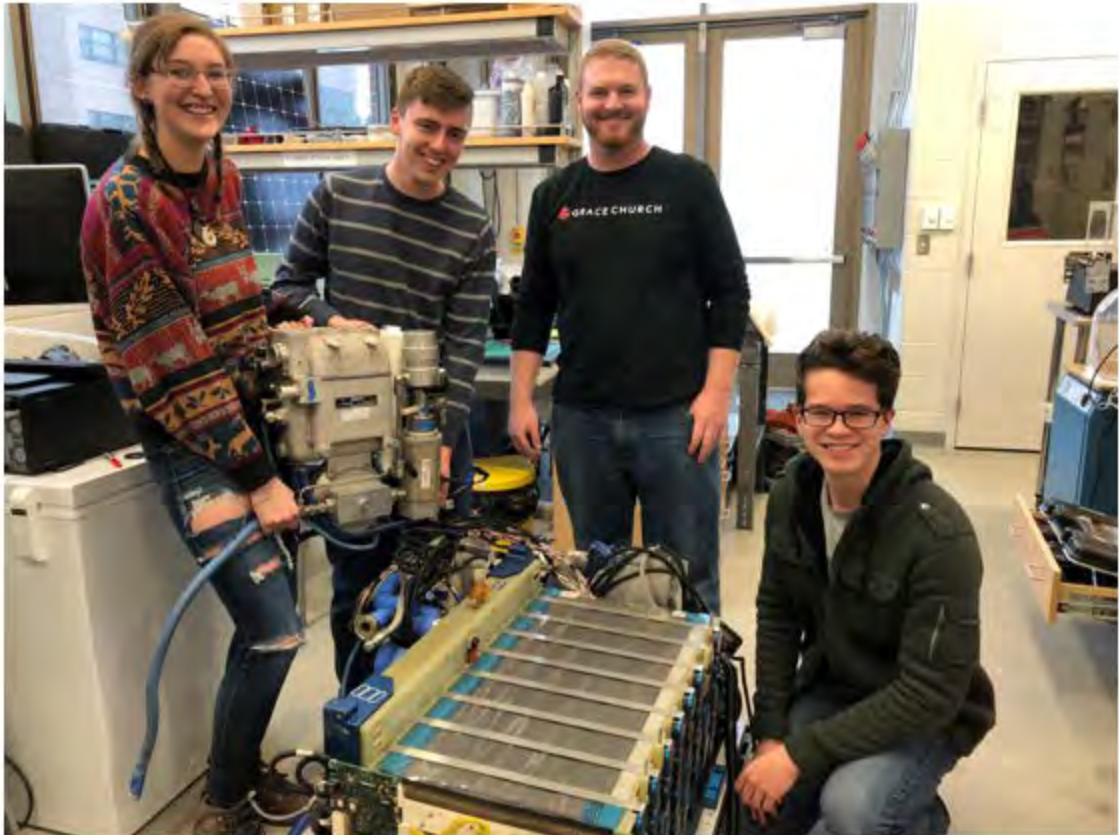


Figure 4 (above). A few students working on a fuel cell module.

MOSFET Junction Temperature Measurements Based on Conducted Electromagnetic Emissions

Student Researcher: Justin C. Demus

Advisor: Dr. Mark Scott

Miami University
Electrical Engineering

Abstract

As power electronics permeate critical infrastructure in modern society, more precise and effective diagnostic methods are required to improve system reliability as well as reduce maintenance costs and unexpected failures. Prognostic Health Management (PHM) systems that analyze changes in the electromagnetic spectrum (E-PHM) of a circuit can be implemented to determine the health of the equipment under test. This research demonstrates the use of E-PHM techniques to measure the junction temperature of a silicon carbide (SiC) MOSFET. The results show the feasibility of training machine learning algorithms to recognize this relationship and determine the junction temperature within 10 °C. This is accomplished, in situ, without interruption of device operation and without altering the system's performance.

Project Objectives

This project seeks to predict the junction temperature of a MOSFET device by measuring the electromagnetic emissions (EM) present in the power supply. Initially, EM data must be gathered from an appropriate test platform via high bandwidth current sensors. The project also focuses on the implementation of a support vector machine (SVM) learning model to predict the temperature of the semiconductor device based on input EMI data. Ultimately, this research is intended to further the study of electromagnetic emissions as a prognostic tool in the application of condition monitoring.

Methodology Used

To model a real life application of power electronics devices, a buck converter topology was designed with a 370 μ H inductor and a 1.02 mF load capacitor drives a 150 Ω load. The SiC MOSFETs (C3M0065090D) were switched at 20 kHz with a 50 % duty cycle. A chassis mounted power resistor was attached to the MOSFET heat sink and used to more effectively control the semiconductor device temperature. Two Line Impedance Stabilization Networks (LISN) monitored EMI in the circuit, feeding frequency data to an MDO3104 oscilloscope/spectrum analyzer. Data collection was organized into three types of noise measurements across two frequency ranges. Common mode noise (CM), differential mode noise (DM), and total noise (TN) were measured at room temperature (\sim 22 °C), 30 °C, in ten-degree Celsius increments until 60 °C. At each temperature, the noise spectrum was measured first between 100 kHz and 1 MHz (LF), then at 1 MHz to 40 MHz (HF).

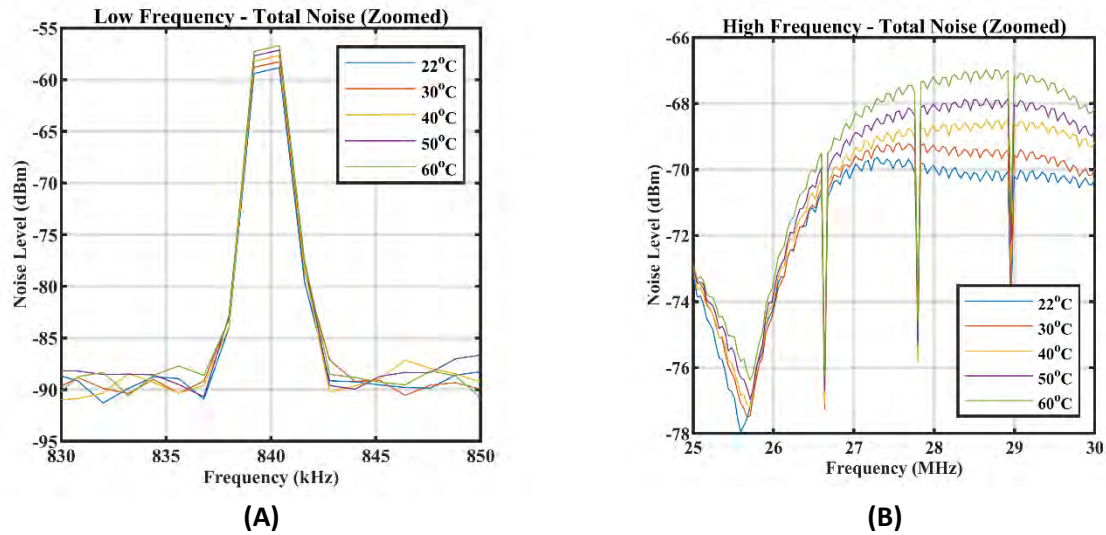
Results Obtained

The preliminary test results for total noise (TN) E-PHM measurements are shown in Fig. 3. The buck converter ran with an input voltage of 270 V, an output voltage of \sim 135 V (135.1 V), and a switching frequency of 20 kHz, yielding a total output power of \sim 135 W. The plots shown were generated in MATLAB from the maximum noise measured in each set of tests. For brevity, measurements are only shown for total noise. Immediately, one can see that the HF measurements yielded results with greater differentiation between temperature tests than the low frequency. Test results in the lower frequency range of 1 kHz to 100 kHz yielded few frequencies in which an outstanding distinction could be made from noise measurements taken at different temperatures. However, in the higher test frequency range

of 1 MHz to 40 MHz, the frequency spectrum 26.75 MHz to 30 MHz yields a significant stratification between the various temperatures, demonstrating the feasibility for determining MOSFET junction temperature using the frequency spectrum of the circuit's EMI.

This research used SVM models to classify the measured data and determine the junction temperature of a MOSFET. The SVM operates by comparing input data to a trained model. These comparisons are used to sort experimental data sets into predefined classes that correspond to a given temperature. Five classes representing each tested temperature were defined for this experiment. A training model was developed using 25 data samples gathered at each MOSFET junction temperature per noise spectrum (TN, CM, & DM). Additional data sets at each temperature were then classified according to the developed model.

Table 1 depicts the resulting confusion matrices of the SVM model using total noise E-PHM measurements. Across all noise spectrums, the model was able to reliably classify junction temperature with at least 94% accuracy, often higher.



Act. \ Dec.	22 °C	30 °C	40 °C	50 °C	60 °C
22 °C	25	0	0	0	0
30 °C	0	25	0	0	0
40 °C	0	2	22	1	0
50 °C	0	0	0	25	0
60 °C	0	0	0	0	25

Table 1. Confusion Matrix for Low Frequency (left) and High Frequency (right) TN E-PHM Temperature Measurements.

Figure 3. (A) Zoomed view of low frequency TN exhibiting higher harmonics at between tested temps. (B) Zoomed view of high frequency TN exhibiting higher noise at evaluated temperatures.

References

1. M. Boubin, J. P. Doran, W. Guo, Y. Rajasekhar and M. Scott, "EMI Diagnostics of Three Phase Inverters Using Machine Learning Algorithms," 2018 IEEE Energy Conversion Congress and Exposition (ECCE), Portland, OR, 2018, pp. 4062-4069.
2. Y. Avenas, L. Dupont, N. Baker, H. Zara and F. Barruel, "Condition Monitoring: A Decade of Proposed Techniques," in *IEEE Industrial Electronics Magazine*, vol. 9, no. 4, pp. 22-36, Dec. 2015.
3. S. Yang, D. Xiang, A. Bryant, P. Mawby, L. Ran and P. Tavner, "Condition Monitoring for Device Reliability in Power Electronic Converters: A Review," in *IEEE Transactions on Power Electronics*, vol. 25, no. 11, pp. 2734-2752, Nov. 2010.

The Effect of Scan Strategy in Additive Manufacturing

Student Researcher: Rachel E. Evans

Advisor: Dr. Joy Gockel

Wright State University

Department of Mechanical and Materials Engineering

Abstract

Laser powder bed fusion (LPBF) is an additive manufacturing (AM) process in which a laser selectively melts layers of material to form three-dimensional structures. The heat transfer during this process is not yet fully understood due to its transient nature, which is difficult and time-consuming to accurately model. However, it is very important to understand this heat transfer in order to move forward with improvements in the LPBF process, as it provides crucial information about the resulting material properties of the final part. This research project uses a semi-analytical approach to simulate the thermal conditions of the LPBF process using variations in the geometry of the scan strategy. The resulting thermal conditions are then plotted on color maps in the spatial domain. These color maps clearly show the patterns within these scans and the differences that are caused by changing the geometry of the scan path.

Project Objectives

There are many factors to consider when manufacturing any type of product. In AM, many of these factors are a direct result of part defects and microstructural variations that are caused by the scan strategy and processing parameters used to build the part. LPBF is a metal AM process in which a layer of powder material is selectively melted by a laser beam. This results in a pool of liquid metal, which then cools to a solid state. This melting and cooling procedure is repeated multiple times to create layers that form a full part. This process is beneficial because it allows for complex parts to be created with a high resolution. However, the heat transfer in LPBF is not fully understood, thus needing more research. This research project uses a semi-analytical modeling method to predict thermal conditions and defects in LPBF. This prediction method is needed to guide an increase in the efficiency and effectiveness of the AM process.

Methodology

This research project models the LPBF process with a semi-analytical approach, which utilizes a transient heat conduction solution to compute temperature data as a result of a circular ring heat source [1-5]. The model assumes a semi-infinite domain and neglects the effects of latent heat and heat loss due to vaporization and convection, while also assuming constant and uniform material properties. However, this model can capture transient effects caused by multiple scanning paths, which is essential in investigating the thermal behavior of the LPBF process.

The semi-analytical solution, which uses the variables given in Table 1, is given by:

$$T(x, y, z) = T_0 + \frac{q}{c_p \rho (4\pi a)^{3/2}} \cdot \int_{\tau_i=0}^{\tau_i=t} \frac{1}{\tau^{3/2}} \exp\left(-\frac{r_0^2 + x^2 + y^2 + z^2}{4a\tau}\right) \cdot I_0\left(\frac{r_0}{2a\tau} \sqrt{x^2 + y^2}\right) d\tau_i \quad (1)$$

Table 1. Variables used in the semi-analytical approach.

Variable	Description	Units
$T(x, y, z)$	Temperature at point (x, y, z)	K
T_0	Initial temperature	K
q	Absorbed power	J/s
c_p	Specific heat	J/K
ρ	Material density	g/cm ³
a	Thermal diffusivity	m ² /s
τ_i	Integration time step	s
t	Time	s
τ	Time available for conduction	s
r_0	Radius of heat source	m
l_0	Bessel function of the first kind, zero order	none

This approach, which has been written into code by Plotkowski et. al [1], computes the temperature and thermal conditions as a result of a laser beam that scans in a user-defined path. This research project introduces MATLAB code that uses data from the heat transfer code to plot a color map of cooling rate in the spatial domain, which is useful in predicting the microstructure of the material.

The first scan strategy comparison in this project relates to the transient effects of the LPBF process. In the first experiment, a simulation of a single laser pass is compared to a scan of 12 passes in a striped pattern. The single bead simulation represents steady-state conditions, while the striped multiple bead scan includes more of the transient thermal effects from the repeated laser passes.

The next scan strategy comparison is used to investigate the thermal effects of changing the geometry of the scanning pattern in the LPBF process. This experiment uses a thick-to-thin geometry, which is composed of a 10 mm square section and a 10 mm by 2 mm rectangular section. These sections are referred to as the “thick” and “thin” sections, respectively. During the printing process, the laser scans across the geometry vertically in a striped pattern, then begins a new layer that scans horizontally. This process is repeated multiple times to create layers that form a three-dimensional cube. Thermal models of these thick-to-thin layers can be used to provide information about the variations in the thermal conditions as a result of changing the stripe width.

The geometry of these thick-to-thin samples allows for some simplifications regarding the necessary number of simulations. First, the thick and thin portions can be simulated as two separate parts because they are scanned separately. This will save on computation time because it allows the simulations to be constrained to smaller areas of interest. Therefore, the separated simulations provide data for only the necessary points in that section. Additionally, the thick section is a square, which means that both the vertical and horizontal scans have stripe lengths of 10 mm in the thick portion. The heat transfer of these two scans are essentially the same, but oriented at an angle of 90° from one another. Similarly, the vertical scan of the thin section also has a 10 mm stripe length. As a result, there are only two necessary simulations that are needed to fully represent the thick-to-thin geometry: the long (10 mm stripe width) scan and the short (2 mm stripe width) scan. These areas of interest are highlighted in Figure 1, with the red portions representing the long scans and the blue portion representing the short scan.

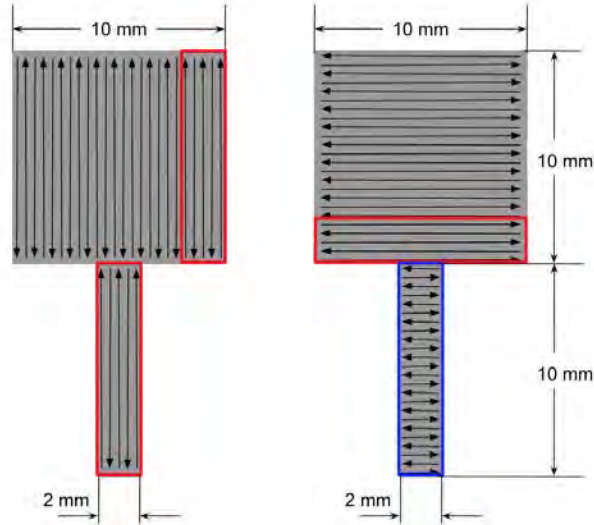


Figure 1. The vertical and horizontal scans of the thick-to-thin experiment. The portions highlighted in red indicate the long scans, while the portion highlighted in blue represents the short scans.

Results

The following results include spatial color maps—shown in Figure 2—for the cooling rate in the single bead and multiple pass experiment. When comparing these two plots, it is clearly shown that the number of stripes influences the magnitude of the cooling rate at solidification. In the single bead path, the cooling rate remains relatively constant throughout the whole path. However, the multiple pass simulation shows that the cooling rate slows down around the edges as the number of stripes increase. These slower cooling rates along the edges are due to the scan path; since the laser turns around and immediately begins scanning the next pass, the beam spends a lot of time on the edge. This causes more heat to be applied to the edge, which takes longer to cool.

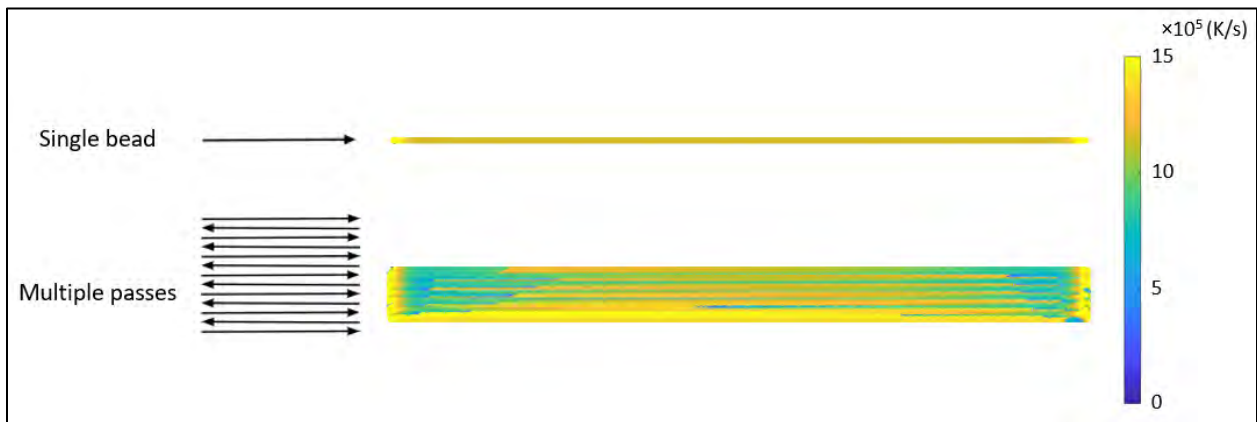


Figure 2. The cooling rate color maps of both the single bead and multiple pass experiments.

The next results shown are the stripe width variations that resulted from the thick-to-thin simulations. In these simulations, it is shown that the long stripe width provides faster cooling rates than the short stripe width. This is because the short stripe width retains more heat, which takes longer to cool. These cooling rate plots are shown in Figure 3.

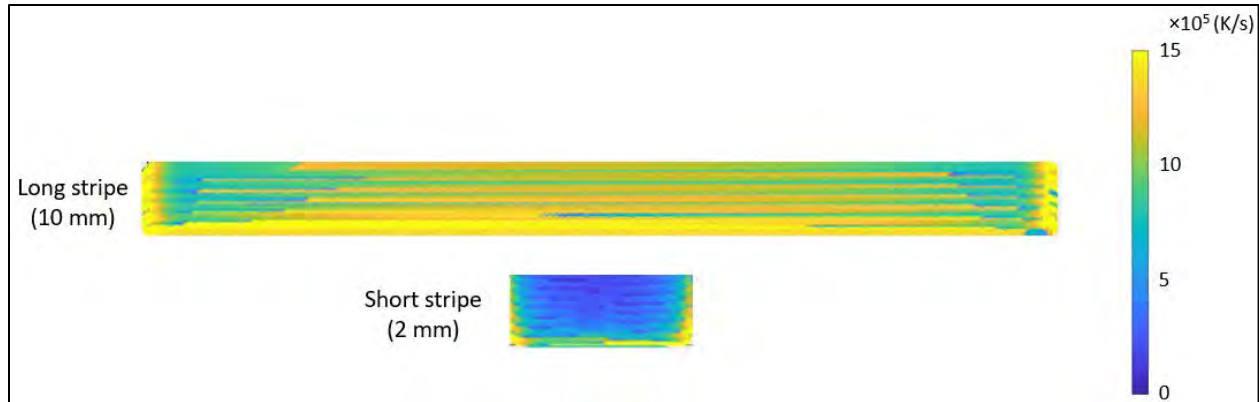


Figure 3. The cooling rate color maps for the long stripe and short stripe experiments.

Significance and Interpretation of Results

The thermal conditions at the onset of solidification are known to be a direct contributor to the microstructure of the material. More specifically, it is known that faster cooling rates result in finer grain structures. In order to validate the conclusions drawn by the simulations, the model results were compared to scanning electron microscope (SEM) images of the actual thick-to-thin builds, which were provided by Joe Walker at Wright State University. These images show that the thick portion of the geometry is composed of a finer grain structure than the thin portion, which supports the results given by the simulations of the same geometry.

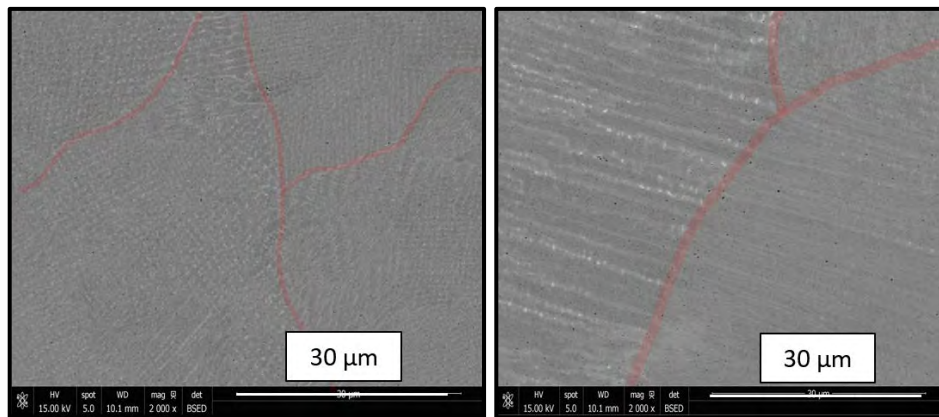


Figure 4. SEM images of the thick section (left) versus the thin section (right).

References

1. A. Plotkowski, M. M. Kirka and S. S. Babu, "Verification and Validation of a rapid heat transfer calculation methodology for transient melt pool solidification conditions in powder bed metal additive manufacturing," *Additive Manufacturing*, vol. 18, pp. 256-268, 2017.
2. H. S. Carslaw, J. C. Jaeger. *Conduction of Heat in Solids*, 2nd ed., Oxford University Press, Oxford, 1959.
3. Z. Hou, R. Komanduri. "Magnetic field assisted finishing of ceramics-part I: thermal model," *Journal of Tribology*, vol. 120, pp. 645-651, 1998.
4. R. Komanduri, Z. B. Hou. "Thermal analysis of the arc welding process: part I. general solutions," *Metallurgical and Materials Transactions*, vol. 31B, pp. 1353-1370, 2000.
5. R. Komanduri, Z. B. Hou. "Thermal analysis of the laser surface transformation hardening process," *International Journal of Heat and Mass Transfer*, vol. 44, pp. 2845-2862, 2001.

Wake Flow Structure of a Seal-Whisker-Inspired Low-Pressure Turbine Blade

Student Researcher: Curtis A. Flack

Advisor: Dr. Wei Zhang

Cleveland State University
Mechanical Engineering

Abstract

One of the challenges in aerospace engineering is continuously improving engine efficiency and reducing fuel consumption of planes. Biomimicry (or biomimetics) is a promising solution which aims to design and renovate engineering components and systems to emulate the performance of living systems or their constructs, especially when an organism's performance exceeds human-engineered technologies. Studies of hydrodynamics of seal whiskers have evidenced highly desirable flow performance in drag reduction and suppression of vortex-induced-vibrations (when compared to non-undulating geometries), solely due to their unique three-dimensional undulating geometry. The application of seal-whisker-like geometry to low-pressure turbine blades by computational fluid dynamics (CFD) shows promising results in improving aerodynamics. However, limited experiments have been conducted to quantify the detailed wake structure under the effects of the undulating whisker-like geometry. The purpose of this study is to quantify the flow effects of the seal-whisker-inspired airfoil in a well-controlled uniform water tunnel, focusing on the modified turbulent wake behind the whisker-like airfoil and a baseline airfoil. Results will be used, not only to optimize the design of low-pressure turbine blades, but also to guide a wide variety of other aerodynamic applications.

Project Objectives

The purpose of this research was to compare the near wake of a seal-whisker-treated low-pressure turbine blade to an untreated blade in a free-stream environment. The objective was to create the two airfoils, based on the Rolls-Royce Variable Speed Power Turbine (VSPT) Blade profile, using fusion deposition modeling, and test it in CSU's water tunnel using particle image velocimetry (PIV). Given previous research results to the testing of seal whiskers (Bunjevac) and CFD results for their application to a low-pressure turbine blade (Shyam), it was expected that the wake of the whisker-inspired blade will display a less-adverse wake when compared to the untreated blade. The properties of the wake to be analyzed were the mean flow field and the turbulence intensity.

Methodology Used

The VSPT airfoil was treated in a whisker-like fashion which was found to have the best results by Shyam et al. The geometry was swept in a sinusoidal fashion creating undulations to the leading edge, trailing edge, and suction side of the blade. The whisker-inspired blade and untreated blade were tested using high-speed PIV in CSU's 0.3m x 0.3m x 2.0m water tunnel at a Reynold's number of 40,000 based on the chord length. High-speed PIV uses a continuous laser sheet parallel to the airfoil profile and a high-speed camera to capture the flow of the water which was seeded with fine glass particles. Both airfoils were tested at AOA = -10° , -5° , 0° , 5° , and 10° .

Results Obtained

To this point, only the results for the VSPT and whisker-treated blade at peak location at AOA = 0° and 10° have been analyzed. Results for the AOA = 0° are presented in Figures 1 and 2. For both angles of attack, the whisker-treated blade had a smaller and less intense reversed flow region and a less extreme streamwise velocity gradient. Streamwise velocities above and below the untreated blade were well

above mean velocity and the region immediately behind the airfoil was characterized by a large strong reversed flow. However, the whisker-treated blade had a much less dramatic velocity gradient and its mean velocity of the reversed flow region was not as intense and was smaller than the untreated blade. This lower velocity gradient allows the wake to recover to freestream velocity quicker, as seen for both angles of attack. For both angles of attack, the mean vertical flow for the whisker-inspired blade was generally less extreme and recovered to lower value sooner than the untreated blade.

The turbulent statistics of the wake were also analyzed. For both angles of attack, the whisker-treated blade was noted to have significantly less intense streamwise turbulence. The vertical turbulence intensity of the whisker-treated blade peaked sooner, was less intense, and recovered sooner than the untreated blade.

Significance and Interpretation of Results

Preliminary results show that when the entire VSPT profile was swept in a sinusoidal fashion to mimic the seal-whisker morphology, it resulted in a decreased velocity gradient, quicker recovery to free-stream velocity, and a less turbulent wake. The results which were found could indicate that the application of a whisker geometry to a low-pressure turbine blade could result in a reduction in fuel consumption. Future work will include processing remaining cases of varying angles of attack, as well as examining the boundary-layer separation on the seal-whisker-treated airfoil.

Figures

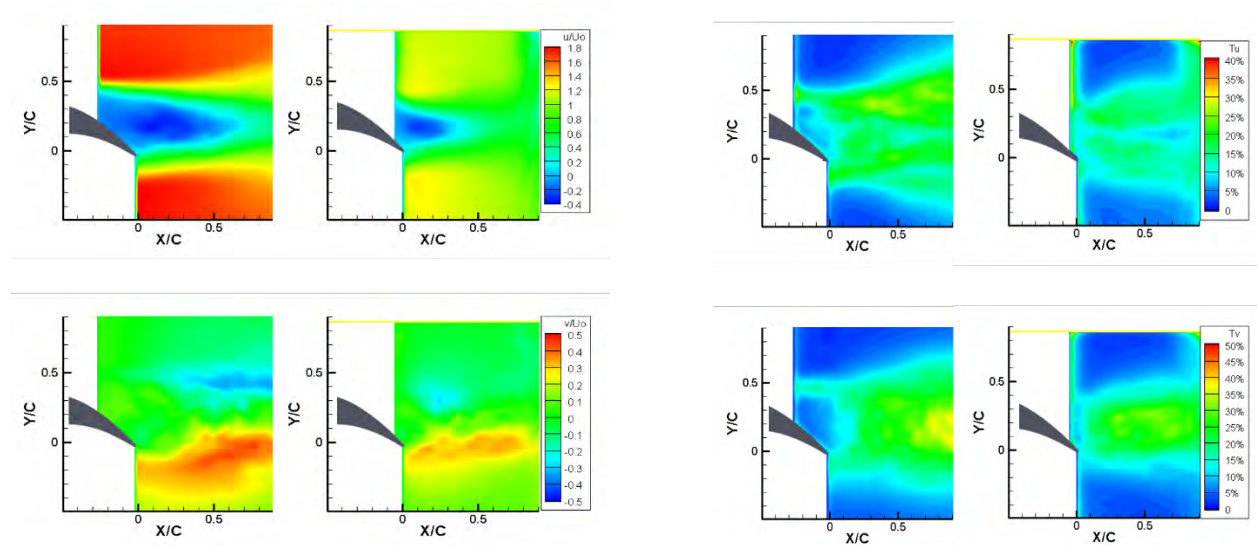


Figure 1. Mean Velocity Fields for the untreated blade (left) and whisker-inspired blade (right) AOA = 0°.

Figure 2. Turbulence intensity for the untreated blade (left) and whisker-inspired blade (right) AOA = 0°.

Acknowledgments

The author would like to thank the Cleveland State University Office of Research for financial support through the Undergraduate Research Award. Thanks to NASA for financial support through the Ohio Space Grant Consortium and for providing the geometry for the VSPT airfoil.

References

1. Bunjevac, J., Turk, J., Rinehart, A., and Zhang, W., "Wake induced by an undulating elephant seal whisker," *Journal of Visualization*, Vol. 21, No. 4, 2018, pp. 597–612. doi:10.1007/s12650-018-0484-4.
2. Shyam, V., Poinatte, P., Kulkarni, S., Schilling, H., Wroblewski, A., Zelek, M., Ameri, A., Thurman, D., Raghu, S., and Eichele, P., "Holistic Concepts for Fixed and Rotary Wing Aircraft Engines," Tech. rep., National Aeronautics and Space Administration, 2018.

Solar Tracker

Student Researchers: Lynnae S. Frisco and Kylon J. Payne

Advisor: Dr. Augustus Morris, Jr., P.E.

Central State University
Manufacturing Engineering Department

Abstract/Objectives

The sun provides one of the cleanest and most abundant forms of energy known as solar energy. Solar energy is used by collecting or absorbing solar radiation emitted by the sun. Solar energy as mentioned before is a clean form of energy but it is hard to capitalize on. In order to create energy, the radiation from the sun must be absorbed, collected and converted into heat or electricity, but the amount of radiation the Earth receives varies from day to day which means the amount of electricity or heat would vary as well. The weather, location, time of day, season and the landscape can affect how much radiation reaches the earth's surface (ENERGY.GOV). When the sun is at its peak point of the day that is when the earth receives all energy possible (Energy.com).

Although the sun provides solar energy it still must be converted into useful energy such as electricity and heat. For example, in the 1830's, British astronomer John Herschel used a radiation from the sun and converted it into heat energy to cook food (EIA.GOV). Since the 1830's solar energy has advanced and can be used for heating water in homes and pools, heat the inside of homes and to heat fluids in solar thermal plants (EIA.GOV). Some examples of the technologies are the Photovoltaic cells (solar cells) and concentrating solar power. The main differences between the two is that one of them are used to convert solar energy into electricity and the other converts it into thermal energy.

Photovoltaic cells (PV cells) are one of the most common examples of converting solar energy to electricity. These cells work by putting a negative layer (usually Phosphorus doped N type silicon) on top of the positive layer (Boron doped P type silicon) which create an electrical field (fsec.ucf.edu). Once sunlight strikes the surface the electrical field provides momentum that results in a current when connected to an electrical load (fsec.ucf.edu). Depending on the size and amount of PV cells determines the amount of electricity that can be used. The bigger the structure the more electricity. It is important that the cells remain focused on the high point of the sun to maximize the amount of electricity.

Another type of solar technology is the concentrating solar power such as the parabolic trough, parabolic towers and dishes (seia.org). Both of these concentrators work similarly by using mirrors to collect scattered rays into one focal point. The mirrors then reflect the focal point and bounce it back to a receiver tube that absorbs the radiation. Usually the tube is filled with a heat transfer substance such as oil or water. This energy is then used to drive a conventional steam turbine to generate electricity, this energy can also be stored for later use (seia.org).

Solar towers use thousands of heliostats (mirrors with tracking capabilities) focus the sun's rays onto a boiler, which sits at the top of the tower and produces steam (nurenergie.com). Towers are not as reliable as parabolic troughs, but it does have one less step than the troughs as it does not require a heat exchanger. Since the towers do not require a heat exchanger that means that they have less energy loss and maximize on the energy (nurenergie.com). Here in the United States there are many solar tower

projects that are currently active, an example are the solar towers in California in the Mojave Desert, the Ivanpah facility (seia.org). This project consists of 173,000 heliostats and three power towers that could provide power to over 100,000 Americans (seia.org).

Parabolic troughs function by setting up a field of mirrors that concentrate the sunlight to a focal point onto a receiver tube that runs across the mirror (Nurenergie.com) The receiver tube is filled with a heat transfer material such as water or oil to produce steam through a heat exchanger. Troughs are one of the most reliable forms of concentrating powers, in fact the United States have many active parabolic trough projects as well. Northeast of Los Angeles is the Abengoa Solar Inc. This is a solar power plant that is spread across 1,765 acres and has the capabilities of powering approximately 90,000 Americans. The disadvantages of the trough is that the mirrors for the trough are more expensive than the towers flat heliostats (nurenergie.com). An advantage for the troughs is that they are more commercially used, 97% of solar power plants use parabolic trough (nurenergie.com).

Solar dishes are similar in concept to both the solar towers and the parabolic troughs. The solar dish has a thermal receiver collects the solar energy and converts it into heat energy, this heat is then sent to the engine or the generator (seia.org). Mainly in dishes the use a Stirling engine that uses the heated fluid to move pistons and create mechanical power (seia.org). In Utah, the US army has begun a solar dish project that is 1.5 MW system with 429 Stirling engine dishes (eia.gov).

Our project is a solar concentrator which will be used to absorb and intensify the radiation emitted from the sun. This concentrator will have a solar desalination system attached with it so as the radiation is being concentrated the system will use that thermal energy to purify salt water. In nature solar desalination occurs by the rain that is made through absorption of sea water. Solar desalination systems function similarly to the earth's water cycle. The concentration of the radiation should be enough for successful use of a solar thermal desalination system.

Solar radiation also known as solar resources is the electromagnetic radiation emitted by the sun (energy.gov). When solar radiation is captured this source can be used by converting it to a useful energy such as thermal energy or electricity. As mentioned previously there are many technologies that can convert solar radiation into a useful energy.

The amount of solar radiation the earth receives in any spot is based in the location, time, season, landscape and the weather. For example, on clear dry days atmospheric conditions reduce the radiation by 10%, but on thick cloudy days radiation is reduced by 100% (energy.gov). This occurs because atmospheric conditions can cause the rays to scatter and diffuse. On cloudy days the atmospheric conditions scatter the rays and into short wavelengths and the earth receives diffused radiation (appdsolarradiation). On clear days the radiation is direct meaning that the solar radiation emitted by the sun directly reaches the earth. There are also reflected radiation which is radiation that is reflected after striking the surface (appdsolarradiation). For example, the ground, grass and snow can all reflect back the solar radiation.

The United States receive the maximum amount of solar energy in the summer because of the positioning of the sun (Energy.gov). On average the earth's distance from the sun is about 9.3×10^7 miles being the closest to the sun around January 1st and becomes further away around July 1st (appdsolarradiation). The intensity of the solar radiation is greater when the incidence angle is less meaning that the angle between the sun and the earth is closer to 0.

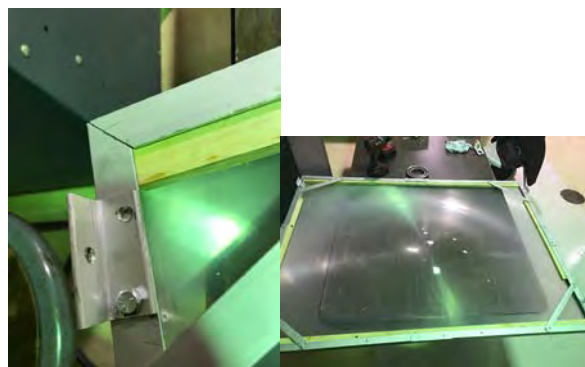
Methodology

We will program a razor scooter to rotate the base of the frame. The motor will be connected to solar panels one with the positive to positive and the other with the positive to the negative. When the sun strikes the solar panel, the panel will power the motor and the panel receiving the solar energy will instruct the motor in the required direction for the motor to turn. The motor will also need to be further programmed that way the motor knows when to stop and to prevent it from turning in a constant circle. In order to achieve this, we will also need to use a raspberry pi to help program the motor. This motors only task is to rotate the base and the use of a shaft prevents the base from moving up and down.

The top of the frame will need an actuator or pulley system that will move the frame up and down.

Optical lens were first discovered in the ancient times, about 700 B.C. They were discovered from ancient Egyptians and Mesopotamians polishing different crystals attempting to reproduce the optical abilities that they observed can be made in water. Friar Salvino D'Armate was a person who changed optics dramatically. In 1284, Friar Salvino D'Armate created the first wearable eyeglass. Optical specifications are used throughout the design and manufacturing of a component or system to illustrate how well it meets certain performance necessities. Specifications are useful because they give the correct limits of important limitations that oversee the performance of the system. Also, they tell you the right amount of time and money that should be used on manufacturing.

It is believed the type of lens that is being used in the project is a Fresnel lens. The basic idea behind a Fresnel lens is a plastic magnifying glass lens and slicing it into a bunch of concentric rings. A common application for a Fresnel lens is the collection of solar light. A Fresnel lens for light collection is known for absorbing light to heat a surface. A Fresnel lens can be used in a home for different applications such as heating the house itself, or possibly a pool. Depending on the size of the screen, a Fresnel lens can cost from \$300 to \$27,000. Our screen is 50 inches long and 38 inches wide, and weighing about 11.384 pounds. There is a piece of wood screwed into each side of the screen. The wood screwed to the 38-inch sides on the screen is 22 inches long weighing about 0.253 pounds each. The wood screwed to the 50 in sides of the screen is 50 inches long weighing about 0.575 pounds each. After the wood, there were pieces of aluminum, which came from an old chalk board, cut down and fitted for each side. The aluminum pieces were cut to be half an inch longer than each side. There were two pieces that are 50.5 inches and weighing 1.57752381 pounds each. The other two pieces are 38.5 inches long and weighing 1.20266667 pounds. Once all of these pieces were assembled, there were four clips screwed on to the 38.5-inch side, 2 clips on each side. The clips are going to be used to attach the aluminum arms to the frame, shown in the pictures below.



The aluminum arms, 38 inches each, were attached to the frame on the clips. The arms that were on the same side were then connected together by a screw to create a pivot point. Also attached with the arms at the pivot are two small wood bases, which will be attached to the base, will also be used to make stabilize and balance the frame. This can be seen in the pictures below.



The base serves as an aid to rotate the lens frame in order to obtain the maximum solar energy by keeping the energy at the lenses focal point. Since the earth appears to rise from the east and sets in the west, we have implemented solar panels to direct the motor to rotate the base either clockwise or counter-clockwise through a shaft, 3 ½ " and 4" sprocket and chain pulley system using sprockets and bike chains. This rotation will follow the solar panels direction as the sun rises and sets.

The base is designed and built to support all of the components of our solar concentrator including the; Frame, Solar Panels, and the weight of the two combined. We will use two 59 inches in diameter circular wooden table tops as our base. The two table tops will be placed in parallel to each other 11" apart with the faces of the table tops facing the earth. In between the two table tops there is a series of things including a 3D printed hub to support the 5/8" in diameter shaft following a bearing. The shaft will be 7" inches long and it will serve as the point of rotation for the table top and or the base. For the bottom half of the table top we designed 4 wooden blocks that has 2" diameter wheels that are free of rotation. The wheels will make it easier for the table top to rotate. Attached to the base are two solar panels that outputs 42 Volts of power. The energy from the solar panels will operate our motors by producing the needed voltage for the motor to run. The motor powered is serving as the rotation of the base through a shaft, sprocket, and chain pulley system. We have 3D printed a hub that fits the shaft of the motor. This hub will be assembled with a bike sprocket to support the pulley system that we've chosen for the base. The shaft of the motor and the shaft of the base are in parallel to support our pulley system.



Motor and shaft with sprocket:



Table tops with wheels:



Center shaft with sprocket

In conclusion, the goal of this project is to absorb and intensify the radiation admitted from the sun by using a solar tracker. A solar desalination system is planned to be attached with the solar tracker so as the radiation is being concentrated the system will use that thermal energy to purify salt water. Solar desalination occurs in nature by the rain that is made through absorption of sea water. Solar desalination systems function similarly to the earth's water cycle. Solar energy is one of the cleanest and most abundant forms of energy, which is provided by the sun. We hope with the success of the project it is able to help countries and/or that lack states that lack the ability to receive clean water.

References

1. Batista-Rodríguez, Carlos R., et al. "Indexes for the Evaluation of a Solar Tracker*." *Ingeniería y Desarrollo*, vol. 36, no. 1, Jan. 2018, pp. 172–186., doi:10.14482/inde.36.1.10945.
2. Chaudhary, Ghulam Qadar, et al. "Small-Sized Parabolic Trough Collector System for Solar Dehumidification Application: Design, Development, and Potential Assessment." *International Journal of Photoenergy*, vol. 2018, 2018, pp. 1–12., doi:10.1155/2018/5759034.
3. Davis, Arthur. "Fresnel Lens Solar Concentrator Derivations and Simulations." *Novel Optical Systems Design and Optimization XIV*, Aug. 2011, doi:10.1117/12.892818.
4. Hijazi, Hamza, et al. "Mechanical Design of a Low Cost Parabolic Solar Dish Concentrator." *Alexandria Engineering Journal*, vol. 55, no. 1, 2016, pp. 1–11., doi:10.1016/j.aej.2016.01.028.
5. Islam, Majedul, et al. "Investigation of the Effect of Physical and Optical Factors on the Optical Performance of a Parabolic Trough Collector." *Energies*, vol. 10, no. 11, 2017, p. 1907., doi:10.3390/en10111907.
6. Muhammad-Sukki, Firdaus, et al. "Solar Concentrators."

Numerical Solutions of Heat Transfer Models to Determine Thermal Properties of Novel Insulating Materials for Hypersonic Aerospace Applications

Student Researcher: Miranda Ghrist

Advisor: Regan Silvestri, Ph.D.

Lorain County Community College
Business Development and Innovation

Abstract

An alumina based insulating material developed for use in aerospace applications has been evaluated using a test method that effectively mimics the thermal loads experienced during hypersonic flight applications. Coined THERMIC for ***THERM*al *I*nsulation *C*haracterization**, the test method comprises of measuring the temperature gradient through layers of insulation as heat is applied to one side in room temperature conditions until a maximum temperature load of 250°C to 300°C is reached. In combination with a 1-dimensional heat transfer model of the test method, this yields calculated values for thermal conductivity and specific heat of a known standard insulation with an accuracy of 80%, demonstrating the validity of this new test method. Presented herein are numerical solutions to the 1-dimensional heat transfer model of the developed test method when applied in Python.

Project Objectives

Develop standard heat forward model with adiabatic boundary condition in Python programming language with the Spyder Integrated Development Environment for scientific applications and plot.ly graphing library for comparison of predicted models versus real data collected from THERMIC setup. Establishing repeatability of the THERMIC testing process and reliability of a numerical solution to heat transfer model used for predicting approximations of results.

Methodology Used and To Be Used

THERMIC setup for current scope of project comprises of an Omega OMB-2416 USB Data Acquisition Module module with TracerDAQ software, Inconel septum plate with approx. 10W/m.K thermal conductivity embedded with four type K thermocouples, rigid insulation frame comprised of SALI™ polycrystalline alumina fiber bound in mullite, a Ti-6Al-4V type Titanium witness plate with 6% aluminum and 4% vanadium embedded with four type K thermocouples, 120V resistance heater and an additional four type K thermocouples as provided by S.D. Miller.

TracerDAQ datasets in CSV format have been imported into Plot.ly graphing application for creation of traces for initial visualization and evaluation. Exported in a Python format for further development the datasets can be averaged and compared the results of the numerical solution of 1 dimensional heat transfer with an expected accuracy of 80%.

Status of Project

After acquiring multiple TracerDAQ datasets in CSV format using physical test setup and acquiring knowledge base of both analytical and numerical approaches to heat and mass transfer problems with varying geometry and environmental conditions, a standard heat 1 dimensional diffusion model with visualization as part of the testing and development process has been created.

References

1. A Simple Transient Thermal Test Assembly for Insulation Materials (2019, February) NASA-TM-2019-220249.
2. Heat and Mass Transfer: Fundamentals and Applications (2010) Cengel, Y.; Ghajar, A., McGraw Hill.

Understanding and Responding to the Physical and Economic Impact of Natural Disasters on Communities and Agriculture

Student Researcher: Kristopher A. Gibboney

Advisor: Dr. Robert Chasnov

Cedarville University

Department of Science and Mathematics

Abstract

Integrating NASA technical data and satellite imagery, this comprehensive lesson activity provides students an opportunity to learn about the hydrologic cycle and thermal-energy transfers, especially as it relates to current events, through discussion and collaboration. This knowledge is then applied in a study on global climate patterns and natural disasters. Students in the STEM Exploration/Immersion class where I was completing field experience at participated in this lesson activity and completed pre- and post-assessments a week prior to and a week after the lesson activity, respectively. This activity allowed the students to learn the hydrologic cycle, how natural disasters have physical and economic impacts on communities and agriculture, and how communities recover from and prepare for disasters.

Lesson

This lesson activity was developed based on this specific school's focus on agriculture, the point in the content reached in the Earth Science class, as well as the point in the content reached in the STEM Exploration/Immersion class.

During the first day, students engaged in a discussion as they learned the necessary vocabulary and concepts involved with the hydrologic cycle, weather patterns, and agriculture. After the discussion, students individually completed a worksheet requiring them to label and explain the parts of the hydrologic cycle, describe how human and animal activity impacts the cycle, and identify ways that natural disasters physically and economically impact agriculture.

On the second day, students engaged in a brief discussion recapping what was learned on the first day. Students then individually researched natural disasters and completed a worksheet stating relevant facts from and citing the NASA technical reports being used. Students also explained how such data would be useful in preparing for future natural disasters and recovering from previous ones. Students spent the last part of class researching smart growth strategies for resilience and recovery as provided by the EPA while considering the NASA technical reports.

On the third day, students formed groups to collaborate in to create theoretical communities, which had to include the location/land formation built on, as well as a smart growth strategy implemented. A random natural disaster was given to them and they had to respond to it, and then reflect on how effective their smart growth strategy was and determine what new smart growth strategy could be implemented to recover, presenting such to the rest of the class.

Objectives

At the end of the lesson activity, students will be able to:

- Label and explain the steps in the hydrologic cycle.
- Summarize the influence of thermal-energy transfers and the hydrologic cycle on the weather.
- Identify the physical and economic impact of natural disasters on communities and agriculture.
- Collect, analyze, evaluate, and cite technical data from NASA.
- Utilize knowledge of smart growth strategies for disaster resilience and recovery.

Alignment

Grade 7 Earth and Space Science Standard 1: *The hydrologic cycle illustrates the changing states of water as it moves through the lithosphere, biosphere, hydrosphere and atmosphere.*

Grade 7 Earth and Space Science Standard 2: *Thermal-energy transfers in the ocean and the atmosphere contribute to the formation of currents, which influence global climate patterns.*

Agricultural CTE Standard 6.2.4: *Explain the hydrological cycle (e.g., condensation, evaporation, transpiration) and how human and animal activity impacts the cycle.*

Grades 6-8 Literacy Standard 1: *Cite specific textual evidence to support analysis of science and technical texts.*

Underlying Theory

This lesson activity is based on a student-centered, constructivist approach to learning in which students learn through experience with the content. As students engage in discussions and collaborate in groups, they construct new knowledge of the content alongside prior knowledge. I facilitated the learning process by helping the students have meaningful, authentic experiences with the content.

Student Engagement

On the first day utilizing discussion, the necessary content was communicated to the students for use in the rest of the lesson. The second day involved mostly research, which greatly limited the engagement with the material, except for the discussions had between each individual student and myself. The final cumulative activity utilized everything from the previous two days of activities and enabled the students to actively engage in meaningful, authentic, and enjoyable ways with the material alongside their peers.

Assessment and Results

Students took a pre-assessment and post-assessment a week prior and a week after the lesson, respectively. These assessments contained the exact same questions to track student comprehension. Student average percentage scores increased by approximately an average of 26%. A one-tailed pair-difference t-test conducted on the scores resulted in a p-value of 0.00003, indicating a very significant increase in student scores after the use of this lesson activity. However, it is important to note that this p-value may be skewed due to the class being composed of only 16 students.

Conclusion

The lesson activity was highly effective in helping students understand the basic concepts of the hydrologic cycle, thermal-energy transfer, weather, and natural disasters, as well as how all these affect communities and agriculture physically and economically. The students greatly enjoyed this lesson activity, as they expressed throughout the lesson and on papers I asked them to provide feedback on.

Mathematical Modeling for Release Kinetic Prediction of LENVIMA

Student Researcher: Andrea Gomez

Advisor: Dr. Tarun Goswami

Wright State University
Biomedical Engineering

Abstract

In the field of pharmaceuticals, side effects that accompany oral medication expose a major weakness to an otherwise progressive area of study. LENVIMA, a differentiated thyroid cancer drug that inhibits various growth factors, has fifteen serious side effects. By analyzing the properties of nanoparticles used in the manufacturing of LENVIMA, specifically hydroxypropyl methylcellulose (HPMC), mathematical relationships can be made. Additionally, understanding the location of dissolution and its properties such as pH and type of intestinal fluid adds other mathematical relationships. The objective of this research project is to develop a mathematical model specific to this cancer pharmaceutical, in order to make its release kinetics predictable. An additional goal of this research is that the model provides a foundation for an improved universal model for other pharmaceutical drugs. The majority project will consist of rigorous literature review on HPMC properties and its use with numerous drugs, data extraction of HPMC dissolution rates of various drugs and in different mediums, research on current mathematical models present, and a foundation of the drug release process. Once all the data is collected and properties are understood, a mathematical model will be proposed based on curve fittings of the data using MATLAB and Design Expert® software.

Project Objectives

The scope of this project deals with two different modeling approaches. The first is based on existing mathematical models and concepts such as determining average dissolution rates in different mediums with its potential transition into the sequential layer model and the Higuchi model. The second approach utilizes the Design Expert software to determine correlations between factors such as pH, dosage, health, and time to develop predictive equations specific to the data collected. Both approaches depended greatly on existing data in literature regarding the pharmacokinetics of lenvatinib and HPMC.

Methodology Used

The pharmacokinetic modeling of LENVIMA required extensive data extraction. This was accomplished through WebPlotDigitizer, an online tool capable of extracting data from plots. Once the data was discretized into Excel, it was compiled into two plots: the first displaying the disintegration of HPMC over time in different mediums, Figure 1, and the second displaying the plasma concentration of lenvatinib over time, Figure 2.

The first mathematical relationship obtained was the average disintegration of HPMC over time, a constant that was named k_{dis} , for each medium the hypromellose capsule dissolved in. These were obtained through linear analysis of Figure 1 by comparing change in percentage capsule dissolved over change in time, shown in equation 1:

$$\frac{P_{max}-P_{min}}{\Delta t} \quad [1]$$

The disintegration constants for each medium were then recorded in Table 1 along with the maximum percentage dissolved in one hour.

The second mathematical relationship obtained was the Higuchi dissolution constant. Equations 2 & 3 below show the Higuchi equation and its simplified version respectively:

$$f_t = Q = A\sqrt{D(2C - C_s)C_s t} \quad [2]$$

$$f_t = K_H\sqrt{t} \quad [3]$$

In equation 2, Q is the amount of drug released in time t, per unit area; A is the unit area; D is the diffusivity of drug molecules; C is the initial drug concentration; C_s is the drug solubility in the matrix media, and t is time. Equation 3 simplifies all information except time into one constant, K_H, called the Higuchi dissolution constant. Utilizing dissolution data from Figure 1, MATLAB converted the data to the linear fit modeled by equation 3, where the Higuchi dissolution constants were obtained for each medium along with their 95% confidence intervals. The results are displayed in Table 2 and Figure 3.

The second part of this project utilized the Design Expert software to create two equations specific to the data extracted. The first equation considers two factors on the disintegration of the hypromellose capsule: pH and time spent in the body. First, the number of factors was inserted into the software, and the data was inputted in the response surface central composite design section. The software then provided the correlation of each factor to the percent capsule dissolved, the best fit for the data with the factors included, ANOVA analysis for the model chosen, and a final equation in terms of actual factors, all displayed in Figure 4 and Table 3. A similar procedure was followed for the second equation, the difference being that the second equation considers three factors influencing the plasma concentration of lenvatinib: dosage, health of patient (normal/healthy patient vs cancer patient), and time spent in the body. These results are shown in Figure 5 and Table 4. These equations were then used in a predictive manner for determining percentage of HPMC capsule disintegrated, Table 5, and lenvatinib plasma concentration, Table 6, based on time spent in the body and location of the capsule in the body.

Results Obtained

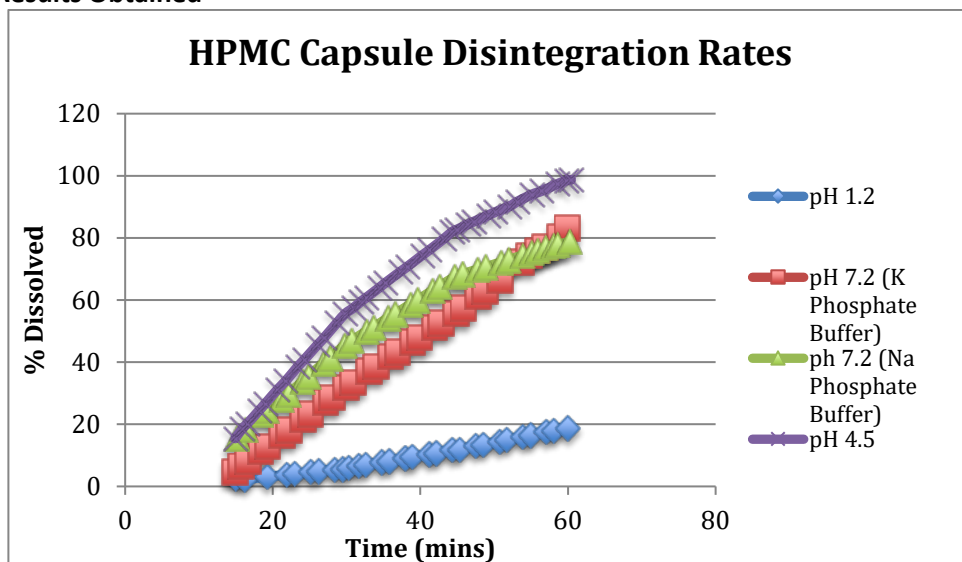
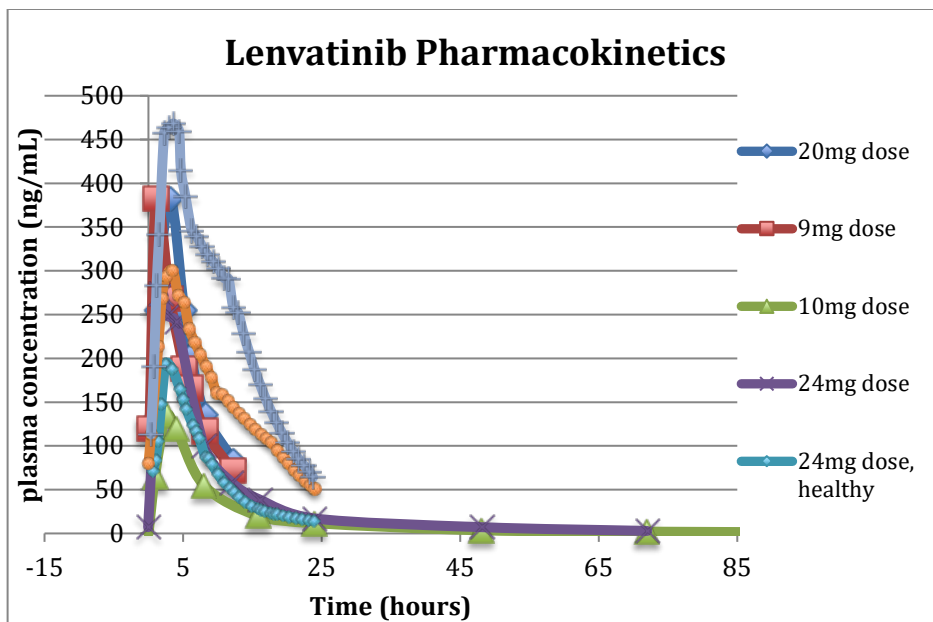


Figure 1. Compilation of disintegration over time in terms of percent HPMC medication dissolved in four different mediums: 0.1 N HCl (pH 1.2), Na acetate buffer (pH 4.5), K phosphate buffer (pH 7.2), and Na phosphate buffer (pH 7.2).

Source: [1] & Author

In the Figure above, data from the disintegration of an HPMC capsule in different mediums was discretized from WebPlotDigitizer. Generally, lower pHs dissolved at a much slower rate than higher pHs, as can be seen when comparing the 0.1 N HCl (pH 1.2) with both phosphate buffers (pH 7.2), however the Na acetate buffer (pH 4.5) presents an exception as it dissolves at a much higher rate. This could be due to properties of the medium rather than pH properties, but this discrepancy was taken into account when creating the final model in equation 4.

Figure 2.
Compilation of lenvatinib plasma concentration over time based on four different doses: 9mg, 10mg, 20mg, and 24mg, as well as plasma concentrations in healthy patients and cancer patients.



Source: [2-5] & Author

In the Figure above, data of plasma concentration of Lenvatinib from different doses was extracted from various sources and compiled into one plot. In this plot, the first-order kinetics from the initial burst effect that occurs with disintegration, and the exponential decay that follows are prominent and are as expected from an oral medication. Generally, with higher doses the plasma concentration increases compared to lower doses and this can be observed when comparing the 24mg doses with the 10mg doses. However there is a difference between healthy patients and cancer patients. Plasma concentrations of the drug are significantly higher with cancer patients than healthy patients, implying that better bioavailability occurs when the patient has differentiated thyroid cancer.

Table 1. Disintegration constants for each medium in terms of minutes and hours as well as maximum percent dissolved in one hour.

pH	k_{dis} [percent/min]	k_{dis} [percent/hour]	Percent dissolved at 1 hour
1.2	0.73	43.8	18.84
4.5	1.83	94.4	80.96
7.2	1.57	109.4	98.7

The Table above shows the results of determining the average disintegration constants based on data from Figure 1. The discrepancy between the disintegration per hour and the actual value of disintegration at one hour is due to the fact that linearity was assumed when calculating the average disintegration, but in reality, as can be observed in Figure 1, the disintegration approaches a zero-order kinetics state as the initial burst-effect has passed. These constants show that the rate of disintegration increases with pH increase, with the exception of the pH of 4.5. As was stated earlier, this could be due to the mediums properties, but can be considered significant as that is close to the pH of the stomach, where a higher disintegration rate is desirable.

Table 2. Higuchi dissolution constants for each medium along with their confidence intervals with alpha=0.05.

pH/medium	K_H	95% confidence interval
1.2	34.41	31.5-37.33
4.5	169.3	164.1-174.5
7.2 (K phosphate buffer)	154.6	149.5-159.7
7.2 (Na phosphate buffer)	129.8	125.3-134.4
7.2 average	142.2	137.4-174.5

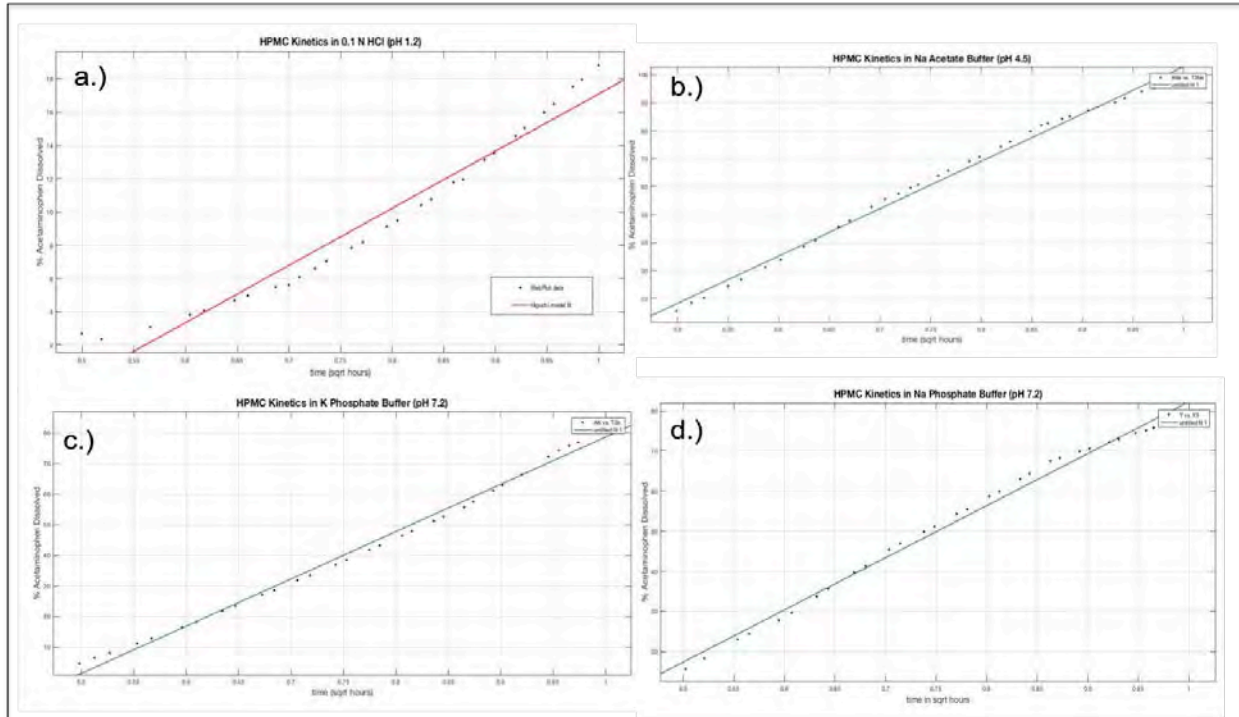


Figure 3. MATLAB fitting to determine Higuchi dissolution constant of an HPMC capsule in four different mediums: a.) 0.1 N HCl (pH 1.2), b.) Na acetate buffer (pH 4.5), c.) K phosphate buffer (pH 7.2), and d.) Na phosphate buffer (pH 7.2).

Source: [1] & Author

The Table and Figure above show the results of determining the Higuchi dissolution constant for each medium based on the data from Figure 1. Based on the original Higuchi model, equation 2, the Higuchi dissolution constant contains information on the diffusivity and drug solubility in each medium. The data implies that at a lower pH such as 1.2, the diffusivity and drug solubility is low, and at a higher pH of 7.2 it increases. Once again, it is interesting that at a pH of 4.5, the diffusivity and solubility is highest, implying that the stomach is an optimal location for drug disintegration.

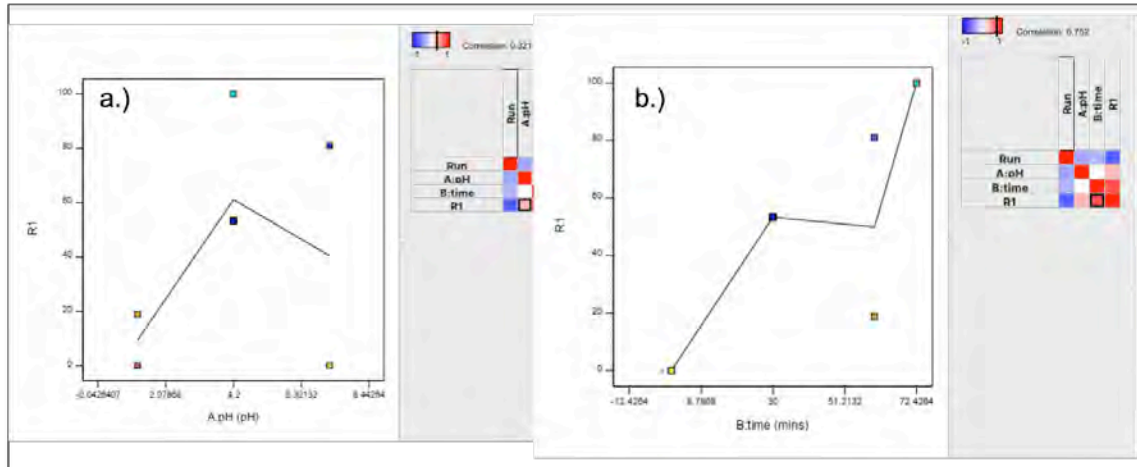


Figure 4. Design Expert correlation results of pH and time HPMC capsule spent in the body to percent capsule dissolved.

Source: [1] & Author

Table 3. Design Expert correlation values of pH and time the capsule spent in the body to percent capsule dissolved as well as equation summaries and ANOVA analysis.

Factor	Correlation	Best Fit Summary	Final Equation [4]
pH (z)	0.321	Quadratic sequential p-value < 0.0001	$A * t^2 + B * z^2 + C * z * t + D * t + E * z + F$
time (t)	0.752		A=0.006324 B=-3.78597 C=0.172556 D=-0.272516 E=31.80215 F=-32.71078
ANOVA analysis of quadratic model			
Source	Sum of Squares	Mean Square	p-value
Model	9372.49	1874.50	<0.0001 (significant)
Pure Error	0.0255	0.0064	
Cor Total	9372.52		

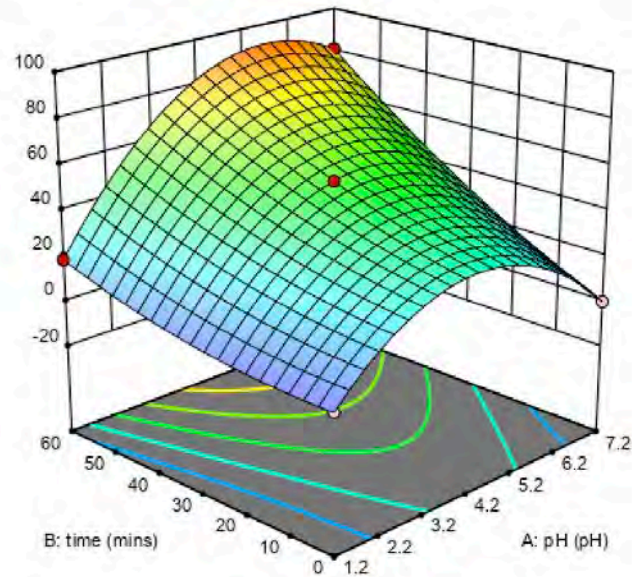
The Figure and Table above display the results of using the Design Expert Software to mathematically analyze the best model for the data of HPMC disintegration. The results show that time is strongly correlated with disintegration, while pH has some influence, but not as much most likely due to the pH of 4.5 showing higher disintegration than the pH of 7.2. The software was then able to create an equation that best fit the data in terms of any inputted pH and time spent in the body.

The surface plot above displays the linear strong correlation time has with the disintegration of an

Figure 5. Surface plot of final equation from Table 3.

Source: Author

HPMC capsule, while the pH's influence is highest near the 4.5 mark, and lower in the 1.2 and 7.2 marks. The plot is also a good visual of why a quadratic model, equation 4, was an appropriate fit when considering the two factors of pH and time.



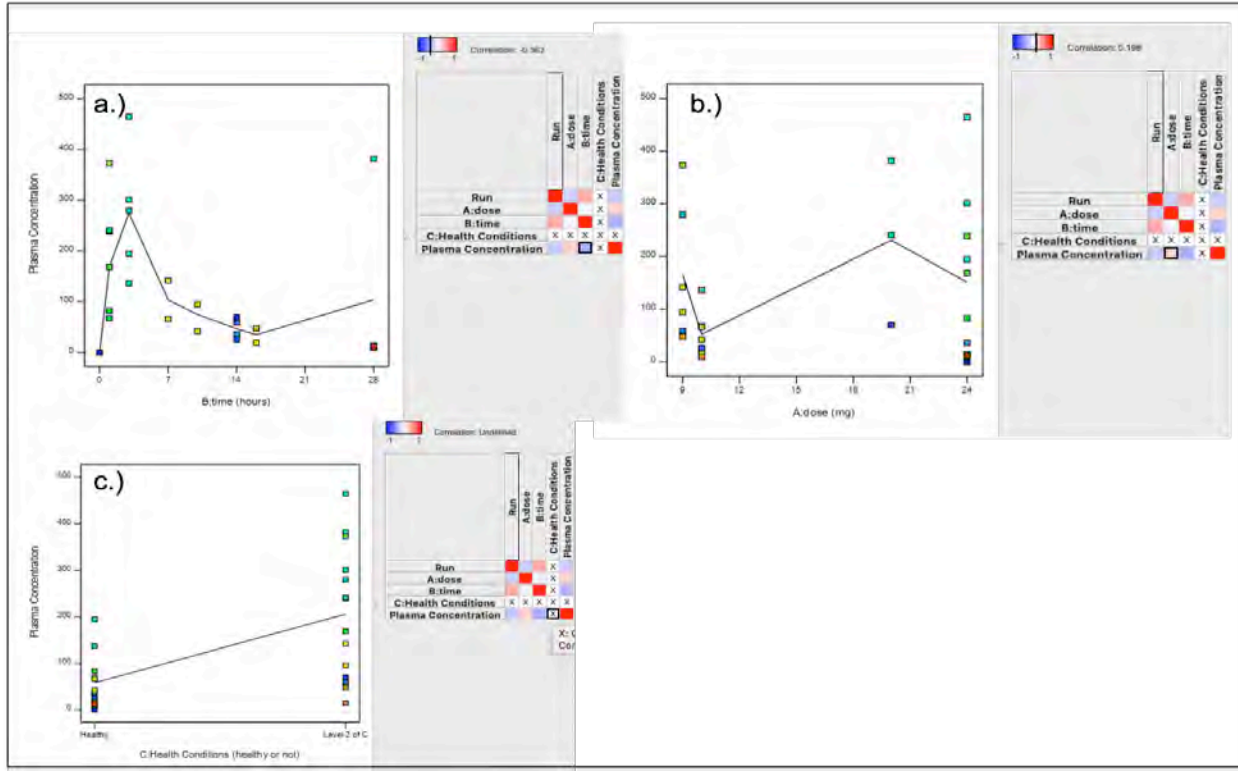


Figure 6. Design Expert correlation results of dose (mg), health (healthy vs cancer patients), and time (hrs) to lenvatinib plasma concentration (ng/mL).

Source: [2-5] & Author

Table 4. Design Expert correlation values of dose (mg) and time (hrs) to lenvatinib plasma concentration (ng/mL), as well as equation summaries and ANOVA analysis.

Factor	Correlation	Best Fit Summary	Final Equation [5]
dose (d)	0.198	Linear sequential p-value = 0.0038	$A * t + B * d + C_i$
health (h)	undefined		$A=4.47627 \ B=2.79459 \ C_{\text{healthy}}=59.90722$
time (t)	0.362		$C_{\text{cancer}}=200.24593$
ANOVA analysis of quadratic model			
Source	Sum of Squares	Mean Square	p-value
Model	198200	66082.38	0.0038 (significant)
Pure Error	15905.84	7952.92	
Cor Total	440600		

The Figure and Table above show the results of using the Design Expert Software to mathematically analyze the best model for the data of lenvatinib plasma concentration. The results show that time is more correlated with the concentration when compared to dose, but they both contain some influence. The health of the patient, however, had an undefined correlation that can be observed in the final equation. The software's equation that best fit the data in terms of any inputted dose, health of patient, and time spent in the body turned out to be linear. The patient's health did influence the result by an additional ~140 ng/mL if the patient happened to be a cancer patient. This strengthens the idea that cancer patients increase the bioavailability of the drug and should be a factor considered in further research of pharmacokinetics. The surface plot to the right shows the linear correlation of both time and dose with the plasma concentration of lenvatinib. These were consistently proportional so a linear model, equation 5, makes sense.

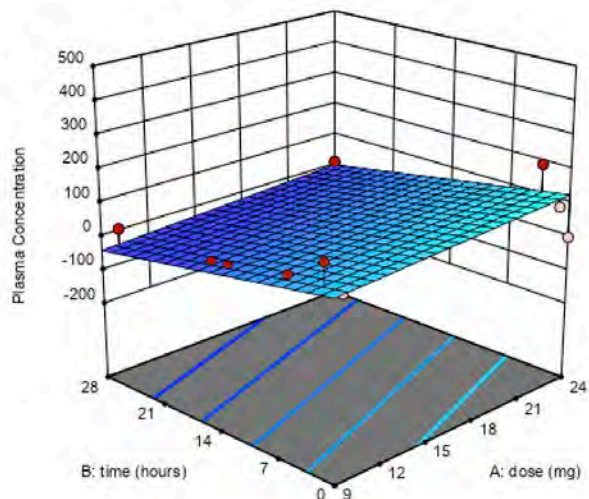


Figure 7. Surface plot of final equation from Table 4.

Source: Author

Table 5. Equation 4 used to predict percent drug remaining in terms of drug's location in the body based on how long on average ingested items remain in each part of the digestive path.

Drug Location	Min Disintegration Scenario (% drug remaining)	Max Disintegration Scenario (% drug remaining)
Saliva	85.95	85.1
Upper Stomach	47.09	10.42
Lower Stomach	33.71	Full disintegration
Duodenum	31.83	Full disintegration
Small Intestine	5.81	Full disintegration

Table 6. Equation 5 used to predict lenvatinib plasma concentration in terms of drug’s location in the body based on how long on average ingested items remain in each part of the digestive path, what dose they were prescribed, and whether they are a healthy patient or a cancer patient.

Capsules in the Market	Time (based on region of body) [hr]	Plasma concentration [ng/mL] – Healthy Patient (MIN-MAX scenarios)	Plasma concentration [ng/mL] – Unhealthy Patient (MIN-MAX scenarios)
4mg	Upper Stomach (0.5-1 hr)	73.3237-75.5619	206.948-209.1862
10mg	Upper Stomach (0.5-1 hr)	90.0913-92.3294	213.6624-215.9006
4mg	Lower Stomach (1.5-4.5 hrs)	77.8-88.9907	218.1387-229.3294
10mg	Lower Stomach (1.5-4.5 hrs)	94.5675-105.7582	234.9062-246.0969
4mg	Duodenum (2-5.5 hrs)	80.0381-95.7052	220.3768-236.0438
10mg	Duodenum (2-5.5 hrs)	96.8057-112.4726	237.1444-252.8113
4mg	Small Intestine (3-10.5 hrs)	84.5144-118.0864	224.8531-258.4251
10mg	Small Intestine (3-10.5 hrs)	101.2819-134.8540	241.6206-275.1927
4mg	Large Intestine(13-28 hrs)	129.2771-196.4211	269.6158-336.7599
10mg	Large Intestine(13-28 hrs)	146.0466-213.1887	286.3833-353.5274

The two tables above show the significance of modeling the pharmacokinetics of drugs utilizing measured data. The specific data to LENVIMA is able to predict the disintegration rate of the capsule with respect to location as well as the actual drug (lenvatinib) plasma concentration with respect to time and location. Predictive models like these provide healthcare professionals a better understanding of the drug a patient is taking that could correlate and help prevent serious side effects. Further research would include testing the model against new data to ensure its efficacy.

References

1. Tuleu, C., Basit, A. W., Waddington, W. A., Ell, P. J. and Newton, J. M. (2002), Colonic delivery of 4-aminosalicylic acid using amylose–ethylcellulose-coated hydroxypropylmethylcellulose capsules. *Alimentary Pharmacology & Therapeutics*, 16: 1771-1779. doi:[10.1046/j.1365-2036.2002.01327.x](https://doi.org/10.1046/j.1365-2036.2002.01327.x)
2. Kazuhiko Y., Noboru Y., Yasuhide Y., Hiroshi N., Yutaka F., Taizo H., Fumiaki K., Kazuto N., Noriyuki K. and Tomohide T. Phase I Dose-Escalation Study and Biomarker Analysis of E7080 in Patients with Advanced Solid Tumors. *Clin Cancer Res* April 15 2011 (17) (8) 2528-2537; DOI: 10.1158/1078-0432.CCR-10-2638
3. Shumaker, R. C, Aluri, J., Fan, J., Martinez, G., Ren, M., & Chen, K. (n.d.). Evaluation of the effects of formulation and food on the pharmacokinetics of lenvatinib (E7080) in healthy volunteers. *Int. Journal of Clinical Pharmacology and Therapeutics*, 52, 284-291. doi: 10.5414/CP201937
4. Shumaker, R. C., Aluri, J., Fan, J., Martinez, G., Thompson, G. A., & Ren, M. (2014). Effect of rifampicin on the pharmacokinetics of lenvatinib in healthy adults. *Clinical drug investigation*, 34(9), 651–659. doi:10.1007/s40261-014-0217-y
5. Gupta, A., Jarzab, B., Capdevila, J., Shumaker, R., & Hussein, Z. (2016). Population pharmacokinetic analysis of lenvatinib in healthy subjects and patients with cancer. *British journal of clinical pharmacology*, 81(6), 1124–1133. doi:10.1111/bcp.12907

Development of Control Systems for Flapping Winged Micro Air Vehicles

Student Researcher: Joel A. Hauerwas

Advisor: Dr. Roger Quinn

Case Western Reserve University
Mechanical and Aerospace Engineering

Abstract

Flapping winged flight has long been a marvel of researchers, dating back to the 11th century and while human powered flight has proved difficult significant progress has been made with unmanned ornithopters. Unlike fixed-winged or rotary aircrafts, a flapping winged system can use much less energy and operate at slower speeds with a greater degree of control. In order to control the flight of ornithopters a rudder is often implemented to steer and assist aerial maneuverability. For very small ornithopters, however, the rudder is less effective. Using biological inspiration from the Tobacco Hawkmoth, *Manduca sexta*, which is known for its stable flight patterns and turning, a new control system can be developed.

Project Objectives

This project aimed to provide the basis for further research into the development of abdominal flight systems. By observing and understanding the movement of air around the moth it will allow for informed design of mechanical control elements. In addition, by developing a standardized testing method for flapping winged micro air vehicles, later tests can be compared to the results of this study to determine the effectiveness of other systems. Work was also done to create a mechanical system which can mimic the abdominal rotation of the hawkmoth, which will eventually be wind tunnel tested in the same manner. These results will eventually be used to create a mechanical system similar to a rudder which can be used to control the flapping winged micro air vehicle.

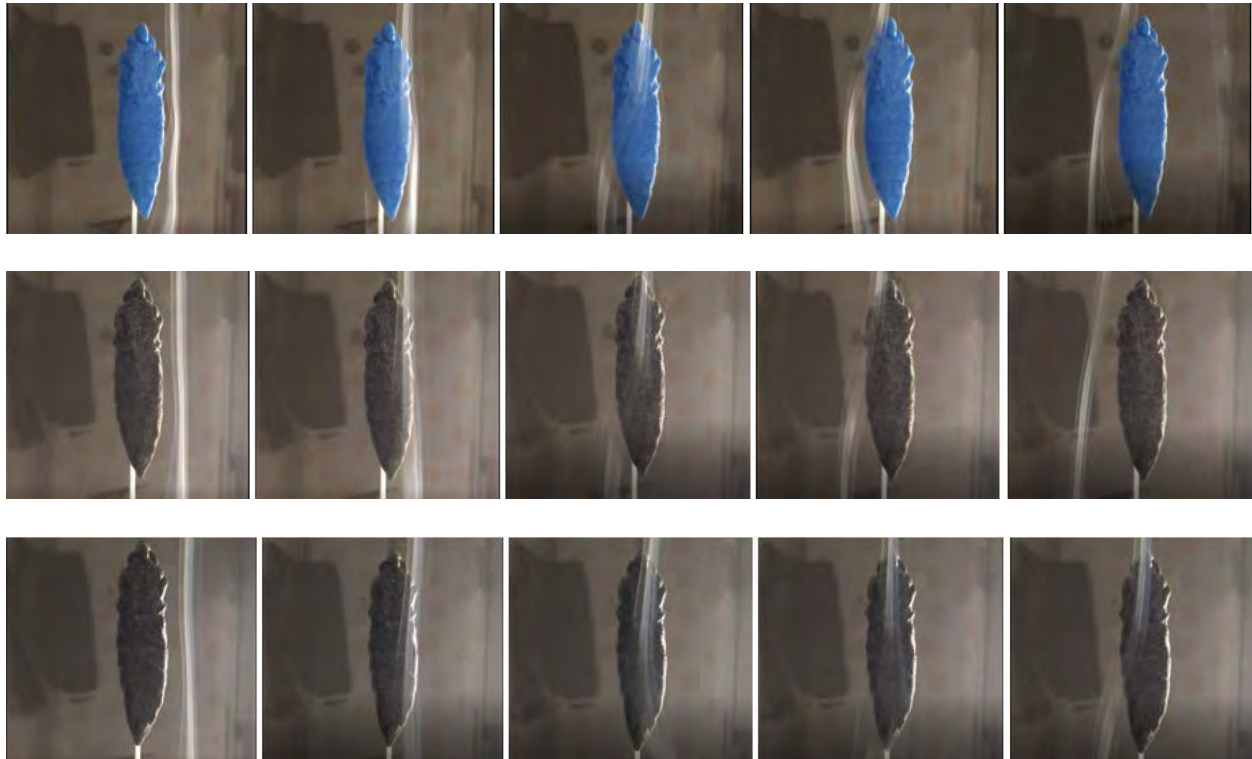
Methodology Used

To test the hypothesis three systems had to be developed: the 3D printed moths which were produced using a 3D scanner and then printed on an Objet 350 Connex, the sting to hold the moths in flight position, and the incense holder which produced an even stream of smoke. Each of these models was produced in Solidworks or Autodesk Meshmixer and then 3D printed. The models were then placed in the wind tunnel along with the recording equipment. From there the speed of the wind tunnel was increased slowly from zero meters per second until the air flow became laminar. The 3D printed models were then put onto the sting so that the flight plane is approximately 20 degrees from the horizontal. Once the experiment was set up, the smoke was filmed from below using a camera. To make contours more visible a dark paper was used to provide additional contrast. Once the incense stick burned across the width of the model, it was extinguished and the footage was combined. To isolate the smoke streams, the streams were arranged side to side and then compared to each other to determine effectiveness of the tests.

Results Obtained

The wind tunnel tests proved incredibly promising. The air flowed as predicted across the abdominal sections and trailed away from the moth in a clean manner. This implies that the force of the air against the abdomen would force the moth in the opposite direction of the airflow causing a strafe. Laying out the tests horizontally as the air moved allows for a clear progression to be shown as the air moves from

one side of the model to the other. More tests will be needed to further confirm these results but early tests are promising for the future of these experiments.



The above models are arranged top to bottom: Left rotation, No rotation, Right rotation. The smoke flows from the right of the model to the left and moves around the abdomen in a predictable manner

References

1. M. Popovic, "Design and Implementation of an Ornithopter," *WPI*, Apr. 2016.
2. Tubbs, Travis & Palazotto, Anthony & Willis, Mark, "Biological Investigation of Wing Motion of the *Manduca Sexta*," *International Journal of Micro Air Vehicles*, 2011.
3. Moses, Kenneth & Prigg, David & Weisfeld, Matthias & J. Bachmann, Richard & Willis, Mark & Quinn, Roger, "Simulating Flapping Wing Mechanisms Inspired by the *Manduca sexta* Hawkmoth," 2018.

**A Novel Mutation Located In the C-terminal Cytoplasmic Domain of the CCR5 Gene
With Potential Effects on HIV Infectivity**

Student Researchers: Ashley E. Innes^{1,2}, Audra L. Fincham^{1,2}, Jabari Fuentes^{1,4}, Matthew Fox¹,
Savannah L. Herbert^{1,3}

Advisor: Dr. Harry W. Kestler, Ph.D.

¹Lorain County Community College, Elyria, Ohio

²Bowling Green State University

³Baldwin Wallace University

⁴Lorain County Community Early College High School

Abstract

A novel mutation in the *ccr5* gene, which codes for the CCR5 protein, was found in one of 5 children in an African-American family. The mother contracted HIV before the birth of her first child in the early 1980s before HIV testing was widely used. The CDC did not recommend testing pregnant women until 1995. She unknowingly exposed all five of her children to HIV through vaginal birth. Out of the five children, the second born did not acquire the infection even though she was exposed to the virus at birth. The other 4 children were HIV infected. The mother and the infected children all carried genetically related HIV and the similarity was inversely correlated with birth order. A missense point mutation was discovered in the carboxyl terminal cytoplasmic domain of the uninfected child's *ccr5* gene. The mutation (TG5), changes a lysine codon at position 314 into an arginine codon. The allele containing the TG5 mutation was amplified by polymerase chain reaction. The DNA fragment containing the mutated TG5 gene was sub-cloned into pLXSN, a retroviral plasmid vector. Clones made from pLXSN-TG5 will be used to transfect the packaging cell line PT67. The PT67 cell line will assemble viral particles containing the TG5 mutation. The retroviral particles will be recovered and introduced into the T-cell line H9 well as other cells. The expression of the TG5 gene in H9 and its effect on HIV infectivity will be tested. It has been reported that CCR5 delta 32 can down-modulate wild-type CCR5 and CXCR4. The ability of TG5 to down-modulate wild-type CCR5 and CXCR4 will be determined.

Octaworm: Semi-Rigid Robotics

Student Researcher: Steven H. Innocenzi

Advisor: Dr. Daniel Deckler

The University of Akron
Biomedical Engineering (Biomechanics)

Abstract

Pipe inspection is an important practice that occurs in all fields of industry and must be completed efficiently and in a cost-effective manner. A semi-rigid robot would be able to achieve both requirements and be able to conform to the unique geometry of most pipe systems. Using 3D printed material in conjunction with simple parts and Arduino programming, a low-cost product that can be easily scaled to a variety of pipe sizes was created. The project builds on previous work completed by the international collaboration between The University of Akron and The University of Chile.

Project Objectives

The efficiency of exploring pipe systems to ensure their functionality depends on a variety of factors to both provide the necessary abilities and remain cost effective. Requirements for the design include having interchangeable parts to allow reusability of supplies, 3D printed ball joints to easily alter the size if needed, and an Arduino board with an 8-channel relay to include low cost coding software. The octahedral design allows the robot to adjust to the environment and attach to surfaces unlike other linear drive robots. The last objective to achieve is developing software and altering the hardware to traverse a variety of turns. The library created can later be referenced to explore pipes using only the schematics to search for any issues.

Methodology Used

The design for the robot was a continuation of the work started at The University of Chile. The design that they completed was a third iteration that relied on 3 solenoids operating on a 3 channel Arduino relay. This was then increased to an 8-channel relay with 8 solenoids to allow the robot to be more deformable and able to navigate through turns of various degrees. With the middle section actuators being controlled independently, the robot could then expand at alternative angles.

Results Obtained

The Octaworm robot was able to perform exceptionally well in a 13" sheet metal pipe. It was able to travel down the pipe both forward and backwards and was able to ascend and descend the pipe at a 90-degree incline without slipping. The robot operated at a pressure of 75 psi to remain anchored in place yet not break any of the components when expanding. Software was created to make several turns of up to 45 degrees which exceeded the original goal of this project which was to perform a 30 degree turn. All the parts, such as the joints and the materials used, were saved in the appropriate drawings so that they can be referenced and altered to scale the robot for other pipes and environments. The Arduino library created will be very useful as the project continues in the future as it contains commands that can be referenced to correctly perform the necessary turn. Figure 1.1 displays the side view of the finished robot.

Future Work

The work completed for this project is a large step forward as the design is now capable to make turns in piping systems. This opens the possibility for it to be scaled to the necessary size and function in real world applications. The next steps for the project would be to gather data for its limitations in different environments and begin making the robot autonomous using either a camera system or ultrasonic distance sensors to determine the type of turn it must execute. These changes could lead to the possibility of the robot to perform in other areas other than pipes such as small confined places behind walls or in voids in a disaster environment. In addition, these changes will continue to lower the cost in the long run by removing the need for schematics of a piping system and an operator standing by to perform the inspection.

Figures/Charts

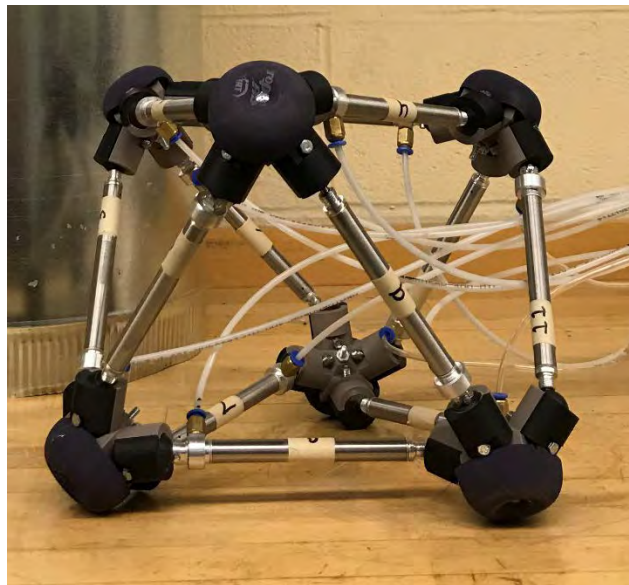


Figure 1.1. Octaworm Robot.

References

1. Grunewald, Scott J. "The 3D Printed OctaWorm Robot Can Go Where No Other Robot Can." *3DPrint.Com | The Voice of 3D Printing / Additive Manufacturing*, 13 Aug. 2015, 3dprint.com/88873/3d-printed-octaworm-robot.

Increasing Mechanical Toughness of a Double Network Hydrogel from Agar, Polyacrylamide and Methylenbisacrylamide

Student Researcher: Madelyn P. Jeske

Advisor: Dr. Jie Zheng

The University of Akron

Department of Chemical and Biomolecular Engineering

Abstract

Hydrogels are soft materials consisting of three-dimensional networks comprised mainly of water have some application in the medical industry for usage; however, they tend to be weak and brittle. Double-network hydrogels have shown promise in the field of having advanced mechanical properties such as a tensile stress of 1-10 MPa, a tearing fracture of 10^2 - 10^3 J/m², and a compression capacity of 17.2 MPa. DN hydrogels are a new field of study and require extensive fundamental research to optimize their features for clinical testing. The double-network hydrogel of interest for the study is of a physically cross-linked first network and a second chemical cross-linked network to create a hybrid polymer. Agar was selected for the first, physically cross-linked network due to the thermoreversible properties. Polyacrylamide (PAAm) is the second with cross-linker methylenbisacrylamide (MBAA). A photoinitiator, hydroxymethyl phenoxyacetic acid (HMP), was selected as well for chemical cross-linking under UV light. All reagents were synthesized into a hydrogel by the one-pot method; an efficient process that will require 2 hours and minimal labor (as opposed to 2-3 days by other experiments). Samples were cut into equivalent sizes and shapes to undergo tensile testing to determine tensile stress, tensile strain, and Young's (Elastic) modulus. These gels achieved maximum tensile stress at 1.02 MPa, a tensile strain at 11.44 mm/mm, and an elasticity modulus of 234 kPa, showing promise as mechanically tough hybrid DN hydrogels that can be used in future medical applications.

Project Objective

The purpose of this study is to develop a novel double network hydrogel that will be able to exhibit greater mechanical properties to become more applicable in the medical field will help to explore fundamental understanding about the double network hydrogels and materials to create them for future development. This specific experiment will determine the optimal ratio of agar, AM, and MBAA, that produce the best mechanical properties.

Introduction

Hydrogels are soft materials consisting of three-dimensional networks comprised mainly of water. The gels possess unique properties such as responsive to outside stimuli from thermal or acidic environments, swelling/deswelling, and anti-fouling. They have become applicable in the medical industry for usage as adhesives, drug delivery, tendon replacements, contact lenses, and repairing tissues. For example, damaged organs need tissues that are indistinguishable from the normal ones, and transplants risk rejection from the immune system. Each day, 20 individuals on the waiting list for organ transplants in the US die from shortage. The need for strong hydrogels to accelerate healing is imperative.

Background

Unfortunately, current hydrogels tend to be weak and brittle. Double network hydrogels have shown promise in the field of having advanced mechanical properties with a tensile stress of 1-10 MPa, a

tearing fracture of $10^2\text{-}10^3 \text{ J m}^{-2}$, and a compression capacity of 17.2 MPa. The double network hydrogel of interest for the study is of a physically cross linked first network and a second chemically crosslinked. The first network is brittle and allows for several small fractures but has the ability to swell immensely in water. Once a second, ductile network is introduced the resulting specimen exhibits greatly increased mechanical properties. Agar was selected as the first network due to its triple helices structure that is thermoreversible. Polyacrylamide (AM) was selected to create the second network. A photocrosslinker, methylenebisacrylamide (MBAA), is necessary once the gel is subjected to UV light to chemically bind the AM to the agar. This is hypothesized to increase the mechanical properties of double network hydrogels for future applications.

The traditional creation of DN hydrogels is lacking; it is tedious, time and material consuming. The first step is to synthesize the first network with a strong polyelectrolyte (PAMPs) that will create a tightly chemically crosslinked gel. The polyelectrolyte is a long chain, charged polymer that when activated by UV light will change its architecture to adopt an expanded conformation that will ultimately affect its solvent affinity. The first network will swell in water and have the ability to absorb 20-30 times the molar concentration of the second network. The neutral polymers of the second network have long, flexible chains that slowly diffuse into the first and extend their chains away from the solution into the hydrogel. The first network's inhomogenous structure is accredited greatly to the strength and ductility of the final product. Unfortunately, the chemical-chemical crosslinkage allows for fractures in the first network to be irreversible and have no recovery rate. The diffusion of the neutral polymer creating a second chemically crosslinked network also requires 1-2 days time and an extreme excess amount of polyelectrolyte.

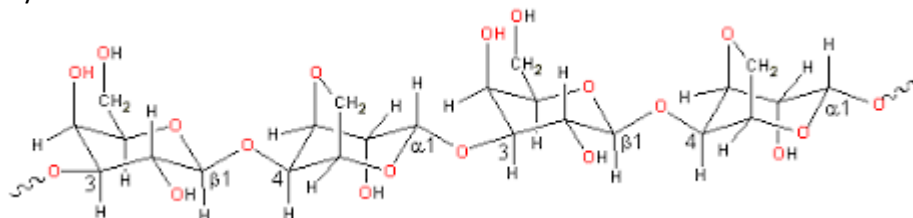


Figure 1. Shows the molecular structure of agar Credit: <http://www1.lsbu.ac.uk/water/agar.html>

Figure 1 displays the molecular dual chair conformation of agar bonded by negatively charged oxygen ions. Several of the branches have hydroxyl groups as well, and these electron affinities owe to agar's high hydrogen bonding properties that create a stable double helical structure when heated and gelled.

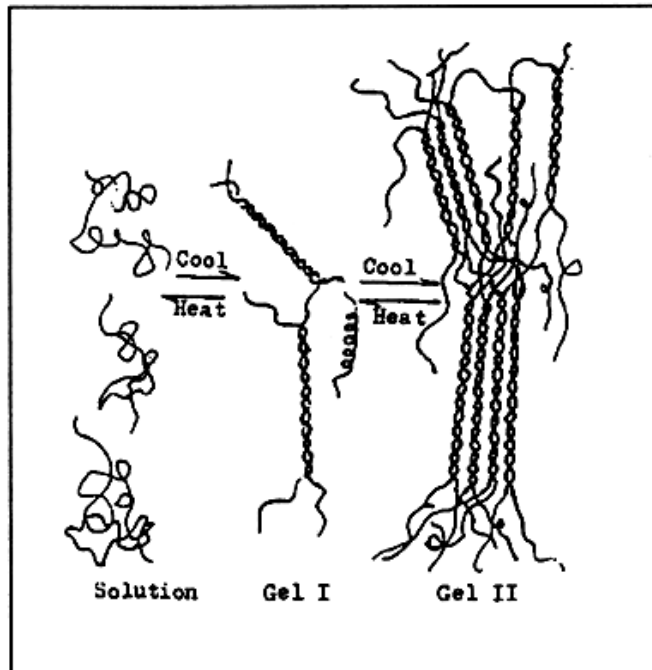


Figure 2. Shows the thermoreversible properties of agar Credit: <http://www.fao.org/docrep/field/003/AB730E/AB730E03.htm>

Figure2 illustrates the thermo-reversible properties of the agar structure. When gelled (cooled from high heat of around 100 Celsius), the equatorial hydrogen atoms on the 3,6-galactose residues (as showed in Figure 1) are united to create a double helical conformation that can be denatured with high temperature. Denaturing, or dissolving, of the structure increases its solubility and affinity for water by freeing the charged hydroxyl groups and creating a polar molecule that favors the polarity of water. The spacing between the helices that forms during cooling is large and traps water-20 times the weight of the agar due to high solubility.

Chen and associates have developed the one-pot method to overcome these issues. The method is done by adding all reactants to “one pot” and using a heating to cooling polymerization method that accounts for the inert (non reactive) interaction of agar with the other polymers. This is done using agar and crosslinked PAAm (Polyacrylamide), where the two networks allow for a physically and chemically crosslinked hybrid structure that does not rely on slow diffusion or exuberant amount of reactant. Agar possesses a thermo reversible solid to gel phase transition and coil to helix structural transition. Although agar is typically insoluble in cold water, heat can dissolve the structural carbohydrate and cooling (or “gelling”) causes a double helical 3D structure to form and whose framework can hold and absorb 20 times its own weight in water. The gelling property of agar is owed to the three equatorial hydrogen atoms on the 3,6-anhydro-L-galactose residues, which constrain the molecule to form a helix. It is a stable, physically crosslinked network with a slight negative charge. Once the first network is created, photopolymerization, a light activated free radical crosslinking technique, from UV light is used to non covalently crosslink PAAm with the first network. The step is a rapid liquid to solid transition of the dissolved components in the “one pot” by a rapid reaction rate that results in uniform hydrogel properties resulting in a DN with an incredible elastic modulus, strength, toughness, fracture energies, extensibility, free shapeable dual polymer. Using a hybrid physical-chemically crosslinked double

network allows for fractures in the first to be reversible with thermodynamics and thus acquire a fast recovery rate with maintaining a strong and ductile hydrogels. The fabrication of the biosynthetic polymer is also weaved in 1-2 hours, exponentially less than the original 1-2 day amalgamation. This method is reliable, depends on a dilute concentration of reactants, and extremely fast in comparison to the traditional method.

These gels will have their mechanical toughness evaluated by maximum tensile stress (MPa), tensile strain maximum (mm/mm), and maximum Young's Modulus (E, KPa). Young's Modulus measures the resistance of a material to elastic (recoverable) deformation. In this case, a flexible material has a low Young's Modulus and can change its shape when stress is applied. A strong material will require high loads to permanently deform it. Tensile strain is the relative elongation of a material when subjected to stress.

Methodology

Double network hydrogels are to be synthesized by a one pot method: all reagents are added at once with several samples of varied compositions. It is an efficient process that minimizes labor and time. Samples will be heated to 100 Celsius and cooled for 2 hours to create the first physically cross linked network. Once at room temperature, samples will be subjected to UV light for 90 minutes to create the second, chemically cross linked network and the resulting hydrogels will undergo tensile tests to evaluate mechanical properties.

Varying compositions of reagents will be studied in independent batches to determine their effects. From Chen, it was determined that the amount of MBAA should be 0.03 mol% of AM, and thus amounts around that value were evaluated for the photocrosslinker.

Table 1. Displays the composition of reagents as determined from Chen's paper, and calculated from 10 mL of water to 4 mL of water for this experiment.

Composition for 10 mL of Water			Composition for 4 mL of Water		
Reagent	Amount		Reagent	Amount	
AM	7	mol/L	AM	1.99	g
Agar	17	mg/L	Agar	0.068	g
HMP	0.4	mol% of AM	HMP	0.024	g
MBAA	0.028	mol% of AM	MBAA	1.2	mg

The effects of MBAA on the mechanical toughness of the double network hydrogel were evaluate at various compositions of the component based on mol% of AM (0.00, 0.01, 0.02, 0.03, and 0.04 mol%). To accurately add the small amounts of photocrosslinker, 0.12 g of MBAA was dissolved in a beaker with 5 mL of water and covered with aluminum foil to prevent premature degradation by UV light. A micropipette (100 micro liters) was calibrated for each of the varying mol% and is recorded in **Table 2**.

T

Table 2. Displays the various compositions of MBAA tested.

mol%	AM (g)	Water (mL)	HMP (g)	MBAA (mL)	Agar (g)
0	1.99	4.00	0.024	0.00	0.068
0.01	1.99	4.00	0.024	0.017	0.068
0.02	1.99	4.00	0.024	0.034	0.068
0.03	1.99	4.00	0.024	0.050	0.068
0.04	1.99	4.00	0.024	0.067	0.068

The effects of agar was evaluated at different amounts (7, 17, 27, 37, 47 g/mL) and can be seen in **Table 3**.

Table 3. Displays the various compositions of agar tested.

Composition	AM (g)	Agar (g)	HMP (g)	MBAA (mL)	Water (mL)
7 g/mL	1.99	0.028	0.024	0.050	4.00
17 g/mL	1.99	0.068	0.024	0.050	4.00
27 g/mL	1.99	0.108	0.024	0.050	4.00
37 g/mL	1.99	0.148	0.024	0.050	4.00
47 g/mL	1.99	0.188	0.024	0.050	4.00

The effects of polyacrylamide were also evaluated at various compositions (5, 6, 7, 8, 9 mol/L) and can be seen in **Table 4**. Note that the amounts of HMP and MBAA also fluctuated with the varied amounts of AM because in **Table 1** their compositions are based upon the molarity of the second network chemical.

Table 4. Displays the compositions of hydrogels when determining effect of concentration of AM

Composition	AM (g)	Agar (g)	HMP (g)	MBAA (mL)	Water (mL)
5 mol/L	1.42	0.068	0.018	0.036	4.00
6 mol/L	1.71	0.068	0.021	0.043	4.00
7 mol/L	1.99	0.068	0.024	0.050	4.00
8 mol/L	2.27	0.068	0.028	0.058	4.00
9 mol/L	2.56	0.068	0.031	0.065	4.00

Once each hydrogel is synthesized, they will be cut into equal sized and shaped samples with a length of 35 mm, width of 3.18, and thickness of 1 mm. These underwent tensile tests on an Instron 3345 MA. The samples were cut using a uniform tool to create a “dog bone” shape. Each end was attached to clamps evenly, and once testing began they were stretched at a rate of 100 mm/minute. Data was collected with Bluehill software and translated into visual graphs with Origin 8.5 software.

Results and Discussion

Using the one pot method, gels were created efficiently within a 2.5-3 hour process as opposed to three days and created optically transparent and testable hydrogels as seen in Figure 3.

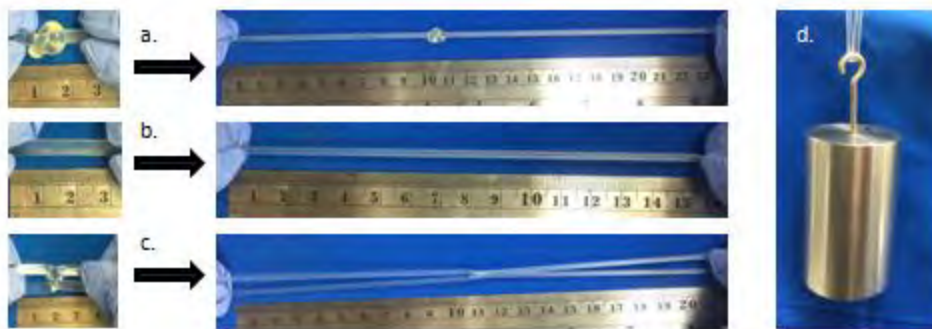


Figure 3. Displays the gels being stretched to demonstrate their mechanical toughness and flexibility. 3a. shows the knotted, 3b. is the normal, 3c. is the double gels. 3d. demonstrates it withstanding 500 g of weight without breaking.

In **Figure 3**, a gel could be stretched 5x its original length. Knotted or coupled with a second hydrogel, it stretched 7x its original length and also shows the hydrogel withstanding 500 g of weight without breaking displaying its mechanical toughness and flexibility as a polymer. Retaining its shape after injection into mold implies that the gel has freeshapeable properties that can be used for future necessary conformations to tailor to a specific need. The use of a physically cross linked network provided for a brittle aggregation of agar helices that absorbed a large amount of water and AM. The second network of AM created a soft, ductile network that upon stress the sacrificial bonds created by the first network to initially dissipate energy would be absorbed and increase the overall mechanical properties.

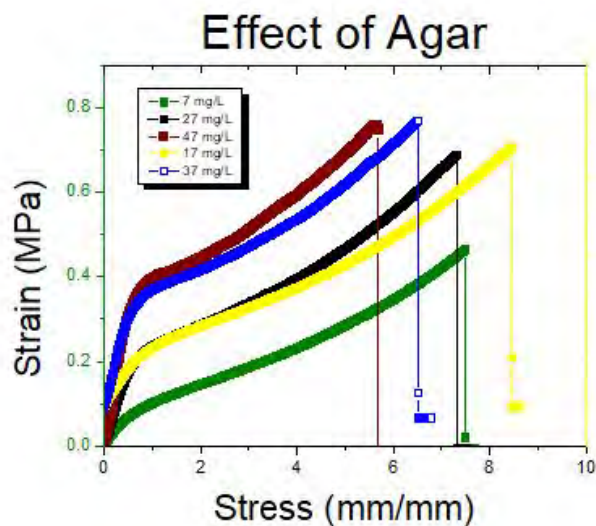


Figure 4. Displays the tensile stress/strain curve for the varied compositions of agar.

In **Figure 4**, the composition of agar was varied to determine its effects. Each sample had identical amounts of AM, HMP, water, and MBAA (0.03 mol%), but the amounts of agar tested included 7, 17, 27, 37, and 47 mg/L. It appears that the lower amounts of agar showed the highest mechanical strength with 17 mg/L showed the maximum tensile stress at 1.02 MPa, a tensile strain at 11.44 mm/mm, and an

elasticity modulus of 234 kPa. Increasing the amount of agar increases the ratio of first network to second, where hydrogels with excessive amounts will be too brittle and not have enough of a second, ductile network to dissipate the energy and lowers the mechanical potential.

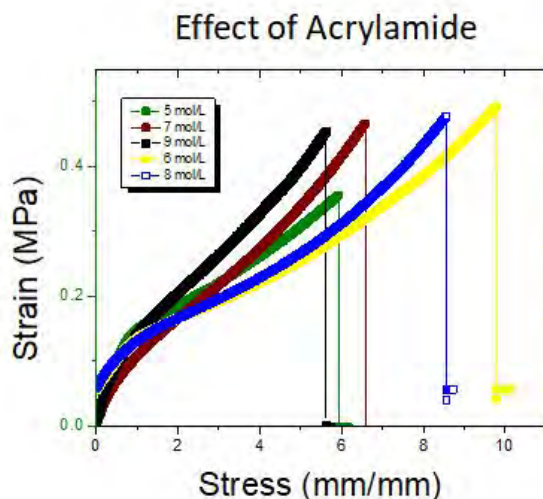


Figure 5. Displays the tensile stress/strain curve for varied compositions of Acrylamide.

In **Figure 5**, the composition of AM was varied to determine its effects. All samples had identical amounts of agar, HMP, water, and MBAA (0.03 mol%), but the amounts of AM included 5, 6, 7, 8, and 9 mol/L. Once again, more median amounts of acrylamide displayed the highest mechanical properties, with the maximum at 6 mol/L having reached maximum tensile stress at 0.796 MPa, tensile strain at 9.79 mm/mm, and $E = 198$ kPa. Increased amounts of AM will decrease the ratio of first to second network. Excessive ratio of AM will not be as tightly bound to the first network with photocrosslinker MBAA and photoinitiator HMP, and a less organized and too soft second network will decrease the mechanical properties.

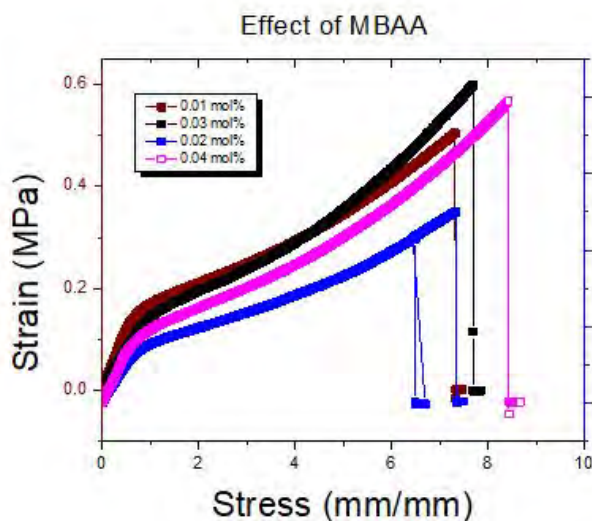


Figure 6. Displays the tensile stress and strain curve for the varied compositions of MBAA.

In **Figure 6**, it is seen that an MBAA composition of 0.04 mol% of AM with a maximum tensile stress of 0.789 MPa, tensile stress of 8.47 mm/mm, and elasticity modulus of 260 kPa. Samples with 0.00 mol% of MBAA were too brittle to test, implying that for these proposed compositions the second, ductile network of AM is too soft and requires the photocrosslinker. Traditionally, MBAA concentrations beyond 0.03 mol% caused excessive crosslinking leading to overly tightly wound second networks that resulted in two brittle structures, both the first and second networks, completely contradicting the point of having a hybrid double network with gelatin/PAAm. Gelatin, however, has a triple helix structure as opposed to agar. The triple helix would have more molecular surface area that could potentially lead to the “over cross-linking” phenomenon observed in gelatin, whereas the double helix in agar does not allow the photocrosslinker to overly bind the long, linear polymer chain of PAAm, and a higher concentration of MBAA would result in heightened mechanical properties of agar/PAAm gels. Another important note is that the physically crosslinked network of agar is formed before the second network, whereas gelatin does not form its network until after the chemical crosslinking in PAAm under UV light.

Conclusion

Double Network hydrogels are three dimensional networks of a soft, mechanically tough material that have been used for drug delivery, agriculture, adhesives, and other widely applicable uses. Using the one-pot method, a single hydrogel can be produced in 3 hours as opposed to the once demonstrated three days. It has been found that with a first, physically cross linked network and a second, chemically cross linked, hybrid double network hydrogels exhibit high mechanical properties and are freeshapeable. Agar is a thermoreversible organic molecule with a triple helix structure that provides an excellent first network that organizes into aggregate bundles once cooled to room temperature (after heated to 100 Celsius) to reform its hydrogen bonds and absorbs 20-30x its weight in water. AM is a long polymer that readily dissolves in water to form a second, chemically crosslinked network (with photoinitiator HMP) that wraps and forms more hydrogen bonds. The increase in chemical activity with long polymer chains forms an organized structure around the lattice matrices created by the first network as reinforcement so that once stress is added to the hydrogel to help dissipate energy from crack propagation in the first, brittle network to create a ductile and soft polymer. Photocrosslinker, methylenebisacrylamide, activated with UV light organizes and increases chemical bonding of AM polymer chains with agar helices to increase the tensile stress/strain of a hydrogel without needing to alter the agar/AM ratio. These gels can achieve maximum tensile stress at 1.02 MPa, a tensile strain at 11.44 mm/mm, and an elasticity modulus of 234 kPa, whereas gelatin/PAAm gels achieve a tearing tensile stress of 0.268 MPa, a tensile strain of 40.69 mm/mm, and $E = 84$ kPa. Agar/PAAm show promise of being a tough double network hydrogel, and have their mechanical strength increased by using photocrosslinker MBAA. Differences in mechanical properties in relation to MBAA concentration may be attributed to structural differences in the previously tested gelatin/PAAm gels versus agar/PAAm gels and sequencing of network formations.

Special Acknowledgments

A thank you to Dr. Jie Zheng who has supported this project through his facility, resources, and as a Principal Investigator.

Also a thank you to Fengyu Yang, a Ph. D candidate at The University of Akron who has helped guide through the project and provided insight and assistance in lab.

And a thank you to the Ohio Space Grant Consortium for funding this research.

References

1. Chen Q, Chen H, Zhu L, Zheng J. Fundamentals of double network hydrogels. *Journal of Materials Chemistry B*. 2015;3(18):3654-76.
2. Clark AH, Richardson RK, Ross-Murphy SB, Stubbs JM. Structural and mechanical properties of agar/gelatin co-gels. Small-deformation studies. *Macromolecules*. 1983 Aug;16(8):1367-74.
3. El-Roz, M., Lalevée, J., Allonas, X., & Fouassier, J. P. (2009). Mechanistic investigation of the silane, germane, and stannane behavior when incorporated in type I and type II photoinitiators of polymerization in aerated media. *Macromolecules*, 42(22), 8725-8732.
4. Jeon S, Yoo YM, Park JW, Kim HJ, Hyun J. Electrical conductivity and optical transparency of bacterial cellulose based composite by static and agitated methods. *Current Applied Physics*. 2014 Dec 1;14(12):1621-4.
5. Jiang, S., & Cao, Z. (2010). Ultralow-fouling, functionalizable, and hydrolyzable zwitterionic materials and their derivatives for biological applications. *Advanced materials*, 22(9), 920-932.
6. Chen Q, Zhu L, Zhao C, Wang Q, Zheng J. A robust, one-pot synthesis of highly mechanical and recoverable double network hydrogels using thermoreversible sol-gel polysaccharide. *Advanced materials*. 2013 Aug 14;25(30):4171-6
7. Kuckling D, Vo CD, Wohlrab SE. Preparation of nanogels with temperature-responsive core and pH-responsive arms by photo-cross-linking. *Langmuir*. 2002 May 28;18(11):4263-9.
8. Slaughter BV, Khurshid SS, Fisher OZ, Khademhosseini A, Peppas NA. Hydrogels in Regenerative Medicine. *Advanced materials (Deerfield Beach, Fla)*. 2009;21(0):3307-3329. doi:10.1002/adma.200802106.
9. Yan, Q., & Hoffman, A. S. (1995). Synthesis of macroporous hydrogels with rapid swelling and deswelling properties for delivery of macromolecules. *Polymer*, 36(4), 887-889.

Effect of DNA Methyltransferase Inhibition in Hypoxic and Normoxic Conditions on Cellular Proliferation and Potential Growth Regulators in Human Diffuse Intrinsic Pontine Gliomas

Student Researcher: Madison M. Jewell

Advisor: Dr. Robert Lober, M.D., Ph.D.

Wright State University
Neuroscience, Cell Biology, and Physiology

Abstract

Diffuse intrinsic pontine gliomas (DIPGs) are aggressive, infiltrative pediatric brain tumors that contain an abysmal survival rate of less than 1-year. A distinct and abnormal epigenetic profile of DIPG is evident in which the most commonly observed mutation occurring in over 80% of DIPGs is a methionine substitution at lysine 27 on histone H3 (H3.3K27M), resulting in observed global reduction of H3K27me_{2/3} and central gain of H3K27me₃. Additionally, variations in expression of p16/ink4A, a tumor suppressor and critical cell cycle regulator of the G₀-G₁ to S-phase transition, have been observed and a mechanism of H3.3K27M-induced repression of p16/ink4A has been proposed in which a DNA methyltransferase inhibitor rescued p16/ink4A expression, thus restoring cell cycle regulation and tumor suppression capabilities. Regions of hypoxia are evident within the solid tumor microenvironment of DIPGs and are associated with a distinct epigenetic profile and therapeutic resistance. Despite the global hypomethylation observed in DIPGs, hypoxic regions are classically hypermethylated, highlighting the importance of determining the efficacy of a DNA methyltransferase inhibitor in both normal and low oxygen states. This study sought to investigate the effects and treatment efficacy of DNA methyltransferase inhibition on the overall proliferation of H3.3K27M expressing DIPG cells as well as the expression of p16/ink4A in both normoxic and hypoxic regions.

Project Objectives

The objective of this project was to investigate the epigenetic changes and overall cellular proliferation that occurs upon treatment of human diffuse intrinsic pontine glioma cell lines with increasing concentrations of a DNA methyltransferase inhibitor, decitabine. Prior studies utilizing murine models displayed evidence at the p16 promoter for increased levels of H3K27me₃ in conjunction with H3.3K27M induced targeted repression of p16/ink4a, a tumor suppressor and critical cell cycle regulator of the G₀-G₁ to S-phase transition. Loss of p16/ink4a is associated with accelerated tumorigenesis and thus it was suggested rescuing p16/ink4a with decitabine as a potential therapeutic avenue in treatment of DIPG tumors harboring p16/ink4a repression. We sought to investigate the effect of a DNA methyltransferase inhibitor on epigenetic changes shown to promote tumor growth and disease progression as well as evaluate the overall cellular proliferation in both normoxic and hypoxia-induced human DIPG cells.

Methodology

A line of human DIPG X cells were utilized in the evaluation of protein expression through western blot analysis. The cells were treated in ten-fold increasing concentration of decitabine ranging from 0.001 micromolar to 10 micromolar in addition to a DMSO treated vehicle. One set of cells were treated in 24 hour pulse hypoxia (0.5% O₂) while another were incubated in a normal oxygenated environment. Lysates were then collected and BCA calculations ensued utilizing the Pierce BSA kit. Western blot results for cells treated in normoxic conditions are shown below in Figure 1, and western blot results for cells treated in hypoxic conditions are shown below in Figure 2.

To evaluate the viability and cellular proliferation following treatment in ten-fold increasing concentration with decitabine as performed prior, a dose response curve over a five day period was obtained utilizing Trypan Blue Assay on human DIPG IV cells. Three trials were performed in normoxic conditions and the analyzed results are shown in Figure 3. Due to logistical difficulty attaining the necessary gas for the hypoxic chamber, only one trial of Trypan Blue Assay pulse-hypoxia (0.5% O₂) and decitabine treated DIPG IV cells was able to be performed. The un-analyzed results are shown below in Figure 4. A comparison of the percent viability between decitabine treated human DIPG IV treated in hypoxia and normoxia occurred and is shown in Figure 5.

Results

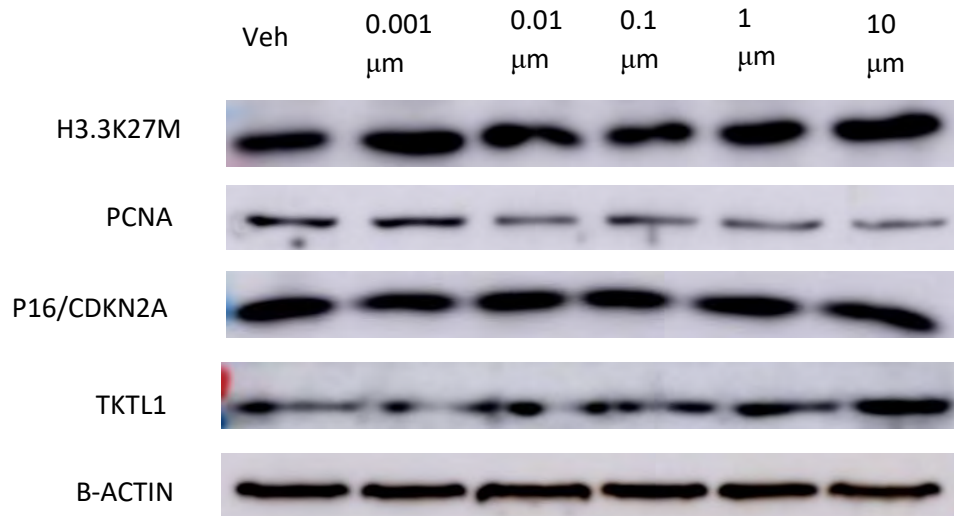


Figure 1. Protein expression with increasing decitabine concentration in human DIPG X cells treated in normoxic conditions.

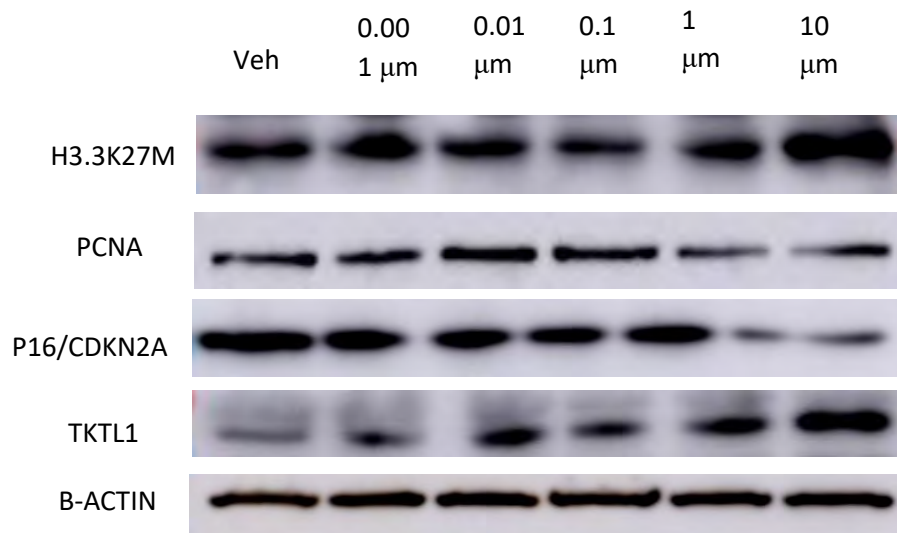


Figure 2. Protein expression with increasing decitabine concentration in human DIPG X cells treated in hypoxic conditions (0.5% O₂ 24 hr).

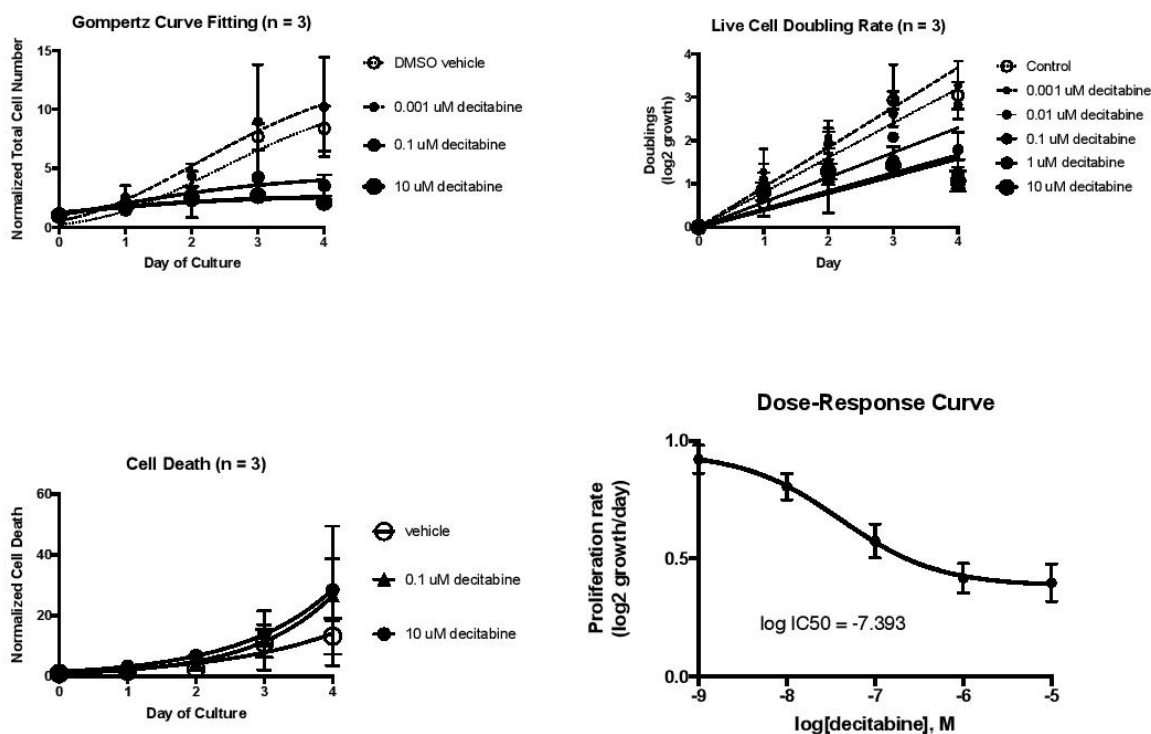


Figure 3. Analyzed trypan blue assay data of total cell number, cell death, live cell doubling rate and dose-response curve for human DIPG IV cells (n=3).

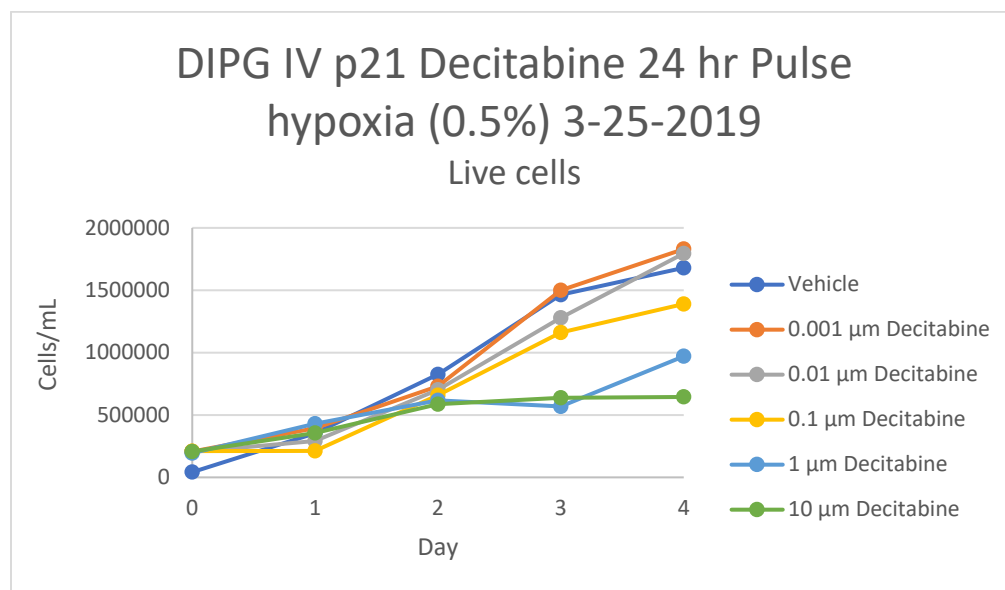


Figure 4. Un-analyzed data for trypan blue assay dose-response of pulse hypoxia (0.5% O₂ for 24 hr) and decitabine treated human DIPG IV cells.

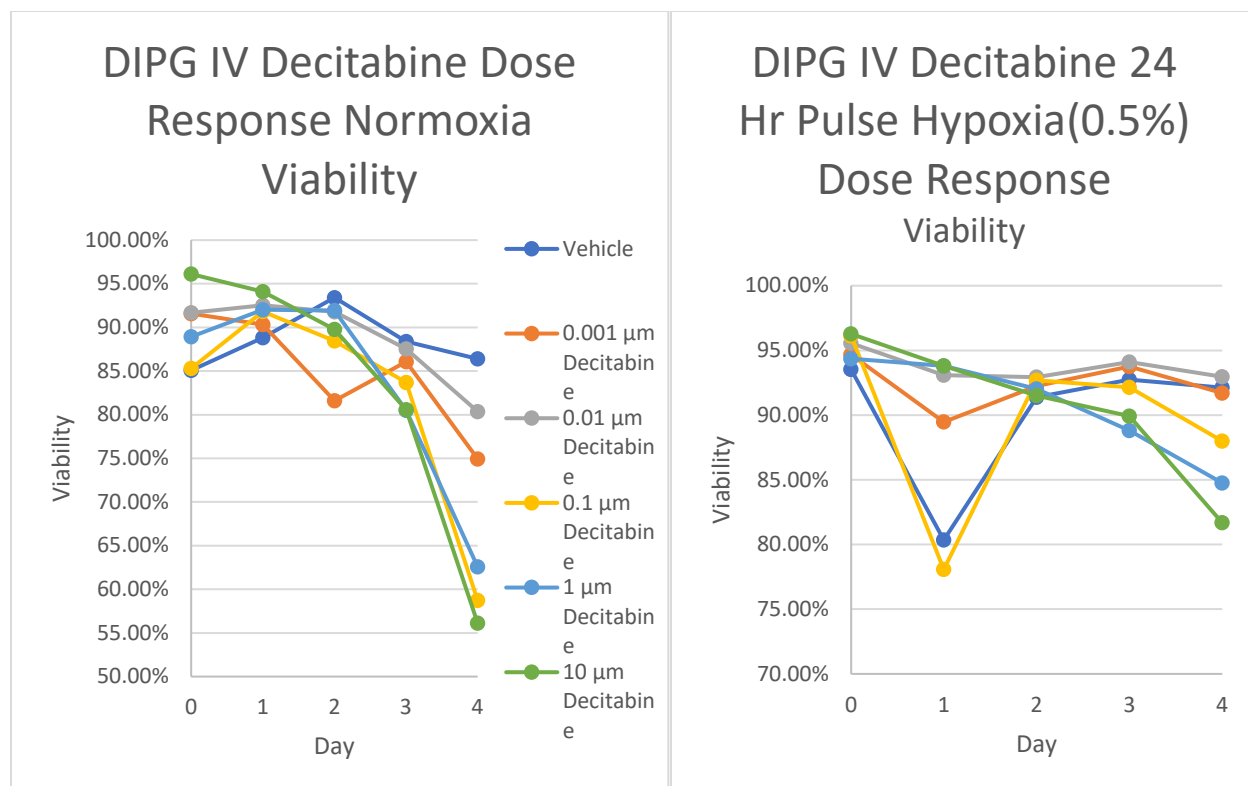


Figure 5. Viability comparison for decitabine treated human DIPG IV cells in hypoxic and normoxic conditions.

Significance and Interpretation

Upon western blot analysis, p16 expression was shown in human DIPG X lines with no considerable changes in expression following decitabine treatment in a normoxic environment. However, expression of p16 appeared to decrease with increasing decitabine concentration in hypoxic conditions. Additional trials will follow to confirm this result. Whether or not the observed expression of p16 is considered repressed compared to normal brain tissue is yet to be determined and could be a possible explanation for the repression observed in prior studies.

The expression of proliferating cellular nuclear antigen (PCNA), which is associated with cellular proliferation and DNA replication, was found to decrease in both normoxic and hypoxic cells, with less decreased repression in hypoxia-treated cells. Decreased DIPG IV cell viability was observed in the trypan blue assay for cells treated in the normoxic conditions as opposed to a higher percent viability of cells treated in hypoxic conditions. This proposes the possibility of decreased efficacy of DNA methyltransferase inhibition in hypoxic conditions, suggesting varying methylation patterns occur between hypoxic and normoxic environments. The variation in methylation pattern was further investigated with the expression of TKTL1, a protein responsible for sensitizing cells to hypoxia and is activated by hypomethylation. Increased expression of TKTL1 was observed in both normoxia and hypoxia treated cells with increasing decitabine concentration. A greater increase of TKTL1 expression was observed in hypoxia-treated cells and suggests a possible role in cellular adaptation to a low oxygen environment, thus offering a possible explanation for decreased efficacy of DNA methyltransferase inhibition observed in a hypoxic environment. However, this relationship warrants further investigation.

Increasing the concentration of decitabine poses possible increased effectiveness due to the higher decrease in cellular viability upon the 72-hour mark following treatment. The upper limit of decitabine treatment concentration remains unknown warranting the capability for further investigation. The next steps in this project are to continue examining the resulting epigenetic changes induced by DNA methyltransferase inhibition as well as the overall cellular proliferation rate with increasing decitabine concentration in both normoxic and hypoxic environments.

References

1. Bertoli C, Skotheim JM, de Bruin RA. Control of cell cycle transcription during G1 and S phases. *Nat Rev Mol Cell Biol.* 2013;14(8):518–528. doi:10.1038/nrm3629
2. Cordero FJ, Huang Z, Grenier C, et al. Histone H3.3K27M Represses *p16* to Accelerate Gliomagenesis in a Murine Model of DIPG. *Mol Cancer Res.* 2017;15(9):1243–1254. doi:10.1158/1541-7786.MCR-16-0389
3. Fang D, Gan H, Cheng L, et al. H3.3K27M mutant proteins reprogram epigenome by sequestering the PRC2 complex to poised enhancers. *Elife.* 2018;7:e36696. Published 2018 Jun 22. doi:10.7554/eLife.36696
4. Hashizume R. Epigenetic Targeted Therapy for Diffuse Intrinsic Pontine Glioma. *Neurol Med Chir (Tokyo).* 2017;57(7):331–342. doi:10.2176/nmc.ra.2017-0018
5. Heller S, Maurer GD, Wanka C, et al. Gene Suppression of Transketolase-Like Protein 1 (TKTL1) Sensitizes Glioma Cells to Hypoxia and Ionizing Radiation. *Int J Mol Sci.* 2018;19(8):2168. Published 2018 Jul 25. doi:10.3390/ijms19082168
6. Mackay A, Burford A, Carvalho D, et al. Integrated Molecular Meta-Analysis of 1,000 Pediatric High-Grade and Diffuse Intrinsic Pontine Glioma. *Cancer Cell.* 2017;32(4):520–537.e5. doi:10.1016/j.ccell.2017.08.017
7. Saratsis AM, Kambhampati M, Snyder K, et al. Comparative multidimensional molecular analyses of pediatric diffuse intrinsic pontine glioma reveals distinct molecular subtypes. *Acta Neuropathol.* 2013;127(6):881–895. doi:10.1007/s00401-013-1218-2
8. Strzalka W, Ziemienowicz A. Proliferating cell nuclear antigen (PCNA): a key factor in DNA replication and cell cycle regulation. *Ann Bot.* 2010;107(7):1127–1140. doi:10.1093/aob/mcq243
9. Thienpont B, Steinbacher J, Zhao H, et al. Tumour hypoxia causes DNA hypermethylation by reducing TET activity. *Nature.* 2016;537(7618):63–68. doi:10.1038/nature19081

Importance of Our Sun

Student Researcher: Lindsay S. Joy

Advisor: Dr. Cathy Mowrer

Marietta College
Education Department

Abstract

In the Ohio science curriculum for first grade, students are focusing on the basic needs of living things and how they are obtained from the environment. Students learn that the sun is the principal source of energy and without the sun there would be no life. In this lesson that will require two weeks to complete, students will discover that plants need sunlight in order to grow. We will begin by reading *The Day Joshua Jumped Too Much*, a suggested book on NASA's website to teach about the sun. This book focuses on the sun's energy and importance to all living things on earth. After reading, we will have a class discussion about how the sun affects earth.

Next, the students will execute the experiment "The Source of Energy Lab" from NASA's Solar Dynamics Observatory – Elementary Learning Unit to apply their knowledge about the sun and basic needs of plants. Students will create a plant box and observe that the plant will grow towards the sun, its primary source of energy. Students will record data on the growth of their plant over a period of two weeks. Throughout this experiment, students will write in a booklet about the growth of their plant that includes: drawings of the plant, their observations, and why they think the plant grew like it did.

Project Standards and Objectives

1. OH-2018.SC.1.ESS.1: The sun is the principal source of energy. After reading *The Day Joshua Jumped Too Much*, students will be able to answer comprehension questions about the importance of our sun.
2. OH-2018.SC.1.LS.1: Living things have basic needs, which are met by obtaining materials from the physical environment. Students will create a graphic organizer about the needs of plants (sun, water, air, and soil).
3. OH-2017.ELA.W.1.7 Participate in shared research and writing projects. Students will complete a plant observation booklet that contains a prediction of plant growth, drawings of the plant, their observations, and why they think the plant grew like it did.

Methodology Used

This learning segment was inspired by "The Source of Energy Lab" from NASA's Solar Dynamics Observatory – Elementary Learning Unit. This lab is created for grades K-5, but I targeted my instruction and standards to first grade students.

Prior to executing this experiment, I developed students' background knowledge of plants by teaching several lessons. The first day I taught about the sun by reading the book *The Day Joshua Jumped Too Much*, which talks about the importance of our sun. Before we read the book, I asked the students to brainstorm what would happen to Earth if there was no sun. Surprisingly, students guessed most of the topics addressed in the book, such as: no light, no heat, no energy, and no food for us. We then read the book as a class, making a list of the many things that would happen to Earth if we did not have our sun. After reading the book, we had a class discussion about the topics students did not think of before reading.

Next, I introduced students to the needs of plants. We completed an interactive graphic organizer while I taught students about plant needs: sunlight, water, soil, and air. We discussed how the needs of plants are similar to the needs of humans and animals.

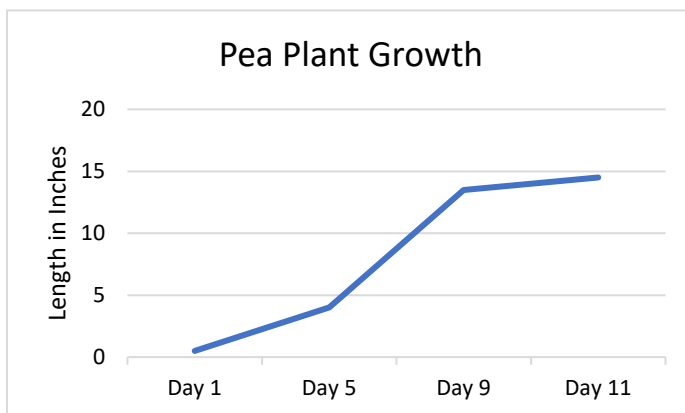
On the third day, I introduced students to the parts of plants. We discussed the name of the parts and their functions as a whole class. I projected a picture of a plant onto the dry erase board and we labeled the parts: seed, roots, stem, leaf, and flower. Then, I passed out the students' plant observation logs and they drew and labeled a plant on the title page.

After developing knowledge of plants with these several lessons, we began our experiment of growing a plant inside a box with a maze. I introduced students to the box and let them design the maze our plant was going to grow through. We stood a box on its side and created a maze out of cardboard pieces glued to the inside of the box. Students placed our sprouted pea plant at the bottom of the box. Then, I taught students about predictions and assisted them to write their prediction for our plant in the first page of our plant log. Most students predicted that our plant would grow through the maze to the top of the box, while a couple students predicted our plant would die or only grow a couple inches. Each day I would call students over in small groups to observe our plant. Then, after each child got to see the plant, we would have a class discussion about what has changed and why they think the change happened. Students would write their observations in their logs with each significant milestone. For example, we wrote in our logs when our plant grew through the hole, which was the first obstacle in the box. Periodically we would measure the height of the pea plant. The size of the plant was measured by following its curved growth around the maze with a string, and then measuring the length of the string in inches. At the end, I had students review their predictions and write in the last page of their logs what happened with our plant and why they think our plant grew the way it did.

Results/Interpretations

Our experiment was a success and the plant grew significantly in the two weeks. The plant started at a half an inch tall when we made our predictions about how it would grow. By the end of the experiment, our plant was 14.5 inches tall. Our plant grew through the maze and made it to the top of the box. Students were able to learn about the importance of the sun and how a plant will grow through a maze to reach the sunlight. Completing the plant observation logs allowed students to demonstrate their knowledge of plants gained in this learning segment. We had several meaningful conversations where students made connections between what they learned about plants and our pea plant experiment.

Pictures/Charts



References

1. The Source of Energy Lab. *Educator's Guide*. EG-2010-01-031-GSFC (2007).
2. Houpt & Littleton. *The Day Joshua Jumped Too Much*. Retrieved from https://sdo.gsfc.nasa.gov/assets/docs/ThinkScientifically_1.pdf
3. Creative Classroom Solutions. *Plant Observation Log – Primary*. Retrieved from <https://www.teacherspayteachers.com>
4. All Students Can Shine. *Interactive Notebook Pages for Your Plant Unit*. Retrieved from <https://www.teacherspayteachers.com>

Mathematical Modeling of Beech Leaf Disease Spread

Student Researcher: Joel R. Kavaras

Advisor: Dr. Aaron Montgomery

Baldwin Wallace University
Department of Mathematics

Abstract

Beech Leaf Disease (BLD), after first appearing in Lake County in 2012, now affects American beech (*Fagus grandifolia*) populations across northeast Ohio, Pennsylvania, southwest New York, and parts of West Virginia and Ontario. The disease attacks the leaves and buds, causing striping and banding followed by shriveling, discoloration, and eventually reduced leaf and bud production. So far, a causal agent remains unknown, while tree mortality (especially in saplings) and the thinning of canopies in larger trees across affected areas make the disease a growing concern each year.¹ To mathematically model the spread of the disease, we used data collected from 2010-2017 on 154 beech-containing plots of land within Cleveland Metroparks to construct a table that marked each plot as either having at least one infected tree in a given year or not, and to construct an array that stored the distance between each pair of plots. We then used MATLAB software to construct a model that created a likelihood function with five parameters that weighted ambient risk of infection against risk of infection from nearby sampled trees. Using the method of maximum likelihood estimation, we found the values of those parameters that best fit the observed data to achieve preliminary results. We then validated the ability of the model to estimate parameter coefficients by having it do so on forests with simulated infections. We also created maps based on sample-blind simulations of the park system forests to test the model against observed data. The model performed well, so we constructed further prediction maps for the outlook of Cleveland Metroparks beech populations. Our model concludes that, after an initial infection event, the most likely source of disease transmission is from within the network of trees throughout the park system, and that distance between trees plays a key role in infection transmission.

Project Objectives

This research project is focused on creating the first mathematical model of BLD spread data by mapping the diseased trees graphically to analyze the spread across Cleveland Metroparks land over time. Our key focus in this second year of research was to analyze the validity of our model and parameter estimates, and, once that had been established, to use GIS software to create maps projecting the probability of disease spread throughout Cleveland Metroparks in the years to come.

Methodology Used

The data for this research was shared with us by Cleveland Metroparks Natural Resources Division, and included data collected from 2010-2017 as part of the park's Plant Community Assessment Program.³ The data we received was specific to beech trees on 300 twice-sampled plots and included the coordinates for each plot, the number of beech trees greater than one meter tall present in each plot, and whether those trees were infected with BLD or not. We curated the data by first using Microsoft Excel to create an array of distances between each pair of the 154 beech-containing plots, which took the form of a symmetrical 154x154 matrix. In addition to this distance array, we also used Excel to create a table of the plots, the year of their second sample, and the infection status of those plots. Using

MATLAB software, we coded a basic Susceptible-Infected (SI) model that assessed each plot from year to year for the three years during which BLD was present on park land. The probability of a given plot transitioning from “susceptible” to “infected” was evaluated using the following formula:

$$\alpha + \sum \beta e^{-\gamma \cdot d(p_i, p_j)}$$

Where α is an ambient infection risk subject to change from year to year, β and γ are scaling parameters that do not change from year to year, and $d(p_i, p_j)$ is the distance between the plots. The sum is taken over all beech-containing plots in the data. This model was used to determine a likelihood function for the infection status of each plot, then, using the method of maximum likelihood estimation, we found the values of the parameters that maximize the likelihood function given the observed data.

Once initial parameter estimates were obtained, we set out to validate the model. Using MATLAB, we constructed fictional “forests” using the same parameters α , β , and γ with known values, then ran the model code over the fictional forest to have it estimate those parameters. This process was automated and repeated over hundreds of iterations with the compiled results analyzed to determine how close the model’s estimates were to the actual parameter values.

After model validation was completed, we used MATLAB to generate code that would run sample-blind simulations of Cleveland Metroparks’ beech-bearing plots, with the only data taken in being the plot coordinates and the distance between each plot. We then set the model to run 10,000 trials of this simulation with the parameter estimates we had established. The output was an array of average probability of infection over the 10,000 trials for each of the 154 plots and for each of 10 years after initial infection.

Results

The maximum likelihood estimators (MLEs) we obtained were:

$$\begin{array}{ll} \alpha_1 = 0.18 & \beta = 0.15 \\ \alpha_2 = 0 & \gamma = 0.72 \\ \alpha_3 = 0 & \end{array}$$

with each α pertaining to a given year after the disease was present in the plots sampled.

The results of our model validation were overall positive. We found that the model performs well when the sum $\alpha + \sum \beta e^{-\gamma \cdot d(p_i, p_j)}$ remains low, i.e. below 1. Otherwise, an overflow problem occurs because probabilities cannot exceed 1 and the code accounts for this by cutting off each sum at 1, meaning information is lost whenever the sum exceeds 1. To correct this problem, we set the model to only search for low values of the parameters α and β and noted that the model then performed quite well. Note that real-world parameter values must also be low as probabilities that exceed 1 are nonsensical. Once the overflow problem was corrected, we obtained new parameter estimates (which are displayed above) and found them to be quite similar to our original estimates before validation took place.

Perhaps an even more compelling version of model validation took place when we obtained the results of our sample-blind simulations of the Cleveland Metroparks plots. The results were in the form of maps produced using ArcGIS that show the probability of each plot being infected in a given year after initial infection took place, and we chose to compare the 2017 simulation map to the 2017 observed data in the graphics below:



Figure 1. The observed infection data collected in 2017 by Cleveland Metroparks. Note that the red dots indicate that a plot had a BLD infection present and green dots indicate a plot free of infection. Note that only about a third of the plots used in our model were sampled in the year 2017.

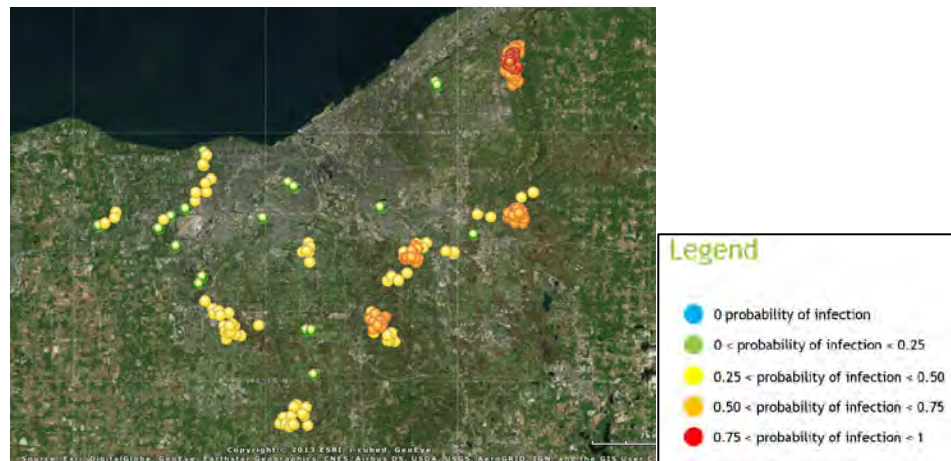


Figure 2. The sample-blind simulation of infection probability created by our model for the year 2017. Note that the areas with high probabilities of infection match up quite well with the observed data map in Figure 1.

Significance and Interpretation of Results

The MLEs produced by this model are noteworthy, especially regarding the α parameters. Particularly, the α_2 and α_3 parameters, which represent the ambient probability of infection in years two and three after the disease appeared in the sample, are significantly less than α_1 , which likewise represents the ambient risk of infection after the first year the disease appeared. This suggests that there may have

been an initial infection event when BLD first appeared in the sample, and then afterward the infection primarily spread between trees within the sample that had become infected. This result is validated to some extent by the relative accuracy of the sample-blind simulation maps, which model quite accurately the spread of the disease as shown by the observed data. The simulations suggest that dense clusters of trees are most vulnerable to the disease, and that the distance between trees plays a key role in the spread pattern of BLD. These results could have an impact on future management practices that seek to slow or stop the spread of BLD.

Acknowledgments

We thank Cleveland Metroparks Natural Resources Division for providing us with the data used to construct our model and we thank Dr. Constance E. Hausman of Cleveland Metroparks for her guidance and consultation on this project. We thank Dr. Kathryn Flinn (Baldwin Wallace University) for her consultation on the biological aspects of this research.

References

1. Pogacnik, John & Macy, Tom. (2016). Forest Health Pest Alert: Beech Leaf Disease. Ohio Department of Natural Resources Division of Forestry.
2. Williams, A. B. (1936). *The composition and dynamics of a beech maple climax community*. Cleveland, OH: Cleveland Museum of Natural History.
3. E. Hausman, Constance & Robison, Terry & J. Mack Jr, John. (2011). Using the generalized random tessellation (GRTS) survey design for monitoring and assessment of terrestrial plant communities at local, regional and ecoregional scales.

Modification of Existing Wire-EDM Wire Lag Models to Include Surface Feed Rate

Student Researcher: Roan M. Kirwin

Advisors: Dr. Muhammad P. Jahan and Dr. James C. Moller

Miami University

Mechanical and Manufacturing Engineering Department

Abstract

Wire Electro Discharge Machining (WEDM) is a type of machining that uses electro-discharges between a wire and a work piece to erode conductive material. WEDM suffers from a phenomenon called wire lag. Wire lag is when the wire electrode is forced behind the top and bottom guides. The lag is generally very small but, when extremely tight tolerances on curved or sharply angled geometry are desired, can be a large source of error. Lag is caused by both electromagnetic forces and explosive forces acting between the wire and the workpiece. This article demonstrates the feasibility of a program to modify machining g code to compensate for wire lag at sharp corners. A model of wire lag was demonstrated and methods for developing modifications to incorporate both surface feed and eliminate the need for a scanning electron microscope. This was done by demonstrating a method for relating pulse on time and voltage with each plasma discharge's area. Lastly an outline for a program that compensates for wire lag at thresholded angles was shown.

Project Objectives/Introduction

As industry pushed the boundaries of material science looking for ever harder, stronger, and tougher materials, machining technology had to keep pace. Applications requiring these properties along with increased complexity and precision require a method for effectively cutting materials like tool steel and titanium. A solution came in the form of Electro Discharge Machining or EDM. Originally developed to remove broken taps from aluminum, EDM uses many small spark discharges to precisely erode the workpiece. As shown in Fig. 1, each spark erodes a small amount of both the workpiece and the electrode. An advancement came in the form of Wire EDM or WEDM, which changed the electrode from a solid piece to a thin wire. This allowed for much more efficient material removal, increased the speed of machining, and smaller kerf widths. WEDM comes with its own complications, including wire lag and numerous amounts of possible input parameters.

There exist many methods for predicting the amount of wire lag due to a set of given parameters. While most are multivariate regression or another type of optimization, some work has been done with physics-based modeling. These models are generally developed from the equation describing a vibrating beam (Eq. 1)[1] or, more simply, using the wave equation (Eq. 2)[2]. The wave equation does not allow for a carried moment or shear by the wire and therefore is a slightly less accurate representation of the wire deflection.

$$F \frac{\partial^2 y}{\partial z^2} - EI \frac{\partial^4 y}{\partial z^4} = \rho S \frac{\partial^2 y}{\partial t^2} + c \frac{\partial y}{\partial t} + q(z, t)$$

F : axial force applied to the wire (N)
 E : Young's modulus (N/m^2)
 I : moment of inertia = $\pi r^4/4(m^4)$
 ρ : wire density (kg/mm^3)
 S : wire section (m^2)
 y : wire deflection (m)
 c : damping coefficient (Ns/m)
 $q(z, t)$: external load (N)

Equation 1: Vibrating string/beam

$$F \frac{\partial^2 y(z)}{\partial z^2} + q(z) = 0$$

Equation 2: Vibrating string/wave

Most models are based on or similar to the model developed by Dauw [1]. Starting with the above beam-based equation and assuming static forces and time independence, it can be simplified to Eq. 3.

$$F \frac{d^2 y}{dz^2} - EI \frac{d^4 y}{dz^4} = q(z)$$

Equation 3: Simplified static string deflection

If it's then assumed that the wire could carry no moment the wave equation would then be achieved. However, in Chen et al. the differential equation is solved with no more simplifications.[3] This method leads to a fourth order polynomial while the wave equation results in a parabolic function. When tested on 90° angles, both methods were able to predict lag within ±10%.[2,3] These models could be further refined through correction factors, or additions to the equations that can account for machine, tool, and work piece specific error sources. These additions would be a regression of terms that are found to be significant factors from experimental analysis. A correction coefficient was implemented in in Abyar et al. [4]

After derivation Abyar's model is as shown in Eq. 4, which is illustrated in Fig. 3.

<p>a) $\delta = \frac{(L - \frac{H}{2})(f \Delta s P_p) \sin(\theta_f)}{(2F\theta_f)}$</p> <p>b) $\theta_f = (\theta_i + 2\pi)$</p> <p>c) $\theta_i = \arccos\left(\frac{g + r}{g_{max} + r}\right)$</p> <p>d) $g = \frac{\text{kerf} - r}{2}$</p> <p>e) $g_{max} = \frac{V}{E_b}$</p>	<p>Where:</p> <p>L : Distance Between Guides (m)</p> <p>H : Height of work piece (m)</p> <p>f : Frequency of Normal Discharges(Hz)</p> <p>Δs : Plasma Channel Area (m^2)</p> <p>P_p : Plasma Channel Pressure (bar)</p> <p>V : Servo Voltage (V)</p> <p>E_b : Breakdown Voltage of Dielectric(V/m)</p> <p>kerf : Kerf Width(m)</p> <p>r : Radius of Wire(m)</p> <p>F : Wire Tension(N)</p>
---	---

Equation 4: Wire Lag Model adapted from Abyar et al.

Abyar's model, being one of the most fully developed models, still has some issues causing it to be difficult to implement in any production environment. The model requires the cross-sectional area of each plasma channel as well as requiring the WEDM to run in servo mode. The cross-sectional area of the plasma channel can be found by measuring the average size of resulting craters on the wire.[5] This is tricky because crater diameters are typically on the order of 1-100 μm , meaning prohibitively expensive measurement equipment is necessary. Servo mode, in the context of WEDM, is where the machine dynamically adjusts the surface feed rate to maintain a certain gap between the wire and workpiece. This is done by measuring the peak voltage of each spark and adjusting the feed up or down to maintain the voltage near the set servo voltage. This model also requires the number of completed sparks, or normal sparks, per second. However, this can be easily calculated by multiplying the set sparking frequency by the percentage of normal sparks. Percentage of normal sparks is measured and reported by most production WEDMs.

This study aims to adapt this model to be more practical in a production environment by investigating how running the EDM in constant feed mode, rather than servo mode, influences wire lag. It also aims to create an approximation of crater diameters corresponding with typical ranges of WEDM parameters. These improvements will then be implemented in a program that can modify machining g code to account for the predicted wire lag at sharp corners. These will allow for a much faster and cost-effective wire lag prediction and compensation in production environments.

Methodology

To perform the experiments an Excetek WEDM will be used hooked up to a RIGOL oscilloscope to measure the waveform produced by the WEDM during machining. The waveform will quantify both the peak voltage as well as the percentage of normal arcs. The waveform will be captured three times during each sample to reduce measurement, and transient sources of error. The experiments will be conducted using 9/16" (14.3mm) grade 5 titanium. This material is commonly machined using WEDM for the aerospace and biomedical industries. Each trial machining path will consist of a straight away and a 90° angle. The deviation at the angle will be used to measure the approximate wire lag.

Based on the limited literature on the subject limiting the wire feed rate will result in two separate regions.[6] The first region will manifest as an increase in servo voltage as the feed rate slows. This can be explained as an increasing gap between the wire and the work piece. The larger gap will lead to larger voltages required to breakdown the dielectric into plasma. It will transition into the second region as the peak voltage reaches the set maximum voltage. After this transition the machine will no longer be able to arc as much as before due to not being able to reach the required breakdown voltage of the dielectric. The feed rate effect on wire lag will be investigated by choosing three presets of parameters for machining for titanium. One sample for each preset will be machined in servo mode while the following are measured:

- Peak Voltage
- Percentage of Normal Sparks
- Average Surface Feed Rates
- Machining Time
- Measured Wire Lag

Using the measured average surface feed rate, a set of experiments will be designed to measure the above values at a set of five percentages of the servo feed rates. From these experiments modifiers for input frequency and servo voltage will be determined using nonlinear regression.

As demonstrated by Tosun[7] using ANOVA the largest contributors to wire crater diameter are pulse duration and voltage. Another set of trials will have to be created to account for possible interplay between pulse duration and voltage. This set of experiments will consist of five levels of both pulse on time and voltage, resulting in 25 trials. During each trial three samples of wire will be collected. The samples will then be examined using a scanning electron microscope to determine the average size of a crater for each trial. A nonlinear regression will then be used to create an equation approximating the crater diameter at typical WEDM settings.

A program will be created that predicts wire lag and compensates it using the cutback method. The cutback method is demonstrated in Fig. 4. Such a method modifies the programmed path of the guides to overshoot sharp angles by the amount the wire is lagging. The guides are then reversed back to the intended corner and the path continues as originally intended. The result is an almost perfectly sharp internal corner and a much closer to square external angle. This method of compensation was investigated by Chen et al.[3] and found to be an effective method for crating sharp corners with WEDM. Inputs to the program will include all parameters previously discussed as well as a maximum desired path deviation. The program will determine the angle that corresponds to the entered maximum deviation and add in cutbacks at all corners with deviations above the threshold. The cutbacks will then be written to a modified machining g code file.

Lastly, the program will be tested for accuracy using settings developed by means of the L9 Taguchi design of experiments covering the gamut of possible settings for titanium.

Preliminary Results/Conclusion

Some preliminary results have been obtained. As part of initial problem search and definition some data regarding surface feeds and both kerf width and surface roughness was gathered. Shown in Figure 5 is two surface feeds with otherwise consistent parameters vs kerf width. This graph demonstrates that higher surface feeds lead to lower kerf widths. This supports the hypothesis of higher surface feeds maintaining smaller spark gaps, leading to lower peak voltages.

As demonstrated in Figure 6 surface roughness increases with increasing surface feeds. This also supports the assumption that the frequency decreases as surface feed decreases due to a lack of required breakdown voltage. This manifests as the machining of any small protrusions, leading to a smoother surface.

These results backup the initial thesis and show promise that the final product could preform as expected.

Figures

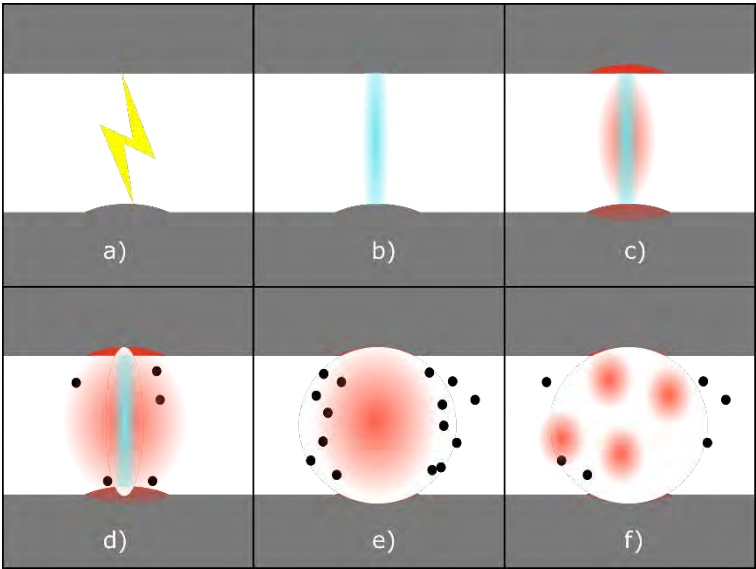


Figure 1. Wire EDM Process: a) breakdown of dielectric, b) formation of plasma, c) melting and bubble formation, d) expansion, e) collapse of plasma and debris ejection, f) bubble collapse.

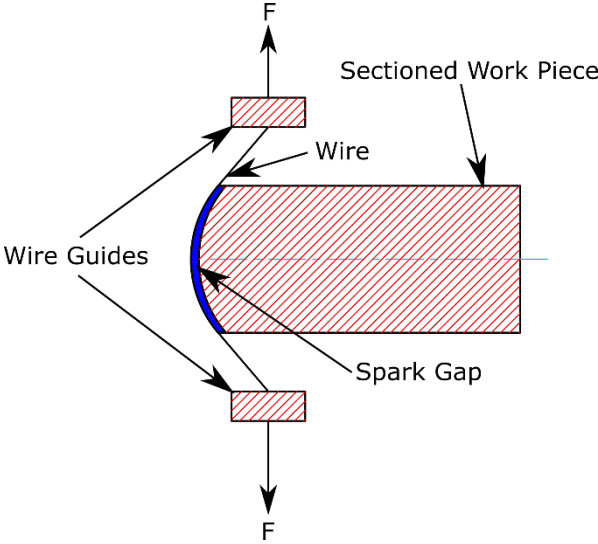


Figure 2. WEDM wire during cutting.

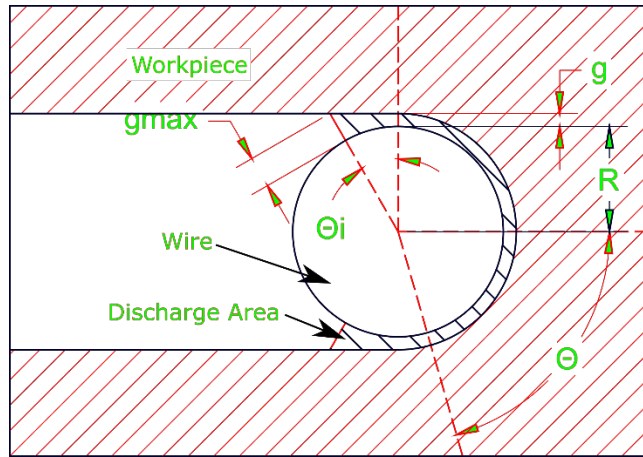


Figure 3. An illustration from above of the wire during cutting.

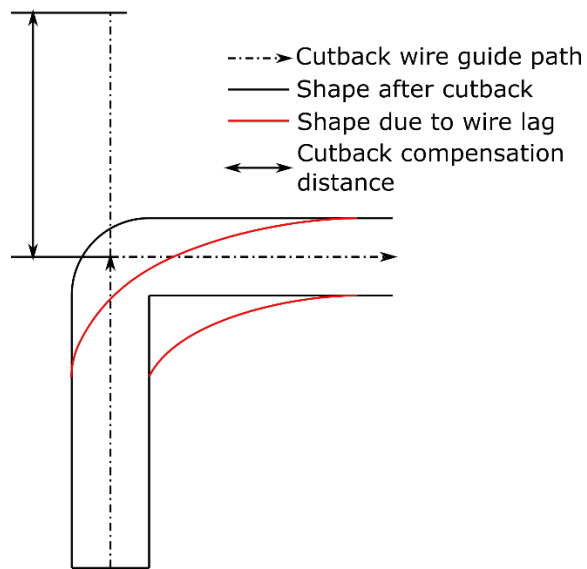


Figure 4. Corner geometry with and without cutback.

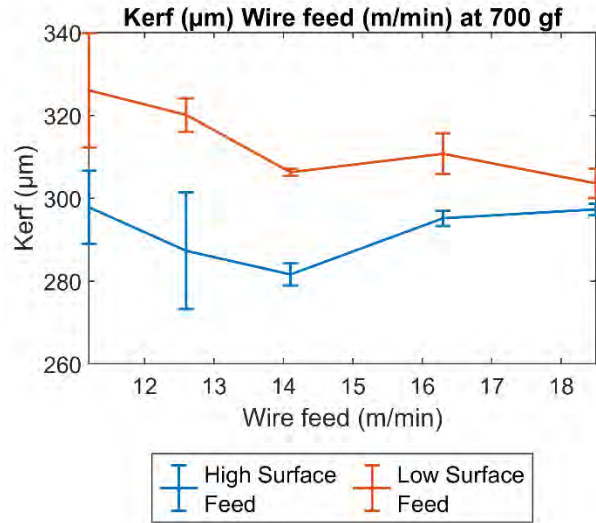


Figure 5. Kerf width vs wire feed at 700 gf tension.

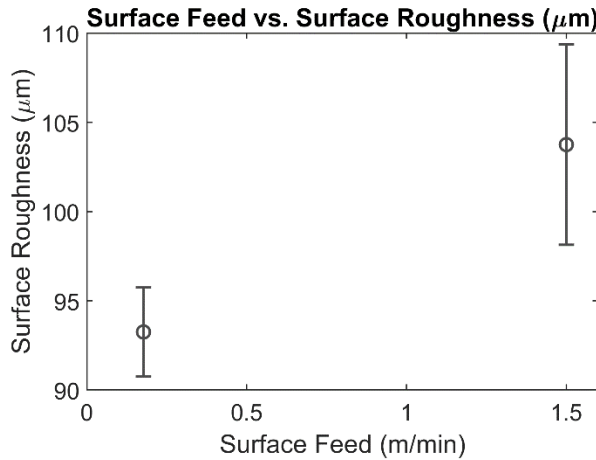


Figure 6. Surface Feed vs. Surface Roughness.

References

1. Dauw, D. F., and Beltrami, I., 1994, "High-Precision Wire-EDM by Online Wire Positioning Control," *CIRP Ann. - Manuf. Technol.*, 43(1), pp. 193–197.
2. Han, F., Zhang, J., and Soichiro, I., 2007, "Corner Error Simulation of Rough Cutting in Wire EDM," *Precis. Eng.*, 31(4), pp. 331–336.
3. Chen, Z., Zhang, Y., Zhang, G., and Li, W., 2018, "Modeling and Reducing Workpiece Corner Error Due to Wire Deflection in WEDM Rough Corner-Cutting," *J. Manuf. Process.*, 36, pp. 557–564.
4. Abyar, H., Abdullah, A., and Akbarzadeh, A., 2018, "Prediction Algorithm for WEDM Arced Path Errors Based on Spark Variable Gap and Nonuniform Spark Distribution Models," *J. Manuf. Sci. Eng.*, 141(1), p. 011011.
5. Abyar, H., Abdullah, A., and Akbarzadeh, A., 2018, "Analyzing Wire Deflection Errors of WEDM Process on Small Arced Corners," *J. Manuf. Process.*, 36, pp. 216–223.
6. Alias, A., Abdullah, B., and Abbas, N. M., 2012, "Influence of Machine Feed Rate in WEDM of
7. Tosun, N., and Pihitili, H., 2003, "The Effect of Cutting Parameters on Wire Crater Sizes in Wire EDM," *Int. J. Adv. Manuf. Technol.*, 21(10–11), pp. 857–865.

Fabrication Methods and Testing of 3D Printed PLA Scaffolds for Tissue Engineering of Bone Restoration Implants

Student Researcher: Jared I. Klimek

Advisor: Dr. Timothy Norman

Cedarville University

Department of Engineering and Computer Science

Abstract

A major challenge in the medical field today is the ability to repair and initiate the healing of large bone defects. While small bone defects may heal unaided, large bone defects require medical intervention. One promising solution is to replace the missing bone tissue with a biocompatible and customizable material such as 3D-printed PLA (polylactic acid). This project builds on previous research that investigated the use of biodegradable scaffolds to stimulate cell growth for healing of large bone defects. The goal was to manufacture scaffolds using a 3D printer with PLA filament, seed them with cells, and observe them for growth characteristics. This project investigates the use of a desktop 3D printer to print PLA bone scaffolds in order to quantify the effects of varying printing parameters on geometric and mechanical quality. Starting with a control specimen made with the standard print parameters used by previous Cedarville biomedical research, multiple printing parameters were varied, including nozzle diameter, extrusion temperature, layer height, print speed and travel speed. A test matrix was created by varying the control specimen by a single print parameter at a time. Finally, all of the specimens were mechanically tested for a stiffness comparison. The results of this project will help future researchers and engineers conduct high-quality production of 3D-printed PLA scaffolds for future use in biomedical applications.

Project Objectives

The overall goal of this research is to design a method for creating biodegradable 3D printed scaffolds that support bone growth for healing large bone defects. Previous research developed a unit cell-based approach to scaffold design that was capable of hosting cell growth. When fabricated using PLA (polylactic acid), this technique could produce scaffolds with stiffness appropriate for implantation in bone defects. The goal of this research project was to investigate the factors that affect 3D print quality of PLA scaffolds. After determining the most significant factors, these factors could be used to improve print quality for future scaffold design. In order to accomplish this goal, the first objective was to develop a method for varying print parameters that could be assessed for print quality. This method would then be used to print a matrix of scaffolds for quality assessment. The second objective was to assess print quality through mechanical testing to determine compression stiffness.

Methodology Used

For this research, a Lulzbot Taz 6 printer running on Cura 3D printing software was used. A special Aerostruder Tool Head was installed on the printer. All specimens were printed using MatterHackers Pro Series 2.85-mm diameter white 3D printing filament. The 3D printer setup is shown in Figure 1. In order to have a consistent specimen to test, a 4 unit cell x 4 unit cell X-scaffold specimen was used, as shown in Figure 1. It was reproduced 36 times according to the different print parameters.

In order to determine the most significant factors affecting print quality, a test matrix was created. In the test matrix, four printing parameters were varied: extruder temperature, layer height, travel speed,

and print speed. For each parameter, three different values were used. The middle value for each parameter was that of a single control specimen to which all other specimens were compared. The result was the test matrix shown in Table 1. The test matrix contains nine specimens: one control specimen and two specimens for the two variations of each printing parameter. Additionally, the diameter of the extruder nozzle was varied to four values: 0.5 mm, 0.4 mm, 0.3 mm, and 0.25 mm. By creating a test matrix of 9 specimens for each of the 4 nozzle diameters, 36 specimens were printed.

The specimens were analyzed for quality and for mechanical properties. For quality, a microscopic evaluation of each specimen was conducted and input into a custom quality equation based on variation from intended scaffold geometry. Higher Q-values indicate lower quality and a lower Q-values indicate higher quality. Q-values were determined by another student (Michaela Crouch) working on the project.

The most relevant mechanical consideration for biological compatibility of the bone implant is stiffness in compression. The mechanical evaluation of the specimens was conducted on a Mark-10 motorized test stand, as shown in Figure 2. The Mark-10 test stand was used to obtain a load-displacement curve which was converted into an effective stress-strain curve.

The effective compressive modulus of elasticity was calculated using the effective cross-sectional area and effective length. Due to the internal architecture of the scaffold, the actual cross-sectional area of material is smaller. For the purposes of this comparative analysis, the effective compressive modulus was calculated for the whole scaffold as if it had a solid cross-section rather than complex geometry. The effective stress, effective strain, and effective elastic modulus were calculated as in Equations 1-3:

$$\sigma_{eff} = \frac{F}{A_{eff}} \quad (1)$$

$$Strain_{eff} = \frac{\Delta L}{L} \quad (2)$$

$$E_{eff} = \frac{\sigma_{eff}}{\varepsilon} \quad (3)$$

This stiffness was determined using the slope of the linear portion of the stress-strain curve, as shown in Figure 2 for the 0.5-mm diameter nozzle control specimen.

Results Obtained

The results of the mechanical evaluation for all 36 specimens are shown in Figure 3. There are 9 groups (corresponding to the 9 parts of the test matrix) of 4 specimens (corresponding to the 4 nozzle diameters). In order to determine the effect of print parameters on scaffold stiffness, a statistical analysis of the results for each printing parameter was conducted, as shown in Figure 4. The data from each parameter variation was combined to show the overall effect of varying that print parameter. There was no significant difference ($p > 0.5$) between specimens when varying print speed, travel speed, layer height, or temperature. However, there was a statistically significant difference ($p < 0.5$) when varying nozzle diameter. The results indicate that a nozzle size of 0.3 mm or lower significantly improves scaffold stiffness.

Significance and Interpretation of Results

The results of this research can be used in future biomedical applications for 3D printed PLA bone scaffold production. Since quality and stiffness are important factors in successful implementation of this biomedical bone scaffold technology, the results could enhance future research and application.

Figures and Tables

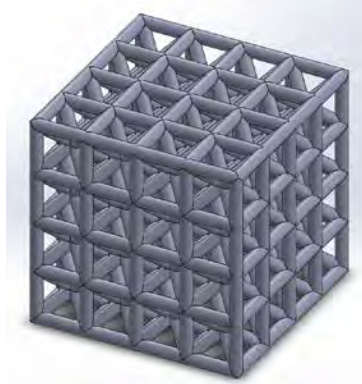
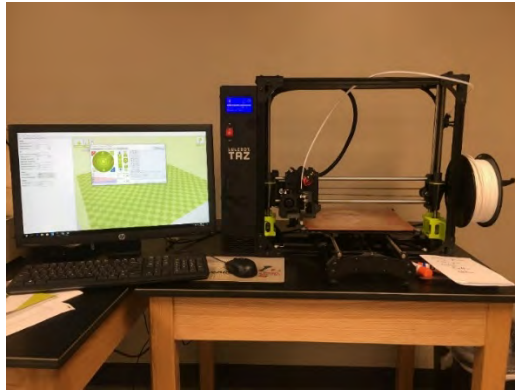


Figure 1. Printer Setup and 4 Unit Cell x 4 Unit Cell X-Scaffold Print Specimen.

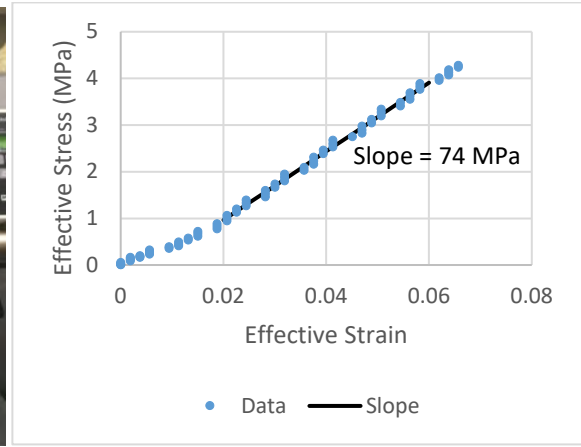


Figure 2. Mark-10 Motorized Test Stand and Effective Stress-Strain Curve with Slope of Linear Region.

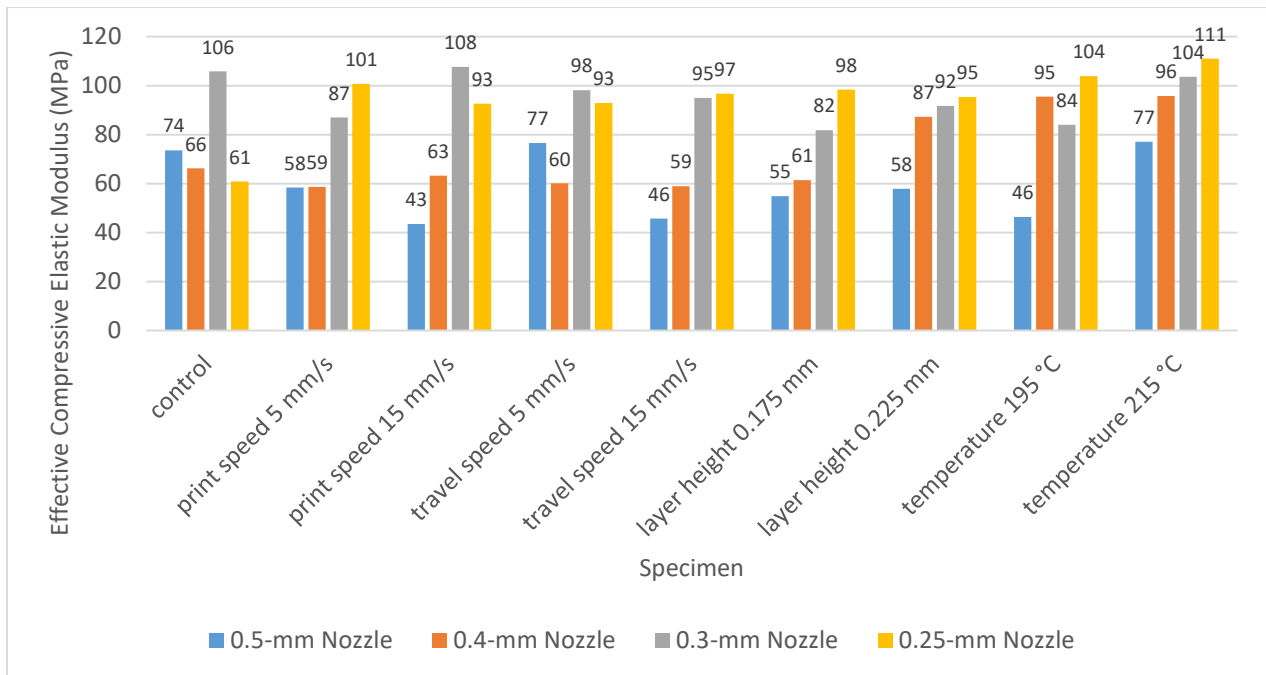


Figure 3. Stiffness Results for All 36 Specimens.

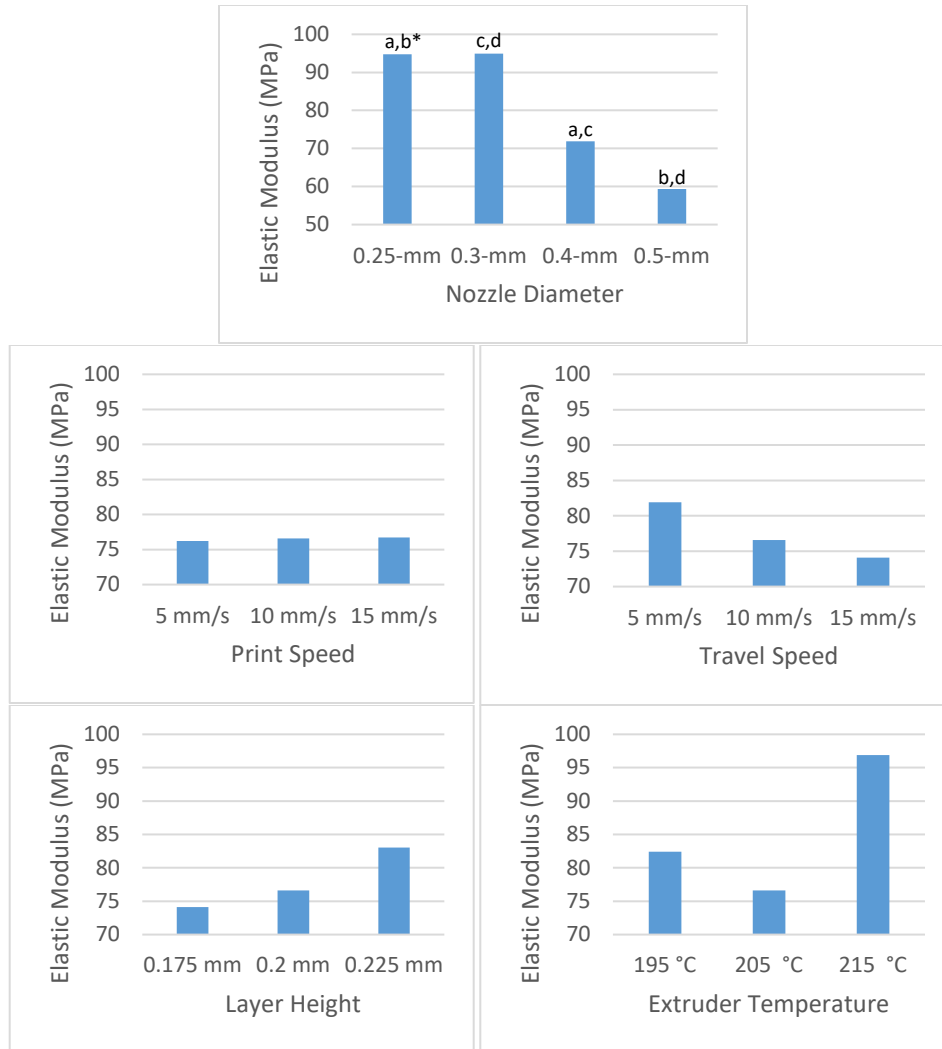


Figure 4. Stiffness Effects Compared for Each Printing Parameter
 *Bars with the same letter are significantly ($p < 0.5$) different.

Table 1. Test Matrix

	4 Variant Specimens	1 Control Specimen	4 Variant Specimens
Print Speed (mm/s)	5	10	15
Fast Speed (mm/s)	5	10	15
Layer Thickness (mm)	0.175	0.2	0.225
Extruder Temperature (°C)	195	205	215

Acknowledgments and References

The author would like to thank faculty research advisors Dr. Timothy Norman (School of Engineering and Computer Science and the Biomechanics Laboratory) and Rocco Rotello (School of Pharmacy) for their help in coordinating this research. The author would also like to thank student researchers Michaela Crouch, Sarah Seman, and Luke Schwan for working together to make the project a success. Finally, the author would like to acknowledge the Ohio Space Grant Consortium for funding the research.

Improvement in Jet Aircraft Operation with the Use of High-Performance Drop-in Fuels

Student Researcher: Shane T. Kosir

Advisor: Dr. Joshua Heyne

University of Dayton

Mechanical Engineering Department

Abstract

This report provides an overview of methods used to bound the economic benefits that high-performance jet fuels (HPFs) can have for commercial airlines. Three approaches were taken to bound HPF economic benefits: identifying and calculating properties for bio-derived molecules via quantum chemistry and equation of state methods, using optimization software to determine blends of conventional and specialty molecules that meet HPF specifications, and simulating flights to correlate HPF performance increases to economic benefits for airlines. Specific energy [MJ/kg] and energy density [MJ/L] of bio-derived molecules have been calculated, and the most promising molecules have been identified. Optimization indicates that alkylated cyclohexanes have performance benefits when used in jet fuel blends while being potentially drop-in ready.

Introduction

If the current rate of global warming continues, the world will reach a temperature of 1.5°C higher than pre-industrial levels by 2040¹. This level of warming would result in greater food shortages, a higher likelihood of heat waves, and more forest fires, amongst numerous other problems. High-performance fuels (HPFs) provide an alternative energy source that could help negate climate change and allow airlines to grow sustainably by helping achieve more efficient specific fuel consumption, eclipsing the cost-benefit threshold of Sustainable Alternative Jet Fuels (SAJFs), and producing significantly less greenhouse gas emissions and particulate matter (PM) than conventional fuels via higher energy content and reduced aromatic concentration. As aircraft account for 9% of US transportation-related greenhouse gas emissions², the impact that HPFs could have is significant. In addition to the environmental impact of conventional jet fuel, it contributes significantly to airlines' annual expenses, totaling close to 135 billion dollars or approximately 19% of the total operating cost globally in 2016³. High-performance fuels have the potential to mitigate fuel cost by reducing the amount of fuel required to complete flights, increasing the number of allowable passengers or cargo on a flight, and by increasing the range of aircraft, allowing airlines to add new flights and generate additional revenue. The goal of this study is to bound the performance and economic benefits that airlines can expect from HPFs created from bio-derived molecules as well as molecules from conventional sources.

Methodology

Three methods were used to determine promising bio-derived molecules, maximum specific energy (SE) and energy density (ED) drop-in HPFs, and the potential benefit of these fuels. (1) Property values of potential HPF bio-derived molecules were calculated via quantum chemical and EoS (Equation of State) methods. (2) Property values were used to determine optimal fuel composition. (3) SE and ED values from these optimal blending results were used to estimate monetary benefits for commercial airlines.

(1) A variety of biologically-derived molecules were identified as potential sources of compounds with energetic properties exceeding those of Jet-A, i.e. >43.2 MJ/kg and >34.9 MJ/L. Most of the biologically-derived molecules contain double bonds and would require hydrogenation to produce fully saturated

fuels. Of particular interest are molecules that hold potential for industrial-scale production through biotechnological or other means. Four classes of organic molecules were considered: cyclic monoterpenes, cyclic sesquiterpenes, branched alkanes, and ladderanes. The contribution of ring strain to SE is expected to be greatly enhanced by the presence of cyclopropane and cyclobutane subunits in the structure compared to larger rings⁴. Therefore, among the numerous biologically produced hydrocarbons, those with three and four membered ring substructures are naturally interesting. Ab initio calculations of SE and density were performed using Gaussian 09⁵ and the SAFT- γ -Mie EoS⁶ respectively. These provided initial screening criteria for potential molecules. Confidence in the accuracy of these calculations was bolstered through comparison with experimental data when it was available.

(2) Fuel composition optimization was done using the Jet Fuel Blend Optimizer (JudO), which is a suite of fuel optimization tools developed around Mixed Integer Distributed Ant Colony Optimization (MIDACO) software⁷. MIDACO is a stochastic optimization program capable of multi-objective optimization. For this problem, SE and ED served as the objective functions which would be maximized, while American Society for Testing and Materials (ASTM) operability limits served as constraints. MIDACO enabled the propagation of SE/ED Pareto fronts, which represent the best possible performance characteristics that could be achieved without violating operability limits. Each point on the Pareto front represents a specific composition of molecules and their corresponding SE and ED. In total, three blending scenarios were considered, which are summarized in Table 1. Specialty molecules considered for optimization were not limited to a specific molecular group, but instead are defined as molecules with SE and ED higher than conventional fuels. Many specialty molecules considered for this study are cyclic molecules that exhibit ring strain, for example tetrahydrodicyclopentadiene (JP-10) and quadricyclane.

Table 1. Optimization blend scenarios.

Blend Scenario	Molecules	Objectives	Constraints
Scenario 1	Conventional	Specific Energy, Energy Density	Flash Point, Freeze Point, Viscosity (-20°C), 10% Distillation Temperature, Final Boiling Point, Density, Aromatic Concentration
Scenario 2	Conventional	Specific Energy, Energy Density	Flash Point, Freeze Point, Viscosity (-20°C), 10% Distillation Temperature, Final Boiling Point, Density
Scenario 3	Conventional, Specialty Molecules	Specific Energy, Energy Density	Flash Point, Freeze Point, Viscosity (-20°C), 10% Distillation Temperature, Final Boiling Point, Density, Aromatic Concentration

(3) Three different aircraft/engine combinations were modeled using NPSS (Numerical Propulsion System Simulation)⁸ and FLOPS (Flight Optimization System)⁹ to determine HPF benefits for aircraft. The aircraft selected were a 50-passenger class regional jet, a 150-passenger class single-aisle transport, and a 300-passenger class wide body transport. The NPSS and FLOPS models were calibrated to public domain information in order to make accurate estimates for each of the three systems. The primary sources of data for model calibration are the Airport Planning Manuals for the aircraft and the ICAO Emissions DataBank¹⁰ for the engines. Three HPF usage scenarios were identified, titled A, B, and C. Scenario A involves maintaining the original payload and range, resulting in reduced HPF fuel requirements on both a mass and volume basis. Scenario B involves maintaining the original range, allowing for additional revenue generation from increased cargo and passenger capacity. Scenario C involves maintaining the original payload, allowing for increased revenue by making new destinations possible. A hypothetical “best-case” HPF was chosen for this study with a SE of 44.9 MJ/kg and a ED of 37.7 MJ/L.

Results

Figure 1 shows the SE and ED of bio-derived molecules relative to conventional jet fuels. Pinane, caryophyllane, cis-carane, and all ladderanes exceed the SE and ED of the HPF region. Pinane, caryophyllane, and cis-carane are especially of interest because they could be blended into the Jet A density range relatively easily, possibly with monocycloalkanes or *iso*-alkanes. Although they do not exceed the HPF threshold, bisabolane, sabinane, p-menthane, and squalane are of interest because they can provide significant performance improvements and remain within the ASTM density range.

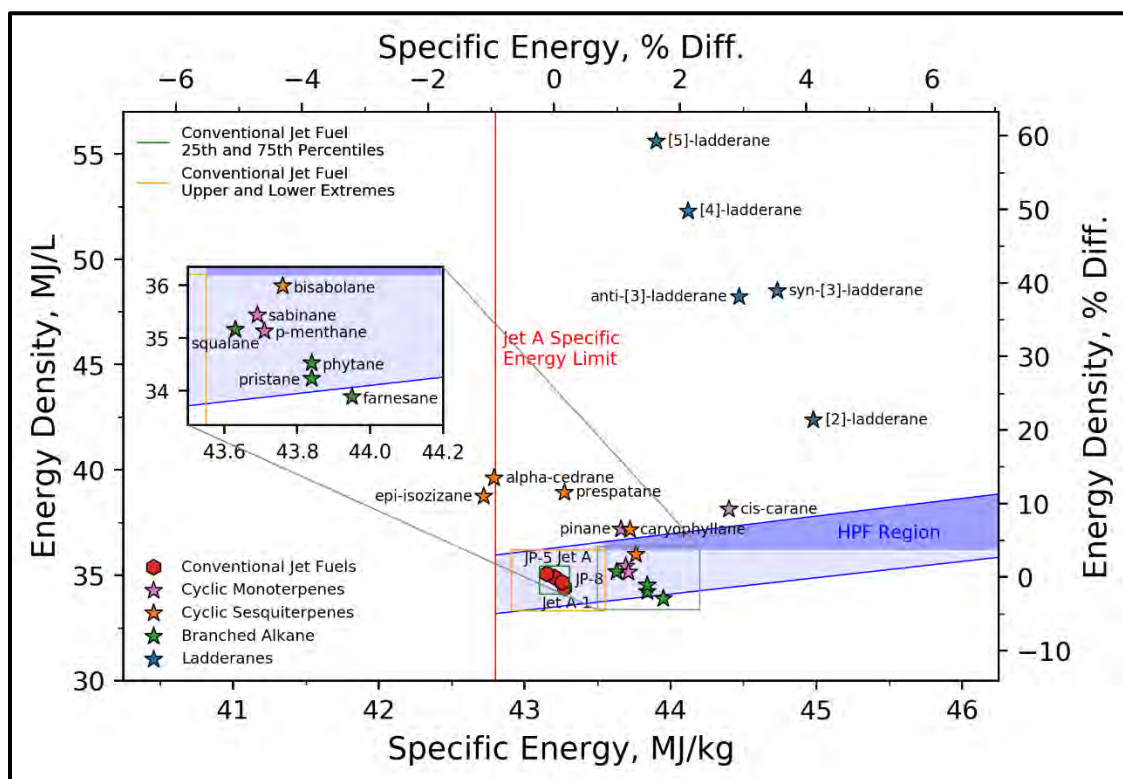


Figure 1. Specific energy and energy density of bio-derived molecules.

Figure 2 depicts SE plotted against ED, providing insight into the performance characteristics of the molecules considered for optimization. *n*-alkanes and *iso*-alkanes considered for this analysis are restricted by their low density and need to be blended to fall within the ASTM density range. Monocycloalkanes are the only class of molecules that are potentially drop-in ready because of their position in the density range. The high densities of dicycloalkanes make them promising for blending with *n*-alkanes and *iso*-alkanes. Both monocycloalkanes and dicycloalkanes are of interest because they exhibit O-ring swelling properties¹¹ and can potentially be used as a substitute for aromatics. Aromatics are generally undesirable from a performance perspective because of their low SE and propensity to form soot. Specialty molecules have significantly higher SE and ED than conventional jet fuels. However, they generally exhibit variability in operability properties and may have thermal stability issues.

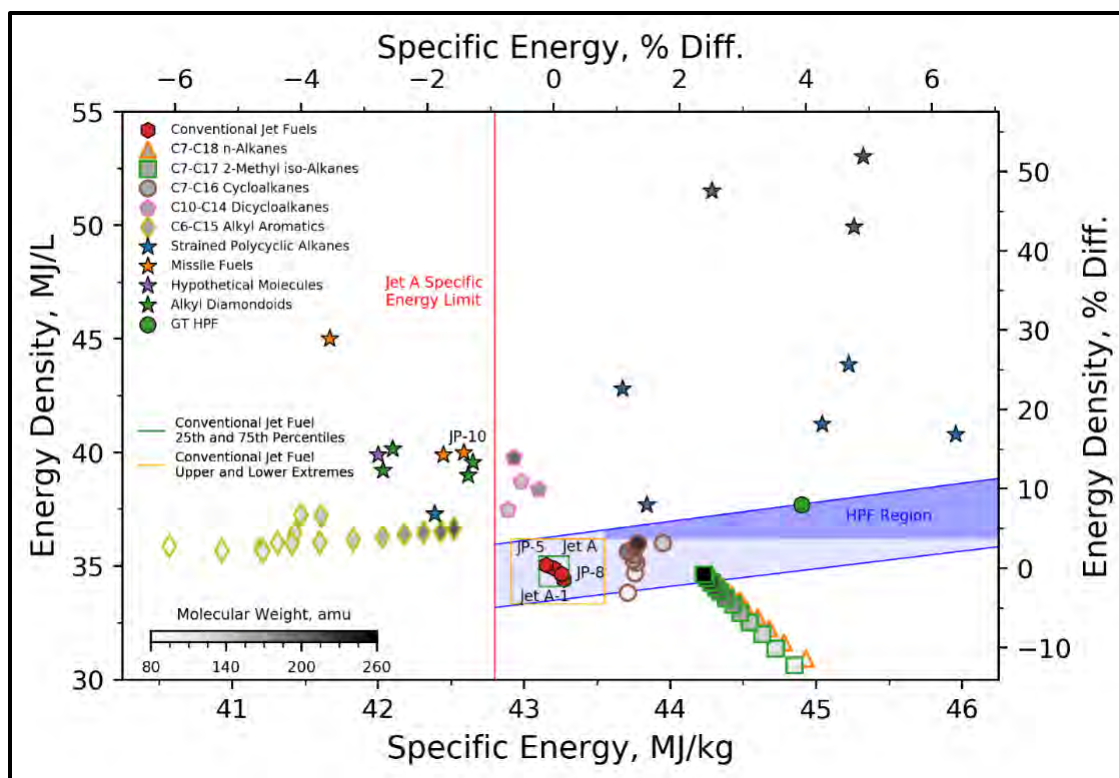


Figure 2. Specific energy and energy density of conventional and specialty molecules. The light blue region bounded by parallel solid blue lines represents the ASTM density range for Jet A, while the HPF region is represented by the dark blue shading.

Figure 3 depicts the Pareto fronts from JudO optimization efforts. Pareto fronts are represented by red (scenario 1), green (scenario 2), and blue (scenario 3) lines. It is apparent that removing the minimum 8% aromatic constraint in scenario 2 had a significant impact on performance compared to scenario 1. Scenario 1 had median SE and ED values of 43.8 and 35.7 respectively. This represents 1.4% and 2.2% improvements compared to Jet A. With scenario 2, the median SE and ED of the conventional fuel optimization increased to 43.9 and 35.8 respectively, representing 1.6% and 2.5% improvements compared to Jet A. Scenario 3 had median SE and ED values of 44.1 and 35.7 respectively, which represent 2.1% and 2.4% improvements compared to Jet A. Additionally, both scenario 2 and scenario 3 intersect the HPF region.

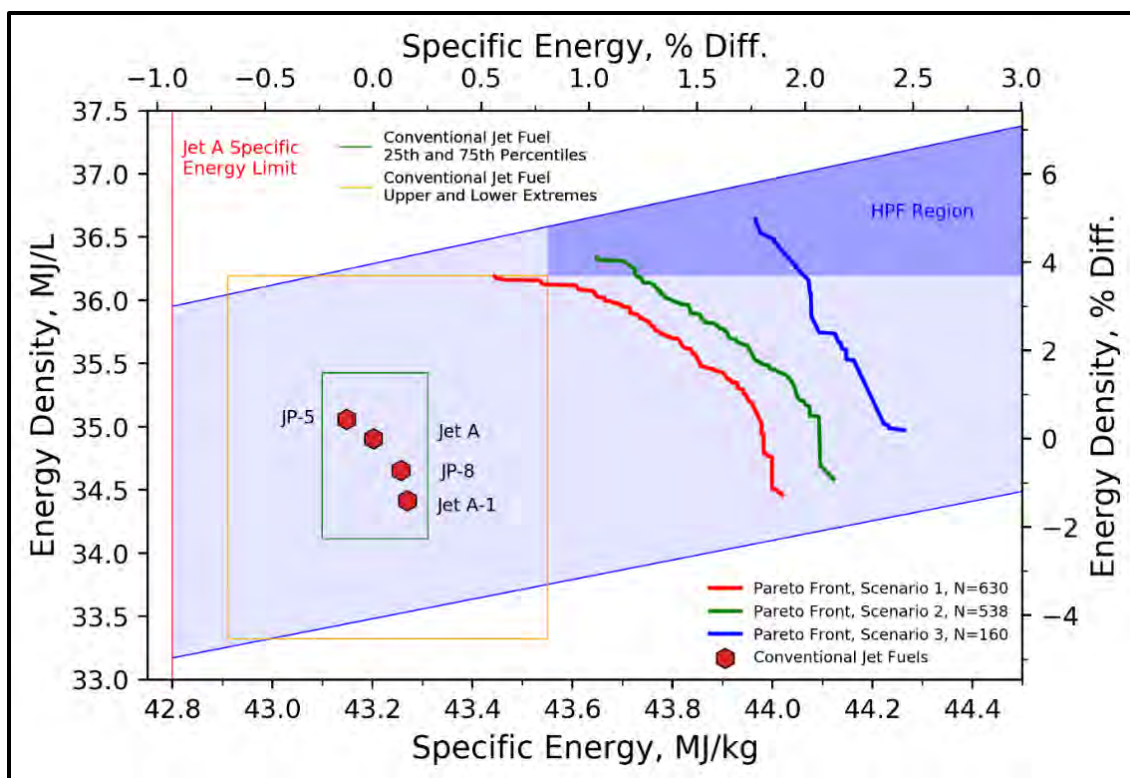


Figure 3. Pareto fronts from optimization. Scenario 1 is represented by the red line, scenario 2 by the green line, and scenario 3 by the blue line.

The NPSS and FLOPS models were run for the representative missions using Jet A fuel properties. Each case was then repeated using the hypothetical HPF properties, according to each of the three usage scenarios described in the previous section. The results are presented in Table 2, which indicates that a fuel with the HPF properties studied could cost 4.6% to 9.9% more than Jet A, depending on the usage scenario.

Table 2. Estimated break-even fuel price ratios for HPF compared to Jet A.

Aircraft	Option A	Option B	Option C
CRJ 900	1.090	1.087	1.046
B737-800	1.092	1.087	1.046
B777-200ER (Domestic)	1.092	1.087	1.046
B777-200ER (International)	1.099	1.081	1.046

Conclusion

To the author's knowledge, JudO is the first drop-in jet fuel performance optimizer. JudO offers the opportunity to determine blend limits for novel SAJFs, determine operability bottlenecks to further blend limits, and can be coupled to many additional objective functions for jet fuel. From property-property plots and JudO exercises, it is apparent that cyclic molecules offer significant benefits for HPFs. Cyclohexanes, in particular, are of interest as they can be produced via multiple pathways. They can be made via hydrotreating aromatic and phenolic compounds, which come from numerous sources including lignin, bio-oils, biocrudes, pyrolysis vapors, mixtures of oxygenated compounds, and simple

alcohols¹². Cyclohexanes provide near- to mid- term opportunities for HPFs. Moreover, cycloalkanes as previously reported can enable the complete removal of aromatic compounds by replicating the swelling functionality offered by aromatics. Specialty molecules considered in this study can possibly provide long-term opportunities for HPFs. The extremity of operability properties and costs that some specialty molecules exhibit poses a significant challenge for their implementation. Future exploration of potential specialty molecules will need to be guided to a greater degree by the availability of the molecules in consideration. Molecules that are byproducts of other processes will be especially promising from an economic standpoint.

Acknowledgments

The author would like to thank the Ohio Space Grant Consortium for their support of this work.

Additionally, thank you to the Department of Energy (BETO) and Sandia National Labs for sponsoring this work (PO#-1884928).

References

1. Myles, A. *Global Warming of 1.5 °C*. (2018).
2. Fast Facts on Transportation Greenhouse Gas Emissions. *Environmental Protection Agency* (2016). Available at: <https://www.epa.gov/greenvehicles/fast-facts-transportation-greenhouse-gas-emissions>.
3. Fuel Fact Sheet. *International Air Transport Association* (2018).
4. Liebman, J. F. & Greenberg, A. A survey of strained organic molecules. *Chem. Rev.* **76**, 311–365 (1976).
5. M. J. Frisch, G. W. Trucks, H. B. Schlegel, G. E. Scuseria, M. A. Robb, J. R. Cheeseman, G. Scalmani, V. Barone, B. Mennucci, G. A. Petersson, H. Nakatsuji, M. Caricato, X. Li, H. P. Hratchian, A. F. Izmaylov, J. Bloino, G. Zheng, J. L. Sonnenberg, M. Had, G. 09: E.-G. R. B. O. (2010). *Gaussian 09*. (2016).
6. Papaioannou, V. *et al.* Group contribution methodology based on the statistical associating fluid theory for heteronuclear molecules formed from Mie segments. *J. Chem. Phys.* **140**, (2014).
7. Schlueter, M. MIDACO-SOLVER. Available at: <http://www.midaco-solver.com/>.
8. Jones, S. M. *An Introduction to Thermodynamic Performance Analysis of Aircraft Gas Turbine Engine Cycles Using the Numerical Propulsion System Simulation Code*. (2007).
9. McCullers, L. A. *Aircraft Configuration Optimization Including Optimized Flight Profiles*. (1984).
10. International Civil Aviation Organization Aircraft Engine Emissions DataBank. *ICAO* (2018). Available at: <https://www.easa.europa.eu/easa-and-you/environment/icao-aircraft-engine-emissions-databank>.
11. Graham, J. L. *Impact of Alternative Jet Fuel and Fuel Blends on Non-Metallic Materials Used in Commercial Aircraft Fuel Systems*. (2011).
12. Abdullah, Z., Heyne, J. & Holladay, J. *Integrated Jet Fuel Report*. (2018).

Electric Generation Potential in the Upstream Oil and Gas Industry

Student Researcher: Derek L. Krieg

Advisor: Professor Craig Rabatin, P.E.

Marietta College

Edwy R. Brown Department of Petroleum Engineering and Geology

Abstract

This is a continuation of last year's project in which I examined a few potential ways that electricity could be generated by the mere production and transportation of hydrocarbons. Last year's study showed that perhaps the most promising potentials are to utilize non-renewables on site and to utilize a natural gas powered electric turbine on site. While the latter option sounds counterintuitive, it actually turns out to perhaps be quite an economical use of the gas. Thus, this year's project focused on designing a simulated oil field in Texas to test this theory. After simulating production values, determining potential electricity generated, running economics, and performing a sensitivity analysis, this unconventional approach of generating electricity on site to sell into the grid deserves deeper looks by today's E&P operators.

Project Objectives

The purpose of this study was to determine if combusting gas produced on site in an electric generator and selling electricity into the grid is worth a deeper look by oil & gas companies.

Methodology Used

The first step was to design a simulated field to be used for the study. I chose to place the case study in the Permian Basin in West Texas. This area was selected because it is the hottest play in the U.S. right now and it is also a liquids play. Thus, the gas produced on site is not viewed as the main moneymaker. Also, producers in this basin sometimes have issues selling into the pipelines and midstream infrastructure at economical prices. Thus, some result to wastefully flaring the gas or end up paying to have their gas "sold." I designed this field to have 9 pads with 2 wells per pad. The wells were all placed in the Wolfcamp formation(s) and were designed with a 7,000' lateral. 20 nearby Pioneer Natural Resources wells were used to fit a production type curve and to determine the field's gas production by month.

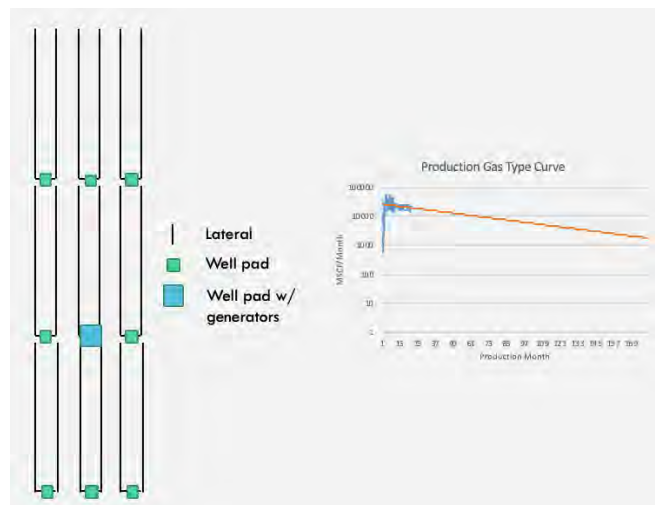


Figure 1. Field layout and production decline curve.

The second step was to convert the gas production to electricity generated. This was done on a monthly basis in accordance with the field's production curve. For this project, I used a 1.1 MW generator from GE which uses 10 MCF/h of gas. From there, I converted the flowrate of gas to the equivalent MWh produced. To meet the initial production of the field, 65 of these generators would be needed. Keep in

mind, if this project was actually to be executed, there are many generators to choose from and this design could be optimized to the fullest extent.

The last step was to run the economics and perform the sensitivity analysis of the project. The results of which will be discussed below. However, to run the economics, I had to decide on what commodity prices to utilize. After looking up current day prices and comparing them to daily prices over the past two years, I decided to use conservative numbers. Thus, I selected \$20/MWh and \$1/MSCF to use for my project. \$20/MWh is based off of the ERCOT market and the \$1/MSCF is based off Henry Hub pricing with basin-specific “basis” applied to it. \$100,000 was also used as the price per generator. The approximated cost for pipelines (and electric lines), extended pad size, and transformation facility was also taken into account. Total CAPEX was approximately \$6,800,000.

Results Obtained

Using the numbers listed above, a 15 year economic study revealed a \$22,000,000 undiscounted NPV for the traditional case of just selling the gas into a pipeline. However, the generation case revealed a stunning undiscounted NPV of \$57,000,000 over the same period. Every sensitivity study also showed the generation case to be the clear winner. For example, when the price volatility for the commodities were taken into account, the traditional case could quickly and easily be swung into a negative NPV due to the everchanging basin differential from Henry Hub. However, when compared to the generate case, the project never failed to be economical. When comparing it with prices over the previous year, \$20/MWh even appeared to be a very conservative number. Perhaps a more representative average for 2018 would have been \$25/MWh which would have yielded nearly a \$70,000,000 NPV.



Figure 2. Economic results slide.

Sensitives ran included commodity pricing (as mentioned above), compressor pricing, discount rates, and field production data. Other sensitivities were discussed such as line and facility cost but deemed unnecessary due to the small effect on the overall CAPEX and NPV. As mentioned before, the generate case won in every study by large margins.

The final conclusion was that this non-traditional approach should be further reviewed by companies actively operating today. It appears to have very good investment potential with a quick payout (roughly six months in our case) and a phenomenal NPV over just 15 years. If this case would be further reviewed by a company who could implement a similar design, they could create much more accurate models, hire consultants, and utilize engineers. Also, this design and approach could be optimized for even higher returns.

Acknowledgments and References

1. ERCOT, pricing info, etc.
2. "Market Prices." *Electric Reliability Council of Texas (ERCOT)*, www.ercot.com/mktinfo/prices.
3. "Home | Next Generation Oil & Gas Tools." *WellDatabase*, www.welldatabase.com.

Alternatives to Decommissioning Offshore Infrastructure

Student Researcher: Johnathan Kungle

Advisor: Professor Craig Rabatin, P.E.

Marietta College

Department of Petroleum Engineering and Geology

Abstract

Water covers 70% of the Earth, yet hydrocarbon discoveries are still made on land despite continuous exploration for the past 150 years—meaning unfathomable amounts of undiscovered oil and gas likely exist beneath our oceans. Two decades ago, 5,000 ft of water was considered an “ultra-deep” offshore well; now, a large majority of offshore rigs are rated for either 10,000 or 12,000 ft of water. Needless to say, offshore technology in the oil and gas field is rapidly growing and will continue to do so as energy demand increases and operators push into deeper water to find more hydrocarbons. Thus, offshore infrastructure is and will continue to become quickly outdated, resulting in a lengthy and expensive decommissioning project for operators. With the ever-growing amount of obsolete offshore structures, it is time the industry investigates alternatives to the standard decommissioning process. This study considers artificial reefing, wind and wave power, tourism, and fisheries as alternatives. It investigates feasibility, potential cost savings and/or profit, and real-world examples.

Project Objectives

Assess each alternative to determine its potential and any obstacles preventing implementation by looking at feasibility and real-world examples.

Methodology Used

The driving force behind this whole project is my summer experience working for a large upstream oil and gas operator as a drilling engineering intern in their Gulf of Mexico operations. Throughout the summer, which included a trip to an offshore drillship, I realized how many offshore structures are decommissioned each year—a trend that will continue well into the future. This prompted further investigation on my part, and I have spent considerable time researching this topic, compiling the data I collect, and analyzing my findings.

Results Obtained

As it turns out, operators have several options when it comes to decommissioning old rigs. Researchers will continue investigating the feasibility of fisheries as current projects progress and new data emerges, but this is a risky and unlikely choice given the current situation. Tourist attractions are a great way to repurpose old rigs, but only so many museums, hotels, and dive centers can be created before that market becomes saturated. Capturing wind and wave energy is a great way to continue harvesting power with this infrastructure, but technology has yet to reach the point where this can be done efficiently and economically. That leaves reefing as the most practical option for operators in what many see as a win-win situation for marine life and the invested company. Given its all-around benefit, companies should design their rigs to easily convert to artificial reefs and then pursue that alternative when the time comes. They should also monitor the market for other alternatives that may eventually emerge as more feasible options, but until then artificial reefs are a great way to save money and support aquatic ecosystems.

Acknowledgments and References

1. Azimov, U. and Birkett, M. 2017. Feasibility study and design of an ocean wave power generation station integrated with a decommissioned offshore oil platform in UK waters. *International Journal of Energy and Environment* 8(2): 161-174.
2. Dexter, C. and Ghorashi, J. 2016. What do you do with an obsolete oil rig?. *The Chemical Engineer*: 38-39.
3. Evans, I. Can we repurpose decommissioned oil rigs for environmental gain?. PacificStandard, psmag.com/environment/rejiggering-the-rigs. Downloaded 3 November 2018.
4. Gaskill, M. Gulf coast oil platforms: save the rigs?. PacificStandard, psmag.com/environment/leave-those-rigs-alone-42598. Downloaded 3 November 2018.
5. How Does Decommissioning Work? Rigzone, www.rigzone.com/training/insight.asp?insight_id=354&c_id=. Downloaded 5 November 2018.
6. Kaiser, M.J. and Narra, S. A hybrid scenario-based decommissioning forecast for the shallow water U. S. Gulf of Mexico, 2018-2038. ScienceDirect, www.sciencedirect.com/science/article/pii/S0360544218316645. Downloaded 5 November 2018.
7. Khan, J. Decommissioned rigs: Precious marine habitats or giant lumps of ocean waste?. ABC, www.abc.net.au/news/science/2018-06-13/decommissioned-rigs-precious-marine-habitat-or-more-ocean-waste/9833084. Downloaded 3 November 2018.
8. McKinney, J. After the oil runs out: rigs to reefs. PacificStandard, psmag.com/environment/after-the-oil-runs-out-rigs-to-reefs-19272. Downloaded 3 November 2018.
9. Newman, N. The sharp rise of platforms decommissioning. Eniday, www.eniday.com/en/sparks_en/platforms-decommissioning/. Downloaded 3 November 2018.
10. Offshore decommissioning. PetroWiki, petrowiki.org/Offshore_decommissioning. Downloaded 4 November 2018.
11. Rigs to Reefs. Bureau of Safety and Environmental Enforcement, www.bsee.gov/what-we-do/environmental-focuses/rigs-to-reefs. Downloaded 5 November 2018.

Self-Sufficient Medical Devices

Student Researcher: Kathleen Marie Licht

Advisor: Dr. Ralph Whaley

Cincinnati State Technical and Community College
Center for Innovative Technologies

Abstract

The concept of self-powered devices is becoming increasingly prominent by those who wish to see our carbon footprint diminish. With solar power and wind power existing and research going into creating more self-powered devices, we could see the world become truly “green” in energy. All of this effort, however, is focused on devices ranging from cell phones to cars with very little thought put into medical devices. This semester I have been fortunate enough to co-op at Cincinnati Children’s Medical Center in their Clinical Engineering Department and I have experienced first hand what goes into making sure that patients are equipped with up to date and fully functioning equipment. However, I have also witnessed first hand how many batteries are disposed of on a daily basis. Batteries, in general, are detrimental to the environment and even though within the hospital they are able to be recycled, most batteries outside the hospital setting are not.

Finding alternative means of energy to help the battery usage within the hospital setting could help with the overproduction and distribution of batteries. There are currently studies being done on what can be termed “Sound Power,” which essentially means harvesting power from sound. Within a hospital, there is never a shortage of sound and if devices are equipped with the technology to harvest the sound around them and turn it into usable energy, then that would eliminate the need for batteries and power cords.

Project Objective

The objective is to research the possibility of eliminating the need for power cords and batteries to power medical devices to instead find an alternative power supply in sound to power these devices.

Methodology Used

Exploring the concept of harvesting sound as a power supply, the term “piezoelectricity” came about. The term piezoelectricity means using crystals to convert mechanical energy into electricity (Woodford 2018). Piezoelectric material acts as a battery by creating a positive and negative terminal on either side of the crystalline material to where when connected into a circuit, current flows. Inside of medical equipment that requires battery usage or a plug, this type of material can be easily substituted into the equipment. Taking a look at the CareFusion Alaris PCU (progressive care unit), this device has not only an AC adapter plug but also a backup battery for when it is not plugged into an outlet. This device can supply power to four separate devices connected to it at a time and when in use on a patient, must always be on. The PCU is essentially the “brain” where it stores the type of care, patient information, drug library, and many other statistics where one can find essential information. If we were to take piezoelectric material and substitute it into the mainframe of the PCU, we would have to make sure that it would be able to not only supply power to the PCU but supply power to operate the other devices connected to it. This same thinking would have to be applied to all types of medical equipment as well so as to ensure that all devices are receiving the necessary power.

Results Obtained

The PCU has a battery life of roughly two years if used properly before the manufacture (CareFusion) recommends replacing it. This overhaul in battery replacement takes a great deal of time to do especially with the number of devices that a hospital's technicians take care of. Also, these batteries need to be reconditioned once a year to help maintain life expectancy. Piezoelectric material, if incorporated into these types of medical equipment could eliminate the amount of time and work spent on the batteries alone. This would free up time to get through more equipment in a day and make the whole process of upkeep easier.

Significance and Interpretation

Piezoelectric material is already used in scanning probes, however, if we were to access the potential energy, then we could change how the whole battery system works. With some batteries being replaced yearly, piezoelectric material could not only help reduce battery waste but could very efficiently run equipment. Knowing even just a fraction of the number of batteries that a hospital goes through within a few months, hospitals would greatly benefit from a power supply that did not include batteries. With alternative energy and power harvesting techniques being done, more research should be conducted to incorporate this into medical equipment. Alternative energy, like piezoelectricity, would not only make equipment better equipped to never have issues with a cord being broken or a battery needing to be replaced, but it would also make it better for the environment. As with all medical care, the best care for a patient is when things go smoothly.

References

1. CareFusion. (2016). Alaris System User Manual – with v9.19 Model 8015. Retrieved from http://www.carefusion.com/documents/guides/user-guides/IF_Alaris-System-8015-v9-19_UG_EN.pdf.
2. Hughes, Mark. "How Piezoelectric Speakers Work." *All About Circuits*, 29 June 2016, www.allaboutcircuits.com/technical-articles/how-piezoelectric-speakers-work/.
3. Johnson Electric Company. "The Piezoelectric Effect - Piezoelectric Motors & Motion Systems." *Nanomotion*, Nanomotion, 28 Aug. 2018, www.nanomotion.com/piezo-ceramic-motor-technology/piezoelectric-effect/.
4. Keim, Robert. "Understanding and Modeling Piezoelectric Sensors." *All About Circuits*, 15 Oct. 2018, www.allaboutcircuits.com/technical-articles/understanding-and-modeling-piezoelectric-sensors/.
5. Woodford, Chris. "Piezoelectricity - How Does It Work? | What Is It Used for?" *Explain That Stuff*, 21 Aug. 2018, www.explainthatstuff.com/piezoelectricity.html.

The Neighborhood Youth Activities Project

Student Researcher: André L. Love

Advisors: Dr. Augustus Morris, Jr., P.E. and Ms. Suzanne Marie

Central State University

Department of Math and Computer Science

Abstract

As a volunteer for the Youth Move group here in Ohio through N.A.M.I., I've worked as a youth leader to guide and help at-risk youth in any way I am able. My experience there along with my interest in consumer behavior and social media led me to pursue my Computer Science Degree. I plan on building the next platform for youth to connect in a healthy manner allowing parents the ability to easily find or create events in their communities such as volunteering events for community enhancement via gardening, or a neighborhood kickball game. The concept could be compared to a crossover between Facebook and Eventbrite, but this would use location services to give the youth points for checking in to events. Those earned points can eventually be redeemed for prizes, giving the youth and their family's greater incentives to partake in events.

Project Objectives

The objective of this project is to stimulate children's relationships and interpersonal skills. Today's youth utilize the majority of their time playing Fortnite or browsing YouTube. Reading clubs were prevalent during my childhood; local libraries would reward you for hours spent within the facility or for the number of books read. The application I plan on developing would do exactly that.

Methodology

In order for this dream to become a reality I must first develop a mobile application. My experience in Java and HTML programming languages allows me a slight advantage to the development of said app. The app would allow myself and other verified hosts to publish events and their prospective locations. Users would have the ability to subscribe to hosts and all of their events or receive notifications from specified events that identify with their selected interests and geographical radius.

Results Obtained

The app is still in the early stages of development. Thus far the GUI (Graphical User Interface) is nearly complete but the functionality is not. These sort of applications are typically created and monitored by a team but in the short time I've had the honor of working on this project I know have the ability to post events and their locations as a host.

Currently, I'm working to develop a verification process for other hosts to upload content. This would immediately disqualify those with criminal records that may be harmful to others or especially unsafe around children. The next step will be to develop a segment of code that will allow users to interact with hosts' events confirming their attendance or connecting via direct message to assist in forming the event.

Acknowledgments

The author of this paper would like to thank Central State University and Dr. Augustus Morris. Jr., and Ms. Suzanne Marie for their assistance and support throughout the course of this research. The author would also like to thank the Math and Computer Science Department of Central State University for their cooperation in providing a susceptible database to utilize to conduct this research.

References

1. D. Cao, et al., Java Programming, SAMPE May, 2018, Wilberforce, OH.

Water Quality Assessment of Euclid Creek Using Remote Sensing and VPCA Analysis

Student Researcher: Nicholas B. Manning

Advisor: Dr. Joseph D. Ortiz

Kent State University
Department of Geology

Abstract

The Euclid Creek Watershed contains multiple rivers of Northeast Ohio and drains into Lake Erie at Villa Angela Beach near Cleveland. The beach has been closed with access to the water restricted multiple times over the past decade, mainly due to *E. coli* bacteria. The problem is amplified during heavy rains where flooding causes multiple combined sewer overflow systems to feed into the stream. This project is a continuation of the work done to assess the content and amount of the contaminant influx near the mouth of Euclid Creek and its interaction with the local beach. Landsat-8 images were combined with the Kent State University (KSU) spectral decomposition method of image analysis, which employs varimax-rotated principal component analysis (VPCA) to determine water quality issues along the creek and in the nearshore area to explore interactions with the aquatic systems of the lake. This is a more cost- and time-effective method that can reduce the potential biases common in traditional remote sensing techniques arising from atmospheric errors or correlated input variables. These errors are limited by decomposing the spectral properties of the image into their individual components by using VPCA, breaking the mixed spectral bands down into their respective and corrected spectral fingerprints.

Introduction and Objectives

Villa Angela Beach, a small beach near Cleveland in Northeast Ohio, has been the subject of multiple water quality advisories due primarily to the influx of combined sewer overflows (CSOs) mixing with the nearshore water, creating a health risk in the waters and making the waters too dangerous to enter. Euclid Creek is the main stream discharging into Lake Erie at this site and is notorious for having contaminated waters. The source of this contamination has been debated, and CSOs, livestock excretions, and avian droppings have all been proposed as a possible cause. Villa Angela beach was closed around 60% of recreational days and Euclid Beach Park was closed 38% of the days from 2002-2007¹. The events of highest concentration of *E. coli* were consistent with human bacteria, not that of gulls or other animals, and were correlated with days of intense rainfall, directly linking the flash flooding of combined sewer overflow systems with beach closings². Heavy rains amplify the influx of *E. coli* bacteria by flooding the combined sewer overflow systems along the Euclid Creek watershed, pushing their contents into the creek which feeds to Lake Erie near Villa Angela Beach. The flooding and CSOs were found to be the direct cause of 97 beach closings in 2010 and 163 in 2011².

Some of the most intense periods *E. coli* contamination correlate with periods of the largest toxic algal blooms on Lake Erie. These blooms are not caused by the same contaminant, but could both arise from intensified precipitation periods leading to larger amounts of discharge. The increased discharge would carry larger amounts of catalytic nutrients (which drive algal blooms) and *E. coli* being delivered to the water body. The algal blooms of the eastern basin, while not cyanobacterial like the western blooms, can mix with the waste and *E. coli* and form a different, but still harmful, bloom. For this reason, I also consider Central and Eastern blooms harmful algal blooms (HABs). The largest HABs occurred during the summers of 2011 and 2015, with 2018 being predicted to be a significant bloom size³. HABs are caused primarily by an increase in nutrient loading (mainly nitrogen and phosphorus), linked to agricultural and

urban runoff⁴. While beaches on the eastern coast close due to influx of *E. coli* bacteria, HABs can also cause problems and provide a visible effect on the water body. If both of these events are linked to times of increased runoff (Villa Angela closings due to *E. coli* from CSO, and HAB growth from nutrient influx), then a statistical link could be created, using images of HAB growth (which can be observed by remote sensing) to predict times of high bacterial contamination and thus, beach closing.

Remote sensing grants the ability to study large-scale temporal and spatial shifts in algal growth quickly and at a low cost, using satellite imagery. A current restriction on remote sensing technology is the inability to detect bacterial contamination in systems, as heterotrophic bacteria may produce no observable pigment signal in water bodies. This project attempts to link the observable trend of HAB growth with non-observable *E. coli* contamination to provide a measurable method of predicting contamination fluxes. Water quality tests could then be conducted more quickly and safely, and trends could be predicted, potentially allowing for beach closing forecasts.

There has been a large effort to study the factors influencing the concentrations of *E. coli* in Lake Erie beaches and surrounding areas, and studies to determine their prevalence in recreational waters^{5,6,7}. Previous studies have been conducted to create models using wastewater as a predictor for *E. coli* concentration in Northeast Ohio beaches using a multiple-linear regression model⁵, with variables including (but not limited to): wave height, turbidity, number of birds on the beach at the time of sampling, and rainfall. Other efforts have been conducted to refine the Ohio Nowcast, a system using models to provide the data and *E. coli* predictive measurements for beach advisories, due to the time it takes *E. coli* samples to be processed in a lab versus the real-time changes in the level of *E. coli* occurring in a hazardous beach. Due to the 18-24 lab processing time, decisions are commonly made using predictive models⁸. Spatial studies have also been conducted on Northeast Ohio beaches (Edgewater and Lakeshore) using piezometers to study the source of *E. coli* bacteria⁹, finding mixed results at the two beaches, with Lakeshore having a significant input from gull fecal matter as well as humans. A 2013 study by Jackson et al.² concluded that pollutants from the flooding of CSOs could be trapped in the nearshore mixing zone of Villa Angela beach and Euclid Creek during various parts of the year. Longshore currents and human-made structures were the main contributors to this mixing, potentially intensifying the pollutants in the nearshore area. This conclusion led to Villa Angela beach and Euclid Creek becoming the area of interest for the current study. While there have been several attempts to use various regression models and Nowcast systems to determine beach closings, there has been no research done comparing beach closing rates with harmful algal bloom rates using remote sensing.

Traditional remote sensing techniques would suggest linking *E. coli* with total chlorophyllide-a. There are multiple possible sources of chlorophyllide-a, however, and the signal may be obscured by turbidity and degradation products of pigments. Conditions amplifying the growth of HABs throughout Lake Erie should increase the proliferation of *E. coli* bacteria. After the processing of the images using the KSU spectral decomposition, involving varimax rotated, principal component analysis (VPCA), which separated the images into their different spectral components, the components are compared against a library of known spectral signatures. If a dominant component of the blooms is discovered to be linked to *E. coli* proliferation, this component could potentially be used as a proxy for *E. coli*, enabling the use of remote sensing to monitor bacterial content in nearshore environments.

Methodology

Level 2 Landsat 8 images of the eastern basin of Lake Erie were selected based on their correlation with times of various flow rates throughout years of large and small HAB, *E. coli* measurements, beach closings, and image quality and availability from the USGS EarthExplorer database. Beach closing dates and *E. coli* measurement values were obtained from the Ohio Department of Health Beachguard information database. Images without significant cloud cover over the area of study were preferentially selected. Daily average discharge rates were retrieved from the USGS National Water Information system at station 04208700, located on Euclid Creek during 2015 (figure 1). This station allowed for the accumulation of CSO influx from other tributaries before the water and runoff enters Lake Erie and is then diluted. Graphs were created to illustrate times of high and low flow during years with large and small algal blooms. Another important factor of the image selection process was selecting images during times with high varying *E. coli* amounts. Images were selected with low amounts of *E. coli* (0-126 cfu/100ml, the EPA limit for recreational waters¹⁰) and high amounts (127-19,292).

Once selected, the image processing is conducted through multiple steps using the Harris Geospatial ENVI / IDL software (ENVI version 5.5 + IDL version 8.7). The selected images were pre-processed using a 3-kernel median smoothing and a modified VPCA technique developed in the Ortiz lab. The method combines reflectance and derivative bands and normalized differences to broadband, multispectral sensor images to differentiation components by providing the VPCA method redundant information to help differentiate the signature of multiple constituents from sensors with poor spectral resolution. This is possible because the VPCA eigenvalue-eigenvector spectral decomposition method is designed to partition redundant information from complex data sets. The normalized difference indices employed are the normalized difference vegetation index (NDVI), the normalized difference water index (NDWI), the modified photochemical reflectance index (MPRI), a variance function (mVARI), and the normalized difference of red and blue bands (NDRB), a function to measure biological productivity. The method “stackings” various bands, derivatives and the normalized difference indices to produce cleaner image results with better separation between components.

When processing Landsat 8 images, ENVI will use the aerosol.tiff file and re-correct it with spatial reference to a format usable in the program. A mask must be created to cover land and isolate water pixels in order to process only water pixels. Once the land mask was created and applied to the Landsat 8 image, the area of interest is subset with a shapefile of the region of interest (ROI). The ROI was created in ENVI over an area encompassing Villa Angela Beach, Euclid Beach Park, a portion of the creek leading to the mouth, and an offshore area large enough to capture the full extent of eastern basin HAB growth. The VPCA process described in Judice et al., 2018¹¹, is now conducted on the prepped image. A principal component analysis is conducted in ENVI to decompose the correlation matrix of the derivative spectrum and obtain the number of components with an eigenvalue greater than 1+1 and to separate signal from noise, producing a set of linear band combinations that are orthogonal to one another^{12, 13}. These eigenvalues are indicative of the number of dominant components present in the image. After this step is conducted, a varimax rotation is applied to maximize the amount of variance explained by each component. The preliminary steps in the KSU spectral decomposition method involve decomposing the entire spectral signature into its individual components, then isolating the individual loading components based on their respective spectral signature. Conducting the KSU spectral decomposition method in this fashion explains the variance of each component, the component loading spectral patterns, and the component score spatial patterns in the ROI. These are compared to pinpoint the identity of the main components in an image. The Z-scores of the VPCA loadings of the dominant spectral band groups (Ultra blue [430-450 nm], Blue [450-510 nm], Green [530-590 nm], and Red [640-

670 um]) are compared to a known library of the loadings of different common materials in a water body using a forward stepwise regression with a 0.05 alpha parameter. The main component is identified, and any auxiliary components are accepted with a Variance Inflation Factor (VIF) of 2.0 or below.

Results Obtained (thus far)

The KSU spectral decomposition method was used on different dates of varying flow rates and *E. coli* contents, and yielded mainly chl-a+carotenoids, phycocyanin, and goethite. The dates observed and analyzed include July 9th, 2014, June 24th, 2017, May 2nd, 2015, June 3rd, 2015, July 28th, 2015, and August 22nd, 2015. The individual analysis and results of each record are shown in Table 1 (appended). The average amount of variance explainable by the identified dominant components was 97.05%. The spatial loading patterns were dominated by nearshore components, with cloud cover and visual obstructions (glint) creating errors in the images. The method shows promise in producing repeatable and accurate results on relevant days with clear Landsat 8 data available.

Discussion

Once these components are identified, they must be interpreted to be able to be put into the context of the system; the presence of one component may mean something else when put into context. A diatomaceous presence, for example, could be a residual bloom from days ago, or a bloom could contain other constituents. The presence of chlorophyllide-a and carotenoids is not necessarily a harmful algal bloom and may represent non-cyanobacterial or non-harmful algae. Chlorophyll a absorbs light from the visible violet to red spectrum (400-700 nm) and reflects green light (500-570 nm), making it a good identifier for plant life and photosynthesis¹⁴. The different components identified using this process can represent different processes. Some more examples include goethite, which is representative of suspended sediment and phycocyanin, which is an indicator of cyanobacterial presence.

Adequate data acquisition proved to provide challenges, with the funds to the USGS (the provider of the main dataset utilized) being limited through the year. Images were unavailable for download on multiple occasions, with problems on EarthExplorer. Out of the images available for download, dominant cloud cover provided another limiting factor. Significant cloud cover could not be corrected for without introducing significant error. Images through the dates of May, June, July, August, and September 2012-2018 with available images without significant cloud cover over the area of study were limited, with only six clear images identifiable and with sufficient data to complete the entire spectral decomposition process. While the method did produce repeatable and accurate results on the images analyzed, there were not enough days to identify a statistically significant link from the components of the water and blooms to *E. coli* present.

Conclusions (thus far) and Future Work

The main components in Euclid Creek were identifiable using the KSU spectral decomposition method and yielded repeatable results, but the collected data was limited. Therefore, no obvious link to *E. coli* between images of high/low flow and high/low *E. coli* content can be confidently identified. Future work consists of two potential routes to increase the amount of data available: either (a) utilizing a method of atmospheric correction in an attempt to remedy the cloud cover over multiple images or (b) using a different satellite (potentially Sentinel 3a or MODIS) to retrieve more images at the cost of a coarser image resolution. Ground work validation would also be helpful to see if the contents of the lake match other methods.

Figures

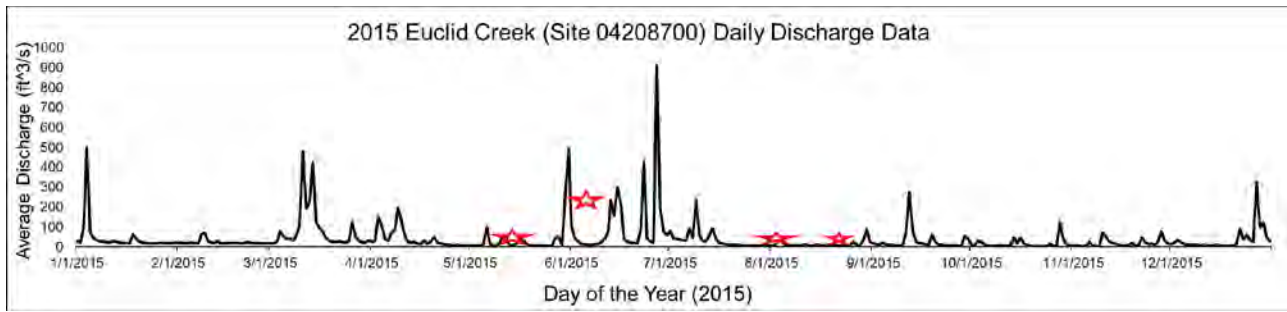


Figure 1. Daily average discharges into Lake Erie from Euclid Creek, with dates of acquired data starred.

Table 1. Dates analyzed and their accompanying statistics.

Date	VPCA	Coefficient	Identification of Component	Flow (daily avg; ft ³ /s)	E.Coli (cfu/ 100mL)	Variance	Total Var. Explained:
70914	1	-1.085	chl-a+carotenoids zscore	73.1 (previous day 318)		4902	42.4712
70914	1	-0.188	myxoxanthophyll zscore				42.4712
70914	2	-1.234	bacillariophyceae zscore				28.734
70914	3	0.993	phycocyanin zscore				17.6691
70914	4	1.050	fucoxanthin zscore				6.40764
70914	4	0.301	bacillariophyceae zscore				6.40764
62417	-1	0.949	chl-a+carotenoids zscore	18.6 (previous day 131)		1741	55.6144
62417	-1	-0.108	a-PEC zscore				55.6144
62417	2	-0.979	illite+kaolinite zscore				21.3456
62417	2	-0.234	trans-neoxanthin zscore				21.3456
62417	3	1.168	phycocyanin zscore				19.6851
62417	3	0.422	chlorophyllide-a zscore				19.6851
62417	4	1.283	illite1.asd zscore				1.82689
82215	1	0.948	phycocyanin 2 zscore		7.1	14	54.2766
82215	1	-0.158	trans-neoxanthin zscore				54.2766
82215	2	1.024	chl-a+carotenoids zscore				23.7237
82215	2	-0.127	haptophyta zscore				23.7237
82215	3	1.229	phaeophorbide-b zscore				12.3776
82215	4	-1.504	chlorophyll a zscore				6.26981
72815	1	-0.815	chl-a+carotenoids zscore		9.7	42	47.4973
72815	2	1.174	phycocyanin 2 zscore				21.2019
72815	2	0.492	illite1.asd zscore				21.2019
72815	3	1.226	chlorophyta zscore				17.4347
72815	4	-0.993	bacillariophyceae zscore				12.1198
72815	4	-0.068	peridinin zscore				12.1198
50215	1	1.062	goethite.asd zscore		7.6 n/a		48.8408
50215	1	-0.315	peridinin zscore				48.8408
50215	2	1.081	bacillariophyceae zscore				43.2402
50215	2	0.237	a-PEC zscore				43.2402
50215	3	-0.991	phaeophorbide-b zscore				3.10988
60315	-1	0.948	phycocyanin 2 zscore	27 (two days after 103)		92	43.7396
60315	-1	-0.158	trans-neoxanthin zscore				43.7396
60315	2	1.024	chl-a+carotenoids zscore				29.2862
60315	2	-0.127	haptophyta zscore				29.2862
60315	3	0.990	phaeophorbide-b zscore				20.994
60315	4	-0.993	chlorophyll a zscore				4.41537

Acknowledgments

I want to thank Dr. Ortiz for notifying me of the OSGC program and asking me to submit a project. It was a welcome surprise and an honor to be asked to participate in a conference of this caliber. A well-deserved “thank you” goes to the lab group of Dr. Ortiz as well, especially Dulci Avouris and Taylor Judice, for helping me piece together what our lab’s work actually means and helping me overcome the inadvertent speed bumps of research. I also have to thank Alex Rosul for collaborating in taking our notebooks full of fervid scribble and changing them into an easy-to-follow standard operating procedure.

References

1. Polensek, M. D. (2008). Lower Euclid Creek Greenway Plan. Retrieved from <http://planning.city.cleveland.oh.us/bike/assets/LowerECGreenwayFinal.pdf>
2. Jackson, P. R. (2013). Circulation, Mixing, and Transport in Nearshore Lake Erie in the Vicinity of Villa Angela Beach and Euclid Creek, Cleveland, Ohio, September 11-12, 2012. *US Geological Survey Scientific Investigations Report, 5198*, 34.
3. US Department of Commerce, & Noaa. (2018, September 04). Lake Erie Harmful Algal Bloom. Retrieved from <https://www.weather.gov/cle/lakeeriehab>
4. Michalak, A. M., Anderson, E. J., Beletsky, D., Boland, S., Bosch, N. S., Bridgeman, T. B., & DePinto, J. V. (2013). Record-setting algal bloom in Lake Erie caused by agricultural and meteorological trends consistent with expected future conditions. *Proceedings of the National Academy of Sciences, 110*(16), 6448-6452.
5. Francy, D. S., Gifford, A. M., & Darner, R. A. (2003). *Escherichia coli at Ohio bathing beaches-- Distribution, sources, wastewater indicators, and predictive modeling* (No. 2002-4285).
6. Lauber, C. L., Glatzer, L., & Sinsabaugh, R. L. (2003). Prevalence of pathogenic *Escherichia coli* in recreational waters. *Journal of Great Lakes Research, 29*(2), 301-306.
7. Francy, D. S., & Darner, R. A. (1998). *Factors affecting Escherichia coli concentrations at Lake Erie public bathing beaches* (No. 98-4241). US Dept. of the Interior, US Geological Survey; Branch of Information Services [distributor].
8. Francy, D. S., Bertke, E. E., & Darner, R. A. (2009). *Testing and Refining the Ohio Nowcast at Two Lake Erie Beaches-2008* (No. 2009-1066). US Geological Survey.
9. Francy, D. S., Bertke, E. E., Finnegan, D. P., Kephart, C. M., Sheets, R. A., Rhoades, J., & Stumpe, L. (2006). *Use of spatial sampling and microbial source-tracking tools for understanding fecal contamination at two Lake Erie beaches*. U. S. Geological Survey.
10. United States Environmental Protection Agency. (2018, May 16). Nationwide Bacteria Standards Protect Swimmers at Beaches. Retrieved from <https://www.epa.gov/beach-tech/nationwide-bacteria-standards-protect-swimmers-beaches>
- a. Judice, T., Falls, W., Widder, E., Ortiz, J., Cristiano, D. 2018. AGU Abstract H43G-2517. Differentiation of Harmful Algal Bloom Signatures in the Indian River Lagoon by Remote Sensing. AGU 2018 Fall Meeting. Washington, D.C.
11. Ortiz, J. D., Avouris, D. M., Schiller, S. J., Luvall, J. C., Lekki, J. D., Tokars, R. P., & Becker, R. (2019). Evaluating visible derivative spectroscopy by varimax-rotated, principal component analysis of aerial hyperspectral images from the western basin of Lake Erie. *Journal of Great Lakes Research*.
12. Avouris, D. M., & Ortiz, J. D. (2019). Validation of 2015 Lake Erie MODIS image spectral decomposition using visible derivative spectroscopy and field campaign data. *Journal of Great Lakes Research*.
13. National Center for Biotechnology Information. (2019). PubChem Database. Chlorophyll, CID=12085802, <https://pubchem.ncbi.nlm.nih.gov/compound/12085802>

Will BIM, VR, & AI Utilization Bring Actual Solves for Construction's Top Issues

Student Researcher: Malia E. Mast

Advisor: Professor Dean Bortz

Columbus State Community College
Construction Management

Abstract

Introduction to key terms

Building Information Modeling (BIM) Building Information Modeling (BIM) is the process of creating and managing 3D building data during all phases of the project cycle. BIM has greatly evolved technology, since its birth during the late seventies, to a complex multiphase process that houses all data inputted from team members on a project. Bim has supported the collaboration and streamline of the construction processes by covering geometry, space, light, geographic information, quantities, and properties of building components. The BIM process can be used at different levels 1- the entire building life cycle, including the design, the processes of construction, prefabrication, and facility operation in real time accessibility. The BIM process is aimed in creating interoperability which is greater communication, collaboration, and visualization of the entire project for all project teams. Some of the perceived and actualized benefits include cost reduction, time savings, enhanced design quality, rework reduction, improved communication and decision making, facilitated modular offsite prefabrication, & ease of panelization and rationalization of the exterior surfaces.

Virtual Reality

Virtual reality (VR) is an interactive computer-generated experience taking place within a simulated environment with auditory and visual feedback. Current VR technology utilize virtual reality headsets or multi-projected environments, in combination with simulated and or actual physical environments or props to produce a simulated artificial environment that A person can move and interact in. Current VR technology is being utilized in many industries including the quick adoption into construction. Utilizing a Bim model, VR technology can be utilized to simulate environments for construction teams and end customers to produce. VR is considered the next phase of the 3D modeling process.

Artificial Intelligence

Artificial intelligence (AI) has become a growing field from the onset off data analysis and customer relationships. Companies not only wanted to store, analyze data, but develop algorithms that support making decisions. Most recent forms of AI make it possible for machines to learn from experience, called machine learning. Machine learning suggests & adjusts to new inputs and perform human-like tasks. AI allows for computers to be trained, process, and analysis large data sets in seconds. Regarding the construction industry, AI initially was synonymous with robotics. Most recent the construction industry is examining how AI can be leveraged in business development and decision making on resource allocation.

Industry Overview

Despite continued and predicted growth in the overall US Construction industry of \$1.4 trillion (excluding engineering 9.6 trillion) by 2021 alone, the industry is challenged with old and new issues. The top issues include labor shortages, production efficiency, and safety are resulting in significant waste, profit loss, and injury stated by prnewswire.com. For construction managers specifically time management minimizing delays, budget management, team management, and compliance are daily site challenges that have significant and critical impact to the total quality of the project delivery. The construction industry's ability in Maintaining profits, controlling cost, managing quality, project completion, and safety have an impact on the entirety and impact the countries GNP.

(Bim), Virtual Reality (VR), and Artificial Intelligence are technologies that have existed more than a decade but, have grown more significantly more sophisticated over the last five years. These improvements also correlate to greater global adoption of the technology in the construction industry including architecture, engineering, and construction (AEC). Comparatively to counterparts such as the United Kingdom, the US market has been slow to adopt. There are arguably many reasons for the slow adoption but the obvious would be that it is not federally mandated in the United States.

Project Objective

My Objective is to research the usability and consistent benefits of BIM, VR, & AI on 3 actual projects already built thru case studies and 1 simulation project:

- 1) Maple Tree Business City, Singapore
- 2) Prince Mohammed Bin Abdulaziz International Airport
- 3) Stanford Neuroscience Health Center Palo Alto California
- 4) School building, Columbus Ohio

I will correlate specific data points the benefits to relate to the current industry issues and predicted future strains to suggest if these technologies are impactfully.

Methodology Used

I used information coming from actual case studies of these locations, additional research white papers, industry organizations, and industry professional interviews.

Significance and Interpretation of Results

From the research and results of actual projects and interview with experts, I feel that the use of these technologies will not only be significantly impactful to reducing cost, time, and improve sustainability. Each case study had correlating results in the following areas:

Precise total team communications were a requirement for each case study. The technologies allowed for greater preplanning discussions, continuity, informed decisions equating to less project disruption and slow downs. Bim Model information empower operations thru out and during facility management. Allowing construction teams accessed real time data on the job site from any digital devices. This improved the speed and accuracy of information workflows, minimizing the miscommunications that often occur during paper or telephone-based reporting.

Reduction of immediate and predicted future costs associated with errors, clashes, and material sourcing was reduced with the technologies. The technologies allowed for prefabrication and clash detection thru simulation that would of require major rework and schedule delay.

Higher levels of productivity were produced thru 3D visualization; improving synergy of the design, preconstruction, and the actual construction process teams including trades in every major facet. Site & logistically coordination was possible due to 3D visualization. Additionally, last-minute changes and unforeseen issues were avoided by enabling easy reviewing and commenting across multiple disciplines. Waste was reduced by the avoidance of clashes. BIM data was accurately & instantly generated for production drawings or databases for manufacturing purposes, allowing for increased use of prefabrication.

Results are dismissing waste, increase efficiency, and reduce labor and material costs.

Utilization of BIM & VR technology was directly impactful in site coordination and safety preparation. BIM allowed the pinpointing of potential hazards. Partnered with future AI sets, Visual risk analysis and safety evaluations can help ensure safety over the course of the project execution.

The technologies supported the Owners' satisfaction rate including facility management, with expected ROI well after project completion. The Bim model and data sets serve as ongoing digital records. In some instances, data can be sent/requested into existing building maintenance software for post-occupancy use.

The technologies produced greater end customer satisfaction thru use of simulated environments.

Conclusion

The results of the study thru use of case studies, governmental, and professionals study suggest that not only would these technologies provide solves to construction's old and future challenges but also additional benefit to the owner, end customer, & construction companies strategic advantage and profitability, and the total industry if mandated. I would argue that these projects would not be achievable without the Bim & VR minimally. I would argue that a national mandate be consider of these technologies for the benefit for the industry and gross domestic product.

References

1. Campbell, D. (2017, June) *6 Ways Virtual Reality Construction Technology Can Save You Money NOW*. <https://connect.bim360.autodesk.com/virtual-reality-construction-technology-saves-money>
2. https://www.sas.com/en_us/insights/analytics/what-is-artificial-intelligence.html
3. Gies, G. (2018, September) *How Artificial Intelligence (AI) is changing the business of construction*. <https://industrytoday.com/article/embracing-ai/>
4. <https://www.epa.gov/smm/sustainable-management-construction-and-demolition-materials>
5. <https://www.epa.gov/facts-and-figures-about-materials-waste-and-recycling/advancing-sustainable-materials-management>
6. Jia, A. (2010). *Implementation of Building Information Modeling (BIM) in Construction: A Comparative Case Study*. Retrieved February 13,2019, DOI: 10.1063/1.3452236
7. <http://biblus.accasoftware.com/en/bim-adoption-in-usa-the-first-country-to-implement-bim-is-now-lagging-behind/>
8. Buildrite. How Technology is Changing the Construction Industry. <https://www.buildriteconstruction.com/technology-changing-construction-industry/>
9. Smith. S. (2017). Construction in the US - Key Trends and Opportunities to 2021. *PRNewswire*. <https://www.prnewswire.com/news-releases/construction-in-the-us--key-trends-and-opportunities-to-2021-300552181.html>
10. <https://www.statista.com/topics/974/construction/>
11. <http://www.constructionworld.org/category/technology/>
12. Sacks, R. Eastman, C., Ghang, L. Teicholz, P. (2018) *BIM Handbook*. Hoboken, New Jersey: Wiley

Interviews

1. Ceton, Gregory, (2019, March 3rd). <https://zoom.us/j/456284142>
2. Gregory Ceton, CSI, CDT Director, Strategic Initiatives and Special Projects
3. D Samuel Hodge, (2019, March 9th). Personal interview with D. Hodge
4. D Samuel Hodge, AI Architect + Blockchain Developer, Advisor, 360 Coach, and Futurist

A Compact and Compliant Electrorheological Actuator for Mobile Haptic Feedback

Student Researcher: Alex J. Mazursky

Advisor: Dr. Jeong-Hoi Koo

Miami University

Department of Mechanical and Manufacturing Engineering

Abstract

Realistic haptic feedback is needed to provide information to users of numerous technologies, such as virtual reality, mobile devices and robotics. For a device to convey realistic haptic feedback, two touch sensations must be present: tactile feedback and kinesthetic feedback. Though many devices today convey tactile feedback through vibrations, most neglect to incorporate kinesthetic feedback. To address this issue, this study investigates a haptic device with the aim of conveying both kinesthetic and vibrotactile information to users. A prototype based on electrorheological (ER) fluids was designed and fabricated. By controlling the ER fluid flow via applied electric fields, the device can generate a range of haptic sensations. The design centered on an elastic membrane that acts as the actuator's contact surface. Moreover, the control electronics and structural components were integrated into a compact printed circuit board, resulting in a slim device suitable for mobile applications. The device was tested using a dynamic mechanical analyzer (DMA) to evaluate its performance. The experimental results indicate that the ER fluid-based actuator is capable of conveying haptic feedback.

Introduction

In recent years, mobile devices have experienced a shift from mechanical buttons to smooth, touch screen keyboards. However, the benefit of larger and more versatile screens comes at a cost to the physical feedback associated with indenting buttons. The information conveyed to the user through these touch sensations is referred to as haptic feedback. In addition to visual and auditory sensations, being able to touch, feel and manipulate objects in an environment, whether real or virtual, offers the user a greater sense of immersion (Srinivasan and Basdogan, 1997). Therefore, haptic feedback is desired for numerous applications including simulators, teleoperation, entertainment and more (Coles et al., 2011; Park and Khatib, 2006). To emulate and restore physical feedback in electronics, haptic technologies are being investigated and applied to bridge the gap between the user and the virtual world. Comprehensive haptic feedback is comprised of two components: (1) kinesthetic feedback and (2) tactile feedback. Kinesthetic feedback provides information about position and movement of joints and muscles. Tactile feedback consists of the sensations felt at the surface of one's skin and just underneath it. When examining an object, humans may rub it to feel its texture and roughness (tactile) and press it to feel its resistance and elasticity (kinesthetic). Therefore, both sensations must be present to completely observe an object through touch (Srinivasan and Basdogan, 1997).

Although the implementation of miniature vibrotactile actuators has been extensive, the development of small-scale kinesthetic actuators has been relatively slow. Research toward kinesthetic devices generally uses alternating current/direct current (AC/DC) motors as the working principle to generate force feedback sensations (Bianchi et al., 2009; Fujita and Ohmori, 2001; Song et al., 2005). However, AC/DC motor-based actuators cannot be easily integrated into mobile devices due to their size and power consumption. Furthermore, active-controlled motors have been found to have issues with instability, making certain haptic applications less feasible (Adams et al., 1998; An and Kwon, 2006).

To avoid the problems associated with motors, many researchers have investigated actuating haptic sensations through the adjustable properties of smart materials, which pose a mechanically simpler solution to traditional actuation.

Magnetorheological (MR) fluid-based haptic devices have been developed in recent years (An and Kwon, 2002; Jansen et al., 2010b; Kim et al., 2016). However, reducing the size of MR fluid-based actuators proves difficult due to the size required of electromagnet coils. To investigate the feasibility of miniaturizing MR fluid-based haptic devices, Yang et al. (2010) proposed a new tunable stiffness display. In subsequent parametric modeling studies, this design was reduced into a miniature button capable of producing a wide range of kinesthetic and vibrotactile feedback (Ryu et al., 2015; Yang et al., 2017). Still, basing an actuator around MR fluid requires precise manufacturing to miniaturize the complex circuitry associated with the solenoid coil.

Electrorheological (ER) fluid, MR fluid's counterpart with a viscosity dependent upon electric field, presents opportunity to address the difficulties of implementing MR fluid in miniature applications. Similar to MR fluid, ER fluid features response times in the order of milliseconds, low power consumption and few issues with control stability (Bullough et al., 1993; Choi et al., 1997; Whittle et al., 1996). Additionally, with Wen et al.'s (2003) fabrication and modeling of giant ER (GER) fluid, GER fluid-based devices are capable of producing high yield stresses, similar in order to those of MR fluid-based designs. However, compared to MR fluid, the electrical design for controlling ER fluid is simpler; only two electrodes spaced approximately 1 mm apart are needed, thinner than the equivalent solenoid coil for MR devices. With a goal of actuator mobility, a basis of ER fluid allows for smaller and more portable designs.

While ER fluid has often been applied to exclusively tactile or force feedback devices, research toward comprehensive haptic devices is limited (Goto and Takemura, 2013; Pfeiffer et al., 1999; Taylor et al., 1996; Tsujita et al., 2010). Among these, no designs focus specifically on ER fluid's potential for device minimization. Mazursky et al. (2018) validated this idea experimentally with a small haptic button (14.5 mm thickness) based on ER fluid in flow mode driven by an elastic contact surface. However, this study left room to further reduce the actuator's size and verify its performance mathematically. In the current study, a pressure-driven flow mode model is presented to characterize the behavior of the proposed haptic actuator.

Project Objectives

This study presents a new design for a miniature haptic actuator to overcome the challenges of decreasing the size of kinesthetic devices for mobile integration. The goals of this study are to design an ER fluid based haptic actuator, to investigate its performance with mathematical modeling, and to experimentally evaluate its ability to produce both kinesthetic and tactile feedback. The actuator is manufactured using printed circuit boards (PCB) to integrate its electrical and structural components. Within the actuator, ER fluid provides the variable resistive force to the button's kinesthetic interface. By supplying high voltage signals to the electrodes on the PCB, the device's force feedback is controlled. Introducing a frequency into the applied voltage results in oscillations in the kinesthetic response to produce a vibrotactile response. Therefore, the proposed ER fluid-based device is capable of producing haptic feedback.

Methodology

Working Principles

Figure 1 illustrates the cross-section and the working principle of the proposed haptic actuator. When pressing the actuator's compliant contact surface, ER fluid flows radially outward through the gap between stationary electrodes, or the activation region. Therefore, it can be said that the actuator operates in pressure-driven flow mode, similar to that of a valve. To compensate for the change in volume due to indentation, radial slots have been included in the GND PCB and cover, allowing the membrane in the slots to expand elastically, creating a reciprocating reservoir (see Figure 1b). When pressure on the contact surface is released, the fluid is pushed by the contracting membrane from the reservoir and the device returns to its pre-contact state. When a voltage is applied to the electrodes, the ER fluid in the resultant electric field forms a fibrous network parallel to the field lines. This liquid-solid transition generates a yield stress with magnitude corresponding to the supplied voltage. Therefore, the force felt by the user's finger when pressing directly corresponds to the yield stress produced by the fluid. For a range of supplied voltage magnitudes and frequencies, a range of feedbacks may be felt by the user.

Fabrication

Figure 2 shows the constructed components and assembly of the prototype actuator. The button-type actuator is comprised of two electrode PCBs, a plastic spacer and O-ring, a thin film silicone membrane and a plastic cover. The HV PCB was treated with a thin polyimide film to prevent arcing at high voltages. The electrode's inner and outer radii measure 7.5 and 11 mm, respectively. The internal volume of the actuator is filled with 1.8 mL of giant ER fluid, thus providing potential for greater yield stresses than conventional ER fluid. The maximum indentation depth or stroke of the actuator is 1 mm. The device was designed and manufactured with a goal of minimizing thickness to convey kinesthetic and tactile feedback in miniature applications. The size of the proposed actuator is significantly thinner than previous designs utilizing smart materials (Jansen et al., 2010a; Mazursky et al., 2018; Ryu et al., 2012; Xu et al., 2018). Additionally, the design is mechanically simple and easily controlled.

Results Obtained

Experimental Setup

To evaluate the performance of the fabricated haptic actuator, mechanical analysis was conducted using a dynamic mechanical analyzer (RSA3, TA Instruments), function generator and voltage amplifier, as shown in Figure 3. This experimentation precisely measured the total resistive force with respect to indentation depth over the device's 1 mm stroke. The performance was evaluated under different input voltage and frequency conditions using an indenter similar in size to a human finger. An indentation rate of 1 mm/s was used.

Kinesthetic Response

To test the actuator's ability to produce a range of stiffnesses, the actuator's resistive force was first measured in its off-state. Then, a high frequency square wave was applied between 0 V and peak amplitudes of 1, 2, 3 and 4 kV to emulate a pulsating DC signal. These results are presented in Figure 4. As evidenced in the figure, as the magnitude of the input voltage and pressed depth increase, the resistive force increases. The off-state resistive force was measured to be about 2.5 N at maximum depth. The maximum force produced was about 3.6 N under 4 kV load. While the force profiles formed by voltages up to 3 kV had similar curvature, the force curve produced under the 4 kV input included a steep increase and decrease in force during the 0.3-0.5 mm range of the stroke. This can be attributed to a build-up of pre-yield ER fluids in the activation region, followed by a rapid yielding event.

Tactile Response

To demonstrate a vibrotactile response, sinusoidal voltage inputs were applied between 0 V and peak amplitudes of 1, 2, 3, and 4 kV and at frequencies of 1, 3, 5, and 10 Hz. Figure 5 presents the resultant force profiles for each set of frequencies and voltages. As seen in the figure, the force feedback responds harmonically when subjected to sinusoidal voltages. As the magnitude of the applied voltage increases, the amplitude of vibration increases as well. These results show that the actuator can convey controllable resistive forces over a range of frequencies. Therefore, the actuator is capable of communicating vibrotactile feedback.

Significance of Results

This paper has presented the design, modeling and experimental evaluation of a novel design for a miniature haptic actuator based on the tunable yield stress of electrorheological fluids. The device was designed in flow mode to minimize actuator thickness and mechanical complexity. An analytical model for the actuator's force output was derived and implemented into a numerical simulation. A prototype actuator was fabricated and tested experimentally using a dynamic mechanical analyzer. The resistive force generated by the actuator along its stroke was measured for both kinesthetic and vibrotactile input voltage signals. The experimental results verified those produced by the model. The results indicated that the actuator's resistive force increases with increased indentation depth and applied voltage. Furthermore, the measured results demonstrate distinct force rates that may be perceived by humans as a range of kinesthetic sensations in application. The vibrotactile performance of the actuator showed significant improvement over previous iterations. Thus, the actuator was confirmed capable of conveying a range of haptic feedback sensations. Future work will include embedding a thin pressure sensor and feedback control to act as a haptic interface by rendering realistic sensations between a user and virtual environment.

Figures

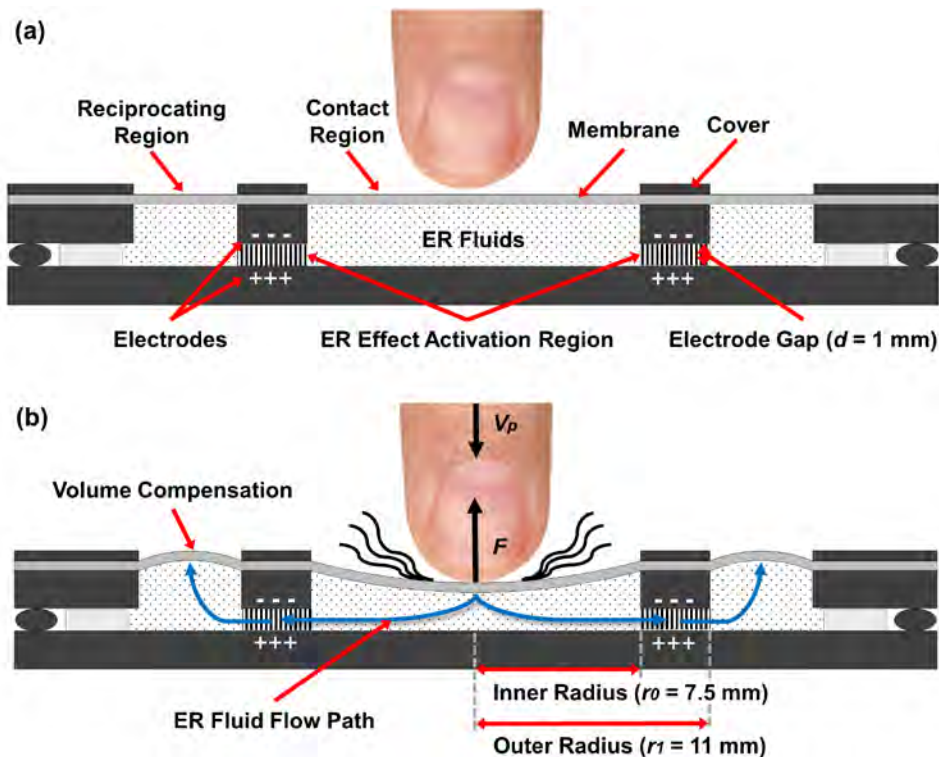


Figure 1. Working principle of the proposed haptic actuator (a) before contact and (b) mid-contact.

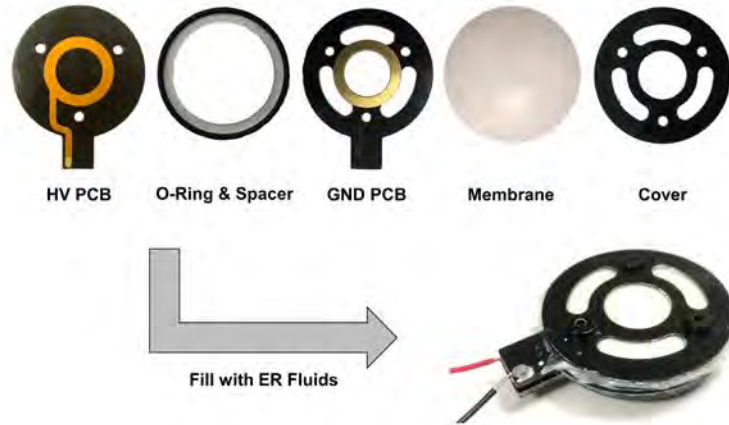


Figure 2. Construction and assembly of the prototype actuator.

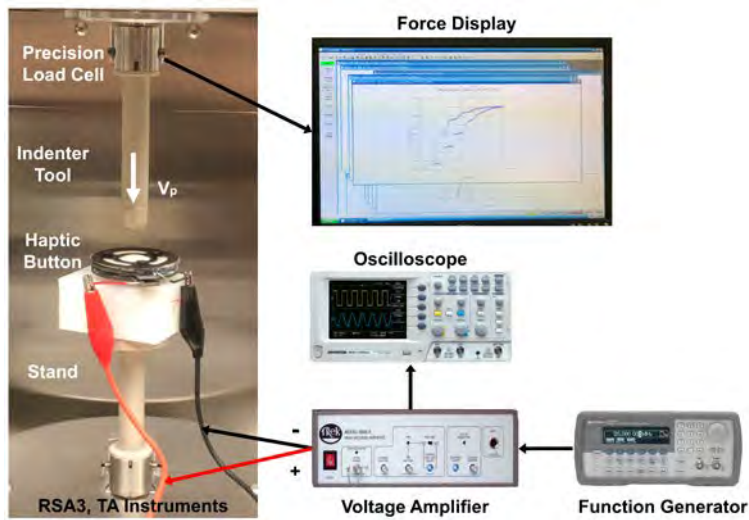


Figure 3. Experimental setup to measure the force generated by the prototype actuator with respect to indentation depth for applied voltage signals.

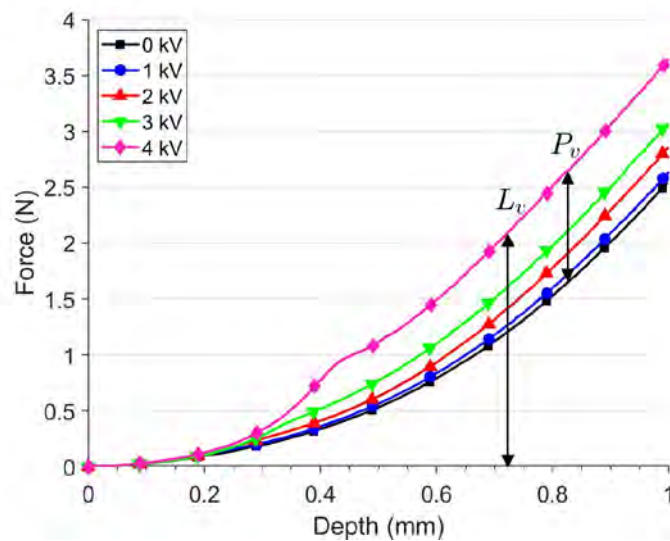


Figure 4. Results of the kinesthetic experimental measurement of the haptic actuator.

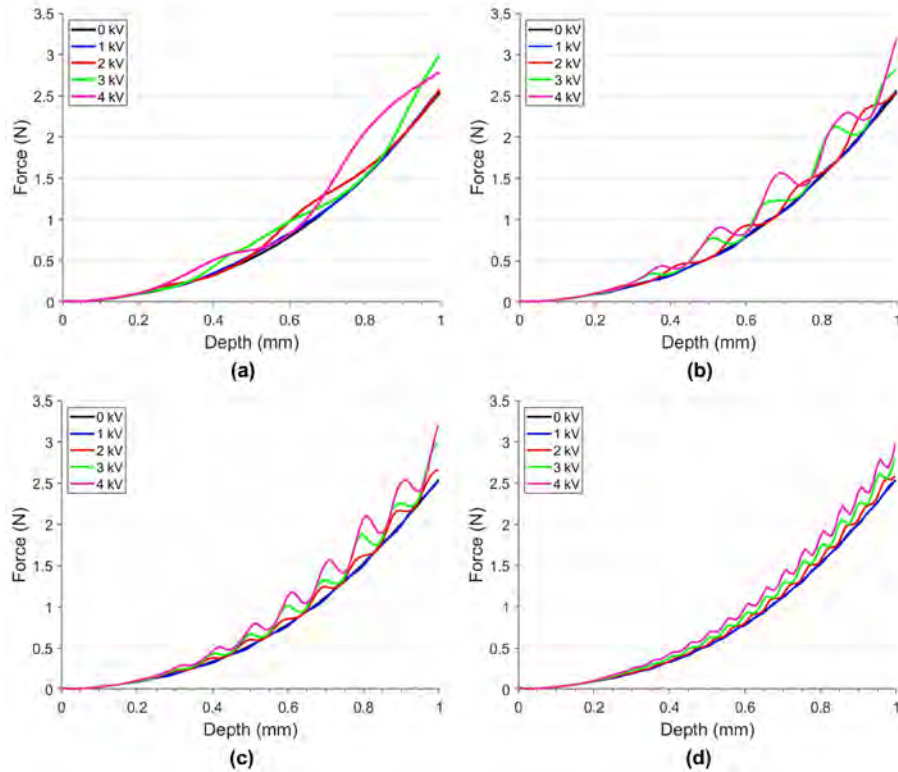


Figure 5. Results of the tactile experimental measurement of the proposed actuator subjected to sinusoidal inputs at (a) 1 Hz, (b) 3 Hz, (c) 5 Hz, and (d) 10 Hz.

Acknowledgments

Thank you to my advisor, Dr. Jeong-Hoi Koo, for his guidance. Thank you to the Ohio Space Grant Consortium for their continued support.

References

1. Adams RJ, Moreyra MR and Hannaford B (1998) Stability and Performance of Haptic Displays : Theory and Experiments. In: *Proceedings ASME International Mechanical Engineering Congress and Exhibition, Anaheim, 1998*, pp. 227–234.
2. An J and Kwon D-S (2002) Haptic Experimentation on a Hybrid Active/Passive Force Feedback Device. In: *Proceedings 2002 IEEE International Conference on Robotics and Automation, 2002*, pp. 4217–4222.
3. An J and Kwon D-S (2006) Stability and performance of haptic interfaces with active/passive actuators - Theory and experiments. *International Journal of Robotics Research* 25(11): 1121–1136.
4. Bianchi M, Scilingo EP, Serio A, et al. (2009) A new softness display based on bi-elastic fabric. In: *Proceedings of Third Joint Eurohaptics Conference and Symposium on Haptic Interfaces for Virtual Environment and Teleoperator Systems, 2009*, pp. 382–383.
5. Bullough WA, Johnson AR, Hosseini-Sianaki A, et al. (1993) The electro-rheological clutch: design, performance characteristics and operation. *Proceedings of the Institution of Mechanical Engineers, Part I: Journal of Systems and Control Engineering* 207(2): 87–95.
6. Choi SB, Cheong CC, Jung JM, et al. (1997) Position control of an er valve-cylinder system via neural network controller. *Mechatronics* 7(1): 37–52.
7. Coles TR, Meglan D and John NW (2011) The role of haptics in medical training simulators: A survey of the state of the art. *IEEE Transactions on Haptics* 4(1): 51–66.

8. Fujita K and Ohmori H (2001) A new softness display interface by dynamic fingertip contact area control. In: *Proceedings of the 5th World Multiconference on Systemics, Cybernetics and Informatics*, 2001, pp. 78–82.
9. Goto M and Takemura K (2013) Tactile bump display using electro-rheological fluid. In: *IEEE International Conference on Intelligent Robots and Systems*, 2013, pp. 4478–4483.
10. Jansen Y, Karrer T and Borchers J (2010a) MudPad : Tactile Feedback and Haptic Texture Overlay for Touch Surfaces. *Proc. of ACM Int. Conf. on ITS*: 11–14.
11. Jansen Y, Karrer T and Borchers J (2010b) MudPad: localized tactile feedback on touch surfaces. In: *Proceedings of the 23rd Annual ACM Symposium on User Interface Software and Technology*, 2010, pp. 385–386.
12. Kim S, Kim P, Park C-Y, et al. (2016) A new tactile device using magneto-rheological sponge cells for medical applications: Experimental investigation. *Sensors & Actuators A: Physical* 239: 61–69.
13. Mazursky AJ, Koo J-H and Yang T-H (2018) Experimental evaluation of a miniature haptic actuator based on electrorheological fluids. In: *SPIE Smart Structures and Nondestructive Evaluation*, Denver, CO, USA, 2018. SPIE.
14. Park J and Khatib O (2006) A haptic teleoperation approach based on contact force control. *International Journal of Robotics Research* 25(5–6): 575–591.
15. Pfeiffer C, Mavroidis C, Bar-Cohen Y, et al. (1999) Electrorheological Fluid Based Force Feedback Device. In: *Proceedings of the 1999 SPIE Telemanipulator and Telepresence Technologies VI*, 1999, pp. 88–99.
16. Ryu S, Yang TH, Kim SY, et al. (2012) Design of a New Miniature Haptic Button Based on Magneto-Rheological Fluids. In: *IEEE International Conference on Automation Science and Engineering*, 2012, pp. 1–4.
17. Ryu S, Koo J-H, Yang T-H, et al. (2015) Mechanical and psychophysical performance evaluation of a haptic actuator based on magnetorheological fluids. *Journal of Intelligent Material Systems and Structures* 27(14): 1967–1975.
18. Song A, Morris D and Colgate JE (2005) Haptic telemanipulation of soft environment without direct force feedback. In: *Proceedings of the 2005 IEEE International Conference on Information Acquisition*, 2005, pp. 21–25.
19. Srinivasan MA and Basdogan C (1997) Haptics in virtual environments: Taxonomy, research status, and challenges. *Computers & Graphics* 21(4): 393–404.
20. Taylor PM, Hosseini-Sianaki A and Varley CJ (1996) An electrorheological fluid-based tactile array for virtual environments. In: *Proceedings of 1996 IEEE International Conference on Robotics and Automation*, 1996, pp. 18–23.
21. Tsujita T, Kobayashi M and Nakano M (2010) Design and development of a braille display using micro actuators driven by ER suspension. *International Journal of Applied Electromagnetics and Mechanics* 33(3–4): 1661–1669.
22. Wen W, Huang X, Yang S, et al. (2003) The giant electrorheological effect in suspensions of nanoparticles. *Nature Materials* 2. Nature Publishing Group: 727–730.
23. Whittle M, Atkin RJ and Bullough WA (1996) Dynamics of an Electrorheological Valve. *International Journal of Modern Physics B* 10(23–24): 2933–2950.
24. Xu L, Li Y, Han L, et al. (2018) A test of giant electrorheological valve in DC and square wave AC fields with different frequencies. *Journal of Intelligent Material Systems and Structures* 29(2): 250–254.
25. Yang T-H, Kwon H-J, Lee SS, et al. (2010) Development of a miniature tunable stiffness display using MR fluids for haptic application. *Sensors and Actuators A: Physical* 163(1). Elsevier B.V.: 180–190.
26. Yang TH, Koo JH, Kim SY, et al. (2017) Modeling and test of a kinaesthetic actuator based on MR fluid for haptic applications. *Review of Scientific Instruments* 88(3).

FTY720 Fails to Increase Protein Phosphatase 2A Activity in a *Caenorhabditis elegans* Model of Tauopathy

Student Researcher: Garrett S. McCue

Advisor: Dr. Jeff Zahratka

Baldwin Wallace University
Neuroscience and Biology Department

Abstract

Protein phosphatase 2A (PP2A) is a serine/threonine phosphatase which acts to regulate signaling pathways through its dephosphorylating enzymatic activity. Inactivation of PP2A is prevalent in Alzheimer's disease (AD) and results in aggregation of hyperphosphorylated tau. Fingolimod (FTY720), typically used to treat multiple sclerosis, has been found to restore PP2A activity and lead to cancer cell death. FTY720 was used to test its therapeutic effects on PP2A activity with aims to increase the life span of a human tau (BR5270) strain of *Caenorhabditis elegans*. It was found that FTY720 does not significantly increase the life span of BR5270 worms because it is hypothesized that the primary target of FTY720, SET, is not conserved in the *C. elegans* model.

Project Objectives

Neurodegenerative diseases, specifically Alzheimer's disease (AD), are characterized by brain volume reduction and neuronal death resulting in impaired neurological functioning. The mechanisms of AD onset and other neurodegenerative diseases are primarily a mystery, but speculation and recent insights have led to the identification of multiple key factors. One of these factors being neurofibrillary tangles (NFTs). The onset of AD is correlated with the increasing accumulation of NFTs. The presence of NFTs are the result of tau protein aggregation stemming from the excessive hyperphosphorylation of tau ^[3].

Protein phosphatase 2A (PP2A) is a serine/threonine phosphatase which acts to regulate signaling pathways through its dephosphorylating enzymatic activity ^[4]. The inactivation of PP2A is prevalent in many diseases such as AD, and this inactivation results in an increase in protein phosphorylation leading to the aggregation of tau and formation of NFTs ^[6]. In conjunction with the decreased activity of PP2A, there is an increase in endogenous PP2A inhibitors ^[6]. The PP2A inhibitors, CIP2A and SET, act to prevent the dephosphorylation that is mediated through PP2A inactivation. This antagonistic relationship between SET/CIP2A and PP2A is a target for the potential increase in PP2A activation. Pre-clinical cancer trials targeting the activation of PP2A using FTY720 (Fingolimod) to inhibit SET activity, have shown promising results which include an increase in PP2A activity and cancer cell death ^[6].

FTY720 is a sphingosine analogue that is FDA approved, and is currently being used for its immunosuppressive effects to treat multiple sclerosis. The immunosuppressive effects of FTY720 stem from its phosphorylation resulting in the active immunosuppressive compound FTY720-phosphate. This compound then binds to sphingosine phosphate receptors (S1P1) allowing for their degradation and internalization of the receptors ^[6]. In the FTY720 cancer trials, it was noted that the phosphorylation of FTY720, in order to make the active immunosuppressive compound, was not necessary in restoring PP2A function and inducing cancer cell death ^[6]. Success with FTY720 in cancer trials, in attempt to disrupt SET/PP2A interaction, has shown its effectiveness in restoring PP2A activity and opens the door to explore the use of FTY720 within other diseases that are characterized by PP2A inactivation. The main

goal of this experiment was to assess the hypothesized therapeutic effects of FTY720 on PP2A activity in a *C. elegans* model of tauopathy.

Methodology

In order to quantify the therapeutic effects of FTY720 within AD there needed to be a comparison between the effects of FTY720 on both AD and cognitively normal individuals which were modeled by *C. elegans*. The model used for AD was the tau mutant BR5270^[7] which is characterized by the overexpression of human tau in all neurons, and the model for the neurotypical group was the *C. elegans* wild type, N2. This model organism was chosen due to the absence of known S1P1 expression within the *C. elegans* genome. This is important to note because it would act to minimize the off-target effects that could occur from FTY720 interacting with the S1P1 receptor as seen during its effective treatment for multiple sclerosis. The FTY720 concentration of 100pM was used as it was found to be the optimal dosage by Miron *et al.* 2010. The use of H₂O as the vehicle and the storage temperature of -20°C were used for FTY720 as suggested by Sigma-Aldrich[®].

Strains were maintained on standard nematode growth media (NGM) plates at 20°C seeded with OP50 *E. coli* bacteria according to standard protocols^[2].

In order to analyze the therapeutic effects of FTY720, the worms were age matched through an axenization protocol. Four days after the axenization protocol the worms were split into four groups, N2 untreated, N2 treated with FTY720, BR5270 untreated, and BR5270 treated with FTY720. The groups each had 4 plates and 5 animals on each plate making it 20 animals per group in each trial. The first treatment was done after the completion of group assignments and the treatments continued every 48 hours until all subjects were dead. During treatments the worms were transferred from the NGM with *E. coli* onto a sterile NGM dish to eliminate possible interactions of FTY720 with the bacteria. Before the worms were transferred, 100µL of 100pM FTY720 or vehicle was micropipetted onto the sterile agar plate. The worms were then transferred into either the vehicle or FTY720 solution, with a platinum wire worm pick, and were left for 30 minutes before they were picked onto a new agar plate with bacteria. This was repeated every 48 hours in attempt to mimic the administration of a prescription, and it ended when the last subject died. This protocol was completed twice, once for each of the trials.

Prior to the start of each administration the number of subjects on each plate was recorded along with the number of dead and censored subjects. Subjects were classified as censored if they were missing or were killed during drug administration by the researcher and therefore would not accurately represent FTY720 effects.

Data analysis was completed using the Mantel-Cox test within GraphPad Prism to compare the survival curves of the four groups and is reported in aggregate. The family-wise error rate was corrected for by using the false discovery rate^[1]. The significance of group comparisons was observed with a false discovery rate (FDR)-adjusted $p < 0.05$.

Results Obtained

The number of subjects was censored first to calculate the number of eligible individuals per group. The N2 untreated group had a final number of 24 worms, and the N2 [100pM] group had 27 worms. The final number for the BR5270 untreated group was 29 and 32 for the BR5270 [100pM] group. The survival curve comparison of N2 untreated and N2 [100pM] had a shared median survival rate of 12 days with an adjusted p value of 0.1452 deeming it not significant (Figure 1a). The survival curve in Figure 1b compares the BR5270 untreated group with the BR5270 [100pM] group and proves it not significant ($p =$

0.862) with the median survival rate being 8 days each. There was significance found between both the N2 untreated and BR5270 untreated group ($p = 0.0008$) as well as between the N2 [100pM] and BR5270 [100pM] groups ($p = 0.0234$) (Figure 2).

The significance between both [100pM] treated groups and both untreated groups is seen as expected, because the BR5270 mutant animals naturally die on average 4 days before the N2 animals. The insignificance found between the untreated and [100pM] treated groups of both N2 and BR5270 strains (Figure 1a-b) does not support the hypothesis and leads to the conclusion that FTY720 does not have any significant effects on altering the life span of either group. It can be concluded further that FTY720 was not successful in tau dephosphorylation by modulating PP2A activity through the inhibition of SET. One conclusion being hypothesized for why FTY720 had no effect on life span is the possibility that the SET pathway is not conserved in the model organism, *C. elegans*. Further research is being completed and it targets the other endogenous inhibitor of PP2A, CIP2A. O’connor *et al.* 2018, demonstrated ceramide’s effectiveness to inhibit CIP2A and SET resulting in the activation of PP2A and thus increasing its phosphatase activity. The *C. elegans* ortholog for CIP2A, B0432.7a.1, was found from a BLAST search of mammalian CIP2A against the *C. elegans* genome. In attempt to increase PP2A phosphatase activity the knockdown of CIP2A through RNA interference is being hypothesized to be a possible solution.

Figures

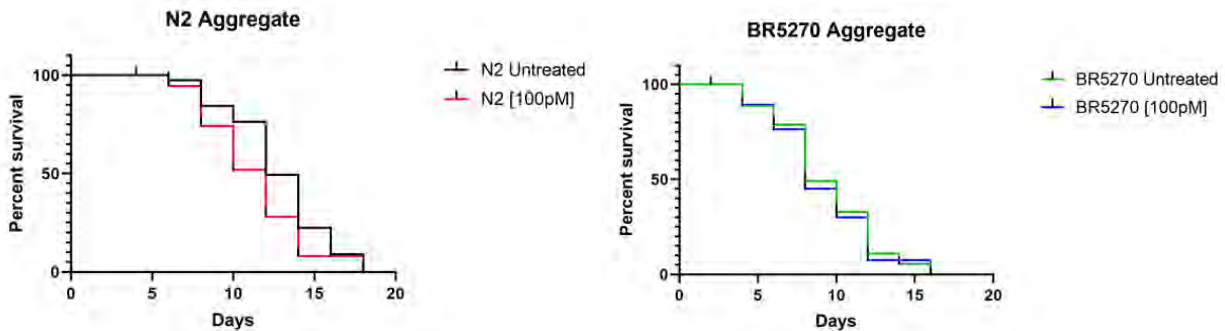


Figure 1. Survival Curves of N2 Aggregate and BR5270 Aggregate (a) Survival curve comparison of the N2 untreated and the N2 [100pM] treated group from both trials. (b) The survival curve comparison of the BR5270 [100pM] and BR5270 untreated groups from both trials.

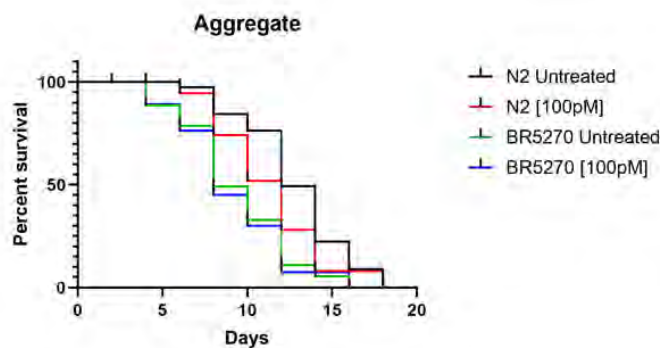


Figure 2. Combined Survival Curves of N2 and BR5270. Survival curve comparing N2 untreated, N2 [100pM], BR5270 untreated, and BR5270 [100pM] from both trials.

Acknowledgments

The author of this paper would like to thank Baldwin Wallace University for supplying the equipment and materials to conduct this research. The author would also like to thank Dr. Jeff Zahratka for the guidance and mentorship during this research.

References

1. Benjamini, Y., & Hochberg, Y. (1995). Controlling the False Discovery Rate: A Practical and Powerful Approach to Multiple Testing. *Journal of the Royal Statistical Society: Series B (Methodological)*, 57(1), 289-300. doi:10.1111/j.2517-6161.1995.tb02031.x.
2. Brenner S. (1974). The genetics of *Caenorhabditis elegans*. *Genetics*, 77(1), 71–94.
3. Fatouros, C., Pir, G. J., Biernat, J., Koushika, S. P., Mandelkow, E., Mandelkow, E., Baumeister, R. (2012). Inhibition of tau aggregation in a novel *Caenorhabditis elegans* model of tauopathy mitigates proteotoxicity. *Human Molecular Genetics*, 21(16), 3587-3603. doi:10.1093/hmg/dds190.
4. Liu, C., Huang, T., Chen, Y., Chen, J., Chu, P., Huang, C., Tseng, L. (2019). Targeting SET to restore PP2A activity disrupts an oncogenic CIP2A-feedforward loop and impairs triple negative breast cancer progression. *EBioMedicine*, 40, 263-275. doi:10.1016/j.ebiom.2018.12.032.
5. Miron, V. E., Ludwin, S. K., Darlington, P. J., Jarjour, A. A., Soliven, B., Kennedy, T. E., & Antel, J. P. (2010). Fingolimod (FTY720) Enhances Remyelination Following Demyelination of Organotypic Cerebellar Slices. *The American Journal of Pathology*, 176(6), 2682-2694. doi:10.2353/ajpath.2010.091234.
6. O'Connor, C. M., Perl, A., Leonard, D., Sangodkar, J., Narla, G. (2018). Therapeutic targeting of PP2A. *Int. J. Biochem. Cell Biol.*, 96 (2018), pp. 182-193.
7. Wang, C., Saar, V., Leung, K. L., Chen, L., & Wong, G. (2018). Human amyloid β peptide and tau co-expression impairs behavior and causes specific gene expression changes in *Caenorhabditis elegans*. *Neurobiology of Disease*, 109, 88-101. doi:10.1016/j.nbd.2017.10.003.

What's the Weather?

Student Researcher: Nya A. McMullen

Advisor: Dr. Rajeev Swami

Central State University
Department of Education

Abstract

This lesson will use data collected by NASA to compare snow and ice over the span of three years. From the data students collect, they will be plotting and analyzing it. They will access their data from the MY NASA DATA Live Access Server. They will need to collect monthly averages for three different years in a city of their choice, compile the data in a spreadsheet, and make a line graph for each year. Students will also create a difference plot to compare and contrast the yearly data. The objective of my lesson is that students will be able to understand how calculations can be performed on data expressed as maps, such as averaging or subtracting. With this data, students will be able to recognize trends and they can start hypothesizing different factors that change the snow and ice levels. Also, students will work in teams and prepare a presentation that they could present to environmental policy makers in regard to global climate change.

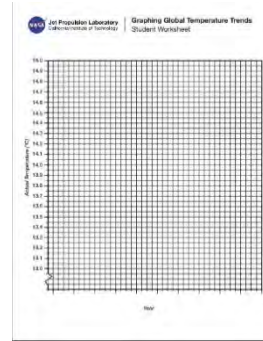
Lesson

The basis of this activity rose from the Common Core Standard which would be: Graphing points on the coordinate plane to solve real-world and mathematical problems. Students will be placed in groups and nobody in the group can pick the same state capital. Collaborative working will allow students to chat and learn through socialization, rather than just learning through the teacher.

The first thing we would do as a class is make sure each student was on the same page of what climate is and how to collect data from the NASA website. Before looking up data they have to hypothesis which of the winter months (December-February) in the three years will the colder temperature. Once students established their hypothesis, students will then pick their state of choice and collect monthly temperature averages for a two-year span of time. Then using an Excel Spreadsheet or Google Spreadsheet they can chart down the averages for each month using a line. For those students who want to just create a graph by hand I will pass out the "Graphing Global Temperature Trends" graphing paper. Once every student is done plotting their point, they must discuss among their group what are some factor that could affect climate changes between the years. Then students will work in their teams and prepare a short presentation that they could present to environmental policy makers in regard to global climate change.

Resources

- Graphing paper
- Laptop/iPad
- Writing Utensil
- Color marker
- NASA DATA Live Access Serve
- Graphing Global Temperature Trends paper



Objectives

- Students will be able to compare the data on a graph
- Students will be able to understand graphing and recognize trends
- Students will understand the role of climate change

Alignment

Grade five Common Core Standards: Graphing points on the coordinate plane to solve real-world and mathematical problems.

Methodology Used

This lesson is using Lev Vygotsky and Social Theories. He suggested that learning takes place through the interaction's students have with their peers, teachers, and other experts. Consequently, I am creating a learning environment that maximizes the learner's ability to interact with each other through discussion, collaboration, and feedback from me and other peers.

Results

Students will begin to learn that even though the climates of some states are increasing at extremely low rates, it can still be harmful to the world. Also, students that dislike math tend to ignore the math they had to do because they working with peers and could receive help from others at ease.

Assessment

I would do an informal assessment of my students. As student were working on the project and collaboration, I was walking around making sure they were staying on task and helping when need be.

Conclusion

This project allows students to work together and research information that allowed them to understand create a statistical chart and be able to understand the information. Also, it helped students understand the importance of climate change and the negative effects of it.

Quantifying Defects from High Throughput Continuous Production of Graphene

Student Researcher: Derek K. Messer

Advisor: Dr. Reza Rizvi

The University of Toledo

Department of Mechanical, Industrial and Manufacturing Engineering

Abstract

Over the past decade, various methods such as liquid phase shear exfoliation have been looked at to develop graphene based two-dimensional (2D) materials to harness their excellent and unprecedented properties. However, these methods can be very time consuming and introduce significant amount of defects. We developed a new exfoliation method called compressible flow exfoliation (CFE) in which 2D layered materials are rapidly jettisoned through a small orifice using high-pressure gases without the need for any time-based treatment. Other advantages include environmentally friendly processing, reduced occurrence of defects along with the ability to be applied to any 2D layered material using any gaseous medium. Our study is designed to compare the flake quality between CFE and the previously investigated processes like sonication.

The new fast and continuous process could broaden the applications for graphene if it is being produced with less defects. This zero-bandgap material is strong, lightweight, flexible, and transparent. Therefore, CFE produced graphene could be used in many applications like conductive ink for flexible electronics.

Project Objectives

At these early stages of development, very little is known about the structure and quality of the 2D nanomaterials after they have been through this process. The quality can be characterized by the length and thickness of the 2D nanomaterials after CFE processing and to compare them to the state-of-the-art top-down method of liquid phase exfoliation (LPE). Liquid phase exfoliation utilizes ultrasound wave energy to break-down 2D layered materials into thin sheets, however significant reductions in length are also observed. The hypothesis of this project is that because of its low residence time, CFE is a milder technique than LPE, and thus results in particles that, for the same thickness, are larger in length than LPE. The understanding of defect and disorder of graphene structures is crucial to find out how it effects their properties for various potential applications. Therefore, the objective is to compare the defect and flake quality between CFE and bath/probe sonication process for producing high-performance conductive ink, electronic devices, etc. from exfoliated graphene.

Methodology

Quality of the 2D nanomaterials could be calculated from the flake length, thickness and chemical defects. In our CFE process, 2D layered materials are rapidly jettisoned through a small orifice using high-pressure gases without the need for any time-based treatment, unlike other shear-based and gas processes. Shear-based exfoliation occurs due to the high velocities that expanding and accelerating gases can achieve in small orifices coupled with viscous friction effects resulting in a high shear rate ($\gamma > 10^5 \text{ s}^{-1}$) experienced by the 2D layered particles. A schematic of this is shown in figure 1. In contrast, in the sonication methods, an ultrasonic transducer is used to induce unstable cavitation bubbles in a liquid medium, which upon their inevitable collapse emanate a shock wave. The energy of this shockwave is enough to fragment nearby bulk 2D layered powders into smaller lengths as well as thickness along the weak, secondary c-axis. But when the bulk particle is fragmented into smaller flakes, a good number of edge and basal plane defect is being introduced into the flakes.

The material of choice will be graphene, a synthetic 2D material that is electrically insulating yet thermally conductive. First, graphene 2D nanomaterials will be synthesized using the optimized processing conditions for CFE. The main processing conditions in CFE include, gas type, gas pressure and nozzle size. These conditions have been previously optimized to provide the highest product yield (% process efficiency) and so they may be far from being optimized for product quality. Two or three other process parameter combinations will be chosen to get a broader representation of CFE 2D nanomaterials. Size separation will be done using high-speed centrifuging as described by Backes et al., (2016). Next, graphene 2D nanomaterials will be synthesized using LPE as per optimized conditions detailed elsewhere by Xie et al., (2015). These samples will serve as the benchmark for assessing the particle quality - length and thickness – during the CFE process. As before, two or three other process parameter combinations will be chosen to get a broader representation.

Many tools will be utilized to help characterize the 2D nanomaterial length and thickness of the CFE and LPE prepared samples. The primary means for characterizing the length and thickness will be atomic force microscopy (AFM) for which a large statistically significant dataset can be obtained. Secondary means for characterizing the length and thickness will be transmission electron microscopy (TEM) which is useful for fast imaging of flake length, and Raman spectroscopy, which is sensitive to the layer numbers (thickness) of the particles. If the project hypothesis is true, then significant differences in particle length and thinness should be observable in the favor of CFE.

Raman spectroscopy can be used to quantify the defects by measuring the D to G peak intensity ratio. The D peak is located at 1350 cm^{-1} and is associated with the nanocrystalline carbon. On the other hand, the G peak is found at 1590 cm^{-1} and associates with amorphous carbon materials that are still sp^2 bonded. Also, the G peak corresponds to the E_{2g} phonon at the Brillouin zone center whereas the D peak is caused by the breathing modes of six-atom rings and requires a defect for its activation as noted by Cançado et al., (2011). Both of the peaks are the result of vibrations of the sp^2 -bonded carbon atoms, but the G peak is the result of in-plane vibrations while the D peak is due to out of plane vibrations. Therefore, the $I(D)/I(G)$ ratio relates to the sp^3/sp^2 ratio. This ratio correlates to the amount of defects present in the material.

Results

The defect arises as the time for sonication increases. Raman spectroscopy is a strong tool to study the defects. Such defects can be interpreted to be either creation of new edges, vacancies or substitutions, with the ratio between the peaks intensities of the D to G peak ($I(D)/I(G)$) providing some limited indication of their population. In our study, we found the ratio of D peak to G peak is significantly less in CFE than that of bath sonicated graphene ($I(D)/I(G)=0.45$ for CFE graphene and $I(D)/I(G)=0.81$ for bath sonicated graphene). The bulk graphite powder had $I(D)/I(G)$ ratio of 0.36 as shown in table 1. Also, the $I(2D)/I(G)$ ratio from our CFE process is 0.46 which is higher than that from the LPE process (0.39). This indicated the quality of graphene obtained from CFE method is better than LPE method. The increased number of the defect in bath sonication may be attributed to the prolonged sonication time which is responsible for new edge creation. The flake quality of exfoliated graphene is also investigated using atomic force microscope (AFM) and transmission electron microscope (TEM).

The TEM was used to determine if the exfoliated graphene were present as sheets or multi-layered platelets. The thickness is observed using extensive high-resolution phase-contrasting imaging which showed exfoliation was successful with only few layers. In other words, the graphene sheets are determined to be thin because of the transparency in the flake images.

Future Work

Applications for the graphene produced by CFE are being looked at. The fast and continuous process is a good first step toward the manufacturability of graphene or even other materials. Graphene is stronger than steel, yet it is strong and flexible. It is also thermally conductive while being transparent. This makes it advantageous for electrical applications like transistors, semiconductors, or conductive ink. Other applications currently being researched consist of biomedical, composites, energy and sensors.

Figures and Tables

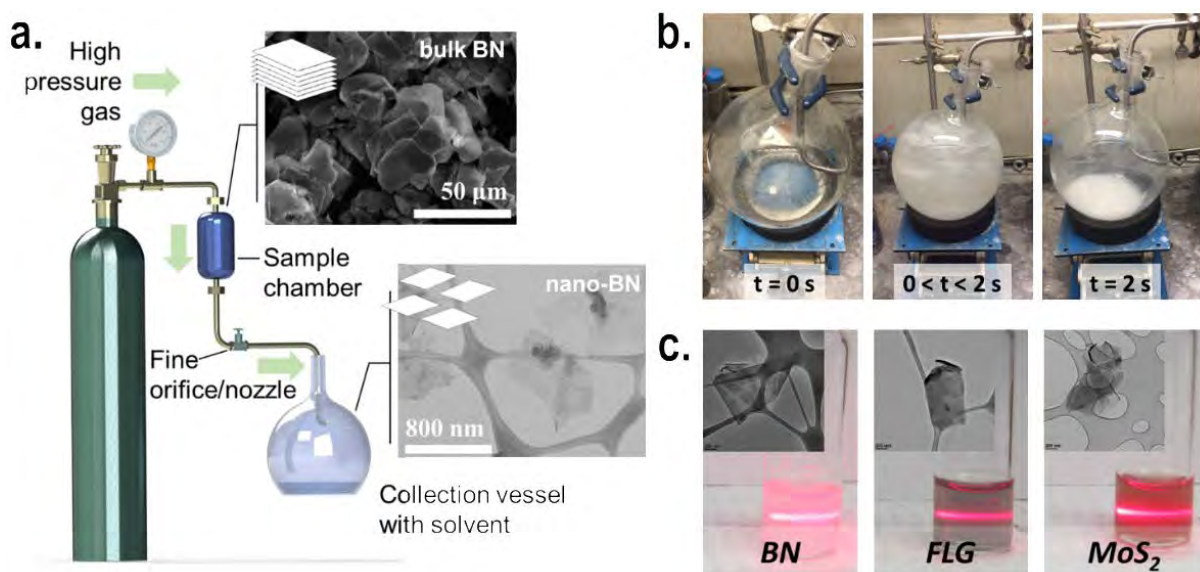


Figure 1. (a) Process schematic of the compressible flow exfoliation setup including a description of the critical components and the initial and final structures of the BN powder. (b) Still images of the collection vessel before, during and after the CFE process for BN powder. (c) Exfoliated suspensions of various 2D layered nano-materials after centrifugation.[1]

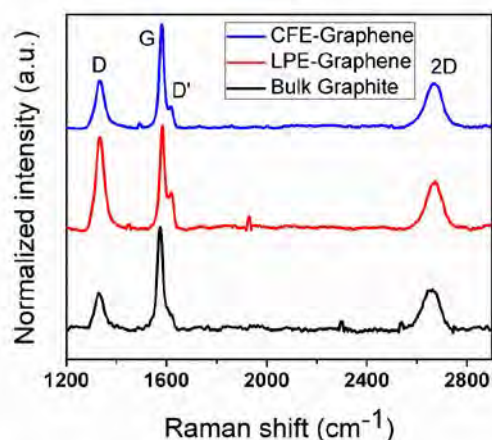


Figure 2. Raman spectroscopy of graphite and graphene processed by LPE and CFE.

Table 1. Defect Ratios.

	ID/IG	I2D/IG
Pristine Graphite	0.36 ± 0.04	0.34 ± 0.03
CFE -Graphene	0.45 ± 0.04	0.46 ± 0.12
LPE-Graphene	0.81 ± 0.09	0.39 ± 0.03

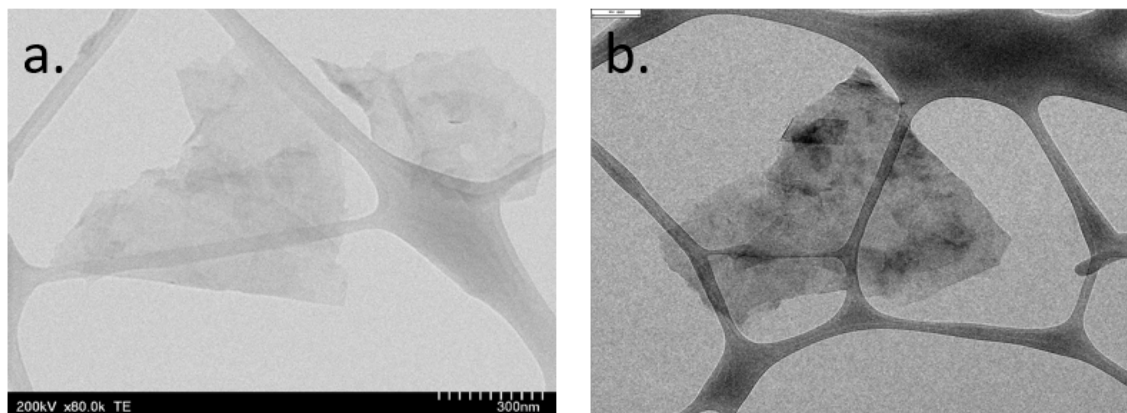


Figure 3. TEM analysis of graphene flakes processed by (a) CFE and (b) LPE.

Acknowledgments

The author would like to acknowledge Dr. Reza Rizvi for serving as the advisor on this project, Dr. Sheik Rasel, for serving as a postdoc in the lab, and Md Akibul Islam for providing guidance as a graduate researcher. Also, special thanks the Ohio Space Grant Consortium along with Dr. Lesley Berhan, the Campus Representative at The University of Toledo.

References

1. Reza, R.; Nguyen, E. P.; Kowal, M. D.; Mak, W. H.; Rasel, S.; Islam, M. A.; Abdelaal, A.; Joshi, A. S.; Zekriar dehani, S.; Coleman, M. R.; Kaneret, R. B. High-Throughput Continuous Production of Shear-Exfoliated 2D Layered Materials Using Compressible Flows. *Advanced Materials* **2018**, *30*, 1800200.
2. Backes, C.; Higgins, T. M.; Kelly, A.; Boland, C.; Harvey, A.; Hanlon, D.; Coleman, J. N., Guidelines for exfoliation, characterization and processing of layered materials produced by liquid exfoliation. *Chemistry of Materials* **2016**, *29* (1), 243-255.
3. Xie, S.; Istrate, O. M.; May, P.; Barwich, S.; Bell, A. P.; Khan, U.; Coleman, J. N., Boron nitride nanosheets as barrier enhancing fillers in melt processed composites. *Nanoscale* **2015**, *7* (10), 4443-4450.
4. Cançado, L. G.; Jorio, A.; Martins Ferreira, E. H.; Stavale, F.; Achete, C. A.; Capaz, R. B.; Moutinho, M. V. O.; Lombardo, A.; Kulmalall, T. S.; Ferrari, A. C. Quantifying Defects in Graphene via Raman Spectroscopy at Different Excitation. *Energies Nano Lett.*, **2011**, *11* (8), pp 3190–3196.

Development of a Sensor Frame Harness Gait Assessment Device for Occupational Health in Nursing

Student Researcher: Amanda M. Miller

Advisors: Manish Kumar, Tamara Lorenz

University of Cincinnati

Department of Mechanical and Materials Engineering

Abstract

Every year, people in physically strenuous fields such as nursing are at risk of work-related injury due to unhealthy, unsafe, and repetitive movements, such as lifting and moving heavy objects. To reduce this risk, we present a novel approach to collecting movement data by applying an Unscented Kalman Filter to the data online data collection from seven inertial measurement units (IMU) located above and below the ankle, knee, and hip joints, allowing the estimation of joint angles. The data from the IMU's are read by an Arduino and is then transmitted to a Raspberry pi, which filters the incoming data. Once the recording is complete, the data is printed to csv files. Points along the user's body will be calculated using the Denavit-Hartenberg method. The current data results represent a proof-of-concept study.

Statement of the Problem

As more baby boomers reach the ages of 70s and 80s, they are placing greater demand on the nursing home industry since they require more care[1]. This large increase in the older population will put more of a strain on the nurses taking care of them since there will be more people to take care of. This extra strain puts the nurses at a higher risk of injury, including such risks as improper posture, stooping, and patient transfers. The incident rate of work related musculoskeletal disorders in nursing and related fields is 249 of 10,000 workers[2].

Background

There are currently many different devices that are used to track and process the user's movements. These devices have two main ways of differentiating them, namely whether or not the sensors are located physically on the body or in their external environment.

The Nadi X Smart Yoga Pants are a new smart yoga pants that is available to any yoga enthusiast. The leggings has integrated sensors in the leggings as well as haptic feedback that can assist the user into obtaining the correct yoga position[3]. This system incorporates a rechargeable, detachable battery to the leggings that allow for the leggings to be machine washable. The pulse battery connects to your smart phone. Unfortunately, the Nadi X fails to offer access to the raw data and is only designed for monitoring specific yoga positions, making it of limited usefulness to our subject area. This is not desirable since no information can be extracted from the suite.

Gravina *et al.* goes into the intricacies of fusing Body Sensor Networks (BSNs) and how multiple sensors are needed at specific locations to acquire the desired data and information[4]. This idea is utilized in this paper since each of the Inertial Measurement Units (IMUs) that are used have three on-board sensors (accelerometer, magnetometer, and gyroscope) and they are fused together to obtain the overall rotation of the IMU.

Project Objectives

The goal of this project is divided into three main objectives. These objectives are the construction and fabrication of a lower limb wearable sensor frame, developing an algorithm for derivation for position of the joint angle transformation, and finally an algorithm for computing the center of mass throughout each movement.

Methodology

An initial sensor frame was created using seven IMUS, located on the foot, calf, thigh and lower body. This allows for each of the joint angles for the ankle knees and hips. Two microcontrollers are used to calculate each of the joint angles as well as filter the data since IMUs tend to have large amounts of noise. The Unscented Kalman filter (UKF) is chosen for filtering it since it has quick convergence to the solution, as well as having predictive capabilities. With this initial system, initial data was collected to test it was well as allowing the post processing of the data to be fine-tuned to allow for quick processing. This post processing uses the Denavit-Hartenberg to find the location of each of the joints. Then with each of the joint locations, the center of mass is calculated. Next, the system is enhanced by having each of the sensors to be housed in a 3D printed case and a custom case to be made for the Arduino and multiplexer, to reduce fatigue on the wires. Next, the system is verified with a motion capture system. Once the validation is complete, then the system is tested with three different movements; sit-to-stand, lifting an object, and walking.

Table 1. Denavit-Hartenberg Variables.

Denavit-Hartenberg Symbols for lower body				
Link	a	α	d	θ
Foot	l_{foot}	0	0	0
Calf	l_{calf}	0	0	θ_{ankle}
Thigh	l_{thigh}	0	0	θ_{knee}
Center Back	l_{back}	$\alpha_{spine\ twist}$	$w_{centerback}$	θ_{hip}

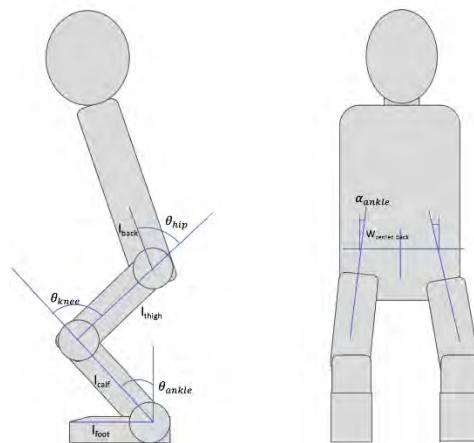


Figure 1. Denavit-Hartenberg Diagram.

Results

Figure 2 is the plot of the ankle, knee and hip angles over time during the sit-to-stand transition. First, the user is in a standing position, and then goes to a sitting position, and then stands back up. This method is repeated, so that it is observed that in the green line the knee angle changes from roughly 0 degrees to 60 degrees.

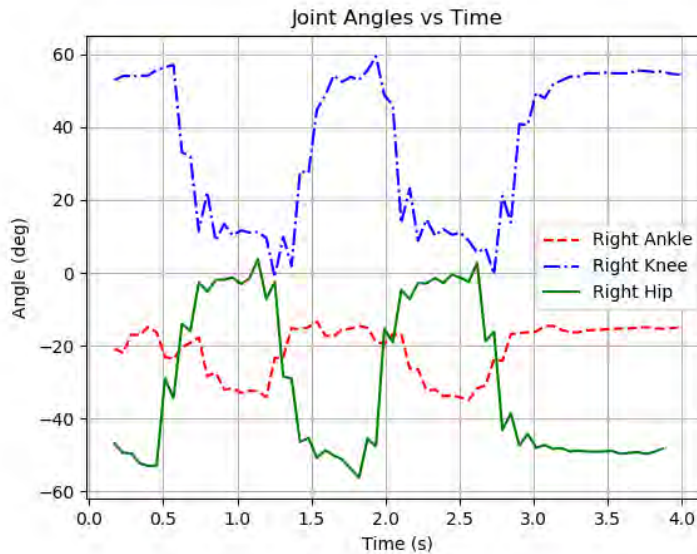


Figure 2. Joint Angles during sit-to-stand transition.

Figure 3 shows the locations of the ankle, knee and hip joints of the user during the sit-to-stand transition. It is seen that initially the user is in a seated position, and that as they stood up, their knee shifts forward during the transition, and once they have almost stood up, they shift back to a more neutral, vertical position. The red line illustrates the center of mass of the user during the sit-to-stand transition.

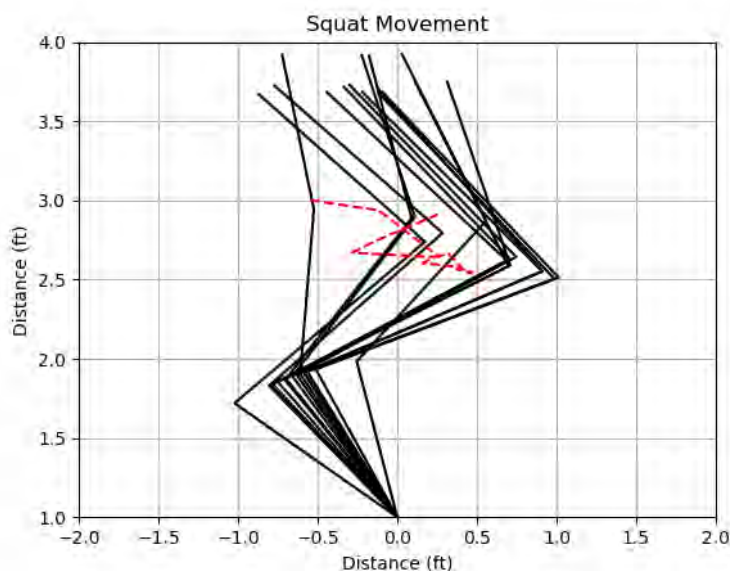


Figure 3. Location of joints during sit-to-stand transition and COM.

Significant and Interpretation of Results

For the sit-to-stand transition test, it is seen that the system is able to observe that the user is able to stand up and sit down twice in Figure 2. This is seen by the Knee angle changing from 60 degrees to roughly zero degrees and back, this is also confirmed with similar trends in the hip and ankle angles, where there are large changes during the same time of movements as the knee. The sensor system does not measure the exact angles of the joints, this is due to the minor shifting of the IMUs on the user.

Figure 3 illustrates the position of the upper body of the user during the sit-to-stand transition of the right leg. It can be seen that it initializes with the user's torso moving forward, and then the body is lifted with the knee, and then the overall posture straitens up. At the end, it is seen that there are some minor errors with the ankle joint angle, which is due to how the sensors are not directly in line with each of the bones of the user, but rather are shifted outward due to the body composition and clothing. Figure 3 also illustrates the tracking of location of the center-of-mas during the sit to stand transition with each step.

Overall, this system is a success in providing a low-cost method for studying the movements and postures of the user for occupational health, since this device is capable of measuring and recording the movement and is able to recognize the different components that make up a specific movement. However, this system does still have noise affecting it, even with the UKF due to the foot strike of the ground. This system presents a strong foundation for future research in gait analysis in occupational health.

Acknowledgments

This research was supported by the National Institute for Occupational Safety and Health through the Pilot Research Project Training Program of the University of Cincinnati Education and Research Center Grant \#T42OH008432.

References

1. B. E. Maki and W. E. Mcilroy, "Control of rapid limb movements for balance recovery: age-related changes and implications for fall prevention*," *Age Ageing*, pp. 12–18, 2006.
2. "Safety and Health Topics | Nursing Homes and Personal Care Facilities | Occupational Safety and Health Administration." [Online]. Available: <https://www.osha.gov/SLTC/nursinghome/>. [Accessed: 03-Mar-2019].
3. "How It Works - Wearable Tech Company | Wearable X." [Online]. Available: <https://www.wearablex.com/pages/how-it-works>. [Accessed: 27-Aug-2018].
4. R. Gravina, P. Alinia, H. Ghasemzadeh, and G. Fortino, "Multi-sensor fusion in body sensor networks: State-of-the-art and research challenges," *Inf. Fusion*, vol. 35, pp. 68–80, May 2017.

Hyaluronan Drug Delivery Systems

Student Researcher: Liam M. Omer

Advisor: Dr. Yang Yun

The University of Akron
Departments of Biomedical Engineering

Introduction

The induction of nanomedicine has created an entire new mindset in the way that we approach medicine. Our ability to diagnose, treat, and prevent disease in patients is revolutionized by the ability to augment our medicine to selectively target areas of the body. Hyaluronan, a hydrophilic, linear polysaccharide is a polymer naturally produced in cellular scaffolding of human tissues. This polymer is a reliable delivery system for chemotherapeutics and hydrophobic materials.

The hydrophilic properties of hyaluronan allow for hydrophobic chemicals to be attached to the polymer as pendant chains and dissolve in aqueous solution. All cells possess expression of CD44 cell receptors that bind hyaluronan. The synthesis of a hyaluronan conjugate with resveratrol (3,5,4'-trihydroxy-trans-stilbene) using carbodiimide chemistry, allows for the production of pendant-chain delivery in aqueous solution.

Experimentation with hyaluronan conjugates has increased the efficacy of drugs at lower concentrations through increased bioavailability and solubility in vivo. This use of Hyaluronan conjugates has also shown a significant change in the window of dosage at which a drug can be delivered increasing flexibility of drug interventions.

Methodology

Hyaluronan (HA) was conjugated to Resveratrol (R) using the chain linking compound EDC HCL. The reaction takes a total of two days consisting of 20 hours of conjugation in ethanol-water solution, followed by eight hours of dialysis in a 50-50 ethanol/water solution and lastly overnight dialysis in pure deionized water. The conjugation process in the first 20 hours binds resveratrol to hyaluronan at pendant hydroxide groups present on hyaluronan. This reaction is done in low light conditions in order to reduce the transformation of resveratrol from its trans- conformation to a cis- conformation.

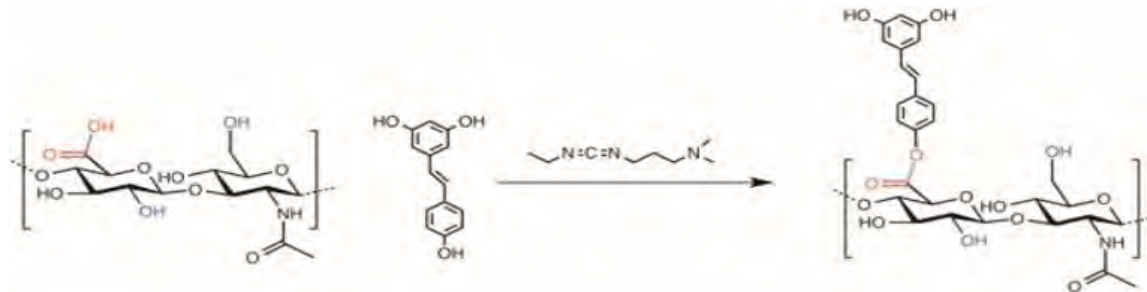


Figure 1. Hyaluronan-Resveratrol Conjugation.

The dialysis of the conjugated solution allows for ethanol and residual resveratrol to be removed from the solution leaving the Hyaluronan-Resveratrol in a pure deionized water solution. After dialysis, the product is then lyophilized for a period of 3 days in low light conditions resulting in solid Hyaluronan-Resveratrol (Ha-R).

The alamar blue assay was used to observe the metabolic activity of cells when subjected to differing drug concentrations. SHSY5Y cells, an immortalized neuroblastoma cell line, were seeded into 96 well plates at 10000 cells/cm² and allowed to adhere for 24 hours. After the cells were observed to be adherent, the cell media was exchanged with new cell media and Ha-R, Resveratrol, and Hyaluronan were titrated in into 3 column sections resulting in 3 titrated columns per drug intervention. Each row contained concentrations from 100 micromolar resveratrol concentration to 0 micromolar concentration resveratrol.

The cells were then incubated for 3 days after intervention. After 3 days, cell media was exchanged for ccm mixed with 10% pure Almar blue and allowed to incubate for 4 hours. After 4 hours, well absorbance at wavelengths of 570 nm and 600 nm was measured. The resulting information from the absorbance was then converted in order to access cell viability (**Figure 2**). The curved fit for each line as well as the IC50, the dosage at which fifty percent of cells die are listed in **Table 1**.

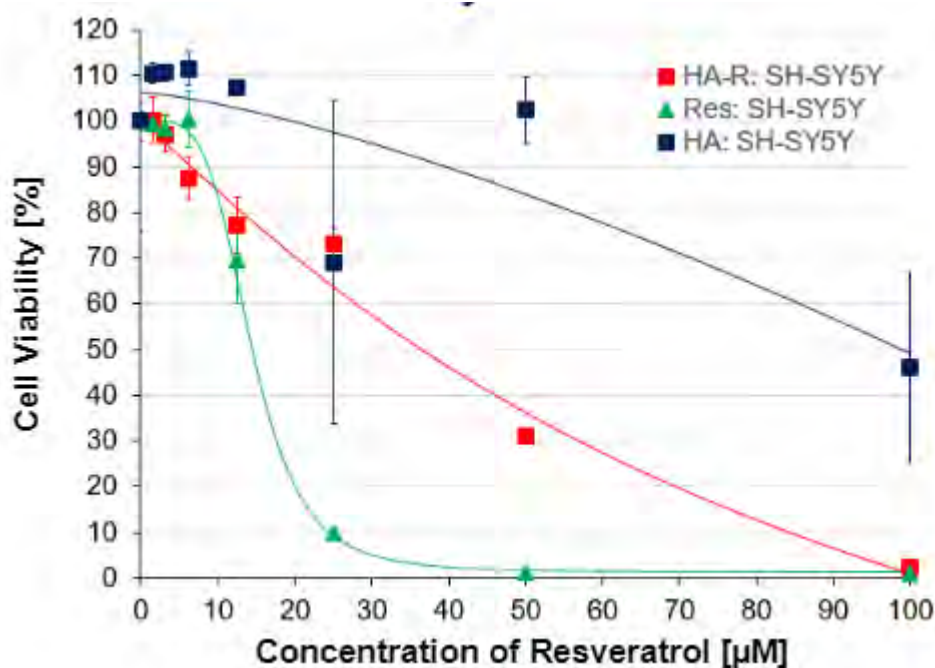


Figure 2. Cell Viability of SHSY5Y Cells.

Table 1. Curve fit and IC50 of SHSY5Y cells in response to HA-R, Resveratrol, and Hyaluronan Results.

	HA-R [µM]	Res with Ethanol [µM]	HA [µM]
SH-SY5Y	36.9	15.5	99.0
Curve Fit	R2 = 0.98	R2= 0.98	R2 = 0.68

There was a significant difference in the IC50 between HA-R and R. There was also an observed difference in the rate at which drug intervention affected cell viability. Ha-R has a much larger range of concentrations at which cells are still viable (>80% viability). Resveratrol's steep drop in cell viability results in an IC50 of 15.5 micromolar concentration of resveratrol in comparison to 35.5 micromolar concentration of resveratrol from HA-R.

Discussion

The effects of resveratrol on different pathways such as sirtuins and NF- κ B manifest desirable decreases in inflammation and has shown to have significant effects on a multitude of pathologies. However, the bioavailability of resveratrol as well as its low concentration IC₅₀ can create barriers in being able to effectively dose and deliver the drug in any beneficial manner. Hyaluronan drug delivery systems present the unique ability to take an insoluble drug and increase its viability and efficacy many folds. HA-R allows for higher amounts of resveratrol to be delivered to SHSY5Y cells with lower rates of cellular toxicity. This enables HA-R interventions to increase resveratrol concentration while also reducing the deleterious effects of resveratrol. SHSY5Y cell were chosen due to their unique morphology and ability to be differentiated into neuronal like cells. When differentiated SHSY5Y cell can be used a model to understand how resveratrol and hyaluronan-resveratrol conjugated may effect brain cells. In the future, cell toxicity and titration of HA-R and Resveratrol to differentiated SHSY5Y cells should be done in order to have a more in-depth understanding of the efficacy of Ha-R in reducing neuronal inflammation. Progression in neuronal inflammatory treatment may have beneficial uses for neurological conditions linked to inflammation such as Alzheimer's. Ha-R may present a beneficial way of delivering insoluble compounds into the brain with higher drug efficacy and lower required concentrations.

Active Flow Control in an Aggressively Offset High-Speed Inlet/Diffuser Model

Student Researcher: Collin J. O'Neill

Advisor: Dr. Mo Samimy

The Ohio State University

Mechanical and Aerospace Engineering Department

Abstract

The more integrated aerodynamics and propulsion components in the next generation of high-speed aircraft are expected to require short, aggressively offset inlet/diffuser ducts. The large offset and compact nature of these ducts can cause strong secondary flows and significant separation at the duct turns [1]. These effects have several negative consequences including flow non-uniformities and swirl at the aerodynamic interface plane (AIP), which results in relatively low total-pressure recovery. These negative effects cause significant stress on the turbomachinery and reduce engine efficiency and life span [2]. Therefore, reducing separation and/or the secondary flows and their resulting consequences could significantly improve the performance of next-generation tactical aircraft. One promising method to control this flow is through the use of plasma actuators. A class of plasma actuators, called localized arc-filament plasma actuators (LAFPAs), have been used successfully for flow control in several high-speed and high-Reynolds number flows [3]. The low power use, scalability, and adaptable control provided by LAFPAs make them well-suited for high-speed inlet flow control. The goal of this project is to implement LAFPAs in a small-scale offset diffuser to mitigate total pressure loss and dynamic distortion at the AIP. Successfully mitigating distortion and total pressure loss at the AIP will increase the performance and lifespan of next generation tactical aircraft. The inlet used in this experiment was tested at two primary Mach numbers of interest, Mach 0.52 and Mach 0.84. The main methods used in this investigation are surface pressure measurements along the centerline of the inlet, pressure measurements at the AIP, and oil flow visualization (OFV) at regions of interest. The centerline pressure measurements and OFV were primarily used to study the fluid dynamics associated with the inlet, while the AIP pressure rake was used to assess total pressure loss and distortion at the AIP. Unexcited results have shown centerline pressure measurements and OFV flow patterns consistent with previous results in literature. AIP measurements for the baseline, unexcited flow showed a total pressure recovery of 96.3% with a face-averaged circumferential distortion parameter of 0.014 at Mach 0.52 and a total pressure recovery of 89.9% with a face-averaged circumferential distortion parameter of 0.022 at Mach 0.84.

Project Objectives

Several flow control methods have been tested to mitigate the negative side effects of offset inlets. Passive flow control methods such as microvane vortex generators are effective, but they can only be optimized for one set of flight conditions. Outside of these on-design conditions, microvane vortex generators can actually create a performance penalty [2]. Unlike passive flow control methods, active flow control methods can be adjusted to perform in off-design conditions. The primary active flow control method tested on offset diffusers so far has been fluidic microjet actuators. These actuators have been proven to be effective, but they require complex tubing and valve systems to transport the necessary air from downstream engine components [1].

The ultimate goal of this project is to assess the efficacy of a new form of active flow control for offset diffusers that does not require air from other engine components. This active flow control method is a class of plasma actuators called localized arc-filament plasma actuators (LAFPA) that have been shown to be effective in controlling several similar flows [3]. A single LAFPA consists of two tungsten electrodes with a small gap between them. A high voltage with a controlled frequency is imposed across the electrodes, creating a repeated plasma breakdown in the air. The rapid, localized heating produced by this breakdown generates a thermal perturbation that propagates throughout the flow. By introducing perturbations at frequencies that match the natural instability frequencies in the flow, plasma actuators can exert significant flow control with minimal power usage [3].

The specific objective of this investigation is to design and fabricate a new inlet/offset-diffuser facility and to use it to obtain baseline, unexcited results to assess flow distortion and pressure loss. The main metrics of distortion and total pressure loss will be measured using a pressure rake at the AIP, while the flow physics will be studied using centerline surface pressure taps, and oil flow visualization (OFV).

Methodology

One of the high speed wind tunnel facilities at the Gas Dynamics and Turbulence Laboratory (GDTL) at The Ohio State University is being used for this experiment. This is a high mass flow, blowdown-type wind tunnel. A modular offset inlet/diffuser test section was designed in SolidWorks and constructed. This facility is shown from the side in Figure 1.

The facility has three main sections. The upstream section is machined aluminum that smoothly transitions from the rectangular outlet of the settling chamber to a D-shaped section at the inlet throat. This transition allows the inlet geometry of interest to interface with the high-speed wind tunnel facility.

The main test section of the facility is a modular, 3D printed design. The geometry was provided by Boeing. The inlet geometry of interest has a throat area of 100.15 cm² and an AIP area of 126.62 cm² with a 12.7 cm inch diameter at the AIP. There are 38 streamwise pressure taps along the top and bottom of the diffuser to observe separation of the flow. These streamwise pressure taps are aligned along the center of the facility with one inch spacing between each adjacent tap. There are also four windows to allow for particle image velocimetry measurements (PIV) and OFV at the upstream and downstream turns. When PIV is not being performed, the windows are replaced by 3D printed blanks that are exactly contoured to match the internal geometry. These blanks are installed in Figure 1. The main test section contains an actuator insert that houses 19 LAFPAs. Each LAFPA is composed of two 1 mm tungsten electrodes flush mounted in a small groove. This groove stabilizes the arc and prevents it from being stretched and carried downstream by the flow. This is critical as it allows the frequency to be precisely controlled [3]. The LAFPAs are connected to a custom-built power supply capable of producing microsecond pulses of several kV. The typical pulse used in this experiment is approximately 4 microseconds at 5 kV. This actuator block is just upstream of the second turn to maximize the LAFPAs' control authority over the separated region nearest to the AIP. This insert is also contoured to match the internal geometry of the diffuser. The facility also contains an opening to allow for an actuator insert at the upstream turn. For the present investigation, this opening is filled with a 3D printed blank that matches the internal geometry of the diffuser.

The downstream section is constructed of machined aluminum. This downstream section houses the AIP pressure rake assembly. The rake assembly contains 40 stagnation pressure probes located in centroids of equal area and 8 equiangularly spaced static pressure probes in total. Beyond the AIP, the downstream section contains a smooth diffusion section that allows the flow to be vented outdoors with minimal losses.

Results Obtained

Centerline pressure measurements along the top and bottom of the inlet were obtained at Mach numbers of 0.52 and 0.84. These pressure measurements were then graphed against streamwise tap location to show the variations in pressure in the streamwise direction. This is shown in Figure 2. OFV was performed on the top surface of the diffuser just downstream of the second turn. This captured the dynamics of the separated region and the surrounding area. The OFV for Mach 0.84 is shown in Figure 3. AIP total pressure contours were created for Mach 0.52 and 0.84. These are shown in Figure 4. The Mach 0.52 case produced a total pressure recovery of 96.3% and a face-averaged circumferential distortion parameter of 0.014. The Mach 0.84 case produced a total pressure recovery of 89.9% and a face-averaged circumferential distortion parameter of 0.022.

Significance and Interpretation of Results

Figure 2 shows the variation of pressure in the streamwise direction. The most interesting insights from this graph come from looking at the inside of the second turn. This corresponds to streamwise coordinates 10-19 on the top of the diffuser. As the flow enters the second turn, it experiences an adverse pressure gradient along the top of the diffuser. This adverse pressure gradient leads to local separation, which would present as a plateau in the streamwise pressure. This separation is marked in Figure 2 with a bracket. OFV from this separated region is shown in Figure 3. The separation line near the top of the image is curved, showing the highly three-dimensional nature of the flow. The separated region is visible in the center of the image, appearing as a region with minimal oil movement. Crossflow on either side of the separated region is also clearly visible. At the bottom of the separated region, there are signatures of two counter-rotating streamwise vortices. This reinforces the importance of secondary flow structures in this application. Figure 4 shows total pressure contours for Mach 0.52 and Mach 0.84. The contours are qualitatively similar, with a concentrated region of high total pressure loss along the top and a more diffuse region of lower total pressure loss along the bottom. These total pressure loss regions are produced by the turns, with the region along the bottom being more diffuse due to the greater distance between the first turn and the AIP. Although qualitatively similar, the total pressure loss rapidly increases with increasing Mach number.

Figures

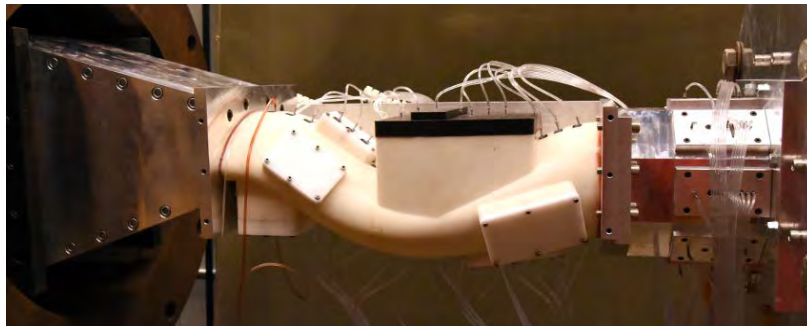


Figure 1. Side view of Offset Diffuser Facility.

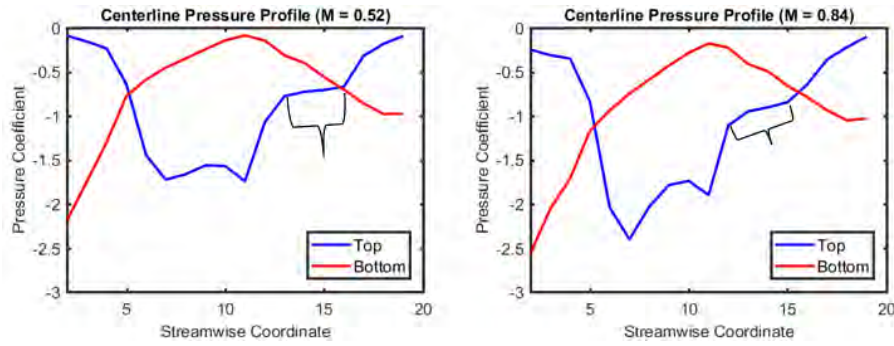


Figure 2. Centerline Pressure Coefficients along Top and Bottom of Diffuser with Separated Region Highlighted by Bracket at (a) Mach 0.52 and (b) Mach 0.84.



Figure 3. OFV of Separated Region at Mach 0.84.

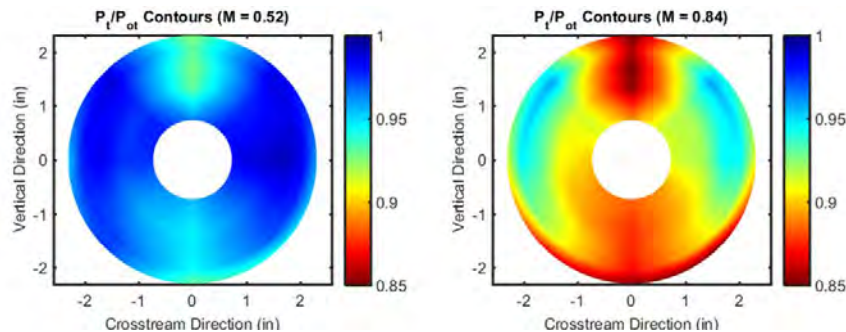


Figure 4. Total-Pressure Loss Contours at AIP at a) Mach 0.52 and b) Mach 0.84.

Acknowledgments

The author would like to thank Dr. Nathan Webb and Dr. Mo Samimy. Their guidance and work was instrumental in completing this research. The author would also like to thank the Office of Naval Research (ONR), Ohio Space Grant Consortium (OSGC), and The Ohio State University for providing funding to make this research possible.

References

1. Rabe, A. C., "Effectiveness of a Serpentine Inlet Duct Flow Control Scheme at Design and Off-Design Simulated Flight Conditions," PhD Thesis Virginia Polytechnic Institute and State University, 2003.
2. Anderson, B.H., Baust, D.H., and Agrell, J., "Management of Total Pressure Recovery, Distortion and High Cycle Fatigue in Compact Air Vehicle Inlets," NASA/TM. 2002-212000, 2004a.
3. Samimy, M., Webb, N., and Crawley, M., "Excitation of Free Shear-Layer Instabilities in High-Speed Flows," AIAA Journal, March 2018. <https://doi.org/10.2514/1.J056610>.

Analyzing the Relative Impact of Spray and Volatile Fuel Properties on Gas Turbine Combustor Ignition in Multiple Rig Geometries

Student Researcher: Katherine C. Opacich

Advisor: Dr. Joshua S. Heyne

University of Dayton

Department of Mechanical and Aerospace Engineering

Abstract

Implementing alternative fuels into the aviation market involves an extensive certification process due to their novel properties and correspondingly unique combustion performance characteristics. The current certification process is not only costly, but time intensive. As a result, the National Jet Fuels Combustion Program (NJFCP) has made it their mission to streamline the approval process of alternative jet fuels by bounding the combustion performance characteristics of alternative fuels to those of conventional fuels. Historically, the impact of alternative fuels on ignition performance, i.e., altitude relight and cold start, for extreme conditions and fuel properties was only moderately explored.

Previous research from Lefebvre et al. shows fuel spray atomization as having a strong influence on ignition behavior. The fuel properties of density, viscosity, and surface tension control spray atomization characteristics. In contrast to Lefebvre's findings, recent statistical results reported previously show that the distillate or volatile properties of a fuel largely affect ignition behavior. These differing results present the question: *Are the spray or volatile properties of a fuel more important in predicting relative ignitability?*

The aim of this research is to utilize statistical analysis techniques to establish a model and qualitative ranking that accurately conveys the impact that a fuel's spray property characteristics have on ignition probability for both cold start and altitude relight Figures of Merit. It is anticipated that this work will be applied toward guiding future computational fluid dynamic (CFD) modeling targets, evolving the gas turbine combustion community's understanding of dominating physics in gas turbine ignition, and finally, defining the properties that are most important for the early screening of alternative jet fuels in the certification process.

The results exhibit that a fuel's surface tension is a better predictor of fuel ignitability at higher temperatures, in contrast to previous results, while viscosity has a greater impact at lower temperature. Rankings between the Honeywell APU and the Referee Rig are nearly consistent for similar conditions. The implications of this and other work suggests that a generic Referee Rig is capable of screening fuels for a multitude of geometries, and that surface tension may need to be a future specification property for the approval of alternative fuels.

Nomenclature

<i>NJFCP</i>	= National Jet Fuels Combustion Program
<i>FOM</i>	= Figures of Merit
<i>LBO</i>	= Lean Blowout
<i>SMD</i>	= Sauter Mean Diameter
<i>FAR</i>	= Fuel-to-Air Ratio
<i>CFD</i>	= Computational Fluid Dynamics

APU = Auxiliary Power Unit
GCxGC = Two-dimensional Gas Chromatography
NIST = National Institute of Standards and Technology

Introduction

The transportation industry is primarily dependent on the consumption and burning of petroleum-based liquid fuels¹. Not only are these fuels likely contributors to climate change due to their greenhouse gas emissions, they also contribute to national security concerns, as their supply is dependent on unstable foreign distributors. To combat these negative effects, the aviation industry, which is forecasted to nearly double passenger trips from 2017 to 2037, is actively pursuing the development of non-petroleum derived alternative jet fuels². Implementing these alternative fuels into the aviation market, however, involves an extensive certification process due to their novel properties and correspondingly unique combustion performance characteristics relative to conventional fuels. In the current certification process, approximately \$3-4 million is expended and 20,000-100,000 gallons of fuel is consumed over a three to five-year period to evaluate the performance characteristics of new alternative fuel blends³.

Therefore, this process is not only costly, but time intensive. As a result, the National Jet Fuels Combustion Program (NJFCP) has made it their mission to streamline the approval process of alternative jet fuels by bounding the combustion performance characteristics of alternative fuels to those of conventional fuels.

Through the NJFCP's experimental work in testing fuels in various combustor rigs and targeting key combustion Figures of Merit (FOM), new tools to help minimize the extent of fuel testing needed are being developed. The three FOMs the program focuses on to determine whether a fuel is safe for use include Lean Blowout (LBO), cold start, and altitude relight. This research focuses on the cold start performance metric. The range of inlet temperatures and pressures on which each FOM falls during a typical flight envelope are shown in Figure 1.

Historically, the impact of alternative fuels on ignition performance, i.e., cold start, for extreme conditions and fuel properties was only moderately explored³. For ignition, the propensity of a fuel to ignite is limited by its ability to form a flammable mixture with air near a spark kernel. The path to ignition is influenced by a fuel's properties, combustor operating conditions, and combustor geometry.

Previous research from Lefebvre et al. shows the strong influence fuel spray atomization, expressed regarding spray Sauter mean diameter (SMD), has on ignition limits⁴. The main purpose of spray atomization is to increase the surface area of the fuel, thereby increasing heat and mass transfer and vaporization⁵. Density, viscosity, and surface tension are the major fuel properties that control these spray characteristics throughout this process, and thus play a determining role in ignition timescales and ignition probabilities.

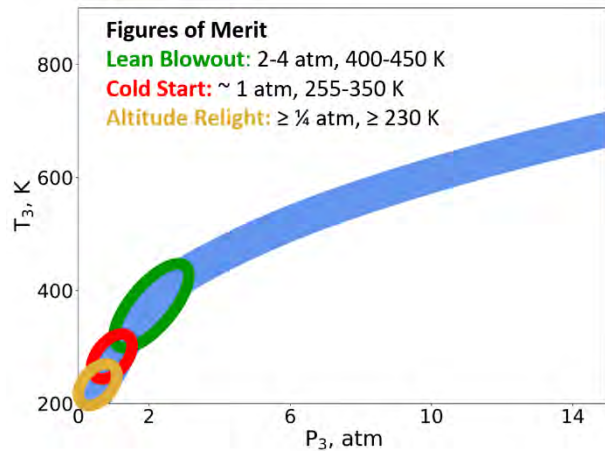


Figure 1. Visualization of inlet temperatures and pressures each FOM can occur at during a typical flight envelope. This research focuses on the cold start figure of merit, which is highlighted in red.

Recently, statistical results from random forest regressions based on NJFCP experimental data have shown that the distillate/volatile properties of a fuel largely govern ignition behavior⁶. This is based on the understanding that the ignition timescales and probabilities are also strongly dependent on the amount of energy it takes to heat and evaporate a critical mass of liquid fuel to form an ignitable mixture with air. The Honeywell ignition feature importance chart, Fig. 2, below illuminates the contrast between these historical (spray property) and contemporary (volatile property) explanations for variable ignition probabilities⁶.

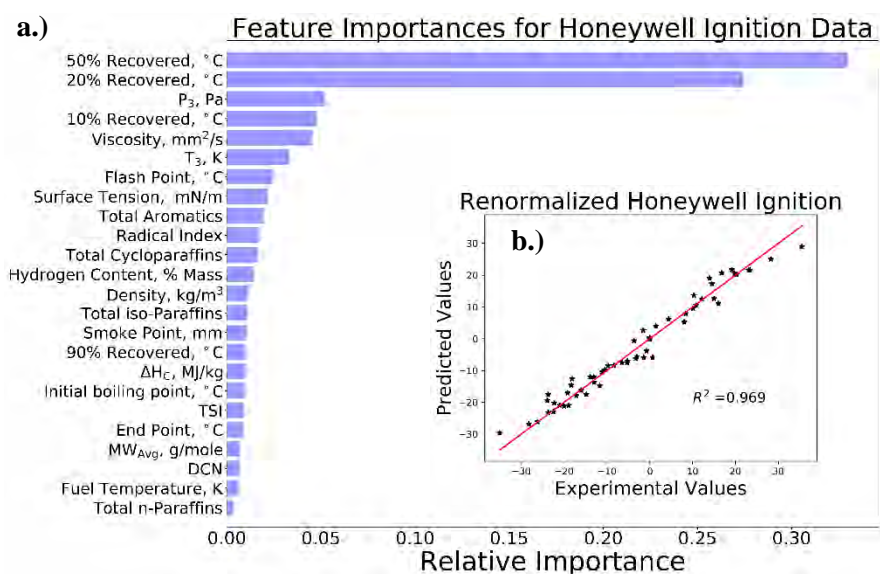


Figure 2. Random forest regression feature importance and fit for minimum ignition fuel-air ratio (FAR) in a Honeywell auxiliary power unit. a) The volatile properties, such as the distillation curve, of the fuel dominate the relative ignition performance of a fuel in addition to the inlet pressure and temperature. b) The predicted versus experimental ignition percent difference FAR values for Honeywell rig at various combustor pressures and inlet conditions. NOTE: Units have been intentionally renormalized such that these numbers are not relevant to actual operating limits⁶.

While the distillation curve correlations are convincing, distillation temperatures have previously been shown to correlate heavily with fuel physical properties, i.e., viscosity, density, and surface tension, that impact spray character. Hence, the distillation curve and physical properties are too correlated to be used within the same regression analysis. Instead, more fundamental and orthogonal variables need to be used to illuminate the actual relative impact of volatile properties versus physical properties. Towards this aim, we focus on answering the questions: *What is the relative importance of five distinct properties, and how do they relate to the ignitability in two rigs at relevant conditions?*

A characteristic study of spray and volatile properties allows this question to be addressed. Here, the fuel spray properties (e.g. density, viscosity, and surface tension) and the fuel volatile properties (e.g. vapor pressure and heat capacity) are each investigated independently as a function of temperature for each of the NJFCP fuels. Once established, the property knowledge is used to improve our previously reported statistical analysis methods. The method will employ similar techniques as reported by Peiffer, Heyne, and Colket⁷.

The aim of this research is to utilize this process to establish a more physically based model that articulates the relative impact of spray and volatile characteristics on ignition probability for both cold start and altitude relight FOMs. It is anticipated that this work will be applied towards guiding future computational fluid dynamic (CFD) modeling targets, evolve the NJFCP community’s understanding of dominating physics in gas turbine ignition, and finally, clarify the properties that are most important in enabling the future certification of alternative jet fuels.

Methodology

Rig Geometries and Test Conditions

The combustor rigs the NJFCP utilized for the ignition testing of alternative jet fuels were selected to represent the geometric variations that exist in actual gas turbine engines. The two combustor rigs that this research focuses on are the Referee Rig and the Honeywell rig. The Referee Rig is a single-cup, swirl stabilized combustor that is a variation of the traditional Rich-Quench-Lean combustor³. The Honeywell rig has the combustor geometry of an aircraft auxiliary power unit (APU), meaning that it is smaller in size than the Referee Rig and contains no swirler to generate a primary recirculation zone³. Table 1 provides an overview of the geometries and operating conditions for each of the above NJFCP rigs.

Table 1. Summary of the NJFCP combustor rig geometries and operating conditions.

Rig Name	Rig Description	Ignition Source	T_{air}	T_{fuel}	P	Institution
Referee Rig	Pressure atomizer, high swirl	APU Igniter	238 and 258 K	238 and 258 K	1 atm	AFRL/UDRI
Honeywell Rig	Pressure atomizer in swirl stabilized APU	Discharge	230 to 288 K	236 and 288 K	0.2 to 1.1 atm	Honeywell

Fuels

The results discussed later in this paper cover the properties and ignition behavior of conventional fuels (Category A) and test fuels (Category C). Category A fuels are petroleum derived jet fuels currently being used in the aviation industry today. The three Category A fuels that were selected for testing captured the wide range of properties that exist in commercialized jet fuel today; A-1 being the ‘best case’ with the lowest flash point, viscosity and aromatic content, A-2 the ‘average case’, and A-3 the ‘worst case’ for these properties. The Category C fuels are non-petroleum derived, alternative jet fuels that were selected for experiments based on their ‘unusual’ properties. Table 2 summarizes the composition and unique properties related to the Category A and C fuels analyzed in this research. Detailed properties of the Category A and C fuels are provided by Edwards⁸.

Table 2. Overview of the NJFCP Category A and C fuels. Category A fuels represent conventional, petroleum-derived fuels while Category C fuels represent alternative jet fuels.

Fuel/Solvent Mixture	POSF Number	Composition, % volume	Description
A-1	10264	Petroleum JP-8	Low flash, viscosity, and aromatics
A-2	10325	Petroleum Jet A	Nominal jet fuel
A-3	10289	Petroleum JP-5	High flash, viscosity, and aromatics
C-1	11498, 12368, 12384	Gevo ATJ, Highly branched C12 and C16 alkanes	Low DCN, unusual boiling range
C-2	11813, 12223	16% <i>tri</i> -methylbenzene + 84% C14 <i>iso</i> -alkanes	Chemically-asymmetric boiling range
C-3	12341, 12363	64% A-3 + 36% farnesane	High viscosity fuel, at viscosity limit for jet fuel at -20°C
C-4	12344, 12489	60% C9-12 <i>iso</i> -alkanes, 40% C-1	Low DCN, conventional, wide boiling range
C-5	12345, 12713, 12789, 12816	73% C10 <i>iso</i> -alkanes, 17% <i>tri</i> -methylbenzene	Flat boiling range

Random Forest Regression Analysis

The following approach was taken to determine whether spray or volatile properties better govern ignition behavior. First, the fuel properties of interest were down-selected to the spray properties of density, viscosity, and surface tension, and the volatile properties of vapor pressure and specific heat. Previous fuel property research conducted by Edwards was leveraged to include the properties above within the combustor rig ignition datasets at the fuel test temperatures⁸.

A statistical analysis of the ignition dataset from each rig was conducted using random forest regressions. Random forest regression analysis is a machine learning technique that generates a ‘forest’ of decision trees to model and develop predictions for complex datasets. To prevent overfitting the model, the random forest creates decision trees based on a smaller dataset that was randomly sampled with replacement from the original dataset. This approach is known as bootstrap aggregating or bagging. Similar to how bagging introduces randomness at the data level, random forests also introduce randomness at the nodal level by randomly selecting m variables from p total variables at each decision tree node.⁶ Each variable’s importance to the model can be identified from the random forest predictor shown in Equation 1, where B is the number of trees, $\{T(x; \theta_b)\}_1^B$ is the actual trees in which θ_b describes the b^{th} tree in terms of split variables, cut points, and terminal-node values⁹.

$$\hat{f}_{rf}^B(x) = \frac{1}{B} \sum_{b=1}^B T(x; \theta_b) \quad (1)$$

The feature importance plots generated from Equation 1 were used to inform which fuel properties were influential in predicting ignition equivalence ratios. For this research, the equivalence ratios used in the random forest regressions were normalized to the A-2 fuel to allow for the comparison of the result across different rigs. In the normalizing equation, Equation 2, Φ is the percent difference of a given

fuel's ignition equivalence ratio, ϕ_i , relative to the A-2 fuel's equivalence ratio at the same test conditions.

$$\Phi = \frac{\phi_i - \phi_{A-2}}{\phi_{A-2}} * 100 \quad (2)$$

These normalized equivalence ratios were the output of the random forest regression, while the inputs consisted of the fuel spray and volatile properties as well as the test conditions of fuel temperature, air temperature, and pressure.

Monte Carlo Simulations

An uncertainty quantification analysis was conducted on the property data using Monte Carlo simulations. Monte Carlo method randomly simulates possible results based on a chosen probability distribution over an error domain. In this research, a normal probability distribution was selected, and the error domain was defined from Edwards' fuel property data⁸ and the experimental reproducibility error listed in the ASTM standards respectively. To quantify the experimental variation within the ignition fuel property datasets, the Monte Carlo simulation was run 10,000 times. A random forest regression was performed against each of the 10,000 simulated property datasets, and the corresponding feature importance output values were recorded. The output importance results for each fuel property were then averaged and the standard deviation, two σ , was calculated. To better illuminate how the property variance affected the random forest results, standard deviation error bars representing the 95% confidence interval were included on the feature importance plots.

Vapor Pressure Prediction

The fuel property of vapor pressure was utilized in this research instead of the distillation curve due to the distillation curve's high correlation with viscosity, density, and surface tension of a fuel. To calculate the vapor pressure of each fuel at the test conditions, the two-dimensional gas chromatography (GCxGC) results for each fuel was utilized along with Raoult's Law and the experimental vapor pressure values provided by Edwards. The GCxGC results provided a mass percentage breakdown of the molecular groups within the fuel. The molecular groups included n-alkanes, iso-alkanes, monocycloalkanes, dicycloalkanes, tricycloalkanes, alkylbenzenes, alkylnaphthalenes, and cycloaromatics. Within each molecular group, the GCxGC results provided the mass percentages of the molecules within the group based on their number of carbon atoms. Only the molecules with a weight percent of 0.90 or higher were included in the vapor pressure analysis. The National Institute of Standards and Technology (NIST) Web Thermo Tables¹⁰ were used to obtain vapor pressure values of these molecules every five degrees Celsius from -38 to 147 degrees. Raoult's law was utilized to combine the molecular vapor pressures to acquire the vapor pressure of each fuel across this range of temperatures (Equation 3). In Equation 3, p_{fuel} is the total vapor pressure of each fuel, p_i is the vapor pressure of each molecular component within the summation, and x_i is the mole fraction of each molecular component within the summation. The mole fraction value for each molecular component was calculated using its mass fraction and molecular weight.

$$p_{fuel} = \sum_{i=1}^n p_i x_i \quad (3)$$

The calculated vapor pressure of each fuel was plotted versus temperature and an equation was fitted to the points using the curve fit python programming command and the Antoine equation shown in Equation 4. In this equation, A , B , and C are Antoine coefficients, p_{fuel} is the vapor pressure of the fuel, and T is the temperature. Equation 4 was used to predict the vapor pressure of each fuel at the provided test temperatures.

$$p_{fuel} = 10^{A - \frac{B}{C+T}} \quad (4)$$

Other Property Predictions

The density, surface tension, and specific heat of each fuel at the rig test conditions was obtained by generating a linear regression equation based on Edwards' experimental property versus temperature data. The viscosity of each fuel at the rig test conditions was predicted by fitting the Walther formula (Equation 5) to Edwards' experimental kinematic viscosity versus temperature data. In Equation 5 A and B are empirical parameters, ν_{fuel} is the kinematic viscosity of the fuel, and T is the temperature.

$$\nu_{fuel} = 10^{10(A - B \cdot \log_{10} T)} - 0.7 \quad (5)$$

Results and Discussion

The results presented in this section focus on the ignition data from the Referee and Honeywell combustor rigs. While previous random forest regression results⁶ showed distillation temperatures as being the most important feature to predicting ignition equivalence ratios, interestingly, when the properties are narrowed down, and the properties of vapor pressure and specific heat capacity are the main volatile properties in the dataset, spray properties appear to have significant influence.

The equivalence ratio at the 10% ignition probability was obtained by using the ignition probability data fits from Hendershott et al. for each combination of pressure, ΔP , temperature and fuel type, which were determined using binomial logistic regression of the Referee Rig ignition data¹¹. These equivalence ratios were then used in the random forest regression to create Figure 3. This figure shows density and surface tension as being the dominant features in predicting ignition equivalence ratios followed by viscosity, vapor pressure and specific heat capacity. The rig's test conditions of fuel and air temperature and pressure were shown to be of lesser importance.

The results for the Honeywell cold ignition dataset in Figure 4 show viscosity as the dominant feature in predicting ignition equivalence ratios followed by density, surface tension, vapor pressure and specific heat capacity. Similarly, the air temperature, specific heat, and vapor pressure/pressure were the least significant features. Lastly, the Honeywell warm ignition regression in Figure 5 shows surface tension as the dominant feature in predicting ignition equivalence ratios followed by density, viscosity, and specific heat. Air temperature, pressure, and vapor pressure were of less significance. Interestingly, using only the fuel properties related to ignition and the corresponding test conditions resulted in R-squared values comparable to the random forest regressions in which all fuel properties were included.

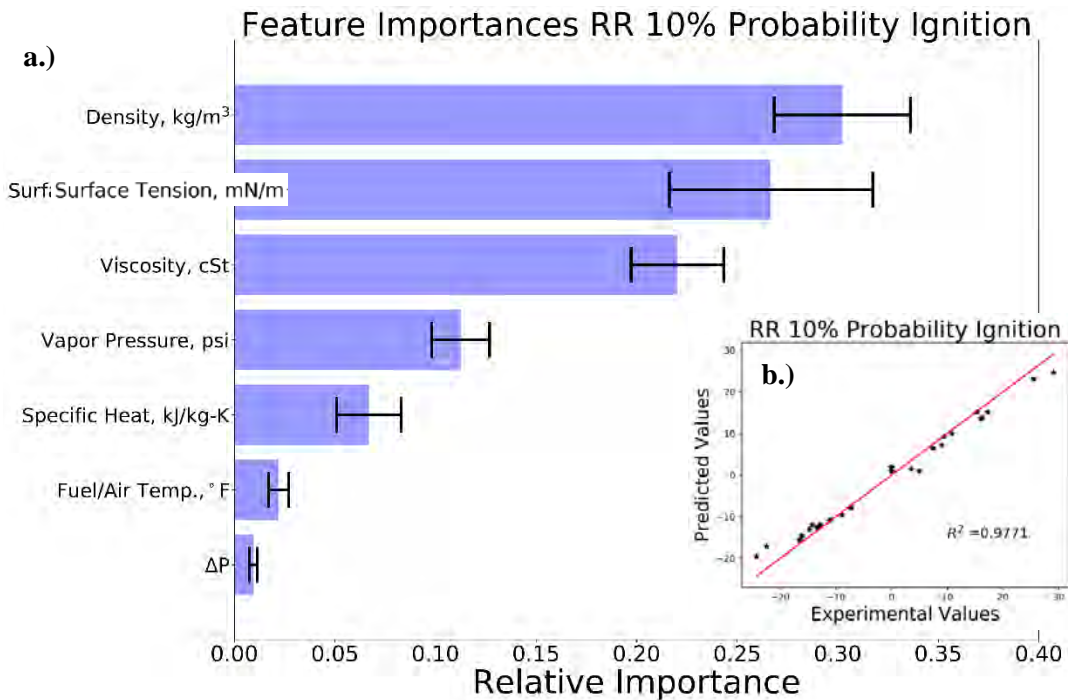


Figure 3. a.) Feature importances from the random forest regression for the Referee Rig show density and surface tension as the most important fuel properties to predicting ignition equivalence ratios. b.) The predicted versus experimental ignition data points are presented here.

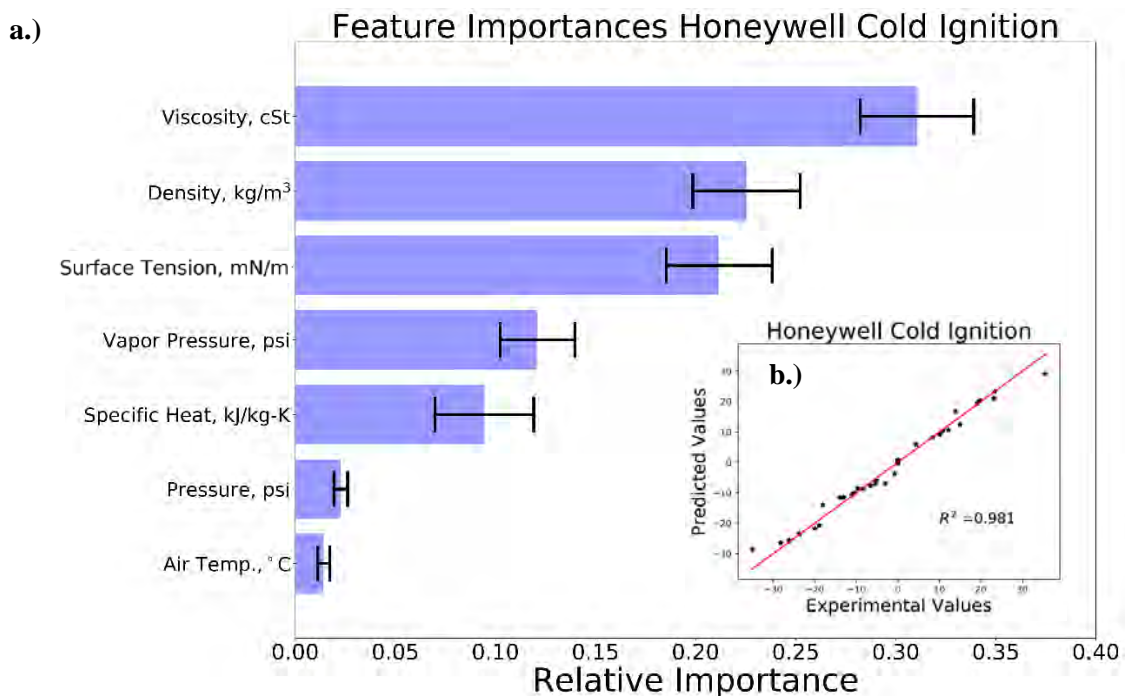


Figure 4. a.) Feature importances from the random forest regression for the Honeywell cold ignition show viscosity as the most important fuel property to predicting ignition equivalence ratios. b.) The predicted versus experimental ignition data points are presented here. NOTE: Units have been intentionally renormalized such that these numbers are not relevant to actual operating limits.

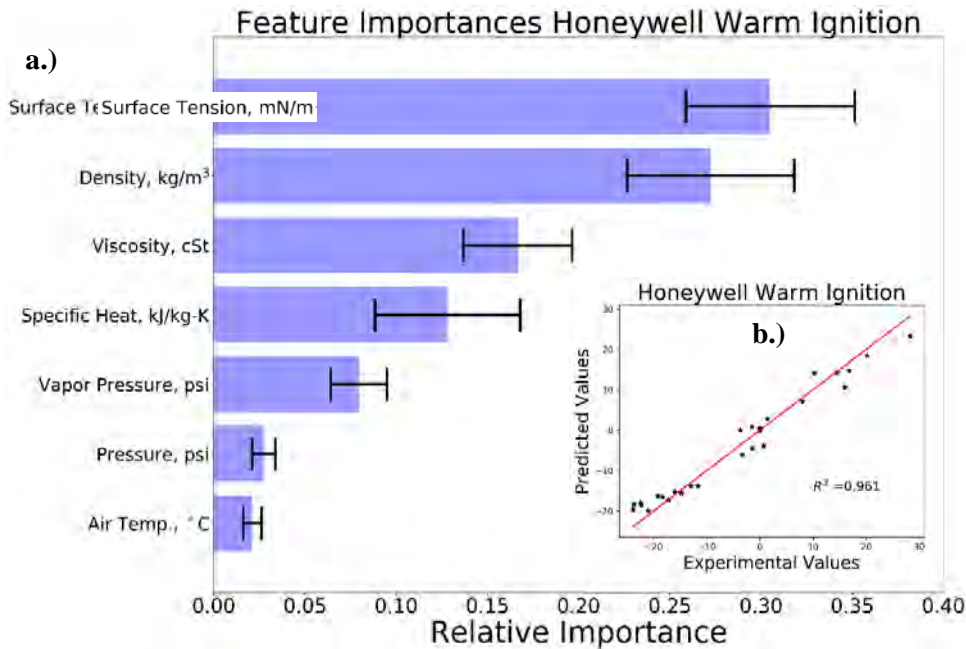


Figure 5. a.) Feature importances from the random forest regression for the Honeywell warm ignition show surface tension as the most critical fuel property to predicting ignition equivalence ratios. b.) The predicted versus experimental ignition data points are presented here. NOTE: Units have been intentionally renormalized such that these numbers are not relevant to actual operating limits.

The Referee Rig and the Honeywell rig regression results both showed that the fuel spray properties of viscosity, density, and surface tension have a more substantial influence on ignition equivalence ratio than the fuel volatile properties of vapor pressure and specific heat capacity. It is theorized that this is mainly due to the impact spray properties have on fuel atomization quality within the gas turbine combustor. A conceptual illustration depicting the path to gas turbine engine ignition beginning with fuel atomization is depicted in Fig. 6. Steps in the process governed by fuel properties are highlighted in purple, while steps governed by combustor geometries are highlighted in orange.

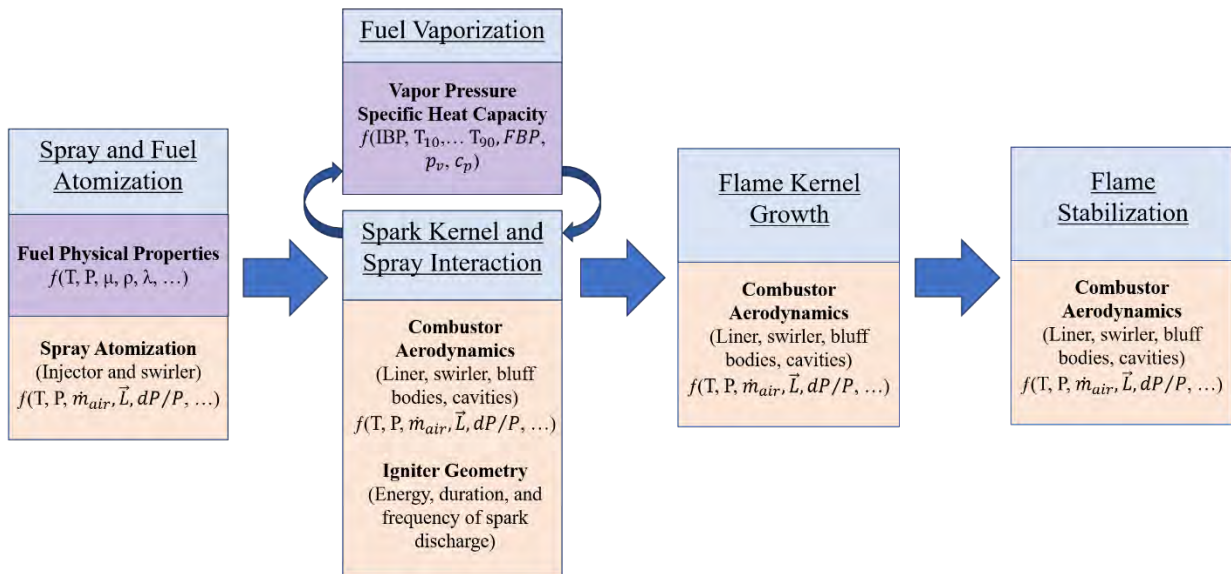


Figure 6. Conceptual illustration of the path to gas turbine engine ignition. The features in the purple boxes represent phenomena associated with fuel effects. The features in the orange boxes are more associated with non-fuel property effects.

In comparing the results between the Honeywell Cold and Warm ignition datasets, the impact of temperature on each spray property's importance ranking is illuminated. At the colder fuel test temperature of 236 K, the viscosity is isolated as the property with the most significant relative impact in governing ignition. In contrast, at the warmer fuel test temperature of 288 K, the viscosity is surpassed by density and surface tension in importance ranking. This illumination by the random forest can be explained by the relationship viscosity, density, and surface tension have with temperature. Viscosity exhibits an inversely proportional relationship with temperature as detailed by the Walther formula. Unlike viscosity, density and surface tension exhibit a negative linear relationship as temperature increases. Therefore, at colder fuel temperatures there is more considerable variation in the viscosity values between fuels as compared to density and surface tension. As temperature increases, the viscosity differences between fuels converge as the density and surface tension differences remain constant.

From regression results for each rig, fuel density was also identified as an essential factor in governing ignition. Historically, the significance of density regarding ignition and atomization performance was thought to be low due to conventional gas turbine fuels exhibiting only minor differences in the property¹². The Category A conventional fuels utilized within this research have an overall density variation of approximately 47 kg/m³ at 295 K. However, when the Category C fuels are included, the total density variation increases to approximately 67 kg/m³ at 295 K. It is hypothesized that because of this increase in variation, density has more of an impact in governing ignition equivalence ratios than previously thought.

The collective regression results also show that surface tension has a significant effect on fuel ignition. However, there is no current specification limit for the surface tension of gas turbine fuels¹². It is hypothesized that this is due to density already having a specification limit of 775 – 840 kg/m³ and surface tension having a strong, linear correlation with density for conventional fuels, bounding it as a result. When alternative fuels are considered, this linear trend breaks down. It is theorized that the unique molecular compositions of these fuels compared to the conventional ones results in this break

from conventional trends. Figure 7 depicts the relationship between surface tension and density for the conventional and alternative fuels as well as the molecules from various molecular subgroups of which the fuels consist at 295 K.

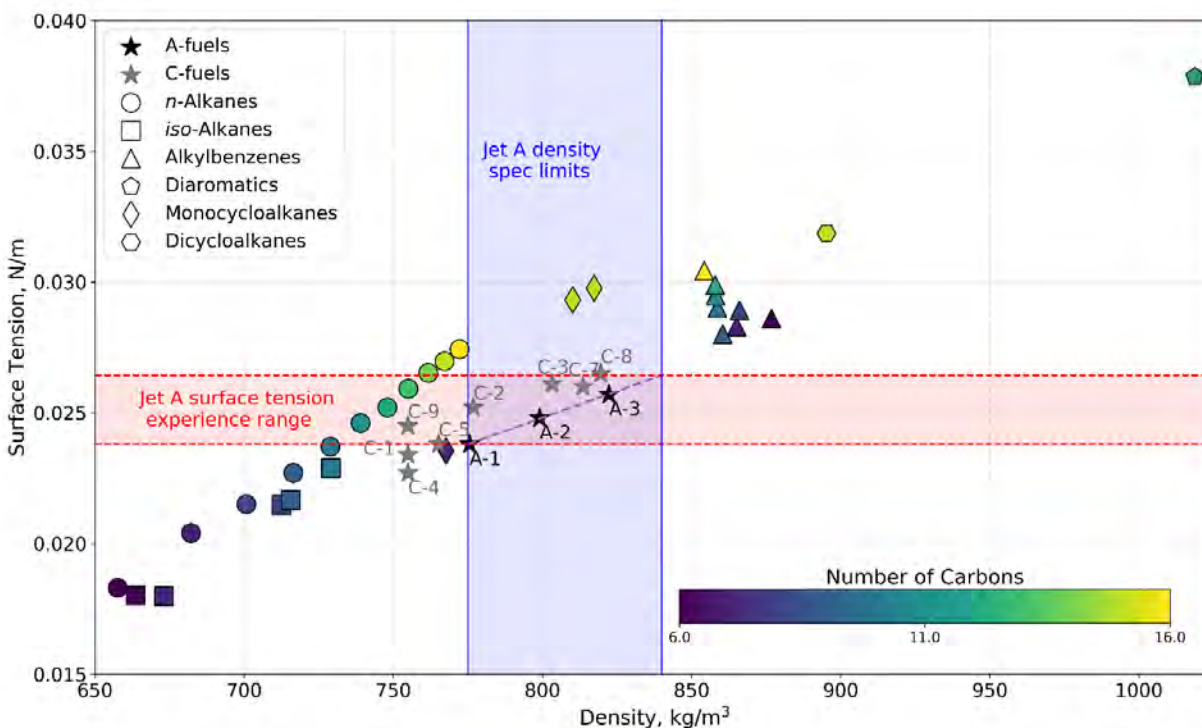


Figure 7. Surface tension versus density plot containing the conventional and alternative jet fuels and molecular subgroups at 295 K.

In the above Figure, the vertical blue lines represent the current gas turbine fuel specifications for density. The purple dashed line depicts the linear surface tension versus density correlation between the conventional fuels. In extending the linear relationship to the current density specification limits, a range of surface tension values can be obtained (signified by the red horizontal dashed lines). Since surface tension was identified as a key spray property in governing ignition, creating specification limits, such as the ones in Figure 7, would aid in accomplishing the NJFCP’s mission of bounding the ignition performance of alternative jet fuels. Furthermore, bounding ignition performance through a surface tension specification would also be a beneficial addition to a fuel pre-screening process that would work to filter out new blends of fuel without the need for expensive engine testing.

Conclusion

This research has sought to explain whether fuel spray of volatile properties better govern ignition behavior through the use of the statistical analysis tool of random forest regressions, Monte Carlo method, and delineating the effects of five volatile and spray properties. The random forest regression results showed that the five down selected properties of viscosity, density, surface tension, vapor pressure, and specific heat capacity explain over 96% of the variance in ignition equivalence ratios for both the Referee Rig and Honeywell rig datasets. Along with this, the spray properties of viscosity, density, and surface tension were determined to have more significant influence over ignition behavior for both the Referee and Honeywell rigs as compared to the volatile properties of vapor pressure and specific heat capacity. Moreover, surface tension is the most important property to predict relative ignitability in the Honeywell Rig at higher temperatures. At lower temperatures, the most important

property for the Honeywell Rig is the viscosity. Conceptually, this makes sense as the surface tension varies approximately linearly with temperature whereas the viscosity varies exponentially with temperature. The competition of these two properties implies a turn-over temperature in which the relative importance of the properties are equal.

In the current certification process for alternative jet fuels, there is no specification limit for surface tension. The need of a surface tension specification limit can be defended based on the results that show that surface tension is a key property in governing ignition and that alternative jet fuels exhibit surface tension behavior that is not directly correlated with density. Future work will involve the development of surrogates that stress the property of surface tension while holding the other properties relatively constant.

Acknowledgments

This research was funded by the U.S. Federal Aviation Administration Office of Environment and Energy through ASCENT, the FAA Center of Excellence for Alternative Jet Fuels and the Environment, project 34 through FAA Award Number 13-C-AJFE-UD-18 under the supervision of Cecilia Shaw. Any opinions, findings, conclusions or recommendations expressed in this material are those of the authors and do not necessarily reflect the views of the FAA.

We would like to acknowledge Tyler Hendershott, Shane Kosir, Erin Peiffer, and Robert Stachler, for their support in this research effort, of which, would not be possible without their help. We would also like to acknowledge Edwin Corporan and Drew Caswell for kindly sharing their work with the Referee Rig.

References

1. Thomas, C. E. S., "Petroleum and coal proven reserves: The case for coal and the demise of OPEC," *Lecture Notes in Energy*, 2017.
2. Schinwald, C., Plötner, K. O., and Hornung, M., "Evaluation of Airport Capacity Optimization Measures," *AIAA Modeling and Simulation Technologies Conference*, Reston, Virginia: American Institute of Aeronautics and Astronautics, 2017.
3. Colket, M., Heyne, J., Rumizen, M., Gupta, M., Edwards, T., Roquemore, W. M., Andac, G., Boehm, R., Lovett, J., Williams, R., Condevaux, J., Turner, D., Rizk, N., Tishkoff, J., Li, C., Moder, J., Friend, D., and Sankaran, V., "Overview of the National Jet Fuels Combustion Program," *AIAA Journal*, 2017.
4. Ballal, D. R., and Lefebvre, A. H., "Ignition of liquid fuel sprays at subatmospheric pressures," *Combustion and Flame*, 1978.
5. Lefebvre, A. H., and McDonell, V. G., *Atomization and sprays*, 2017.
6. Heyne, J. S., Peiffer, E., Colket, M. B., Jardines, A., Shaw, C., Moder, J. P., Roquemore, W. M., Edwards, J. T., Li, C., Rumizen, M., and Gupta, M., "Year 3 of the National Jet Fuels Combustion Program: Practical and Scientific Impacts of Alternative Jet Fuel Research," *2018 AIAA Aerospace Sciences Meeting*, 2018.
7. Peiffer, E. E., Heyne, J. S., and Colket, M. B., "Characteristic Timescales for Lean Blowout of Alternative Jet Fuels," *2018 Joint Propulsion Conference*, Reston, Virginia: American Institute of Aeronautics and Astronautics, 2018.
8. Edwards, J. T., "Reference Jet Fuels for Combustion Testing," *55th AIAA Aerospace Sciences Meeting*, 2017, pp. 1–58.
9. Hastie, T., Tibshirani, R., and Friedman, J., *The Elements of Statistical Learning The Elements of Statistical Learning Data Mining, Inference, and Prediction, Second Edition*, 2013.
10. Kroenlein, K., Muzny, C. D., Kazakov, A. F., Diky, V., Chirico, R. D., Magee, J. W., Abdulagatov, I., and Frenkel, M., "NIST/TRC Web Thermo Tables (WTT)," *US Secretary of Commerce*.

11. Hendershott, T. H., Stouffer, S., Monfort, J. R., Diemer, J., Busby, K., Corporan, E., Wrzesinski, P., and Caswell, A. W., "Ignition of Conventional and Alternative Fuel at Low Temperatures in a Single-Cup Swirl-Stabilized Combustor," *2018 AIAA Aerospace Sciences Meeting*, 2018.
12. Arthur H. Lefebvre & Dilip R. Ballal, *GAS Turbine Combustion: Alternative Fuels and Emissions*, 2015.

Solar Tracker

Student Researchers: Kylon J. Payne and Lynnae S. Frisco

Advisor: Dr. Augustus Morris, Jr., P.E.

Central State University
Manufacturing Engineering Department

Abstract/Objectives

The sun provides one of the cleanest and most abundant forms of energy known as solar energy. Solar energy is used by collecting or absorbing solar radiation emitted by the sun. Solar energy as mentioned before is a clean form of energy but it is hard to capitalize on. In order to create energy, the radiation from the sun must be absorbed, collected and converted into heat or electricity, but the amount of radiation the Earth receives varies from day to day which means the amount of electricity or heat would vary as well. The weather, location, time of day, season and the landscape can affect how much radiation reaches the earth's surface (ENERGY.GOV). When the sun is at its peak point of the day that is when the earth receives all energy possible (Energy.com).

Although the sun provides solar energy it still must be converted into useful energy such as electricity and heat. For example, in the 1830's, British astronomer John Herschel used a radiation from the sun and converted it into heat energy to cook food (EIA.GOV). Since the 1830's solar energy has advanced and can be used for heating water in homes and pools, heat the inside of homes and to heat fluids in solar thermal plants (EIA.GOV). Some examples of the technologies are the Photovoltaic cells (solar cells) and concentrating solar power. The main differences between the two is that one of them are used to convert solar energy into electricity and the other converts it into thermal energy.

Photovoltaic cells (PV cells) are one of the most common examples of converting solar energy to electricity. These cells work by putting a negative layer (usually Phosphorus doped N type silicon) on top of the positive layer (Boron doped P type silicon) which create an electrical field (fsec.ucf.edu). Once sunlight strikes the surface the electrical field provides momentum that results in a current when connected to an electrical load (fsec.ucf.edu). Depending on the size and amount of PV cells determines the amount of electricity that can be used. The bigger the structure the more electricity. It is important that the cells remain focused on the high point of the sun to maximize the amount of electricity.

Another type of solar technology is the concentrating solar power such as the parabolic trough, parabolic towers and dishes (seia.org). Both of these concentrators work similarly by using mirrors to collect scattered rays into one focal point. The mirrors then reflect the focal point and bounce it back to a receiver tube that absorbs the radiation. Usually the tube is filled with a heat transfer substance such as oil or water. This energy is then used to drive a conventional steam turbine to generate electricity, this energy can also be stored for later use (seia.org).

Solar towers use thousands of heliostats (mirrors with tracking capabilities) focus the sun's rays onto a boiler, which sits at the top of the tower and produces steam (nurenergie.com). Towers are not as reliable as parabolic troughs, but it does have one less step than the troughs as it does not require a heat exchanger. Since the towers do not require a heat exchanger that means that they have less energy loss and maximize on the energy (nurenergie.com). Here in the United States there are many solar tower

projects that are currently active, an example are the solar towers in California in the Mojave Desert, the Ivanpah facility (seia.org). This project consists of 173,000 heliostats and three power towers that could provide power to over 100,000 Americans (seia.org).

Parabolic troughs function by setting up a field of mirrors that concentrate the sunlight to a focal point onto a receiver tube that runs across the mirror (Nurenergie.com) The receiver tube is filled with a heat transfer material such as water or oil to produce steam through a heat exchanger. Troughs are one of the most reliable forms of concentrating powers, in fact the United States have many active parabolic trough projects as well. Northeast of Los Angeles is the Abengoa Solar Inc. This is a solar power plant that is spread across 1,765 acres and has the capabilities of powering approximately 90,000 Americans. The disadvantages of the trough is that the mirrors for the trough are more expensive than the towers flat heliostats (nurenergie.com). An advantage for the troughs is that they are more commercially used, 97% of solar power plants use parabolic trough (nurenergie.com).

Solar dishes are similar in concept to both the solar towers and the parabolic troughs. The solar dish has a thermal receiver collects the solar energy and converts it into heat energy, this heat is then sent to the engine or the generator (seia.org). Mainly in dishes the use a Stirling engine that uses the heated fluid to move pistons and create mechanical power (seia.org). In Utah, the US army has begun a solar dish project that is 1.5 MW system with 429 Stirling engine dishes (eia.gov).

Our project is a solar concentrator which will be used to absorb and intensify the radiation emitted from the sun. This concentrator will have a solar desalination system attached with it so as the radiation is being concentrated the system will use that thermal energy to purify salt water. In nature solar desalination occurs by the rain that is made through absorption of sea water. Solar desalination systems function similarly to the earth's water cycle. The concentration of the radiation should be enough for successful use of a solar thermal desalination system.

Solar radiation also known as solar resources is the electromagnetic radiation emitted by the sun (energy.gov). When solar radiation is captured this source can be used by converting it to a useful energy such as thermal energy or electricity. As mentioned previously there are many technologies that can convert solar radiation into a useful energy.

The amount of solar radiation the earth receives in any spot is based in the location, time, season, landscape and the weather. For example, on clear dry days atmospheric conditions reduce the radiation by 10%, but on thick cloudy days radiation is reduced by 100% (energy.gov). This occurs because atmospheric conditions can cause the rays to scatter and diffuse. On cloudy days the atmospheric conditions scatter the rays and into short wavelengths and the earth receives diffused radiation (appdsolarradiation). On clear days the radiation is direct meaning that the solar radiation emitted by the sun directly reaches the earth. There are also reflected radiation which is radiation that is reflected after striking the surface (appdsolarradiation). For example, the ground, grass and snow can all reflect back the solar radiation.

The United States receive the maximum amount of solar energy in the summer because of the positioning of the sun (Energy.gov). On average the earth's distance from the sun is about 9.3×10^7 miles being the closest to the sun around January 1st and becomes further away around July 1st (appdsolarradiation). The intensity of the solar radiation is greater when the incidence angle is less meaning that the angle between the sun and the earth is closer to 0.

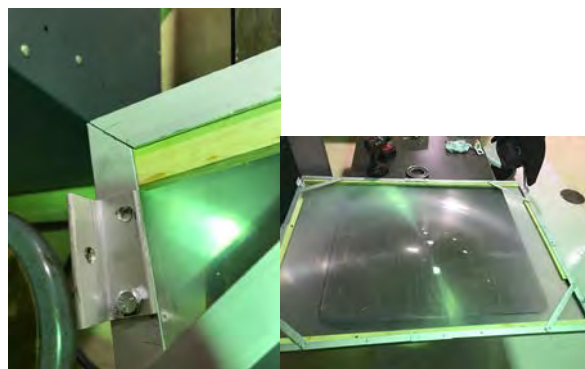
Methodology

We will program a razor scooter to rotate the base of the frame. The motor will be connected to solar panels one with the positive to positive and the other with the positive to the negative. When the sun strikes the solar panel, the panel will power the motor and the panel receiving the solar energy will instruct the motor in the required direction for the motor to turn. The motor will also need to be further programmed that way the motor knows when to stop and to prevent it from turning in a constant circle. In order to achieve this, we will also need to use a raspberry pi to help program the motor. This motors only task is to rotate the base and the use of a shaft prevents the base from moving up and down.

The top of the frame will need an actuator or pulley system that will move the frame up and down.

Optical lens were first discovered in the ancient times, about 700 B.C. They were discovered from ancient Egyptians and Mesopotamians polishing different crystals attempting to reproduce the optical abilities that they observed can be made in water. Friar Salvino D'Armate was a person who changed optics dramatically. In 1284, Friar Salvino D'Armate created the first wearable eyeglass. Optical specifications are used throughout the design and manufacturing of a component or system to illustrate how well it meets certain performance necessities. Specifications are useful because they give the correct limits of important limitations that oversee the performance of the system. Also, they tell you the right amount of time and money that should be used on manufacturing.

It is believed the type of lens that is being used in the project is a Fresnel lens. The basic idea behind a Fresnel lens is a plastic magnifying glass lens and slicing it into a bunch of concentric rings. A common application for a Fresnel lens is the collection of solar light. A Fresnel lens for light collection is known for absorbing light to heat a surface. A Fresnel lens can be used in a home for different applications such as heating the house itself, or possibly a pool. Depending on the size of the screen, a Fresnel lens can cost from \$300 to \$27,000. Our screen is 50 inches long and 38 inches wide, and weighing about 11.384 pounds. There is a piece of wood screwed into each side of the screen. The wood screwed to the 38-inch sides on the screen is 22 inches long weighing about 0.253 pounds each. The wood screwed to the 50 in sides of the screen is 50 inches long weighing about 0.575 pounds each. After the wood, there were pieces of aluminum, which came from an old chalk board, cut down and fitted for each side. The aluminum pieces were cut to be half an inch longer than each side. There were two pieces that are 50.5 inches and weighing 1.57752381 pounds each. The other two pieces are 38.5 inches long and weighing 1.20266667 pounds. Once all of these pieces were assembled, there were four clips screwed on to the 38.5-inch side, 2 clips on each side. The clips are going to be used to attach the aluminum arms to the frame, shown in the pictures below.



The aluminum arms, 38 inches each, were attached to the frame on the clips. The arms that were on the same side were then connected together by a screw to create a pivot point. Also attached with the arms at the pivot are two small wood bases, which will be attached to the base, will also be used to make stabilize and balance the frame. This can be seen in the pictures below.



The base serves as an aid to rotate the lens frame in order to obtain the maximum solar energy by keeping the energy at the lenses focal point. Since the earth appears to rise from the east and sets in the west, we have implemented solar panels to direct the motor to rotate the base either clockwise or counter-clockwise through a shaft, 3 ½ " and 4" sprocket and chain pulley system using sprockets and bike chains. This rotation will follow the solar panels direction as the sun rises and sets.

The base is designed and built to support all of the components of our solar concentrator including the; Frame, Solar Panels, and the weight of the two combined. We will use two 59 inches in diameter circular wooden table tops as our base. The two table tops will be placed in parallel to each other 11" apart with the faces of the table tops facing the earth. In between the two table tops there is a series of things including a 3D printed hub to support the 5/8" in diameter shaft following a bearing. The shaft will be 7" inches long and it will serve as the point of rotation for the table top and or the base. For the bottom half of the table top we designed 4 wooden blocks that has 2" diameter wheels that are free of rotation. The wheels will make it easier for the table top to rotate. Attached to the base are two solar panels that outputs 42 Volts of power. The energy from the solar panels will operate our motors by producing the needed voltage for the motor to run. The motor powered is serving as the rotation of the base through a shaft, sprocket, and chain pulley system. We have 3D printed a hub that fits the shaft of the motor. This hub will be assembled with a bike sprocket to support the pulley system that we've chosen for the base. The shaft of the motor and the shaft of the base are in parallel to support our pulley system.



Motor and shaft with sprocket:



Table tops with wheels:



Center shaft with sprocket

In conclusion, the goal of this project is to absorb and intensify the radiation admitted from the sun by using a solar tracker. A solar desalination system is planned to be attached with the solar tracker so as the radiation is being concentrated the system will use that thermal energy to purify salt water. Solar desalination occurs in nature by the rain that is made through absorption of sea water. Solar desalination systems function similarly to the earth's water cycle. Solar energy is one of the cleanest and most abundant forms of energy, which is provided by the sun. We hope with the success of the project it is able to help countries and/or that lack states that lack the ability to receive clean water.

References

1. Batista-Rodríguez, Carlos R., et al. "Indexes for the Evaluation of a Solar Tracker*." *Ingeniería y Desarrollo*, vol. 36, no. 1, Jan. 2018, pp. 172–186., doi:10.14482/inde.36.1.10945.
2. Chaudhary, Ghulam Qadar, et al. "Small-Sized Parabolic Trough Collector System for Solar Dehumidification Application: Design, Development, and Potential Assessment." *International Journal of Photoenergy*, vol. 2018, 2018, pp. 1–12., doi:10.1155/2018/5759034.
3. Davis, Arthur. "Fresnel Lens Solar Concentrator Derivations and Simulations." *Novel Optical Systems Design and Optimization XIV*, Aug. 2011, doi:10.1117/12.892818.
4. Hijazi, Hamza, et al. "Mechanical Design of a Low Cost Parabolic Solar Dish Concentrator." *Alexandria Engineering Journal*, vol. 55, no. 1, 2016, pp. 1–11., doi:10.1016/j.aej.2016.01.028.
5. Islam, Majedul, et al. "Investigation of the Effect of Physical and Optical Factors on the Optical Performance of a Parabolic Trough Collector." *Energies*, vol. 10, no. 11, 2017, p. 1907., doi:10.3390/en10111907.
6. Muhammad-Sukki, Firdaus, et al. "Solar Concentrators."

Cant Angle Effect on Winglet Performance

Student Researcher: Nathaniel M. Payne

Advisor: Dr. Jed E. Marquart, P.E.

Ohio Northern University
Mechanical Engineering Department

Abstract

Winglets are used in many aircraft to improve performance. The performance of the wing is improved with the winglet by reducing drag due to wing tip vortices. Winglets also improve the lift to drag ratio of the aircraft. This paper discusses the effect of the cant angle on the performance of the wing. The lift to drag ratio (L/D) and the wing tip vortices was observed and compared between the various geometries. Of the cant angles studied, it was found that the 60° cant angle has the lowest drag coefficient. This geometry is optimal when fuel cost savings are a driving factor in the aircraft's design. The 30° case had desirable performance as well with the highest L/D.

Project Objectives

Induced drag is the component of drag that is due to the lift generated by the wing. The flow near the end of the wing has a strong effect on the induced drag because of the formations of wingtip vortices. One method of reducing drag due to wing tip vortices is the use of winglets. Because of the reduction in drag, the use of winglets is common in commercial aircraft as a fuel saving measure. Winglets are short, angled protrusions at the end of a wing that smooth the airflow at the tip of the wing. Winglet geometry is broken into three different parameters: sweep, twist and cant angle. The design parameter discussed in this paper is the cant angle of the winglet which is the angle the winglet makes with horizontal. Currently there is not considered to be an optimal geometry if general guidelines are followed. [1] The optimization of the design parameters of winglets for each application can lead to reduced drag and lower fuel costs for companies.

Three wing geometries were modelled using Solidworks with cant angles of 30°, 45° and 60°. Apart from the cant angle, the wings were identical. The airfoil used was the S1223 RTL which is a low Reynolds Number, high lift airfoil. This is the airfoil currently being used by the ONU SAE Aero team and is a perennial favorite amongst teams competing in the competition. The solid model was based upon dimensions that fall within the competition constraints as a base model.

To minimize the total number of points needed in the grid, only half of the wing was modelled. The half span of the wing was modelled as 2.0 m where the winglet length was 25% of the half span at 0.5m in length. There was no twist, sweep or taper in the wing or winglet. Figure 1 shows the dimensions of the wing for all three cases. The cant angle was varied between the three cases.

Methodology Used

The preceding geometries were next modelled in the Pointwise software. A flow block was created around the geometry. An unstructured grid was generated inside of the flow block. A symmetry boundary condition was applied to the domains in the wake block and flow block at the root of the wing. The domain at the front of the flow block was defined as a source boundary condition, causing flow in the positive X direction. The boundary conditions for the domains on the wing were defined as an adiabatic no slip solid wall. The following boundary conditions were defined as farfield.

To improve the results of the CFD run, a wake block was set up around the wing. The wake block consisted of an unstructured grid, finer than the rest of the flow block. Anisotropic tetrahedral extrusion meshing was used off the surface of the wing to better capture the boundary layer flow. A growth rate of 1.2 and triangle and quad cells were used. A maximum number of layers of 25 and full layers of 5 was used to generate the mesh.

The full grid was composed of around 2 million points and 8 million cells. Initial conditions were set to model the speeds seen at take-off where wing tip vortices are a more prevalent. The take-off speed for ONU's plane for the SAE Aero competition is estimated to be approximately 40 mph. Because the wing geometry is modelled around the same constraints, the initial conditions for the flow were based upon that velocity. Table 1 shows the initial conditions that were used.

Results Obtained

After running the three cases in Cobalt, the drag and lift coefficients were compared as well as L/D. The resulting values are shown in Table 2.

Based on these results, the 30° geometry provides the greatest increase in performance according when observing the lift coefficient and L/D. The 60° geometry had good performance as well with a comparable L/D and the lowest drag coefficient of the cases.

Post-processing was completed using the Fieldview software. The wing tip vortices can be observed in the wake of the wing as shown in Figure 2. Within the post processing the growth of the vortex was observed until it reached a maximum.

The streamline function of Fieldview was also used to model the flow inside and around the vortex. Seeds for the streamlines were placed near the leading edge along the winglet. The streamline paths show that the flow rotates about the center of the vortex as expected. Flow closer to the centerline of the vortex rotate about the centerline while moving away from the wing at a fast rate. Observing the streamlines further from the centerline shows similar rotation but at a slower rate.

Significance and Interpretation of Results

Of the cant angles studied, it was found that the 60° cant angle has the lowest drag coefficient. This geometry is optimal when fuel cost savings are a driving factor in the aircraft's design. The 30° case had desirable performance as well with the highest L/D.

If the study were to be repeated it is recommended to test a wing without a winglet. This would serve as a control to show the improvement over the wing without the winglet. Next would be testing at different angles of attack. Testing in this study was done at a 5° angle of attack. Variations in angle of attack would show how winglet flow characteristics change and has been done in other studies on winglet geometry. [3]

Figures and Tables

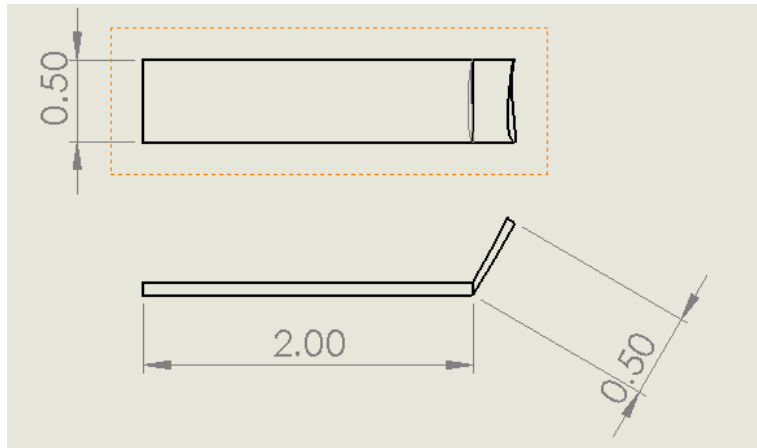


Figure 1. Dimensions of wing.

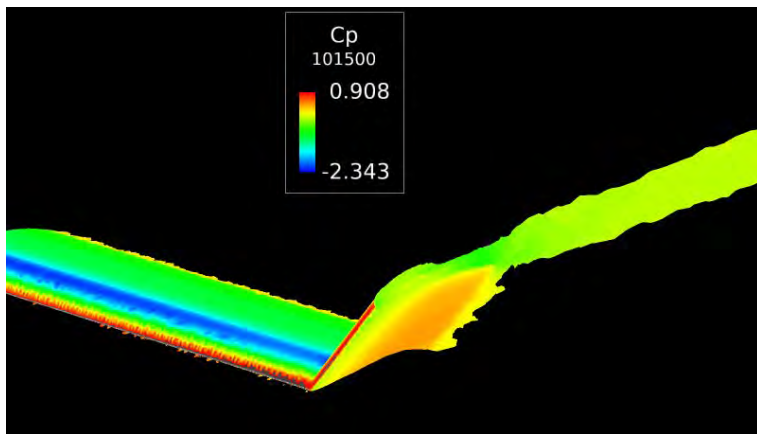


Figure 2. Wing tip vortex for 60° cant angle.

Table 1. Initial conditions used.

Pressure	101.3 kPa
Temperature	288 K
Mach	0.05213
Angle of attack	5°

Table 2. Results of Various Cant Angles.

	C_l	C_d	Pressure Drag Coefficient	Frictional Drag Coefficient	L/D
30 degree	1.5566	0.15935	0.15003	0.00932	9.77
45 degree	1.3419	0.17283	0.16375	0.00907	7.76
60 degree	1.4177	0.1541	0.1449	0.00919	9.20

References

1. Eslam Said Abdelghany, Essam E Khalil, Osama E Abdellatif and Gamal elhariry (2016) Air Craft Winglet Design and Performance: Cant Angle Effect. *J Robot Mech Eng Resr* 1(3): 28-34.
2. Cobalt Manual, Version 7, Cobalt Solutions, LLC, Dayton, OH, 2015.
3. Khalil, E. E., Helal, H., Abdellatif, O., & Elharriri, G. M. (2017). Aircraft-Blended Winglet Performance Analyses. *55th AIAA Aerospace Sciences Meeting*. doi:10.2514/6.2017-1838
4. Pointwise User Manual

Sizing the Solar System

Student Researcher: Nicole A. Peters

Advisor: Dr. William Jones

Cedarville University
School of Education

Abstract

Sizing the Solar System is a lesson geared towards Middle School Students and is focused on the planets in our universe and allows for interdisciplinary content in mathematics. The goal for this lesson is for students to have a greater understanding of how large the universe is and the planets that are in it. Students, in groups, will be comparing and contrasting the different sizes of the planets as well as their location from one another. Students, using a number of written clues, will complete a space mission by determining the volume and diameter of each planet in our Solar System. Students will have to use their knowledge of spheres, the circumference formula, and proportional reasoning to determine the diameter of each planet. After finding all of the information about each planet students will be provided with a hands on scale model of the solar system using everyday items like basketballs, tennis balls, etc. which all represent a specific planet. Using the scale model items of the solar system the students will determine which object represents which planet and manipulate them to put them in the correct order from the Sun to Neptune. This lesson requires students to use their background knowledge of the solar system as well as collaborate and communicate with their group to complete the space mission assigned to them.

Lesson

Students will work in groups of 3-4 to complete the space mission presented to the class. The students are assigned the mission at the beginning of the class period and will fill out the worksheet as they work through each clue. Students will start the mission by receiving one clue in an envelope. Students must find the diameter of the planet asked for before moving onto the next clue. There are eight clues total and the group will move on to the next clue after finding the diameter of the planet from the clue before. Each clue provides the group with enough information to find the diameter of another planet through proportional reasoning, converting miles to km, or converting radius to diameter. At the end of the lesson the students will list the planets from smallest to largest based on their diameter. All groups, after completing the mission, will work together to create a scale model of the solar system using the items available using what they learned about the different sizes of the planets. Each planet matches with one ball proportionally, Sun: exercise ball, Mercury: pool ball, Venus: baseball, Earth: tennis ball, Mars: cricket ball, Jupiter: volleyball, Saturn: basketball, Uranus: soccer ball, and Neptune: soccer ball.



Name:

Space Mission

"Hello, scientists NASA needs your help! Today with 3-4 other scientists you will be given a number of clues to help complete the mission. Each clue will give you enough information to find the diameter of one planet before moving on to the next clue. You will need to use what you know about proportional reasoning, converting miles to km, and converting a radius to diameter to determine the diameter of each planet. The mission is complete when you have found the diameter of each of the 8 planets. Make sure you record all diameter measurements to the best place and show your work! When your group is finished check your work with the head scientist in the lab."

Space Mission Clue:

Given:

Diameter of the sun is 1,392,000 km

Clue one: The center of the solar system is the Sun and what fun that its diameter is about 285.29 times bigger than Mercury. What is the diameter of Mercury?

Mercury:

Clue two: The earth relies on the sun for energy and lots of things. The sun is about 109.125 times bigger than the earth. What is the diameter of Earth?

Earth:

Clue three: Venus is Earth's neighbor in the solar system. Earth's diameter is 652 km more than Venus. What is the planet Venus's diameter?

Venus:

Clue four: Saturn has many rings and has a radius of 90,265 km. What is the diameter of Saturn?

Saturn:

Clue five: You have made it this far you get a bonus planet:

Jupiter which has 67 moons has a diameter of 83,865 miles

Scientists use the metric system for their measurements looks like you'll have to convert miles to km first

1 mile = 1.609 km

Jupiter:

Clue six: Uranus, also referred to as the ice planet, is 2.7911 times smaller than Jupiter. What is the diameter of Uranus?

Uranus:

Clue seven: Neptune, the 7th planet from the sun, is 1,590 km less than Uranus. What is the diameter of Neptune?

Neptune:

Clue eight: Mars, also called the red planet, has a diameter of 4,217 miles. What is the diameter of Mars?

Scientists use the metric system for their measurements looks like you'll have to convert miles to km first

1 mile = 1.609 km

Mars:

- List all 8 planets and the sun from smallest to largest:

Congratulations! You and the other scientists have completed NASA's mission!

Space Mission Answer Sheet

Clue 1. Mercury: 4,879 km

Clue 2. Earth: 12,756 km

Clue 3. Venus: 12,104 km

Clue 4. Saturn: 120,536 km

Clue 5. Jupiter: 142,984 km

Clue 6. Uranus: 51,118 km

Clue 7. Neptune: 49,528 km

Clue 8. Mars: 6,792 km

- List planets and sun from smallest to largest:

Mercury, Mars, Venus, Earth, Neptune, Uranus, Saturn, Jupiter, Sun

Objectives

The goal for this lesson is for students to have a greater understanding of the immensity of our universe and the planets that are in it.

- Students can compare and contrast the different planets and the sun based on their size
- Students can use proportional reasoning and measurement conversions to find the diameter of each planet in the solar system.
- Students can create a scale model of the solar system using everyday items.

Alignment

- English Language Arts

SL.5.1 Engage effectively in a range of collaborative discussions (one-on-one, in groups, and teacher-led) with diverse partners on grade 5 topics and texts, building on others' ideas and expressing their own clearly.

- Math

Convert like measurement units within a given measurement system.

5.MD.1 Know relative sizes of these U.S. customary measurement units: pounds, ounces, miles, yards, feet, inches, gallons, quarts, pints, cups, fluid ounces, hours, minutes, and seconds. Convert between pounds and ounces; miles and feet; yards, feet, and inches; gallons, quarts, pints, cups, and fluid ounces; hours, minutes, and seconds in solving multi-step, real-world problems.

Understand the place value system.

5.NBT.4 Use place value understanding to round decimals to any place, millions through hundredths.

- Science

EARTH AND SPACE SCIENCE (ESS)

5.ESS.1: The solar system includes the sun and all celestial bodies that orbit the sun. Each planet in the solar system has unique characteristics. The distance from the sun, size, composition and movement of each planet are unique. Planets revolve around the sun in elliptical orbits. Some of the planets have moons and/or debris that orbit them. Comets, asteroids and meteoroids orbit the sun.

Underlining Theory

This lesson is based on a constructivist learning approach. This theory suggests that students' gain knowledge and meaning from their experiences. Students have the opportunity to interact with new science content through experience. The students throughout this lesson will construct new knowledge about the immensity of the solar system through hands on group and class activities. Students will be collaborating with other students in their group to complete the space mission. The mission activity requires students to apply science and math content they know to successfully complete the mission. The new information gained during the class group activity allows the students to work with the whole class to create a hands on scale model of the solar system.

Student Engagement

The group activity incorporates a hands on approach and the success of the mission depends on the communication and collaboration of each member in the team. Students are working in groups of 3-4 to complete the space mission. This lesson also provides the students with time to come together and complete the solar system scale model activity using the new information gained from their group work. Students are gaining information about the different planets and their sizes through the group activity as well as the hands on scale model activity completed by the whole class. All groups at the end of the class will come together and discuss what information they all gained from their group activity so they can successfully construct the scale model.

Resources

Each group will need a calculator and each student will need a pencil and a space mission worksheet. Each group will need all 8 of the clues in a separate envelope. The whole class will be creating a scale model at the end of the space mission activity which requires nine different sports balls. They will need to be a bucket or box in the classroom with a yoga ball, basketball, two soccer balls, pool ball, tennis ball, cricket ball, baseball, and volleyball which will all be used to represent one of the planets or the sun in the solar system scale model. The worksheet that each student receives to complete the space mission was altered from the "Scale Models of the Solar System" lesson plan in the Aerospace Education Services Project.

NASA Resources:

1. https://www.nasa.gov/sites/default/files/546148main_ESS8_ScaleModelsOfTheSolarSystem_C3_Final.pdf
2. <https://nssdc.gsfc.nasa.gov/planetary/factsheet/>

Results

The results of this lesson should be each individual student working in a group to complete the space mission worksheet. Each student should complete and turn in their own worksheet which has the measurements of all the diameters of the 8 planets. Each student should also list the planets from smallest to largest based on the diameter on their own worksheet. The whole class should accurately construct a scale model of the solar system including the sun and the 8 planets using nine different sports balls based on the measurements found in the group activity.

Assessment

Each student will be assessed based on group participation and completion of their own worksheet. The worksheet requires the team to piece together the eight clues to find the diameter of each planet. Students will be graded on the accuracy of those eight measurements and if they listed the 8 planets and the sun from smallest to largest correctly.

An additional assessment could be a creative writing assignment. The students could write a 4-5 sentence paragraph about the immensity of the solar system. The students can look to the scale model of the solar system created in class of the planets and the sun for ideas.

Conclusions

The lesson allows students to work in groups to compare and contrast the sizes of the different planets in our solar system. After gaining correct measurements from the eight clues about the measurements of the planets the students can correctly create a scale model of the solar system. Students will be able to communicate and work through the mission with their fellow classmates through a group and class hands on activity.

Fuzzy Logic Based 2-Player Tetris

Student Researcher: Lynn K. Pickering

Advisor: Dr. Kelly Cohen

University of Cincinnati
Aerospace Engineering

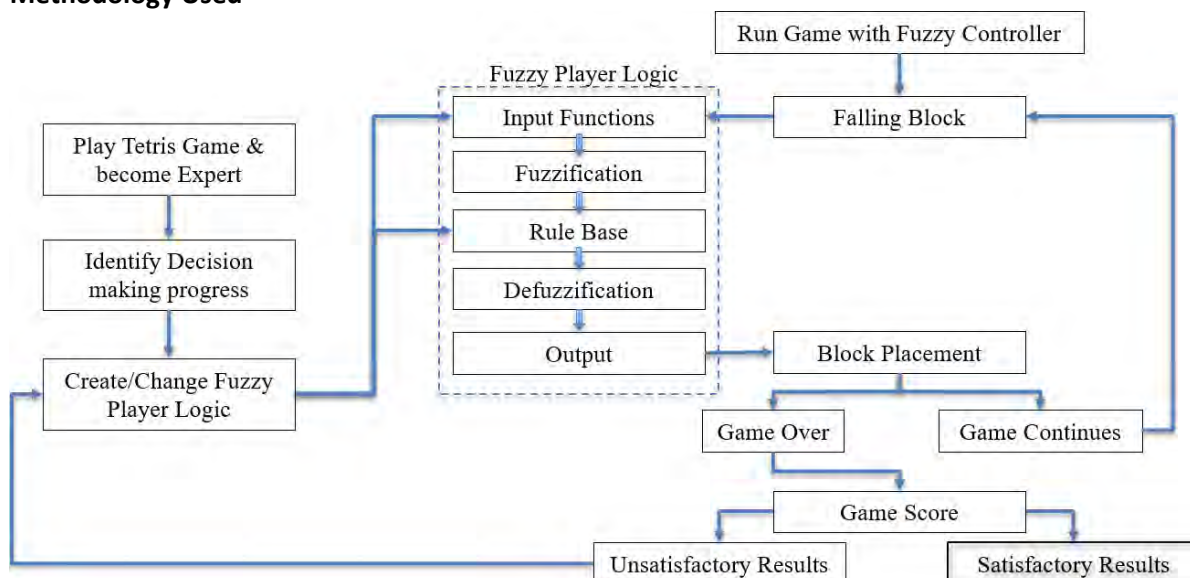
Abstract

Tetris is normally a single player game, the objective being to place four-piece blocks and clear as many rows of blocks as possible. The game requires quickness and flexibility in its decision making, which makes it a good candidate for Fuzzy Logic decision making. To test the capabilities of a Fuzzy Logic Tetris Player, a two player Tetris game was created, so it could be directly tested against a human. After the game was played repeatedly, input functions and rules were created and iterated upon using identified faulty decisions from previous runs. The Fuzzy Logic Tetris Player scores similarly to a beginner Tetris Player. In a two-player game the Fuzzy Logic Tetris Player shows its strength in the upper levels due to its faster decision making than the human but shows its weakness on the earlier levels when the human player can use the extra time to make better decisions. Because of the complexity added by any further inputs, a Genetic Algorithm would be needed to train the inputs, membership functions and rules to achieve a higher level for the Fuzzy Player.

Project Objectives

In this project the objective was to create a Fuzzy Logic Tetris Player and test the player against a human opponent in a two player Tetris game. The goal was for the Fuzzy Logic Player to be comparable in skills to a beginner human Tetris player. To achieve this, the project was broken down into three sub-objectives. First, the decision making process behind playing the Tetris game is determined. Then a Fuzzy Logic Tetris Player is created based on these processes. Finally, a two player Tetris game is created with one of the players the Fuzzy logic player.

Methodology Used



There are three inputs that the Fuzzy Logic Player uses to position the falling block. For the Holes input the Fuzzy Player calculates the number of holes created for each spin of the block (4) and each position of the block (10): 40 total combinations. For the balance input the Fuzzy Player calculates the height the blocks will reach for each spin of the block (4) and each position of the block (10): 40 total combinations. For the row input, the Fuzzy Player calculates how many rows will be cleared for

each spin of the block (4) and each position of the block (10): 40 total combinations, because in Tetris, the more rows cleared at once, the higher score received.

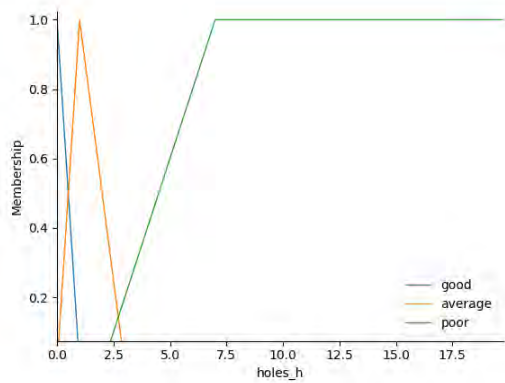


Figure 1. Input Holes.

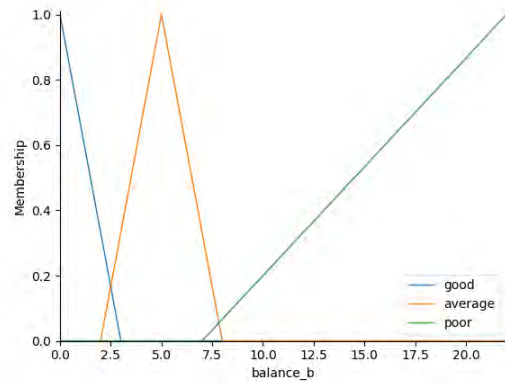


Figure 2. Input Balance.

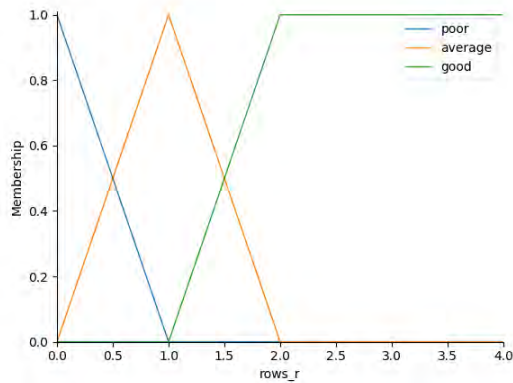


Figure 3. Input Rows.

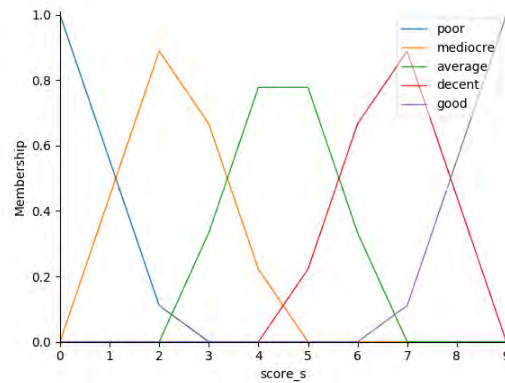


Figure 4. Output.

Results Obtained

The Figure below shows ten trial runs of the Fuzzy Tetris Player playing the Tetris game by itself. The Fuzzy Logic Tetris Player scores similarly to a beginner Tetris Player. In a two-player game the Fuzzy Logic Tetris Player shows its strength in the upper levels due to its quick decision making, and shows its weakness on the earlier levels when the human player can use the extra time to make better decisions.

Trial	Lines Cleared	Level	Score
1	16	3	4593
2	21	4	3528
3	30	6	7376
4	43	8	12723
5	22	4	3739
6	18	4	5404
7	17	3	3755
8	15	3	4221
9	24	5	5876
10	31	6	6064

Figure 5. Sample Tetris Runs (Single Player).

Acknowledgments

Without the help and Guidance of my mentor, Dr. Kelly Cohen, and the support from the Ohio Space Grant Consortium, this project would have not been possible. Thank you!

Robot to Clean Fresh Water Pipes

Student Researcher: David B. Prigg

Advisors: Dr. Roger Quinn and Dr. Richard Bachmann

Case Western Reserve University
Mechanical Engineering Department

Abstract

Clean water is at the core of any city's infrastructure. Clean tap water is often something that is taken for granted, however when water systems get old, impurities can build up in the water pipes causing cloudy and unpleasant drinking water. These piping systems travel from the purification plants to major cities for distribution. A pipe cleaning robot would allow for an automatic, uninterrupted way to prevent sediment buildup in pipes. This robot would agitate particulate on the bottom of the pipe and suck it up through a filter to remove it. For the process to be automated, the robot must be able to navigate through the pipe system, be able to recharge, and clean the filters. The unit will be fully submerged in a high-pressure environment. The robot must not release any harmful toxins as it will be in contact with already treated drinking water. Optimal locomotion, filtration, and control will be tested and compared, then combined to create a functional prototype. From here, iterations can be made to improve performance and make the design more robust. This paper is an introduction to the layout of the project along with more detailed locomotion testing.

Project Objectives

The main problem this project sets out to solve is cleaning sediment in fresh water pipes, particularly Cleveland Water Department water system. In this system, water is taken from four main intakes deep in Lake Erie and pumped to one of four different treatment sites. Alum is used as a coagulant, creating large particles that can be easily filtered out. The water goes through a sand and coal filter process as well as receives added chemicals such as chlorine and fluoride. The treated water is then pumped to storage locations as well as for residential use [5]. However, some of this alum, sand, and charcoal gets through, building up overtime on the bottom of the concrete and steel pipes. These pipes also break down and chip away or corrode, adding unwanted particulate to the water. Once the sediment builds up enough it can be swept up by turbulence, causing the tap water to come out cloudy and dirty. The goal of this project is to determine the most feasible methods for creating a fresh water pipe cleaning robot. The first step is to quantify many of the key problems that will be faced, then determine the best possible solution or solutions to perform lab testing on. The main systems are locomotion, filtering, power systems, and control. Some of these topics are heavily interdependent and require compatibility to be a single functioning product.

Beyond a general overview of the project, the focus will be locomotion. Overall shape and size of the robot can be determined as well as a method for navigating the pipe system. Before starting a basic design, a model of the environment must be built. This will include any parameters and information needed to make design decisions, either gathered through previous research and studies or from the Cleveland Department of Water directly.

Methodology Used

The robot's overall operation will require autonomous control which begins at a base "home" station which would be a storage location for the robot when recharging, swapping filters, or receiving maintenance. This area will be able to be drained of water and depressurized. Once released into the pipe, the robot will begin cleaning along a designated path. Depending on battery life and storage capacity, smaller robots might be used to bring more battery packs and swap filters with the cleaning robot. This could be more time and energy efficient and will have to be studied further.

In order to begin comparing different design decisions, an understanding of the environment and task needed to be further developed. The size of piping is between 42 and 54 inches. Some sections of pipe are made from steel while others are made from a steel wire compressed concrete (PCCP). The size and material of the pipes will drive many of the design decisions since the robot must fit within the pipe and be able to maneuver sufficiently. The pipe systems are quite vast, the area of focus is many miles long. Due to the long stretch of pipe required to be traveled, an efficient locomotion method must be chosen. When comparing maneuverability, complexity, traction, and stability, wheels or treads were the two top options. Looking at past robots under similar conditions, most used wheels or treads [1, 3].

The main difference with the current robots for cleaning and probing pipes is that they are tethered. This means that they can receive power and assistance from an outside source. Since we want this robot to be autonomous and be able to clean many twisting and turning passageways of the water mains, having a tethered robot is not feasible. Ideally, the robot will be able to be powered by batteries which can be swapped out and recharged. Forming a self-sustaining system will be a point of focus for many of the design decisions.

Further examining the locomotion aspect of the robot, it must be able to withstand the flow of the water in the pipe. Using data given by the Cleveland department of Water, the normal average flow rates experienced are between one to two feet per second. The maximum average flow rate is upwards of five feet per second. This will cause a significant amount of force on the robot. In order to minimize the drag force on the robot, a low profile aero-dynamic design should be incorporated. To combat the high drag, the robot should be relatively heavy, adding a higher normal force, increasing friction. It is likely that a method of downforce production will be required to further increase the friction between the robot and pipe in order to sufficiently move and stabilize it under heavy flow conditions. Taking the five feet per second flow case, we can model the robot as a rectangular box. Initial estimates will one-hundred kg for the mass of the robot, a width of 0.5m, height of 0.25m, and length of 0.8m. Since the Reynolds number of this flow in all the pipe shapes is around the maximum allowable number for laminar flow, as an initial calculation it should be safe to assume the flow is laminar with a Reynolds number of 2300. Assuming a non-laminar boundary layer (just using average velocity), the total drag on the robot is:

$$D = C_D * 0.5\rho U^2 A = (2.5)(0.5) \left(\frac{1000\text{kg}}{\text{m}^3} \right) \left(\frac{1.524\text{m}}{\text{s}} \right)^2 (0.25\text{m})(0.5\text{m}) = 362\text{N}$$

D is the drag force, C_D is the drag coefficient, ρ is the fluid density, U is the average velocity, and A is the cross-sectional area. The largest force the robot should feel due to the flow is around 362N. In order to counteract this, the frictional force would have to be larger than this value. Assuming a friction coefficient for rubber and wet concrete contact to be around 0.3 [4]. After subtracting the buoyancy force, the friction force is only 196N, not enough to safely maintain contact between the surface. Due to the pipe shape and surface conditions, suction will not be possible. A mast will need to be designed to provide this downforce.

A debris study will be another point of interest. With the vastly differing size particles as mentioned previously, filtering could be a challenge. Varying filter systems will be tested to determine what kind of filtering combinations work best. For the larger particulate, cyclonic filtering will be tested, and various filter sizes will be used to get the finer particulate. We have concluded that actual lab testing of samples will lend the best results as sludge particulate varies widely depending on the location of the water and pipes.

Results / Future Work

Since this is just the planning stage of the project, nothing has been physically built or tested. However, initial calculations and flow simulation lead to the requirement of the mast to create downforce as the drag force is too high for the robot to overcome with just the friction due to the weight of the vehicle. This is helpful to know, since this was a major design consideration to ensure proper and safe functionality.

The first things to be tested is the filtering method as well as the locomotion. Power and control systems will be kept in mind shortly after. Once preliminary designs and tests have been simulated. A prototype will be built and tested in lab experiments to simulate the pipe conditions.

References

1. Albitar, Houssam, et al. "Underwater Robotics: Surface Cleaning Technics, Adhesion and Locomotion Systems." *International Journal of Advanced Robotic Systems*, vol. 13, no. 1, 2016, p. 7, doi:10.5772/62060.
2. Saenz, Jose, et al. "Robotic Systems for Cleaning and Inspection of Large Concrete Pipes." 2010 1st International Conference on Applied Robotics for the Power Industry (CARPI 2010), 2010, doi:10.1109/carpi.2010.5624448.
3. Law, Wei Chuan, et al. "A Study of In-pipe Robots for Maintenance of Large-Diameter Sewerage Tunnel." *The 14th IFToMM World Congress*, pp. 1-8, 2015
4. Engineers Edge, LLC. "Coefficient of Friction Equation and Table Chart - Engineers Edge." Engineersedge.com, www.engineersedge.com/coefficients_of_friction.htm.
5. "Cleveland Water Department." Cleveland Water Department, www.clevelandwater.com/.
6. "Internal and External Flow." *Introduction to Thermal Systems Engineering: Thermodynamics, Fluid Mechanics, and Heat Transfer*, by Michael J. Moran, Wiley, 2003.

Effects of Fuel Oscillation on Flame Spread in Microgravity

Student Researcher: Evan N. Rose

Advisor: Dr. Vedha Nayagam

Case Western Reserve University

Department of Mechanical and Aerospace Engineering

Abstract

The rate at which flames spread over a solid fuel surface gives a measure of the flammability of the fuel in a given environmental condition. Historically, opposed and concurrent flame spread rates over stationary solid fuel samples have been studied in great detail, and standardized flammability test methods have been developed based on flame spread rates to screen materials used in a spacecraft. This project supports a study to investigate the effect of longitudinal vibration on opposed-flow flame spread over thin solid fuels. The longitudinal vibration of the fuel is hypothesized to alter the boundary layer characteristics adjacent to the fuel surface, and accelerate the flame spread process. Preliminary tests under normal gravity conditions support this hypothesis. An experimental setup was to test flame spread rates in microgravity onboard the Blue Origin New Shepard suborbital vehicle, which provides a microgravity environment for approximately two minutes. During the experiment, the fuel vibration frequency and acceleration will be varied and the resulting flame spread process will be recorded for later analysis.

Background and Project Objectives

Research on flame behavior in space is used to improve safety standards for manned microgravity environments such as crew capsules and the International Space Station. Combustion in an oxidizing environment that is not constrained by gravity spreads rapidly in all directions (controlled by diffusion) and could be deadly to the astronauts on board. Specifically, NASA Technical Standard NASA-STD-6001 details comprehensive flammability requirements for materials intended for use in space environments [1]. However, this standard does not take into account certain operating conditions that may increase material flammability; oscillating materials, such as those mounted to vibrating machinery, could pose a greater fire safety risk.

In Earth's gravity, downward flame spread over a thin solid fuel is controlled by convective flow from air due to buoyancy. The high temperature in the combustion zone pulls more air towards the flame, increasing the reaction rate. This effect can be approximated by inducing an air flow over the fuel surface to simulate the convective air flow, and can be described using a simplified convective-conductive energy balance:

$$\rho_s c_s V_f \tau (T_v - T_\infty) = k_g \delta_x \frac{(T_f - T_v)}{\delta_y} \quad (1)$$

where ρ_s is the fuel density, c_s is the fuel heat capacity, V_f is the flame spread rate, τ is the fuel thickness, k_g is the thermal conductivity of the gas, and T_v , T_∞ , T_f are the fuel vaporization temperature, ambient gas temperature, and flame temperature, respectively.

For forced flow or natural convective flow, forward conduction length δ_x is assumed equal to the flame standoff distance δ_y , so the balance becomes:

$$V_f = constant * \left(\frac{k_g}{\rho_s c_s \tau} \right) \frac{T_f - T_v}{T_v - T_\infty} \quad (2)$$

The forward conduction length, which is dependent on flow velocity, cancels out of the equation; this shows that flame spread is independent of gas-phase velocity. Results from previous studies of opposed forced flow on flame spread over solid fuels by Hirano and Sato [2] and Fernandez-Pello et al. [3] support this finding as shown in Figure 1.

Gomaa and Al Taweel [4] showed that the introduction of oscillatory motion onto a flat vertical plate enhances heat transfer by creating a Stokes boundary layer on the surface of the plate. Their findings can be applied to the current problem by approximating the thin solid fuel as a flat plate. Additionally, the oscillating boundary layer has a significant effect on the gas-phase velocity, causing a further increase in flame spread rate. In this system, δ_x and δ_y are no longer equivalent; they become $\delta_x = \frac{g}{\omega^2}$ and $\delta_y = 2\pi \sqrt{\frac{2\nu}{\omega}}$, and flame spread is related to vibrational acceleration and frequency as follows:

$$V_f \propto \frac{g}{\omega^2}$$

The goal of this experiment is to investigate the effect of longitudinal vibration on flame spread in thin solid fuels in microgravity. The fuel used is cellulose-based filter paper, a commonly-used fuel for solid-fuel microgravity combustion. While the lack of convection during combustion under microgravity conditions causes a quiescent environment with no air flow, we hypothesize that the movement of the fuel induces a Stokes oscillating boundary layer and enhances the heat transfer to the fuel. This increases the temperature, and therefore the reaction rate, of the combustion reaction. This hypothesis has been corroborated by preliminary testing in normal gravity conditions. While NASA-STD-6001 provides a comprehensive list of test procedures, it does not include the influence of vibration on flame spread, which could increase the flammability of a previously approved material beyond acceptable levels.

The microgravity environment for this experiment will be provided by the Blue Origin New Shepard suborbital vehicle. Figure 2 shows the flight profile for the New Shepard. The suborbital vehicle will travel to a maximum altitude of 100km, and will provide microgravity conditions of less than 0.001g for 130 seconds. This provides sufficient time to measure flame spread rate in microgravity for several vibration frequencies. Our experiment is designed as a payload for the NanoRacks Feather Frame system, which places severe restrictions on the overall design. The experiment receives flight telemetry data from the suborbital vehicle, and is controlled autonomously using a Raspberry Pi microcomputer.

Methodology

The NanoRacks Payload User's Guide [5] specifies physical, functional and environmental design requirements associated with the experimental payload space, and describes the mechanical, electrical, and data interfaces between the payload and the New Shepard suborbital vehicle.

The payload design was driven mainly by the structural, safety, and interfacing requirements specified by Blue Origin and NanoRacks. The payload was required to comply with maximum dimensions of 101.6 mm x 101.6 mm x 203.2 mm and a maximum mass of 500 g, while providing enough rigidity to support a 15 lb load for an extended period of time. Heat release from the combustion reaction occurring within the experiment was required to be contained without igniting or transferring heat to neighboring payloads. As such, the enclosure was custom-designed from a combination of 3D printed ABS and laser-cut PMMA plastics to meet the specifications. Figure 3 shows the design of the experimental payload.

The experiment is controlled autonomously using a Raspberry Pi Zero microcomputer receiving telemetry data from the suborbital vehicle. The microcomputer triggers each experiment step and controls the other electronic components in the payload. The controller powers a wide-angle video camera that is able to capture the entire length of the fuel sample in-frame from with a short focal distance, and powers a motor to induce oscillation. It also controls a 5V supercapacitor that supplies power to a Kanthal igniter circuit used to ignite the fuel.

In preliminary ground testing of vibrating fuels, vibration was provided using an electrodynamic shaker, where frequency and amplitude were specified to provide the desired acceleration profile. However, the shaker exceeded the weight requirements of the payload, so a different method of providing vibration was developed to correspond with the new experiment constraints. The solid fuel sample is attached to a custom-designed fuel holder, which is restricted to one direction of motion by a set of low-friction slider rails. Vibration is produced using a Scotch yoke mechanism, which converts rotational motion from a DC motor to perfectly sinusoidal linear motion. Both components are fixed to an aluminum plate in the center of the payload, which increases the system's rigidity and decreases the tolerances for moving parts.

The fuel used in this experiment is Whattmann Grade 44 ashless filter paper, measuring 9.25 cm long, 2.5 cm wide, and 0.018 cm thick. The thickness of the sample is such that it can be considered a thermally thin fuel for practical purposes. The ambient gas aboard the New Shepard vehicle is air with 21% oxygen at approximately 1 atm and 15.6—29.4°C.

The experimental procedure to gather flame spread data during the suborbital flight is as follows: When the suborbital vehicle begins providing power and data to the payload, the microcomputer turns on and the supercapacitor begins charging. When the measured acceleration is less than 0.001 g, the camera begins recording and the igniter wire ignites the fuel. The burning lifetime of the fuel is divided into four 30-second periods: stationary, low-speed, medium-speed, and high-speed oscillation. After the burning period, the camera stops recording and the video is saved to a memory card on the microcomputer. The microcomputer then turns off for the remainder of the flight. This procedure can be conducted in normal gravity using simulated telemetry provided by Blue Origin.

Flame spread rate is computed using images from the video recordings of the test shown in Figure 4. Image processing using a MATLAB program identifies both the position of the flame and the edge of the remaining fuel paper at every frame with RGB image thresholding. The fuel length can then be measured over time, and a linear regression of the results is used to calculate an approximate flame spread rate.

Results and Discussion

Preliminary testing at NASA Glenn Research Center used an electrodynamic shaker to vary the amplitude and frequency of oscillation for identical filter paper fuel samples. Figure 5 shows a linear relationship between the flame spread rate and the scaling parameter $g/\omega^{\frac{3}{2}}$ described above. Additionally, characterization testing of the oscillating mechanism in the microgravity experiment payload exhibits a similar trend. As the fuel is enclosed in a much smaller space inside the payload, flame spread rates are smaller for all oscillation speeds. With large values of the scaling parameter (above 0.1), the flame spread rate is more than double the no-oscillation spread rate, showing that oscillation plays a much larger role than natural convection on flame spread.

While the New Shepard suborbital vehicle will not have launched by the time of publication, so microgravity data is not yet available, it is expected that the microgravity data will show a larger increase in flame spread rate with the introduction of oscillation. As natural convection is characteristically absent in microgravity, the flame spread rate will be much smaller than in normal gravity when no oscillation is present. The fuel oscillation will induce a comparatively larger increase in flame spread, which should demonstrate that material oscillation is an important factor to consider when evaluating fire safety.

The results of this study are summarized as follows:

- Opposed-flow flame spread on a vertical thin solid fuel (ashless filter paper) is enhanced when longitudinal oscillation is applied to the fuel in normal gravity. The flame spread rate is shown to increase with a vibrational scaling parameter g/ω^2 .
- An experimental payload to investigate this behavior in microgravity was designed for operation on the Blue Origin New Shepard suborbital vehicle, which will launch in April 2019. It is capable of igniting and oscillating a solid fuel sample at several different frequencies, and meets the payload maximum mass and volume requirements of 500 g and 2.10 L, respectively.
- Microgravity results are expected to follow the same trend as in normal gravity, as the effect of the oscillating boundary layer is independent of gravitational effects.

Figures

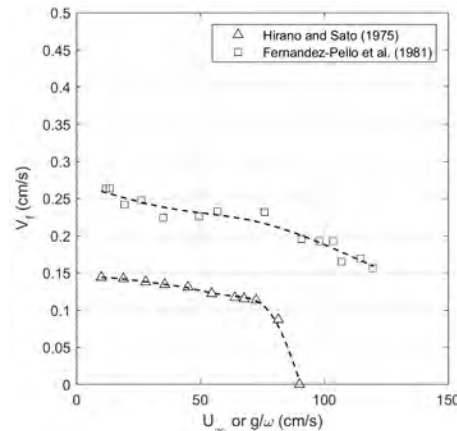


Figure 1. Results from previous studies showing flame spread rate as a function of flow velocity for thin paper fuels under normal gravity conditions.

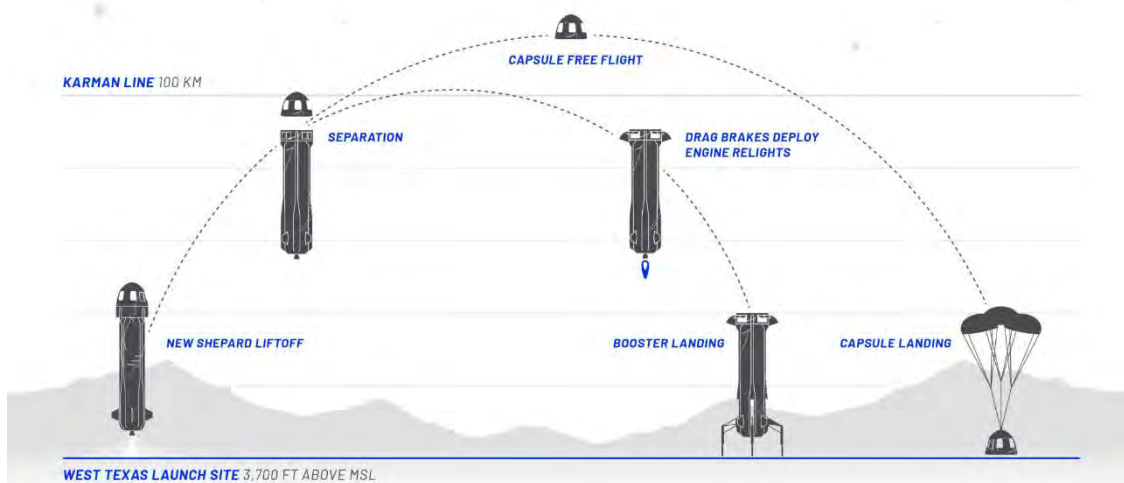


Figure 2. Flight profile for Blue Origin New Shepard suborbital vehicle.

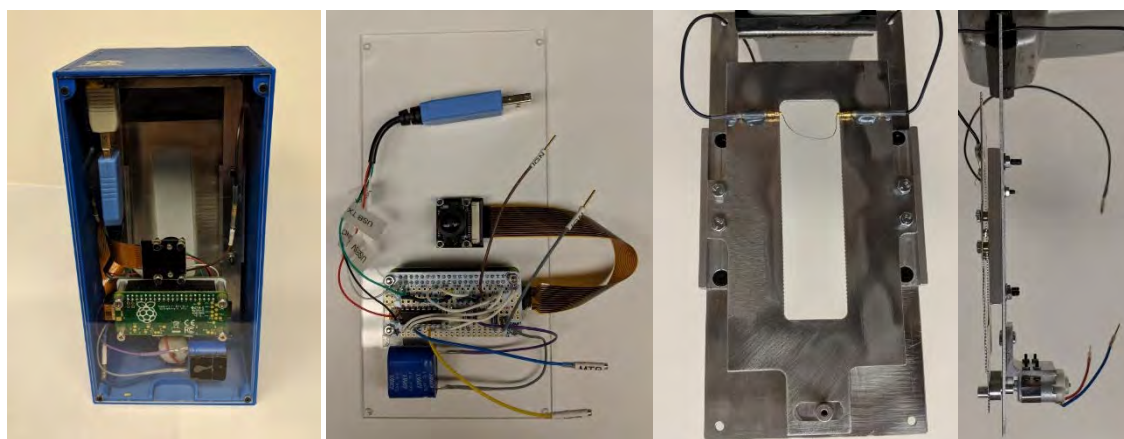


Figure 3. Images of microgravity experimental components shown, from left to right: Experiment enclosure, circuitry (including microcomputer, camera, and supercapacitor), fuel holder and oscillating mechanism (front and side view).

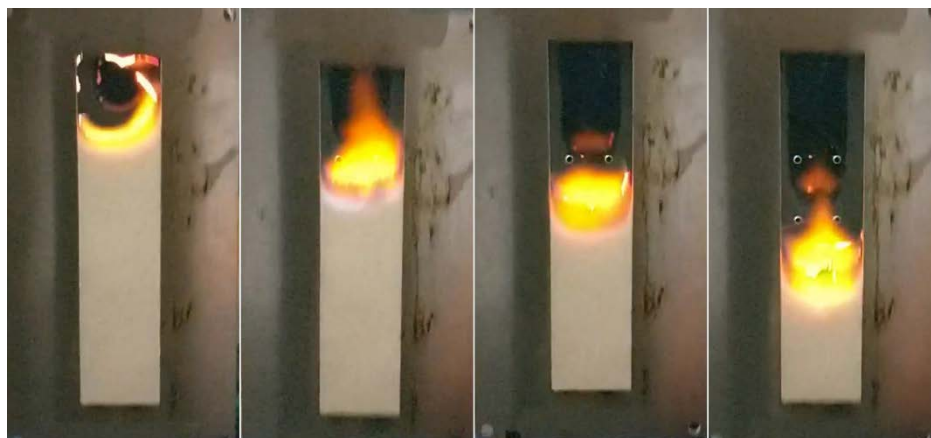


Figure 4. Image sequence showing flame spread along oscillating solid-fuel sample.

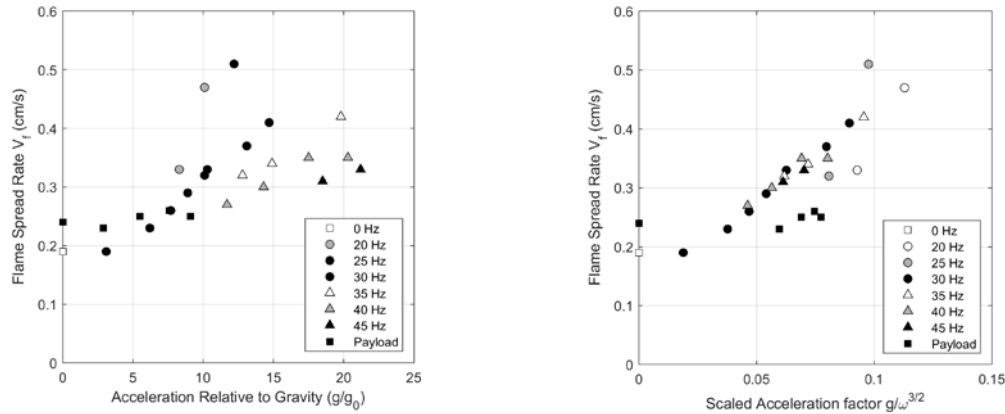


Figure 5. Flame spread rate as a function of vibrational acceleration (left) and scaling parameter (right).

Acknowledgments

We would like to thank S. Nayagam, B. Sun and S. Srinivasan for their significant contributions to the design and testing of this experiment. We gratefully acknowledge the help of R. Chapek (NASA/GRC/Retired) and G. Lindamood (NASA/GRC) for his valuable experience and input regarding the mechanical elements and manufacturing of the payload. Blue Origin and NanoRacks are changing the world by opening the field of microgravity research to all, and their teams were invaluable in enabling us to meet the launch vehicle's payload requirements. This experiment is supported by the Ohio Space Grant Consortium, American Society for Gravitational and Space Research, the American Institute of Aeronautics and Astronautics, and CWRU think[box].

References

1. W. Fraser, "Flammability, Offgassing and Compatibility Requirements and Test Procedures," NASA, Washington, D.C., 2016.
2. T. Hirano and K. Sato, "Effects of Radiation and Convection on Gas Velocity and Temperature Profiles of Flames Spreading Over Paper," *Proceedings of the Combustion Institute*, vol. 15, pp. 233-241, 1975.
3. A. C. Fernandez-Pell, S. R. Ray and I. Glassman, "Flame Spread in an Opposed Forced Flow: the Effects of Ambient Oxygen Concentration," *Proceedings of the Combustion Institute*, vol. 18, pp. 579-589, 1981.
4. H. Goma and A. M. Al Taweel, "Effect of oscillatory motion on heat transfer at vertical flat surfaces," *International Journal of Heat and Mass Transfer*, no. 48, pp. 1494-1504, 2005.
5. NanoRacks, "NanoRacks Feather Frame Payload User's Guide," Houston, 2018.

The Future of Geothermal Energy

Student Researcher: Reannah N. Rymarz

Advisor: Professor Craig Rabatin, P.E.

Marietta College

Department of Petroleum Engineering

Abstract

In a dynamic world of continuous technological improvements, the energy industry is no exception. As energy demands change, so must the methods of cultivation. Geothermal methods are becoming increasingly utilized, creating a need for research into feasibility on a larger scale. Recent studies have investigated the application of geothermal energy production as a long term, large scale, sustainable resource. Geothermal energy is respected as a widely available and useful method of energy generation. This study evaluates the current and future applications of geothermal energy methods and how technology plays an important role in the evolution of the process.

Introduction

Geothermal energy is a viable resource with many similarities to current energy production methods. As research prevails, geothermal systems become more applicable and cost effective. Recent studies identified new methods of geothermal recovery that increase the areas of potential. The additional areas add many new prospects across the country and the world. Enhanced Geothermal Systems utilize a technique called hydro shearing which is similar to hydraulic fracturing methods used in the oil and gas industry. The process is still in the phase of research, but some studies are being put into practice in Canada, Europe and New Zealand. The future is not clear on the prominence of geothermal plants, but the uses are vastly growing. Further research has been conducted on repurposing old oil and gas wells for geothermal energy given the existing infrastructure and thermal gradient. The industry is expanding and will continue to for years to come.

Findings

Geothermal energy is defined as the heat within the Earth. Geothermal energy is harnessed commercially through the use of geothermal plants. There are three general types of plants: dry steam, flash steam and binary cycle. Dry steam plants collect naturally occurring steam directly from the underground reservoir, bringing it to the surface to turn generator turbines to produce electricity. Flash steam plants inject water at high pressure that absorb heat and circulate through a production well to the surface to become steam that powers turbines to produce electricity. Lastly are binary cycle plants which adopt the same process as flash steam accept the hot water is used to heat a secondary fluid that becomes steam. Though the geothermal plants are successful, they require high hydrothermal activity to be successful. Recent systems called enhanced geothermal systems are designed to collect the heat trapped within impermeable rock that otherwise is not accessible with conventional methods. This now allows for the collection of energy from areas without requiring high hydrothermal activity. The expansion of areas of operation makes it possible to obtain or produce energy in areas that may not have access to conventional forms of energy. The process is also able to provide base load energy meaning it is not intermittent and can be depended on for energy at any time. In a 2013 study conducted by Stanford University different Enhanced Geothermal Systems scenarios were evaluated based on numerous parameters such as depth, plant type, temperature, and power sales. The study designed a model to evaluate the different scenarios to select the optimum scenario. The levelized cost

of electricity was calculated based on the cost of the well and the power produced. It was found that the best scenario was at a depth of 3 kilometers with a levelized electricity cost of \$0.24 which is about double the average state cost, but this demonstrates the potential for more cost reduction. Overall geothermal energy has lengths to go to compete with current conventional producers, but the industry is making large strides in the direction of feasibility.

Resources

1. Mines, Greg, and Jay Nathwani. "ESTIMATED POWER GENERATION COSTS FOR EGS." US Department of Energy, 11 Feb. 2013, pp. 1–6., pangea.stanford.edu/ERE/pdf/IGAstandard/SGW/2013/Nathwani.pdf.
2. "Repurposing Oil & Gas Wells for Geothermal Development – a New Database for Alberta, Canada." Think GeoEnergy - Geothermal Energy News, www.thinkgeoenergy.com/repurposing-oil-gas-wells-for-geothermal-development-a-new-database-for-alberta-canada/.
3. Lukawski, Maciej, et al. "Cost Analysis of Oil, Gas, and Geothermal Well Drilling." Journal of Petroleum Science and Engineering, Elsevier, 4 Apr. 2014, www.sciencedirect.com/science/article/pii/S0920410514000813.

Extraterrestrial Geology

Student Researcher: Rachel E. Sauder

Advisor: Dr. Todd France

Ohio Northern University

Department of Biological and Allied Health Sciences, Department of Chemistry and Biochemistry,
Department of Education

Abstract

This project is intended as a lesson for high school geology or earth sciences classes, and will focus extraterrestrial geology, and will include information from other planets and moons in our solar system, such as Venus and Ceres. Background knowledge and figures for the lesson will be drawn from NASA resources, such as images collected from the Dawn spacecraft in 2011. Students will observe and analyze images and maps to better understand geologic features, compare them to similar features on earth and their formation, and present their information to the class.

Project Objectives

By the end of the workshop, students should be able to:

1. Describe a geologic feature of another planet/dwarf planet/moon, and the technology used to capture images of the feature.
2. Relate the geologic feature to something similar on earth, and describe the formation of the feature on earth.

Methodology to be Used

Day 1: Introduction and Research: Students will be introduced to the assignment and be given most of the class period to ask questions about requirements and begin researching their project.

Day 2: Research: Students will be given additional time to research and prepare their project, and ask questions if they arise.

Day 3: Presentations: Students will give short presentations on their chosen extraterrestrial geologic formation.

Depending on student progression through research, this part of the project may be extended another day or assigned as a homework assignment.

Depending on the size of the class and group progress through the presentations, and additional day of presentations may be needed.

Assessment

Student presentations will be assessed based on accuracy of content material, preparation of the presentation (images, project turned in on time, completion), and the oral presentation itself.

Materials

Students should each have access to a computer in class, either in the classroom or in a school computer lab. NASA resources can be accessed from links posted in the Google Classroom or classroom website. Physical maps and images can also be used to supplement online resources, depending on the class and what types of tools help them excel.

Acknowledgments and References

Thank you to Dr. Todd France for guidance throughout the project.

Fabrication of Periodic Poled Lithium Niobate for Three-wave Mixing

Student Researcher: Christina E. Scott

Advisor: Dr. Imad Agha

University of Dayton

Department of Physics

Abstract

Lithium niobate (LiNbO_3 , LN) is a ferroelectric crystal used as a generation medium via nonlinear optical conversions. By periodically poling LN (PPLN) nonlinearities are enhanced for select wavelengths. This is due to the longer interaction length of the crystals in PPLN, instead of sub-mm it increases to a few cm, which produces a crystal with a high degree of effective nonlinearity. Poling LN causes a localized reversal in the direction of the permanent polarization of the crystal (i.e. domain reversal). In this work, we report our efforts towards the development of PPLN using photolithography and applying the bias voltage in a conductive aqueous solution. Ultra-high biased voltages show great promise for fabricating PPLN. The ultimate goal of this work is to use PPLN crystals for three-wave mixing and terahertz (THz) generation.

Background

LN is considered a ferroelectric material, meaning it has spontaneous electric polarization which can be reversed by an electric field. This is important in our experiment because the crystal must be poled so that the waves stay in phase within each domain switch. The more the waves are in phase, the more efficient the conversion output. LN also has a high degree of nonlinearity which allows us to observe into the infrared (IR) and allows for THz generation. If we dope the LN with magnesium oxide (MgO) the nonlinear properties are even more favorable.

Periodic poling is the process of swapping the electrical domains of a material to force favorable conditions for quasi phase matching (QPM). QPM is the technique of creating a phase mismatch, meaning the photons will stay in phase in certain regions of the material. This technique results in a high conversion efficiency of input photons to generated photons through the material.

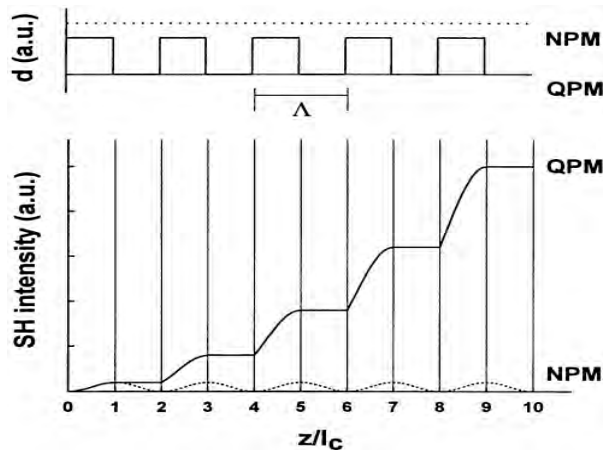


Figure 1. This is a diagram of the effects of quasi-phase matching in comparison to no phase matching. Source: P. G. Kazansky and V. Pruneri, "Electric-field poling of quasi-phase-matched optical fibers," J. Opt. Soc. Am. B **14**, 3170-3179 (1997).

QPM increases the amount of generated photons in a nonlinear crystal by forcing the photons to stay in phase with each other within the boundary conditions.

Three-wave mixing is a process where two waves are mixed in a nonlinear material to produce an output signal. Two main types of this process that can be examined were Sum Frequency Generation (SFG), and a subset of this type called Second Harmonic Generation (SHG) and Difference Frequency Generation (DFG). SFG combines, or “sums” a pump wave and a signal wave in a nonlinear material resulting in a single frequency output. DFG subtracts the pump output from the beam input and outputs that difference along with the initial pump output separately.

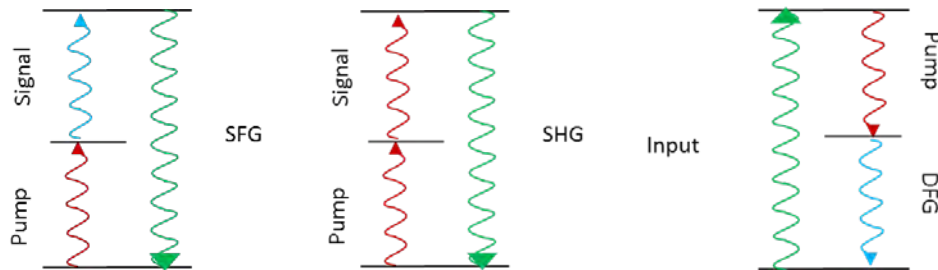


Figure 2. This is a diagram depicting what happens to the input/output signals during SFG, SHG, and DFG.

The poling period, Λ , is described through the function below which relates the different states of the three-wave mixing process.

$$\Lambda = \frac{2\pi m}{\Delta K} \tag{1}$$

Where Λ is the poling period, ΔK is the wavevector mismatch, and m refers to the Sellmeier’s equation constant. QPM is achieved when $\Delta K=0$. The plots below show what affect the signal has on the poling period during SFG and DFG.

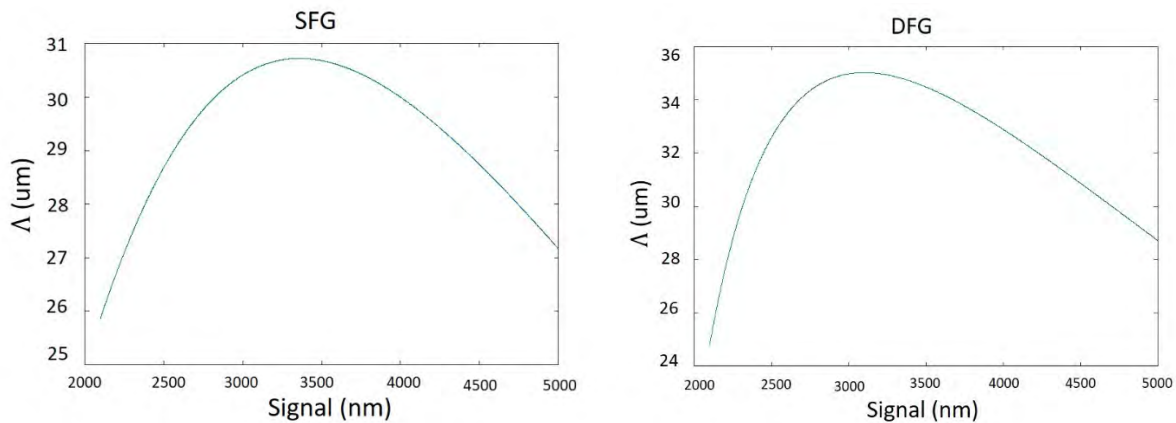


Figure 3. The plots above show how Λ changes due to increasing signal beam with the poling period for LN when using a 1550 nm pump.

Methodology

For PPLN, the type of wave mixing we aimed for first was SFG. The pump and signal should enter the wafer, travel through the waveguide, sum up and exit at a new frequency. The equation below shows how those frequencies add.

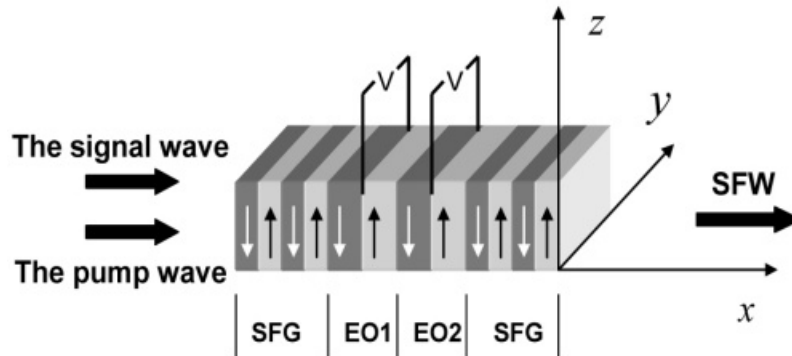


Figure 4. Above is a diagram of how SFG works through PPLN. Source: Xiao-shi Song, Zi-yan Yu, Qin Wang, Fei Xu, and Yan-qing Lu, "Polarization independent quasi-phase-matched sum frequency generation for single photon detection," *Opt. Express* 19, 380-386 (2011).

$$\omega_1 = \omega_2 + \omega_3 \quad (2)$$

A LN wafer doped with MgO was mechanically polished on two edges using 9 μm and 3 μm grit for 20 minutes each, 1 μm grit for 10 minutes, and 0.5 μm grit for 2 minutes. The polishing of the sides was to allow light to couple through the waveguides of the wafer. Next, the LN was periodically patterned with photoresist, through a process called photolithography. Finally, the wafer was placed inside a conductive electrolyte solution (supersaturated lithium chloride (LiCl)) and a high voltage pulse, 3-5 kV, was applied through the solution contacting the wafer where the resist was absent. The contact caused a domain reversal in those areas called periodic poling.

A trek-amplifier was used to generate the high voltage used during the poling process. The voltage across the crystal (R crystal on the diagram below) was then read using a data acquisition system (DAQ). Every part of the experiment was controlled and analyzed through a program made within LabView.

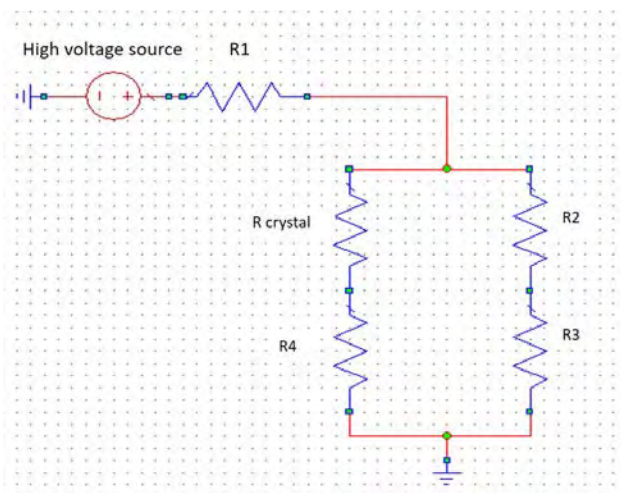


Figure 5. This is a diagram showing the circuit set up used to pole the LN.

Results

Finite element simulations of the mode-field of a waveguide of the fabricated PPLN were produced via reverse proton exchange (RPE). The overlap of the mode was found to be about 90% using a single mode fiber, as shown below.

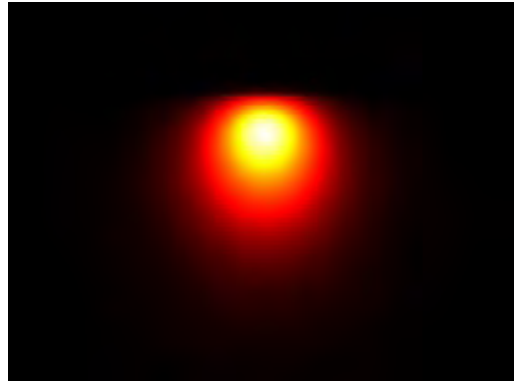


Figure 6. Mode-field of a wave-guide showing 90% overlap.

Next, conversion efficiency vs. pump power for an RPE waveguide was analyzed for material efficiency and quality using IGOR Pro.

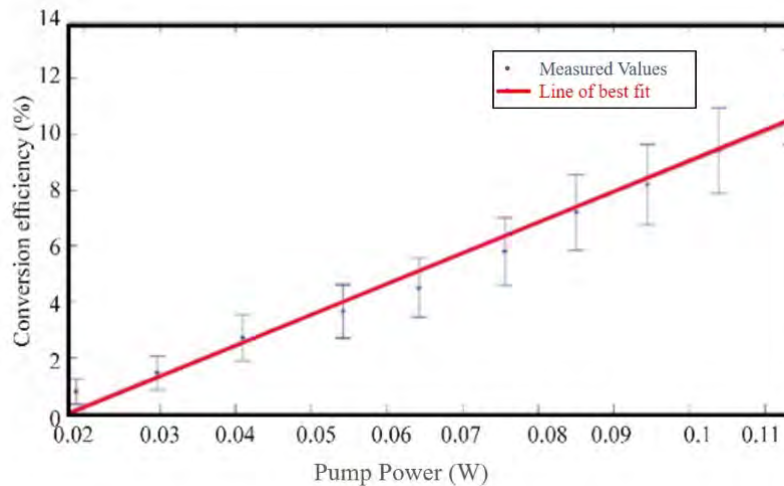


Figure 7. Graph of the conversion efficiency of the pump.

The graph data resulted from experiments at the University of Dayton as well as collaboration with Srico Inc. experimental data.

Future Plans

Given its nonlinear optical properties that allow the IR spectrum to be observed, along with the high conversion efficiency of an optimal PPLN crystal, we will be able to convert the IR spectrum to the visible spectrum. This conversion will allow us to make recombination measurements. Using the three-wave mixing process, specifically DFG, we can now generate THz with PPLN. Lastly, we would like to make an Optical Parametric Oscillator (OPO), which uses SFG to study how atoms interact with squeezed light and most recently found to be able to be used as an all-optical random number generator without post-processing.

Acknowledgments

This research was funded in part by the Ohio Space Grant Consortium Fellowship, the University of Dayton's Dean's Summer Fellowship, the National Science Foundation and the Air Force Research Laboratory. I would also like to thank co-author Matthew Mircovich, Joshua A. Burrows who helped with fabrication, and my co-advisor Dr. Jay Mathews.

Resources

1. L. E. Myers, R. C. Eckardt, M. M. Fejer, R. L. Byer, W. R. Bosenberg, and J. W. Pierce, *Optical Society of America* 12, 2102 (1995).
2. M. Nakamura, M. Kotoh, H. Taniguchi, and K. Tadatomo, *Japanese Journal of Applied Physics* 38, (1999).
3. P. E. Powers and J. W. Haus, *Fundamentals of Nonlinear Optics* (CRC Press, Taylor & Francis Group, Boca Raton, 2017).

Role of PADI2 on Actin in Myelination

Student Researcher: Sarah M. Shapley

Advisor: Dr. Jacqueline Morris

Baldwin Wallace University

Program in Neuroscience, Department of Biology and Geology

Abstract

Multiple Sclerosis (MS), is a neurodegenerative disease in which the immune system targets the myelin sheath causing degradation and removal. Current treatments for MS do not treat remyelination or repair of degraded myelin; instead, these target immune responses.^[1] Recent research focuses on understanding mechanisms of myelination and its stability. The peptidyl arginine deiminase isozyme (PADI2) enzyme is implicated in oligodendrocyte differentiation and maturation^[2] through citrullination of myelin basic protein (MBP). Citrullination is when an arginine amino acid converts to citrulline through cleavage of an amine group.^[3] In our working model of myelination we propose citrullinated MBP decreases its ability to interact with the membrane. To determine if PADI2 inhibition alters myelination through actin polymerization, we will measure actin levels, actin polymerization proteins, and myelin proteins in the presence of PADI2 inhibitor 2-chloroamidine (2-CA) in a zebrafish model.

Project Objectives

A current model for active oligodendrocyte myelination proposes a relationship between actin and MBP through a competitive membrane model.^[4] Active myelination occurs in two parts: wrapping and compaction. Wrapping occurs when MBP is inhibited from interacting with the membrane, and actin polymers (filamentous actin) are broken apart into monomer subunits (globular actin) by the actin disassembly proteins, gelsolin and cofilin-1. Then, during the compaction stage, MBP can bind to the membrane while actin is polymerized to stabilize the myelin sheath.^[4] This project aims to understand the role of MBP in the actin polymerization model. Our current model suggests that MBP binds to the oligodendrocyte membrane after membrane wrapping; however, during wrapping MBP is citrullinated and is unable to bind to the membrane. Our objective is to understand if PADI2 is inhibited, then will MBP bind to the membrane prematurely and, consequently, reduce myelin thickness. The decrease is due to a premature assembly of the actin cytoskeleton because MBP is bound the oligodendrocyte membrane and compacts the myelin layers.

We will use pharmacological interference to PADI2 to study the relationship between MBP, actin, and PADI2 during wrapping and compaction in zebrafish. Currently, the main treatments for MS target the immune system response rather than remyelination.^[1]

Methods

In zebrafish, oligodendrocytes begin differentiation at 36 hours post fertilization, while 60 hours post fertilization oligodendrocytes start active myelination or wrapping membranes around axons. Mature myelin is present in the ventral hindbrain at 10 days post-fertilization while the forebrain will continue myelination until 3-4 months post fertilization.^[6] In addition to well-characterized myelination, zebrafish PADI2 is approximately 56%^[7] conserved amino acid sequences between humans and zebrafish.

2-chloroacetamidine (2-CA) is a chemical which inhibits citrullination. We expect 2-CA to decrease MBP citrullination and thus prevent active wrapping of axons, while inducing early compaction. The

citrullinated MBP is hypothesized to outcompete actin disassembly proteins on the membrane and actin will remain in its polymerized form. When 2-CA is used to inhibit PADI2, other isozymes are not present in zebrafish to compensate for decreased PAD. Another drug, Latrunculin A (Lat-A) prevents the polymerization of actin. Lat-A acts independent of MBP's interaction with the membrane, serving as a positive control for the actin ratio assay. We hypothesize Lat-A will increase active myelination, but not compaction of the membrane. For this experiment, Zebrafish at 5, 7, and 10 days post fertilization were exposed to either 1 μ M 2-CA or 1 μ M Latrunculin A for 12 hours. After drug exposure, animals were homogenized, and proteins collected.

Results Obtained

Preliminary results (**Figure 1.**) show a significant ($p < 0.05$) increase in actin protein expression in 1 μ M 2-CA treated zebrafish at 5 days post fertilization compared to DMSO vehicle control. Data are from relative band intensities obtained from the ImageJ software, standardized against Ponceau S stain peak intensities. [8] An increase in overall actin expression in zebrafish exposed to 2-CA (1 μ M) supports a role for PADI2 in actin expression or organization. Further analysis should be conducted to determine if the increase in actin is due to increase in filamentous actin, actin polymerization, or an overall increase in actin production.

Figures/Charts

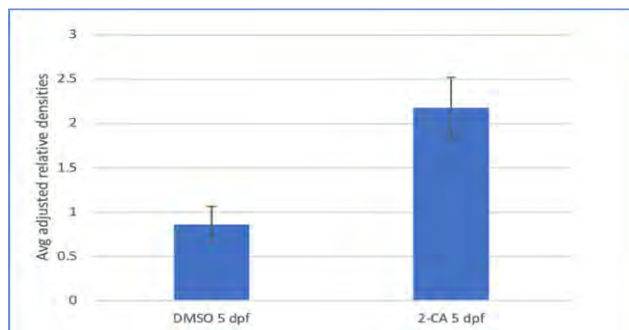


Figure 1. Zebrafish exposed to 2-CA (Padi-2 inhibitor) had an increase in overall actin protein as demonstrated by western analysis. Relative peaks of protein were standardized against Ponceau red protein stain to control loading differences.

Acknowledgments and References

1. Soleimani B., Murray K., Hunt K. Established and Emerging Immunological Complications of Biological Therapeutics in Multiple Sclerosis. *Drug Safety* (2019).
2. Falcao A. M., et al., PADI2-Mediated Citrullination Is Required for Efficient Oligodendrocyte Differentiation and Myelination. *bioRxiv 425348* (2018).
3. Sunish Mohanan, et al., Potential Role of Peptidylarginine Deiminase Enzymes and Protein Citrullination in Cancer Pathogenesis. *Biochemistry Research International*.11 pgs (2012).
4. J. B. Zuchero et al., CNS Myelin Wrapping Is Driven by Actin Disassembly. *Dev. Cell*. **34**, 152–167 (2015).
5. M. A. Moscarello, F. G. Mastronardi, D. D. Wood. The Role of Citrullinated Proteins Suggests a Novel Mechanism in the Pathogenesis of Multiple Sclerosis. *Neurochemical research*. **32**, 251-256 (2007).
6. Jenea M. Bin and David A. Lyons, Imaging Myelination in Vivo Using Transparent Animal Models. *Brain Plasticity*, 2; 3–29 (2016).
7. Szymon Chojnacki, et al., Programmatic Access to Bioinformatics Tools from EMBL-EBI Update: 2017. *Nucleic Acids Res.* 2017 Jul 3; 45(Web): W550–W553.
8. Schneider, CA Rasband, WS & Eliceiri, KW. "NIH Image to ImageJ: 25 years of image analysis", *Nature methods* **9(7)**: 671-675(2012).

Dual Functional Materials for CO₂ Conversion

Student Researcher: Joshua B Steiner

Faculty Advisor: Ana C. Alba-Rubio

The University of Toledo

Department of Chemical Engineering

Carbon dioxide is one of the largest byproducts of almost all major industrial processes. Any combustion of a carbon-containing fuel (coal, coke, wood, natural gas, etc.) produces a multitude of gases, being carbon dioxide one of the most abundant. The composition of carbon dioxide in flue gas (the exhaust gas produced at power plants), can vary depending on the fuel source, but on average it is around 15%. In the typical scenario, flue gas is released to the atmosphere, given that it is a complete combustion reaction (all fuels are converted into carbon dioxide and water). If the reaction is incomplete, where both carbon dioxide and carbon monoxide are present in the gas, it must be further combusted until all carbon monoxide is converted to carbon dioxide. In the end, this yields nearly identical concentrations of carbon dioxide in the flue gas.

Carbon dioxide currently exists at in the atmosphere at 411 ppm (0.0411%) but has been steadily climbing at a rate of about 2.5 ppm per year (Butler, 2018). Industry alone was responsible for 21% of carbon dioxide world emissions in 2009. (International Energy Agency, 2011) Currently, a majority of the industrial uses of carbon dioxide require capturing it and using it in its unaltered state. (Butler, 2018) A much better way to use carbon dioxide would be to capture and convert it into value-added chemicals, such as methanol, which has a wide range of uses across many different industries.

Different metal-metal oxide catalysts have been reported in the literature for CO₂ conversion to methanol. We hypothesized that an increase in the concentration of carbon oxide in vicinity to the active sites of the catalyst could result in an increased conversion of carbon dioxide to methanol. . To explore that, we decided to functionalize the silica support with amine groups, which are well-know for their CO₂ capture capacity. The success of the synthesis was confirmed by different characterization techniques, such as Thermogravimetric Analysis (TGA) and Carbon, Hydrogen, Nitrogen (CHN) chemical analysis. The absorption of CO₂ by the amine-functionalized silica samples was studied by CO₂-Temperature Programmed Desorption (CO₂-TPD). This allowed us to determine the amount of CO₂ absorbed per gram of material and evaluate the efficiency of amine groups to create CO₂ microenvironments around the catalyst surface. In order to increase the concentration of CO₂ around the catalyst even more, future experiments will focus on the functionalization of the surface with amine dendrimers. This will be done through a Michael-type addition reaction starting with the Propylamine group, followed by iterations of methyl acrylate and ethylenediamine. Finally, our hypothesis will be verified by running the hydrogenation of CO₂ to methanol in presence of the catalyst and the amine-functionalized catalysts.

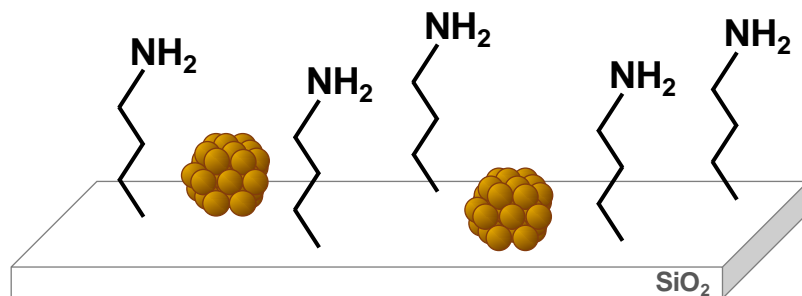


Figure 1. Catalyst functionalized with propylamine groups.

Methods

Throughout the semester, four different samples were created. The first were propylamine functionalized silica particles with no active sites (similar to figure 1, without the orange molecules). This was primarily to test the feasibility of grafting these functional groups to the silica surface. The first part of this reaction was carried out by taking fumed, washed silica, a known amount (12.3 mmol) of (3-Propylamine) trimethoxysilane in toluene as the solvent. This was heated and kept under reflux for 24 hours. It was then purified using a Soxhlet Apparatus and toluene as the solvent again. This removed any other impurities trapped in the catalyst. The apparatus was left to run continually overnight again, and the catalyst that was recovered was dried in an oven and ground to a fine powder. This surface molecules resembled the molecules in figure 2. In figure 2, the flat line represents the silica surface. They are bonded to the surface with Si – O – Si bonds. The silicon atom is then grafted to the functional group.

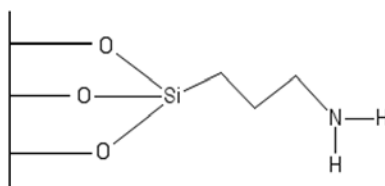


Figure 2. Propylamine groups functionalized on silica surface.

This same process was followed with butylamine groups, but the 12.3 mmol of (3-Propylamine)trimethoxy silane is replaced with an equimolar amount of (4-Butylamine)trimethoxy silane. The reason this test was done was to ensure that attaching both amino and butyl amines to the surface was possible. In the future, the proximity of the amine group to the surface of the catalyst may affect how well the CO₂ microenvironment is reacted to the catalyst.

The next sample that was prepared was almost identical to the first sample, but it was functionalized with copper nanoparticles. During the creation of this catalyst, some surface -OH molecules are used in order to attach the copper particles. These sample -OH molecules are used to attach the functional groups to the surface of the silica. This was done to ensure that the amine groups would still have suitable sites on the surface of the catalyst to attach. Another purpose of this sample was to test how much the catalyst degraded at running temperatures. Typically, the copper on the catalyst is passivated (removing of a small oxide layer) at 150°C for around 90 minutes. The amount that the functional groups degrade is vital to knowing the lifespan of this catalyst.

Finally, catalyst using PAMAM (poly amidoamine) dendrimers was formed. This was done through a “Michael-type” addition. First, a Propylamine sample was used. It was then reacted with an excess of methyl acrylate in ethanol at room temperature for 24 hours to add half of the “generation” of this polymer. Next, the sample was reacted with an excess of ethylene diamine in ethanol at room temperature for 55 hours. Doing this completed the first “generation” of the polymer. These steps could be repeated continually, growing the polymer to larger lengths and increasing the amount of amine active sites. Unfortunately, no tests were able to be performed on this catalyst due to time restrictions.

Results

The following are results from both thermogravimetric analysis (TGA) and CHN combustion analysis. TGA measures how weight degrades with a ramping temperature, while CHN analysis measures the mass of carbon, hydrogen, and nitrogen in a sample.

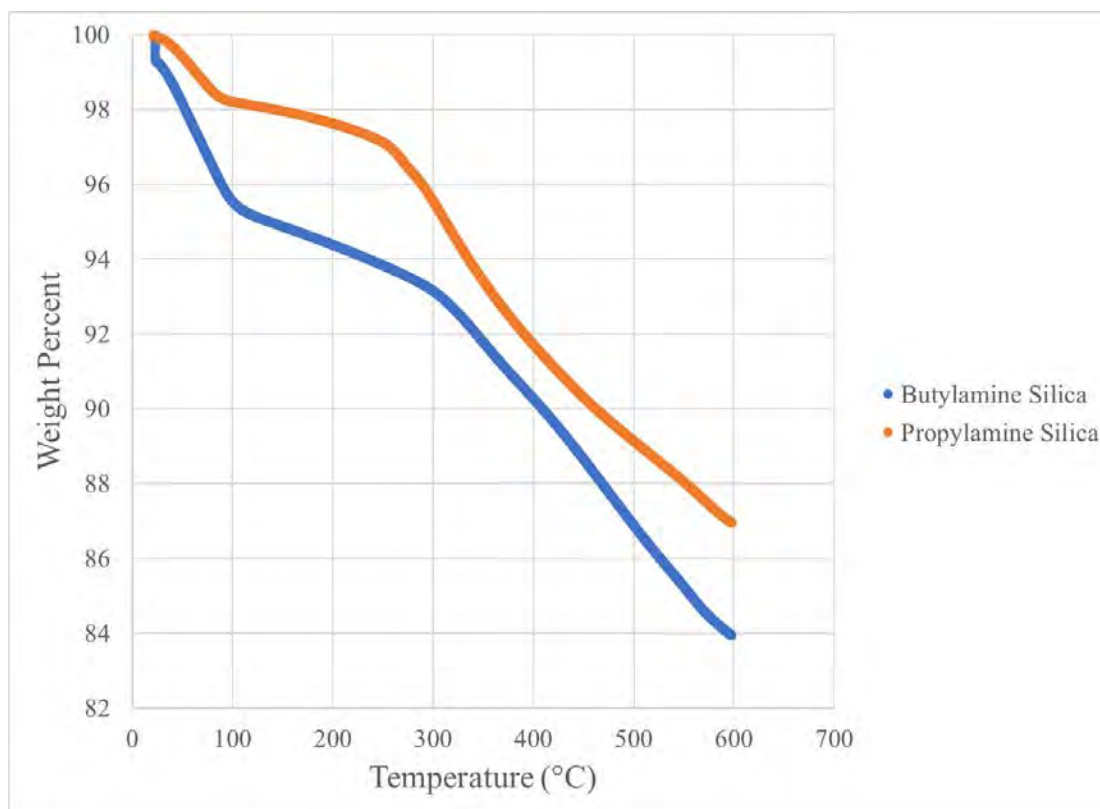


Figure 3. TGA of both propylamine and butylamine functionalized silica.

In Figure 3 we can see that both samples had fairly high thermal stability until around 300°C. It also makes sense that the butylamine groups have a higher amount of degradation on a weight percent basis, due to the fact that the butylamine groups have a higher mass from the extra carbon.

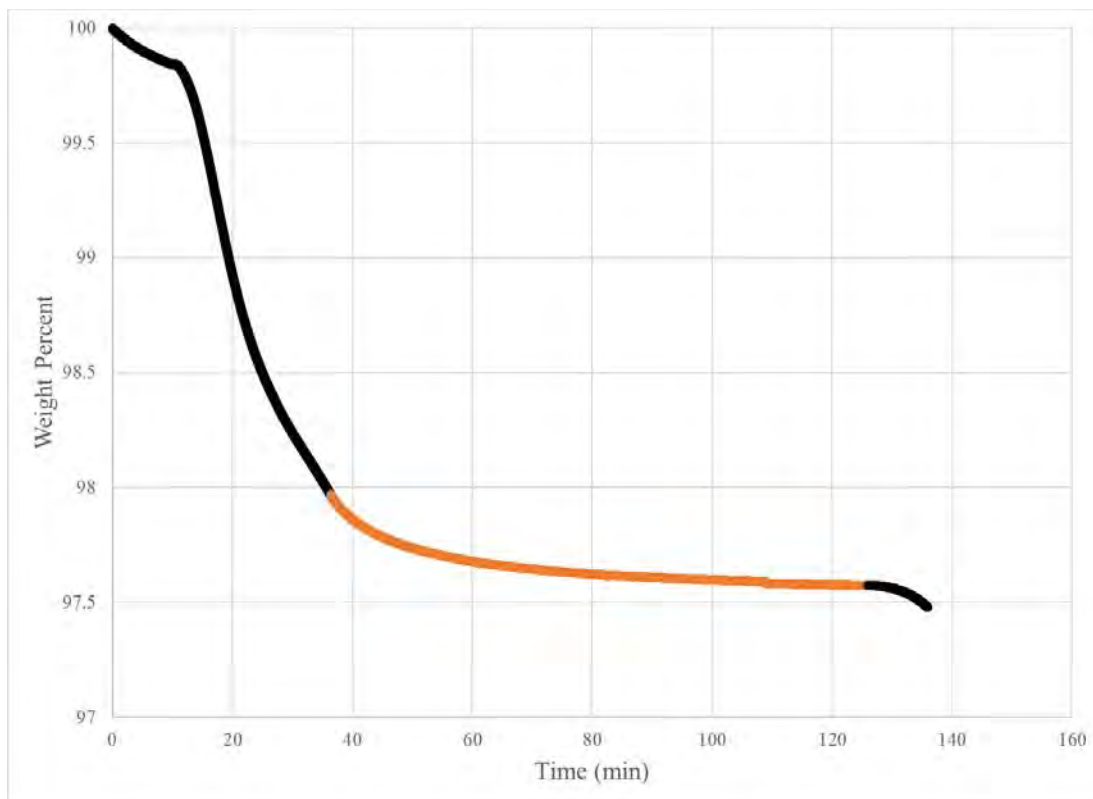


Figure 4. TGA of Butylamine Functionalized Cu/SiO₂ Sample Simulating Passivation at 150°C at a rate of 5°C/min with a 90 Minute Isotherm at Passivation Temperature.

Figure 4 is the simulation of a passivation of the active sites on the catalyst. The orange section of the graph represents the passivation at 150°C, and it can be seen that less than half of a weight percent was lost during this passivation. This is good news, since the passivation should only taken place once, then the catalyst will be active, therefore preserving the dendrimers.

Table 1. TGA of Propylamine, Butylamine on Silica, and Butylamine on Cu/SiO₂.

	Carbon	Hydrogen	Nitrogen
Fumed Silica Standard, Run 1	0.37	0.87	0.04
Fumed Silica Standard, Run 2	0.31	0.55	0.04
Propylamine Sample 1, Run 1	8.79	1.93	2.81
Propylamine Sample 1, Run 2	9.04	2.11	2.92
Propylamine Sample 2, Run 1	8.79	2.08	2.8
Propylamine Sample 2, Run 2	8.72	1.82	2.75
Average of Propylamine Samples	8.835	1.985	2.82
Butylamine Sample, Run 1	8.19	1.46	1.99
Butylamine Sample, Run 2	8.26	1.49	2.07
Average of Butylamine Samples	8.22	1.47	2.03
Cu/SiO₂ Standard, Run 1	0.24	0.3	0.11
Cu/SiO₂ Standard, Run 2	0.25	0.5	0.18
Cu/SiO₂ Butylamine Sample, Run 1	8.8	1.54	2.08
Cu/SiO₂ Butylamine Sample, Run 2	8.82	1.55	2.12
Average of Cu/SiO₂ Butylamine Samples	8.81	1.54	2.10

From the CHN combustion analysis allowed for the masses of carbon, hydrogen, and nitrogen to be determined. As is evident from the graph, all of the treated samples had an increase of all carbon, hydrogen, and nitrogen, showing that there is presence of the amine groups on the surface of the different catalysts.

References

1. Butler, David A. "Industrial Gases Production, Equipment Supply and Services." *Universal Industrial Gases, Inc. - UIG Gas & Liquid Plants Supplier - UCG Onsite Gas Supplier / Producer of Nitrogen & Oxygen - Air Separation Plant Supplier - New Cryogenic Nitrogen Plants, Oxygen Plants, Air Separation Plants and Liquefiers Manufacturer*, 2018, www.uigi.com/index.html.
2. Dillon, Jeff. "A Daily Record of Atmospheric Carbon Dioxide from Scripps Institution of Oceanography at UC San Diego." *The Keeling Curve*, 2015, scripps.ucsd.edu/programs/keelingcurve/.
3. Induspray. "Smoke Stack, High-Heat Stack, Flare Stack, Incinerator Stack Painting | Industrial Stack Painters." *INDUSPRAY USA - Industrial Painting Contractors*, 2000, www.indusprayusa.com/industrial-stack-painting/.
4. International Energy Agency. "CO2 Emissions from Fuel Combustion 2011." *CO2 Emissions from Fuel Combustion*, 2011, doi:10.1787/co2_fuel-2011-en.
5. Mokhtary, M. J IRAN CHEM SOC (2016) 13: 1827. <https://doi.org/10.1007/s13738-016-0900-4>
6. Rapson, Paul. "Furnace At An Oil Refinery by Paul Rapson." *Fine Art America*, 2013, fineartamerica.com/featured/furnace-at-an-oil-refinery-paul-rapson.html.
7. Ritchie, Hannah, and Max Roser. "CO₂ and Other Greenhouse Gas Emissions." *Our World in Data*, 11 May 2017, ourworldindata.org/co2-and-other-greenhouse-gas-emissions.
8. Sreeranganathan. "Developing a Mechanical Integrity Program for Fired Heater Tubes." *Inspectioneering*, 2017, inspectioneering.com/journal/2017-10-26/7004/mechanical-integrity-program-for-fired-heater-tubes.
9. Team, ESRL Web. "ESRL Global Monitoring Division - Global Greenhouse Gas Reference Network." *ESRL Co2 Trends RSS*, 1 Oct. 2005, www.esrl.noaa.gov/gmd/ccgg/trends/weekly.html.
10. US EIA. "U.S. Energy Information Administration - EIA - Independent Statistics and Analysis." *How Much Carbon Dioxide Is Produced When Different Fuels Are Burned? - FAQ - U.S. Energy Information Administration (EIA)*, 8 June 2018, www.eia.gov/tools/faqs/faq.php?id=73&t=11.
11. US EPA. "Sources of Greenhouse Gas Emissions." *EPA, Environmental Protection Agency*, 9 Oct. 2018, www.epa.gov/ghgemissions/sources-greenhouse-gas-emissions.

How Camber and Angle of Attack Impact Drag, Lift and Pressure Coefficients of NACA 4-digit Airfoils

Student Researcher: Mallory L. Taylor

Advisor: Dr. Jed E. Marquart, P.E.

Ohio Northern University
Mechanical Engineering

Abstract

The drag and lift on NACA airfoils between airfoils that had camber and airfoils that did not have camber were determined and compared. The selected non-cambered airfoils were the NACA 0012 and 0015, and the corresponding NACA 2412 and 2415. Conclusions were drawn regarding the effect of camber on the performance of these selected NACA four-digit airfoil shapes.

The drag and lift were also compared using the same four airfoils, but this time varying the angle of attack. Lift and drag values, as well as the pressure distributions, were compared between the airfoils over a range of angles of attack. A summary was provided regarding the effect of the angle of attack on cambered and non-cambered airfoils.

Methodology

The program used in this research was DesignFOIL. This program is a user friendly program which allows the user to select various airfoils and determine their characteristics. NACA airfoils 0012, 0015, 2412, and 2415 were evaluated. Figures 1 - 4 show the NACA four-digit airfoils chosen.



Figure 1. NACA 0012 Airfoil.



Figure 2. NACA 2412 Airfoil.



Figure 3. NACA 0015 Airfoil.

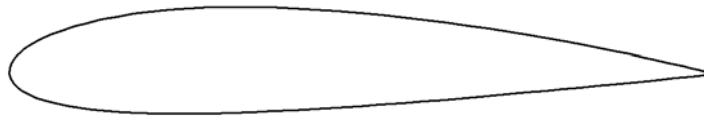


Figure 4. NACA 2415 Airfoil.

Results

The airfoils that had no camber and were tested were the NACA 0012 and NACA 0015. The cambered airfoils were the NACA 2412 and NACA 2415. Each of the airfoils were compared at the same conditions, at a Reynolds Number of 300,000 and at an angle of attack of zero degrees. Table 1 shows the data taken from each airfoil.

Table 1. NACA 4-digit Airfoils Lift and Drag Coefficients.

	NACA 0012	NACA 2412	NACA 0015	NACA 2415
Lift Coefficient	0.000	0.266	0.000	0.275
Drag Coefficient	0.0068	0.0068	0.0071	0.0072

Table 1 shows that non-cambered airfoils have a zero lift coefficient while cambered airfoils have a positive lift coefficient. A camber causes air to travel faster over the top of the wing, causing a lower pressure. This change in pressure increases lift. Therefore, it was confirmed that camber increases lift, which allows cambered airfoils to be more efficient than flat, non-cambered airfoils. [1]

Lift and drag coefficients of NACA 4-digit airfoils were compared over a range of angles of attack between -10 and 10 degrees. Figure 5 shows the lift coefficients displayed for all four airfoils over the range of angles of attack. The cambered airfoils have a constantly higher lift coefficient than the un-cambered airfoils. The difference is approximately 0.3 and is steady across the angle span. From this, it was determined that cambered airfoils have a higher lift coefficient than un-cambered airfoils across all angles of attack.

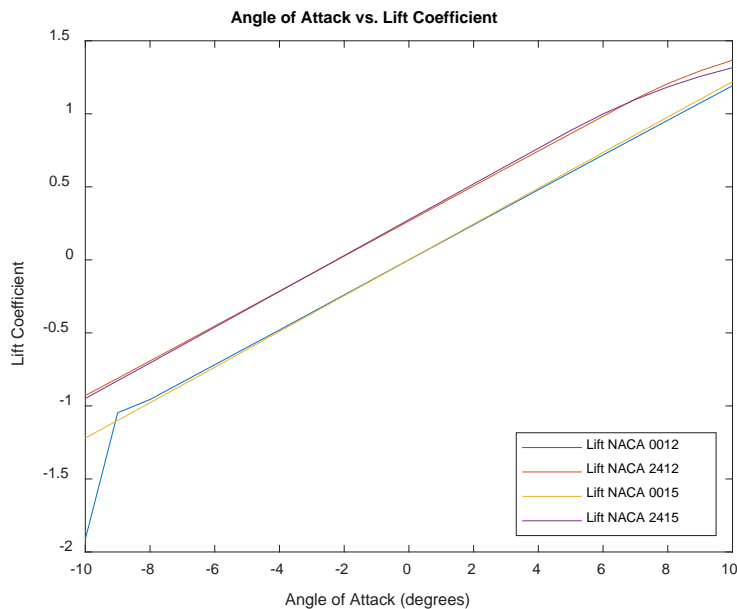


Figure 5. Lift Coefficients of NACA 4-digit Series.

Figure 6 shows the drag coefficients for all four airfoils across the same range of angles of attack. All airfoils show similar responses to the change in angle, at zero, all airfoils have their lowest drag coefficients. Unlike the figure above, at -10 degrees, the un-cambered airfoils have a higher drag coefficient than the cambered foils. At 10 degrees however, they switch and the cambered foils have a higher drag coefficient. The change occurs at zero degrees. From Figure 6, it was determined that while descending, a cambered airfoil will have a lower drag coefficient and while ascending an un-cambered airfoil will have a lower drag coefficient.

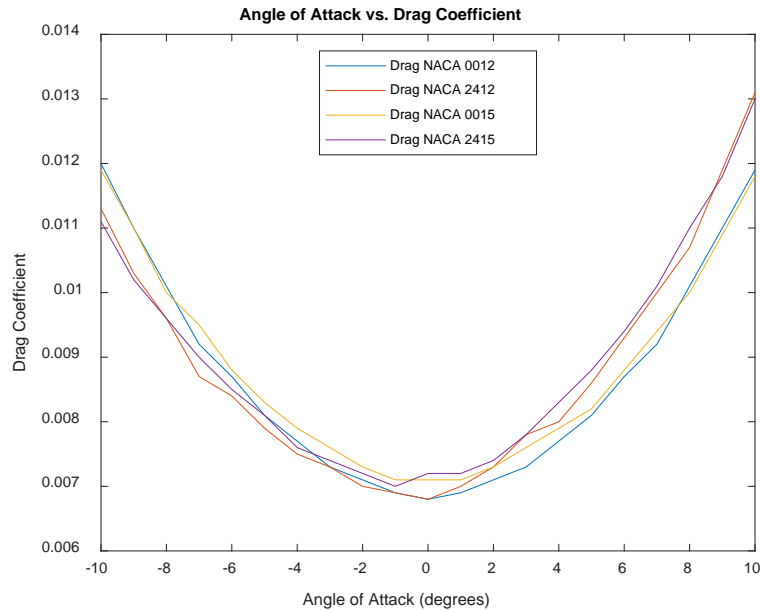


Figure 6. Drag Coefficients of NACA 4-digit Series.

Figures 7 through 10 display how the pressure coefficient varies as the angle of attack is changed at an interval of two from -10 degrees to 10 degrees. An airfoil has stagnation points at the beginning and end of its chord length. These stagnation points are at the stagnation pressure which is zero. For each angle of attack, there are two lines shown in the figure. The lines display the pressure coefficients on the upper and lower surfaces of the airfoil. The top line of each demonstrates the pressure coefficient on the upper surface and the bottom line of each demonstrates the pressure coefficient on the lower surface. The pressure coefficient on the lower surface starts at the stagnation pressure and drops to a peak at a negative number. The pressure coefficients then slowly increase back to the stagnation point at the tip of the foil. The pressure coefficients on the upper surface start at zero at the stagnation point then peak at one and continue to decrease to zero. The upper surface pressures show little variability from 30% to 95% on each airfoil. The pressure change is very small and then drops to the same stagnation pressure. The lower surface coefficients prove interesting because as the angle of attack is decreased in the negative direction, the coefficients continue to peak lower. For the upper surface, all coefficients peak around 1.0. However, for the lower surfaces, the pressure coefficients have a bigger change along the airfoil. Camber does not impact the point at which the negative peak occurs.

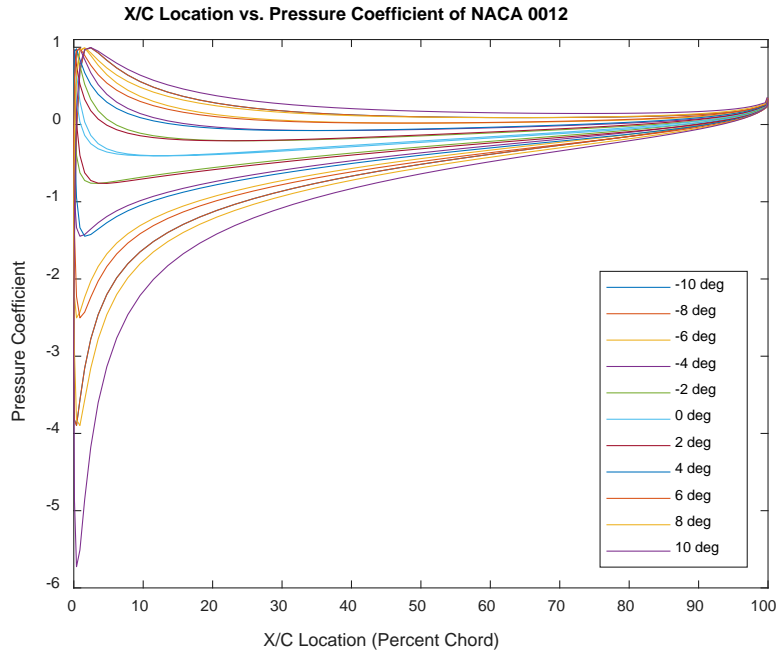


Figure 7. NACA 0012 Pressure Distributions.

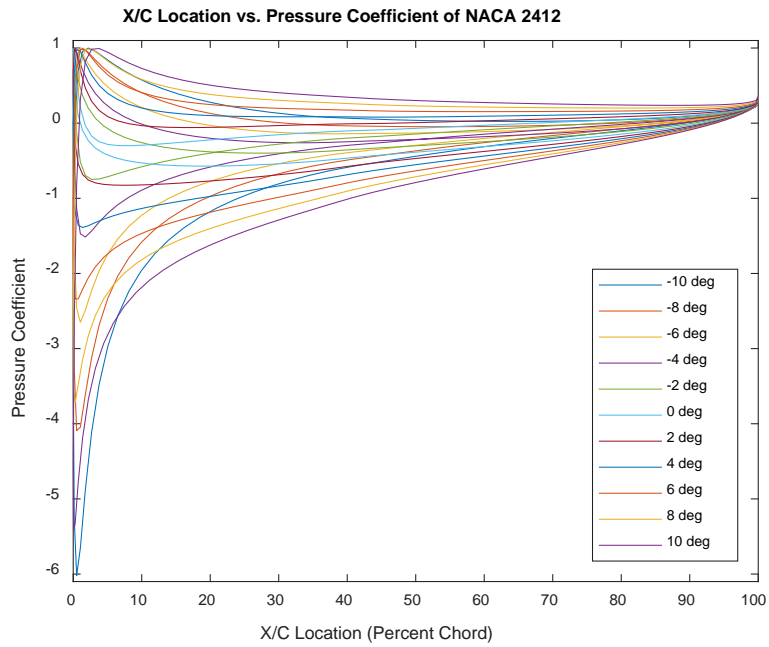


Figure 8. NACA 2412 Pressure Distributions.

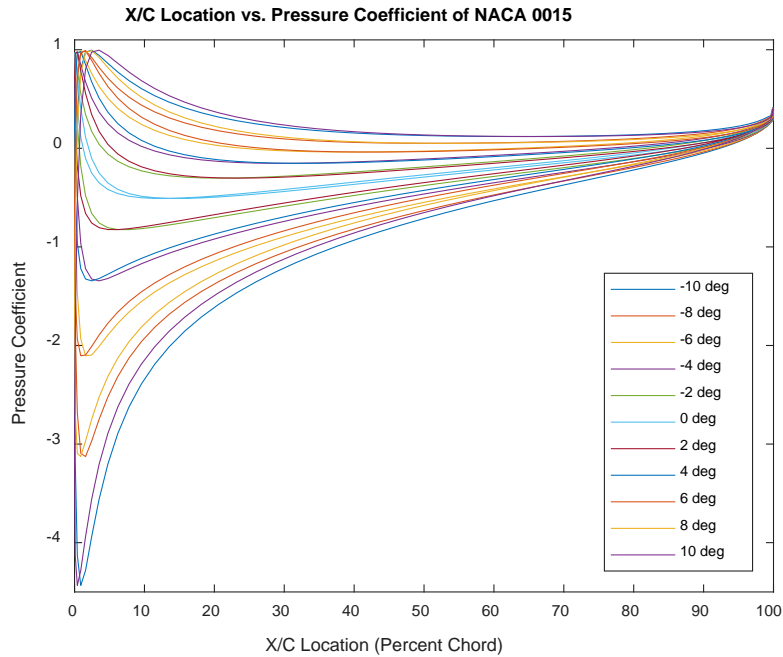


Figure 9. NACA 0015 Pressure Distributions.

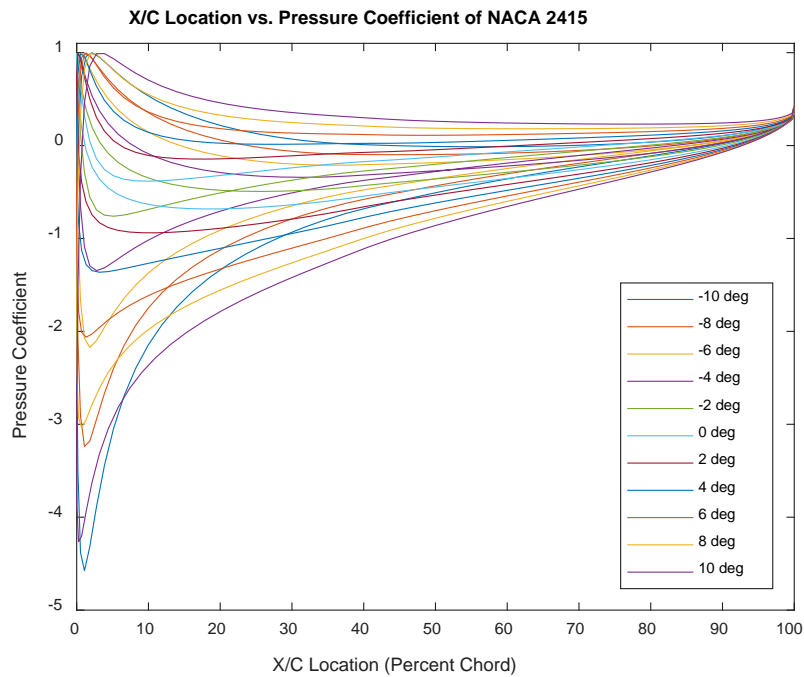


Figure 10. NACA 2415 Pressure Distributions.

References

1. Hand, M. (2019). *Cambered Wings*. [online] mansfieldct.org. Available at: <https://www.mansfieldct.org/Schools/MMS/staff/hand/flightcamberedwings.htm> [Accessed 20 Mar. 2019].
2. *Airfoil Design*. (2016). [video] Directed by W. Liebhaber. Youtube.

Design of Heat Exchanger for Intense Cooling of Inlet Bleed Air at High Mach Numbers

Student Researcher: Erin M. Tesny

Advisor: Dr. Wei Zhang

Cleveland State University
Department of Mechanical Engineering

Abstract

Boundary-layer bleed is typically used in high-speed aircraft inlets to improve inlet performance and enhance inlet stability. At Mach numbers greater than about 3.0, the bleed air is at high temperature and low pressure, necessitating large bleed ducts that add significant weight and volume to the vehicle. A compact heat exchanger using cryogenic fuel as the working fluid is a potential method of intensely cooling the bleed air in order to reduce bleed duct size. This paper proposes a potential design of such a heat exchanger. However, the feasibility and efficiency of such a device remains unknown. A computational fluid dynamics model of the heat exchanger is set up using SolidWorks Flow Simulation. A single tube is evaluated to determine the ideal grid resolution. A parametric study is then performed using a quasi-axisymmetric bleed air model to find the optimum tube configuration. A final tube configuration is proposed to optimize heat exchanger efficiency.

Project Objectives

Bleed air from the boundary layer of high-speed aircraft inlets allows for increased performance and stability (Fig 1)^{1,2}. At high Mach numbers the bleed air is at high temperature and low pressure, necessitating large bleed-air ducts that increase both vehicle drag and weight (Fig 2). Intensely cooling the bleed air would reduce these effects by decreasing the necessary duct size. One possible method of cooling the bleed air is through a compact heat exchanger that uses a cryogenic fuel as the working fluid. Here we explore the design and feasibility of such a device that uses liquid hydrogen.

A heat exchanger was initially designed at NASA Glenn Research Center and will be the point-of-departure for this study^{2,3}. The original device was designed for a proof-of-concept (POC) test to be conducted at NASA GRC. The limitations of the test rig designed for this original study will be used here to dictate the boundary conditions of the heat exchanger performance. The original POC design utilized a radial heat exchanger, where the bleed air enters the heat exchanger through a central tube and moves radially outward past the liquid hydrogen tubing. Each hydrogen tube makes seven passes through the chamber moving inward with each pass. This configuration makes for a cross-flow heat exchanger with counter-flow passes. This small-scale test was designed to cool approximately 1% of the core flow, with an approximate flow rate of 0.038 lb_m/s³.

This study will first run an analysis using computational fluid dynamics of the original design to determine the heat exchanger efficiency for the given air mass flow rate. The results will look at the average air outlet temperature as a measure of heat transfer rate. Subsequent designs will alter the angle between the hydrogen tubes and the incoming air radial air flow. By increasing the angle of the section of maximum surface area relative to the flow, the heat transfer rate is predicted to increase.

Methodology Used

The heat exchanger is designed to cool the mass flow rate of air dictated by the test rig (0.038 lb_m/s) down to just above its liquefaction point of 116 °R. It is assumed that 100% of the stoichiometrically required hydrogen is available to cool the air. Fouling of the heat exchanger is not accounted for in this analysis, nor is the condensation of water vapor or carbon dioxide suspended in the air. It is assumed that for the POC test dry air will be used in the testing facility.

The original design of the heat exchanger consisted of 350 straight tubes with slot-shaped cross-sections of a high aspect ratio to increase the surface area per tube (Fig 4). The tubes are positioned in seven rows at alternating 45° angles from the core flow. The tubes are arranged in seven concentric circles of fifty tubes each. Therefore each individual row of tubes can be analyzed as a single cross-flow heat exchanger, while the device as a whole works as a counter flow heat exchanger. The simple energy balance for a heat exchanger equates the heat transfer rate required to cool the hot fluid with the rate required to heat the cold fluid⁴.

$$\dot{Q}_h = \dot{m}_h c_{p,h} (T_{h,in} - T_{h,out}) \quad (1)$$

$$\dot{Q}_c = \dot{m}_c c_{p,c} (T_{c,in} - T_{c,out}) \quad (2)$$

There is some loss of heat to the aluminum tubing that separates the two fluids. The original tube thickness is 0.02". The total heat loss to the solid can be calculated using Fourier's Law and is approximately 1.82 Btu/s (3).

$$\dot{Q}_{cond} = -kA\Delta T \quad (3)$$

At this point every quantity is known except for the exit temperature and mass flow rate of the liquid hydrogen. The final temperature of the hydrogen is not a crucial part of the analysis but the mass flow rate must be an initial condition of the simulation. The initial design analysis conducted by NASA GRC used an estimated 0.0555 lb_m/s mass flow rate for hydrogen. This will be the start point of the inputs to the CFD simulation. From the final temperature of the air in the simulation, the heat transfer rate can be found using Equation 1. This quantity can then be compared to the theoretical maximum heat transfer rate (4). In this way the different heat transfer configurations will be compared at different hydrogen mass flow rates.

$$\dot{Q}_{max} = C_{min} (T_{h,in} - T_{c,in}) \quad (4)$$

The chosen tool is SOLIDWORKS Flow Simulation because of its compatibility with the existing CAD model of the original heat exchanger. Flow Simulation, or FlowSim, has the ability to model heat conduction in solids which is critical to the heat transfer between the liquid hydrogen and air. Flow Simulation does not have the capability to model two-phase flow, so the air will not be cooled before liquefaction and the hydrogen will remain supercritical.

A quasi-axisymmetric model of the heat exchanger was used, using a 36 degree slice of the device (Fig 6). The mass flow rates of the hydrogen and air were scaled down to one tenth of the flow rate of the overall heat exchanger. The original design placed the hydrogen tubes at a 45 degree angle relative to the incoming radial air flow. This angle was modified from 0 to 80 degrees to investigate which angle resulted in the greatest heat transfer between fluids (Fig 7). A 90° configuration could not be tested because the hydrogen tubes began to overlap when placed at this angle. The average outlet temperature of the air was used as a metric of the heat transfer rate because the two are proportional

(1,2). For each angle five different hydrogen flow rates were tested from 0.027-0.888 lb_m/s. A grid refinement was done with a single straight tube. The global mesh control was set, and a local mesh was seeded around the hydrogen tube itself. The same automatic mesh controls were used for the pie slice simulation runs.

Results Obtained

The average outlet temperature of the air was shown to decrease with increasing hydrogen mass flow (Fig 5). Similarly, the average outlet air temperature decreased with increasing angle relative to the flow for the same mass flow rate. This is likely due to the increase in surface area perpendicular to the incoming air flow. Because the outlet temperature is linearly related to heat transfer rate, the heat transfer rate increases with mass flow as well (Fig 8). There is a discrepancy in the data trend that shows the 45 degree configuration results in a high outlet temperature and therefore less heat transfer than the 30 degree configuration. This may be due to the limitations of the mesh size used and needs further study. The 80 degree configuration was the closest to the theoretical maximum heat transfer rate. However, although the 80 degree angle configuration resulted in the lowest outlet temperature (and therefore the greatest heat transfer rate), placing the tubes at this angle may be impractical from a mechanical design perspective. Placing the tubes at this angle may induce excessive stresses on the tubes leading to yield or buckling. Further study is needed to confirm that this configuration is a realistic design.

Significant and Interpretation

This initial study of radial heat exchanger geometry shows that a larger tube angle relative to the direction of the flow in the shell increases heat transfer between the hot and cold fluids. However, having a 80 degree angle may result in structural problems in the design of the device. Continuing work is examining other aspects of tube placement within the radial heat exchanger, including helical tube profiles. The final project will include a complex geometry that optimizes heat transfer of the heat exchanger.

Figures/Charts

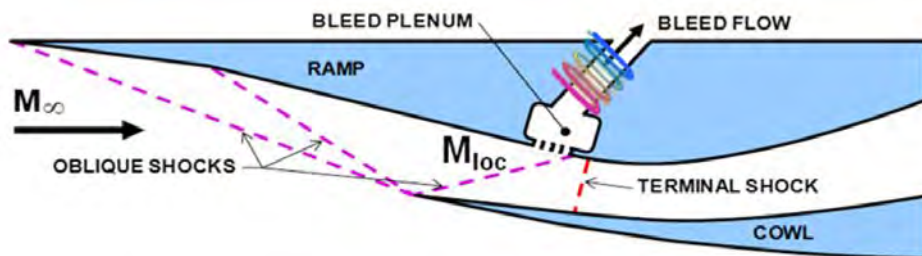


Figure 1. Mixed Compression Inlet¹

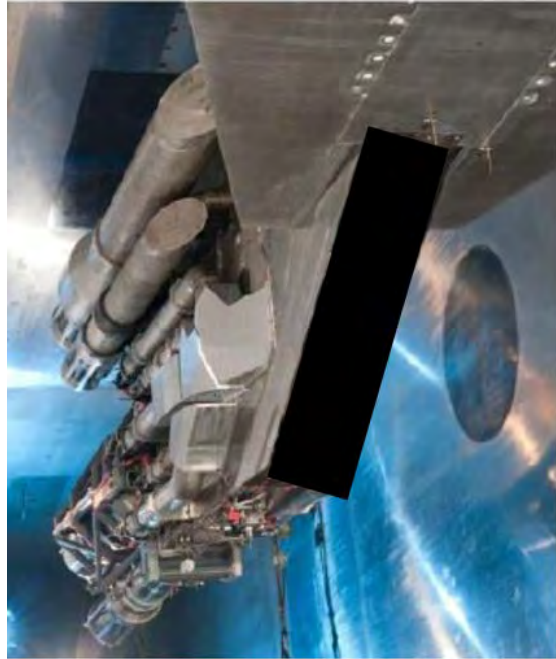


Figure 2. High Mach Number Bleed Ducts¹

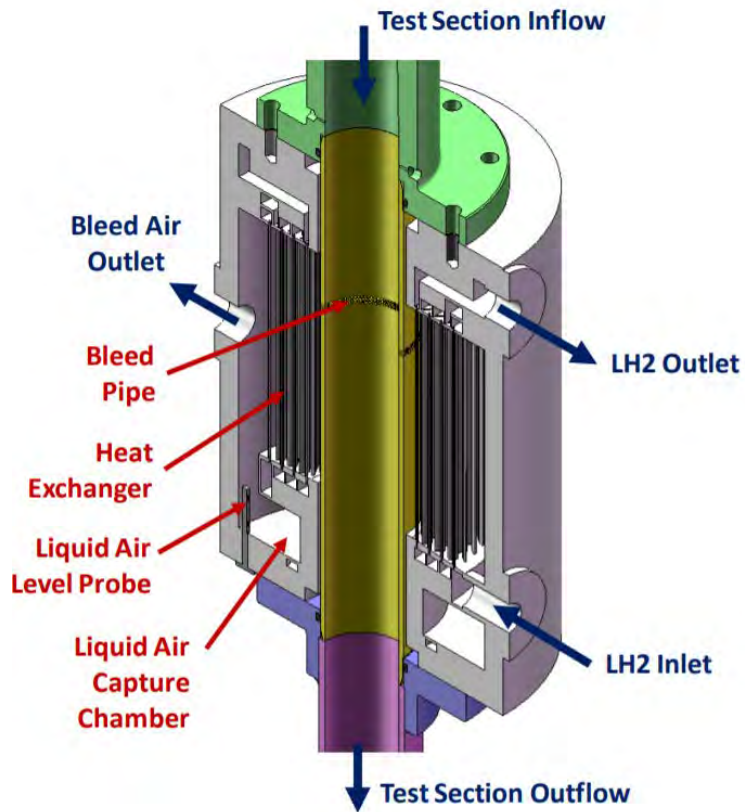


Figure 3. Side view of original Heat Exchanger²

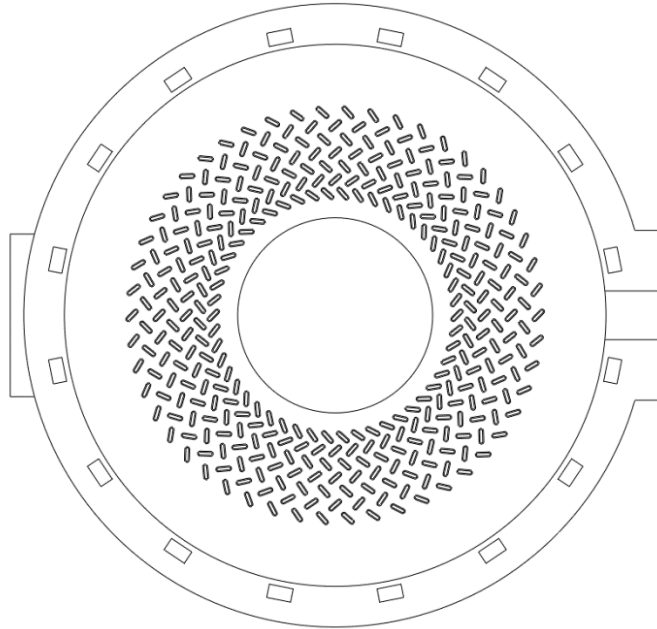


Figure 4. Top View of Original HX Design.

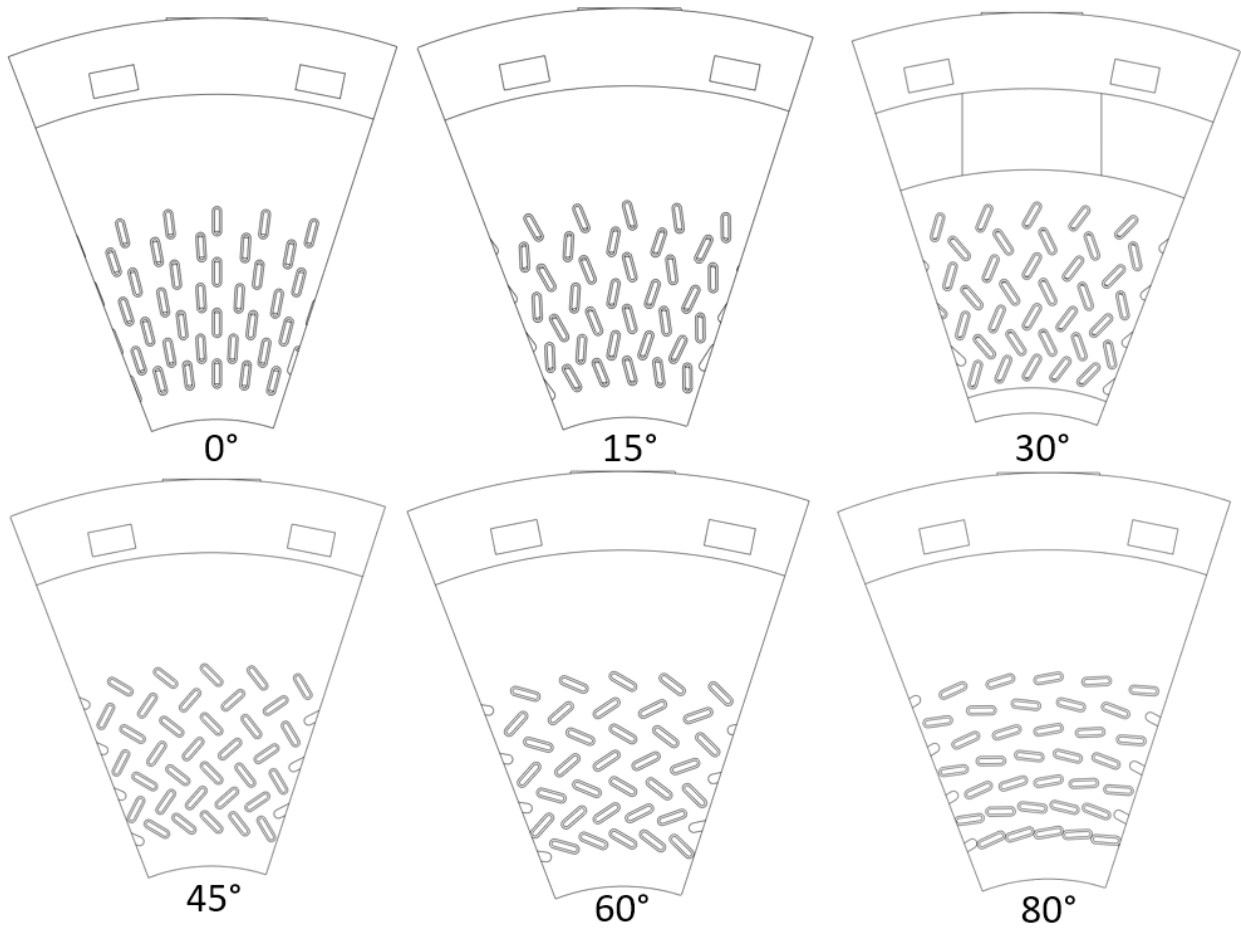


Figure 5. Top View of Heat Exchanger Slice with Different Hydrogen Tube Angles.

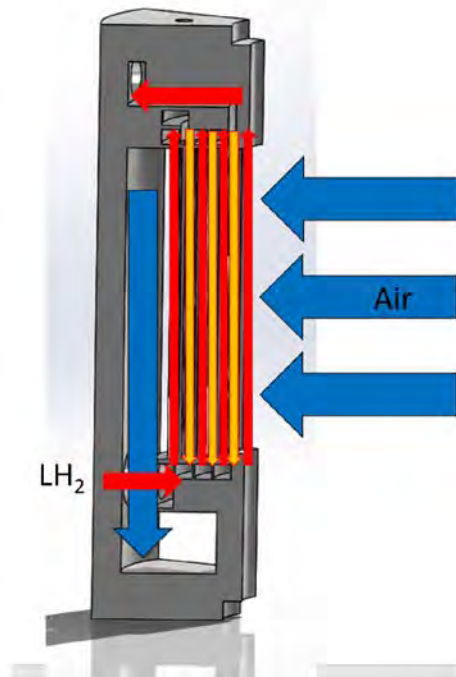


Figure 6. Side View of 36° Slice Showing Air and LH₂ Paths.

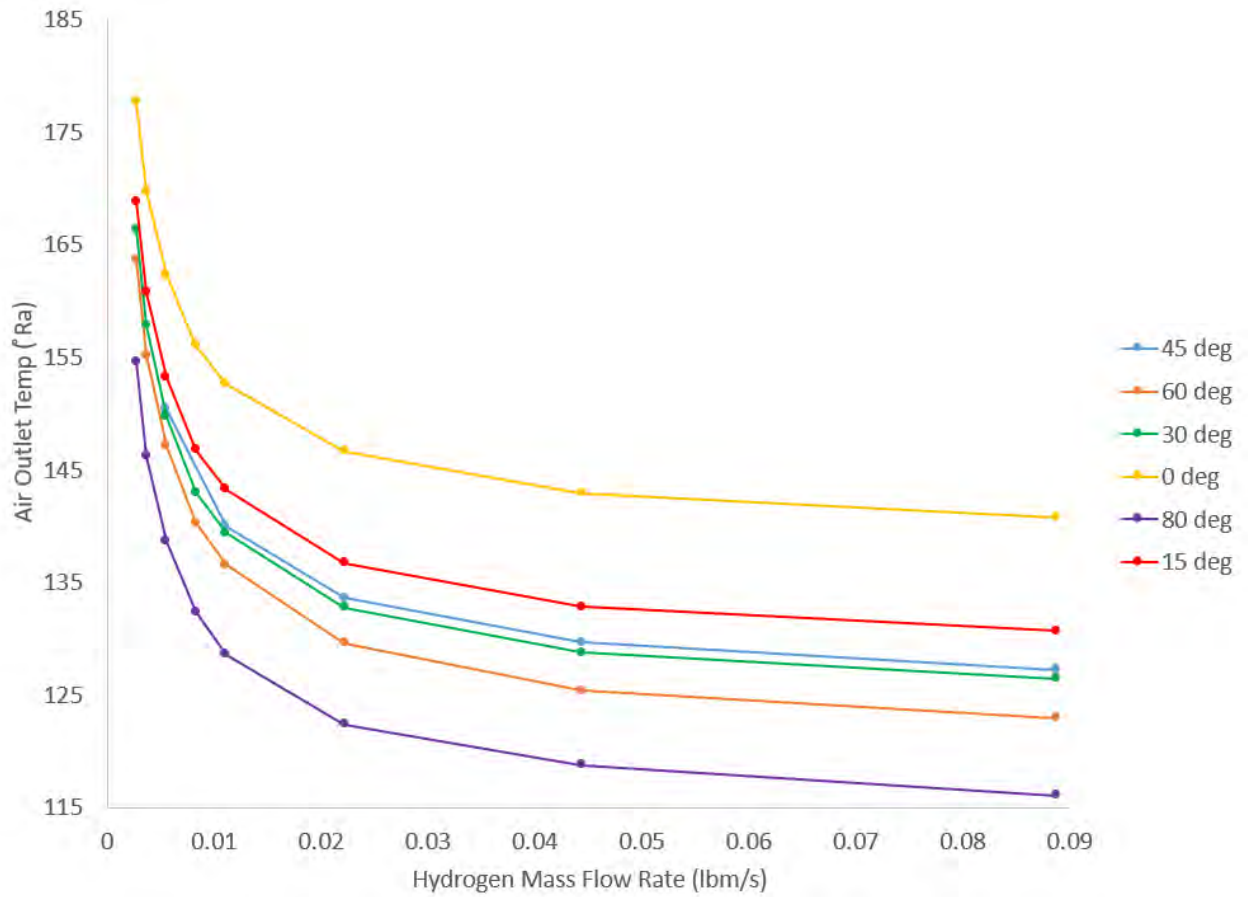


Figure 7. Plot of Hydrogen Mass Flow vs. Air Outlet Temperature.

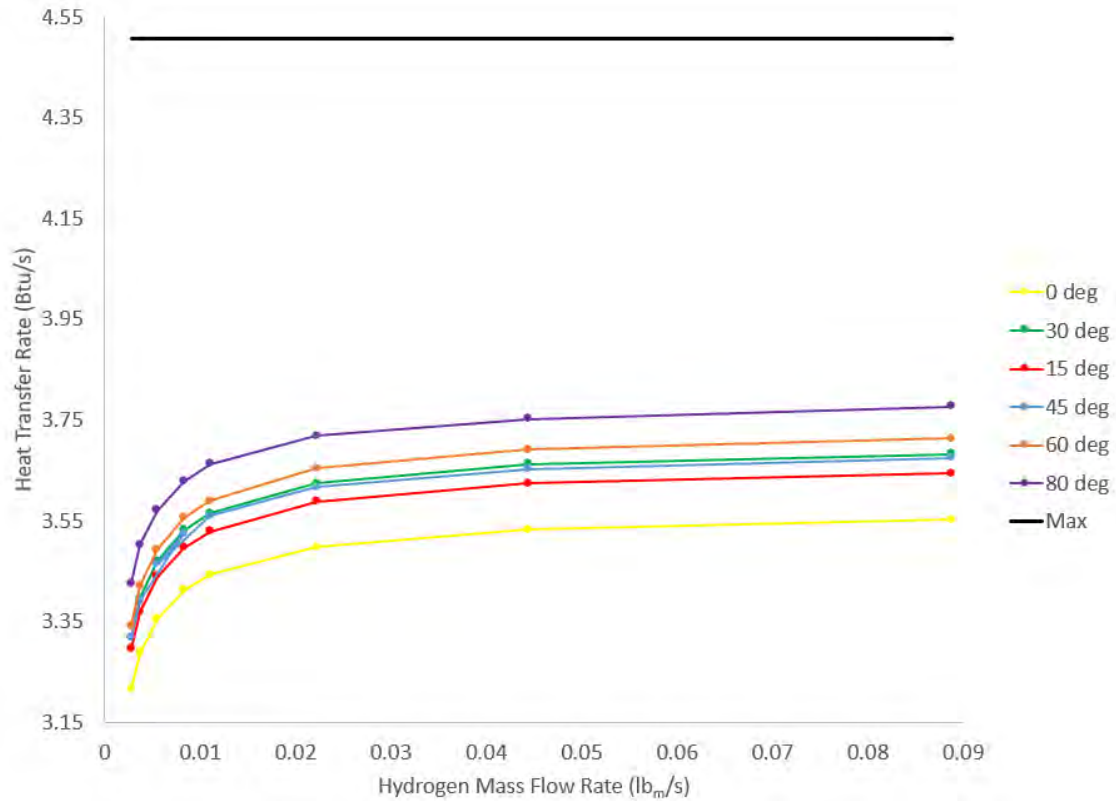


Figure 8. Plot of Hydrogen Mass Flow vs. Heat Transfer Rate.

Acknowledgments

The author would like to thank the Ohio Space Grant Consortium for sponsoring this work and Dr. David Davis for his help and guidance.

References

1. Harloff, G., & Smith, G. (1995). On supersonic-inlet boundary-layer bleed flow. 33rd Aerospace Sciences Meeting and Exhibit. doi:10.2514/6.1995-38.
2. Saunders & Davis. (2013) Liquefied Bleed for Stability and Efficiency of High Speed Inlets. NASA Internal Document.
3. Saunders & Davis. (2016) Small-Scale Liquid-Bleed (SSLB) Test Requirements. NASA Internal Document.
4. Çengel, Y. A., & Ghajar, A. J. (2015). Heat and Mass Transfer: Fundamentals and Applications. New York, NY: McGraw-Hill Education.
5. Shaver, D., Carasik, L., Merzari, E., Salpeter, N., Blandford, E. (2019). Calculation of friction factors and Nusselt numbers for twisted elliptical tube heat exchangers using Nek5000. Journal of Fluids Engineering. doi:10.1115/1.4042889.

Signal Analysis and Decomposition of Musical Instruments

Student Researcher: Timothy M. True

Advisor: Dr. Steven Gollmer

Cedarville University

Department of Science and Mathematics

Abstract

This project examines signal inputs from various musical instruments. The project focuses on decomposing the source input and analyzing the resulting content; the end goal is to determine several characteristics about the input signal, including pitch, instrument, and rhythm. We began by analyzing a single tone of one instrument, using FFT analysis to observe the spectral content. A windowing technique was created to break down a dynamic signal. The resulting frequencies were then outputted, producing a type of auto-scoring function. This function was then expanded to include input from multiple instruments. Adaptations allowed for basic analysis of this much more complicated situation. Continued effort will also be made to modify the decomposed signal in an advantageous way, and then recombine it into a usable form. This will allow audio files to be edited in a way that removes one instrument/source and allows others to remain intact.

Project Objectives

The goal of this study was to learn about signal analysis, particularly with application to musical instruments. Throughout this project, I examined signal inputs from various musical instruments. The project focused on decomposing the source input and analyzing the resulting content; the end goal was to determine several characteristics about the input signal, including pitch, instrumentation, and rhythm. An effort was also made to modify the decomposed signal in an advantageous way, and then recombine it into a usable form.

Methodology

The entirety of the numerical processing for this project was done in MATLAB. The use of this program throughout the semester provided a lot of practical coding experience. The Fast Fourier Transform function (FFT) was used to obtain the frequency data from the original audio file. Limited by time-frequency resolution constraints, I created a windowing function which broke down the original audio file into separate windows. I then took the FFT of each window, applying a Hanning filter to smooth the transition into and out of each window. I also had to work with merging overlapping frequency data back into one complete array in the time domain. This proved to be a challenge, but an educational experience nonetheless.

Results

One main completed accomplishment during the course of the past eight months was an auto-scoring function, which dictated the notes played by a single instrument. This required several pieces of code, including a windowing function and frequency identification function. The computer was able to successfully identify pitches from a melody. This melody contained various notes/pitches and various rhythms/lengths, and because of the windows I still could separate out the individual musical "events." As the project developed, there were several problems encountered. Original code relied on the relative intensities between the frequency peaks to determine the fundamental frequency present. This technique worked in basic situations, but in even slightly complex scenarios it starts to break down. For

example, see Figure 3. In this graph, the higher frequencies are dominating; it confuses the program as to the actual fundamental. However, by examining the ratio between the frequency value of the peaks, the fundamental could be correctly identified.

Through analyzing a cello, clarinet, and piano, I created a small database of characteristic instrument timbres. While the melody lines will be constantly unique, the upper harmonics will be related similarly as any given instrument performs (i.e. a cello will always sound like a cello). Given enough time and practice, a neural network could be created that taught the program how to more quickly and accurately identify various instruments. This would take practice and quite a few additional samples. However, it is very feasible to think that given enough examples, MATLAB would be able to match the upper harmonics present to a particular instrument. I was unable to decompose signal from multiple instruments. However, I created a substantial amount of the coding framework (over 400 lines) necessary to do so. By leaving much of the code general and applicable to a variety of situations, later efforts could still allow this. Presently, the harmonious relationship between pitches confuses distinction between a second fundamental and additional harmonics.

Conclusion

The IFFT process—modifying the signal in the frequency domain then converting back to the time domain—proved beyond the scope of this project. Efforts toward such an end revealed an oscillating imaginary component that leads to gaps in the audio data. This error comes from discretization of the audio signal and may not be entirely removable. The current windowing technique is functional but may have room for improvement. Instead of simply overlapping two windows all the time, ideally users would strategically overlap based on the audio data present. This would involve multiple “passes” through the data. A first pass would determine where the notes change. A second pass would then line up the windows with where the notes were known to change. The amount of overlap could also be varied. The windowing technique should also end up being frequency dependent. For the lower frequencies (i.e. a bass line), longer windows must be used. For the higher frequencies, shorter windows must be used. Finally, future work on this project will involve improving and implementing filtering. I used basic Hanning techniques to go from the time domain to the frequency domain, but I still need a way to filter/smooth my frequency data back into the time domain. Additionally, when the program learns what a particular instrument “sounds” like spectrally, it can filter it out. From this filtered frequency data, I will attempt to recreate a legitimate sounding audio file—minus the instrument I subtracted. If I can isolate the frequencies present which correspond to a particular input source, filtration opportunities will continue to abound.

Figures

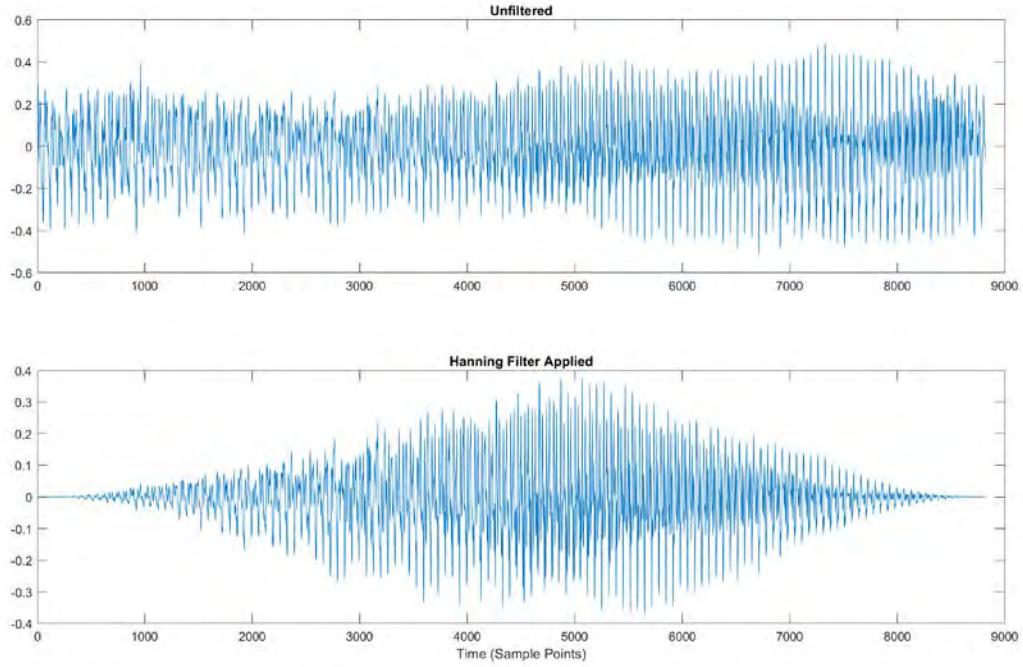


Figure 1. A small sample of time data, before and after the Hanning filter window has been applied.

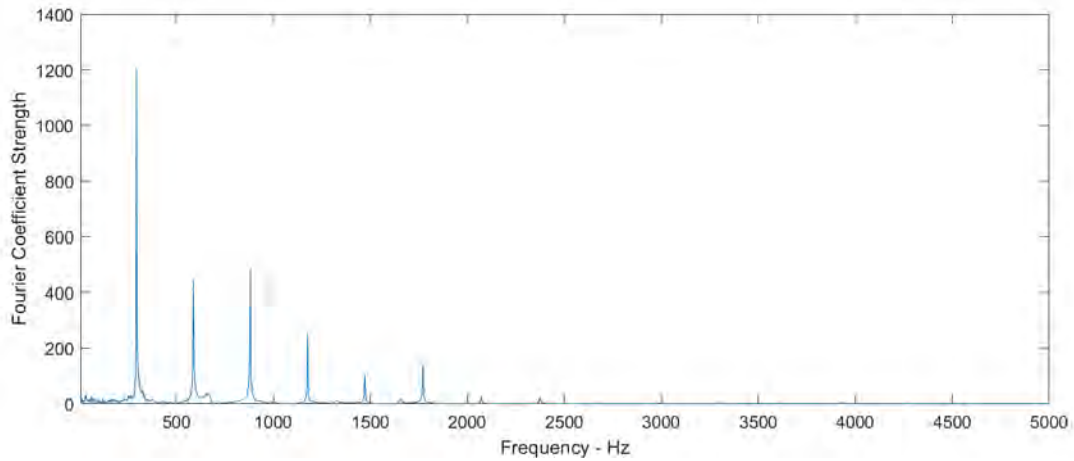


Figure 2. An example window of FFT data. This data was taken from a solo piano line. Note the clear integer spacing of upper harmonics.

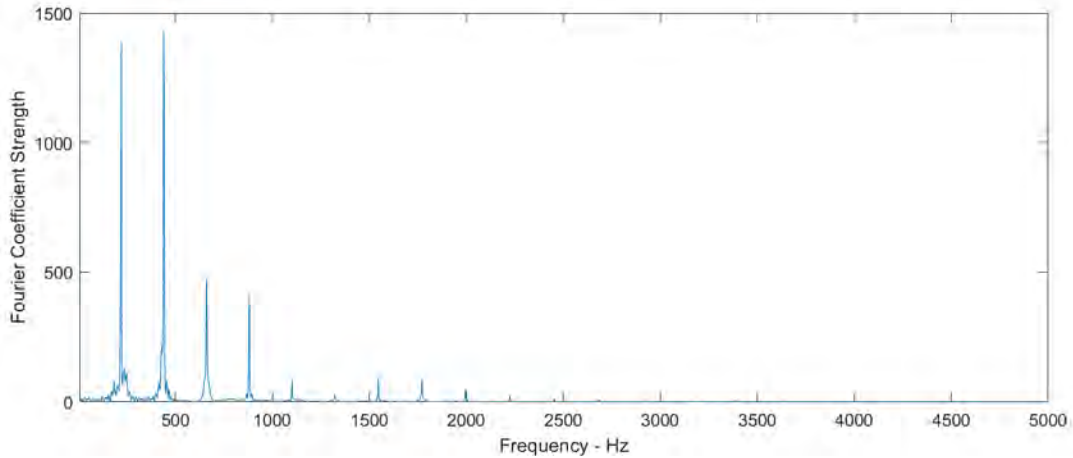


Figure 3. An example of high frequencies becoming more present than the fundamental. In such situations, the presence of lower harmonics--and the ratio between the harmonics--must be used to correctly identify the fundamental pitch.

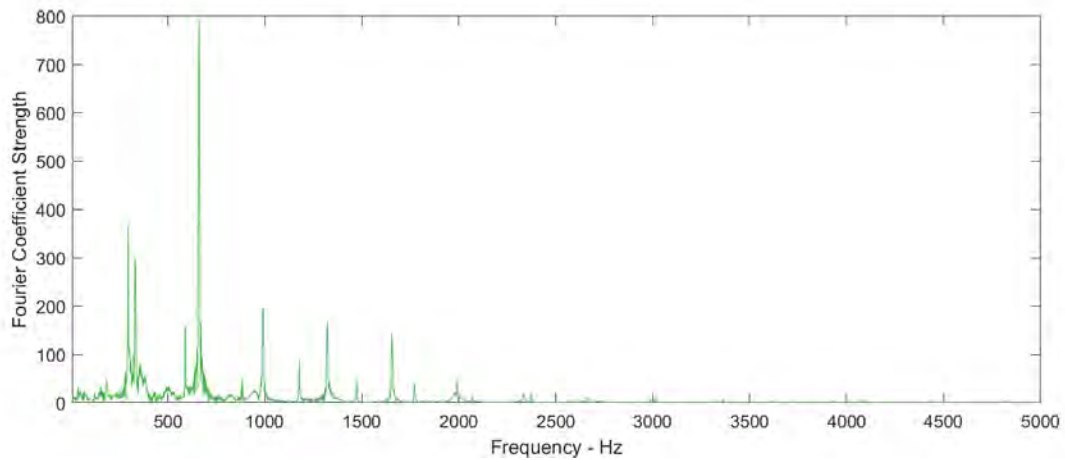


Figure 4. An example of a window encompassing a note change. Closely adjacent spikes show that the window started while one note was sounding and ended while a different note was sounding. Notice also the increased baseline noise throughout the frequency spectrum, caused by the piano hammer striking the string.

Calibration of Optical Paints for Aerodynamic Testing

Student Researcher: Grant A. Wagner

Advisor: Dr. Kevin J. Disotell

Youngstown State University

Department of Mechanical, Industrial and Manufacturing Engineering

Abstract

The use and calibration of pressure- and temperature sensitive paints allow for an easily operational, accurate, and cost-effective aerodynamic testing technique. Pressure- and temperature-sensitive paints (PSP/TSP) are image-based measurement techniques that provide full-field pressure and temperature maps across the surface of a wind-tunnel test model. Each pixel of the camera becomes a pressure/temperature sensor, greatly reducing instrumentation costs. The current work is focused on building a paint calibration apparatus to determine the relationship between measured pixel intensity and engineering units of pressure and temperature.

Project Objectives

The overall objective of the research is to design and construct a PSP/TSP static calibration apparatus for determining the Stern-Volmer relationship for a specific paint sample. Initially, this project was divided into two phases. Phase One would take place during the Junior year of the scholarship and has focused on designing the apparatus and gathering the necessary hardware and components for construction. Phase Two will occur during the Senior year of the scholarship and will focus on building, coding, and testing the apparatus to determine the Stern-Volmer relationship.

Methodology Used

The static calibration of the PSP operates on the oxygen quenching properties of the paint. (TSP is an encapsulated version of PSP which responds to the local thermal environment instead of oxygen quenching.) Based on these principles, the measured light intensity can be converted to the pressure (for PSP) and temperature (for TSP) at each point on a painted test surface. This relationship is given by the Stern- Volmer Equation,

$$\frac{I_{ref}}{I} = A(T) + B(T)(P/P_{ref})$$

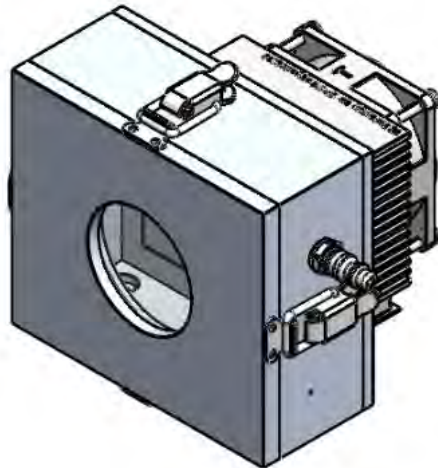
where I is the pixel intensity from a camera image, P is the local pressure, A and B are calibration coefficients which are functions of temperature (T), and the subscript ref denotes a reference (wind-off) condition [1]. Ultraviolet light is used to illuminate a test coupon of the paint and is subjected to a known pressure/temperature environment. From this known state, a uniform light intensity across the specimen surface is captured by a high-definition camera, generating calibration data for the relationship above.

Results Obtained

The following table shows the research progress over the past academic year of 2018-19, including key milestones.

September	-Initial research on PSP and TSP innerworkings was conducted. -Researched GE Druck Pace and Peltier heating devices.
October	-Quotes for pressure controller with 50psi barometric range obtained from 3 vendors. -Quotes for a Peltier Heating Element, Cold Plate, and Temperature Controller obtained. -Initial chassis design was generated in Solidworks. -Initial design was presented to research group.
November	-Initial chassis design revised. -Pressure and temperature control modules ordered.
December	-Preliminary Design Review of chassis was presented to research group. -Bill of materials updated.
January	-K-type thermocouple was researched and selected for apparatus. -Pressure and temperature controllers received.
February	-Chassis design was edited and finalized.
March	-Chassis design package was prepared for fabrication quotes.
April	-Fabrication quotes will be reviewed and selected. -Bill of materials will be finalized.

The chassis shell will be made of 0.5-in. aluminum plates with a detachable “front plate” to allow for maintenance and set-up, as shown below. A 3-in. optical quartz lens will be used for optical access.



References

1. Quinn, M., Spinoso, E., & Roberts, D. (2017). Miniaturization of Pressure-Sensitive Paint Measurement Systems Using Low-Cost, Miniaturized Machine Vision Cameras. *Sensors* 17(8), 1708. doi:10.3390/s17081708

Cortical Bone Mechanics Technology (CBMT) and Dual X-Ray Absorptiometry (DXA) Sensitivity to Bone Collagen Degradation in Human Ulna Bone

Student Researcher: Sarah M. Warnock

Advisor: Dr. Anne Loucks

Ohio University

Honors Tutorial College-Biological Sciences

Abstract

Bone is often regarded as a mostly inorganic tissue. Osteoporosis, a skeletal metabolic disorder characterized by increased bone fragility and fracture risk, is currently diagnosed by Dual X-Ray Absorptiometry (DXA) scan. However, DXA scanning is a poor predictor of fracture risk and bone quality, as it only assesses the mineral content of bone. Recent research increasingly suggests that other nonmineral parameters contribute to bone strength, such as size, geometry, and organic collagen. As a result, it is imperative to find a better diagnostic tool that more accurately encapsulates these other factors. One potential solution is Cortical Bone Mechanics Technology (CBMT), a novel technology being developed at Ohio University that uses a noninvasive, radiation-free three point mechanical loading test. Because CBMT is a mechanical test, it is believed to better detect changes in nonmineral factors. To assess this, denaturation of the organic collagen matrix was induced using 1M potassium hydroxide (KOH), which does not affect bone mineral. Paired cadaveric human forearms (n=16) were treated with either 0.9% saline (n=8) or 1M KOH (n=8) periosteal immersion for 39 hours. Arms were assessed with DXA and CBMT both before and after treatment. A statistically significant decline of 20.6% \pm 6.1% in ulna bending stiffness EI was observed using CBMT (p=0.01). DXA scanning did not detect a statistically significant decline in areal bone mineral content (aBMC), areal bone mineral density (aBMD), or area after treatment with KOH.

Introduction

Bone is an active, dynamic tissue and thus its strength is determined by multiple structural factors such as trabecular and cortical microarchitecture, collagen, geometry, and the degree of bone mineralization as determinants of bone strength (Viguet-Carrin, Garnero, & Delmas, 2006), (Fonseca, Moreira-Goncalves, Coriolano, & Duarte, 2014) (Felsenberg & Boonen, 2005). The current "gold standard" for osteoporosis diagnosis and fracture risk prediction is Dual X-Ray Absorptiometry (DXA). DXA uses a dual photon beam to differentiate bone mineral from the surrounding soft tissue; however, it is a poor predictor for risk of fracture and uses analysis of a two-dimensional scan and does not detect the contributions of the other structural factors. Cortical Bone Mechanics Technology (CBMT), however, is a mechanical test in development at Ohio University to assess bone and assesses bending stiffness (EI), which is highly correlated with bone strength and may be more useful in detecting decline in nonmineral strength parameters. To assess this, paired human cadaveric ulnas were submerged for 39 hours in either 1M potassium hydroxide (KOH) or calcium-buffered 0.9% saline so that the periosteal surface of the bone was exposed to KOH. KOH has previously been shown to not affect bone mineral but is hypothesized to denature collagen; saline has been established to have no effect on bone (Wynnyckyj et al., 2010).

Project Objectives

The objectives of this project were twofold: to demonstrate that 1M KOH negatively affected bone collagen undetectable by DXA, and to detect this change using CBMT.

Methodology

Paired fresh-frozen cadaveric human arms were obtained from a human tissue bank (Science Care, Inc., Phoenix, AZ). A randomized experimental design was used in which eight pairs of ulna bones excised from cadaveric human arms were immersed in 1M potassium hydroxide (KOH) solution or a calcium-buffered 0.9% saline solution. Tissue from the forearm and the upper arm was removed exposing the bone. The radius was also removed. The elbow joint was left intact to allow the humerus to support the proximal end of the ulna during CBMT testing. CBMT and DXA testing was performed before and after the KOH or saline 39 hour immersion.

DXA scanning was performed using a Hologic Discovery W 13.4.2 model scanner. Prior literature describes good correlation between *in vivo* and *ex vivo* DXA measurements (Turner et al., 1995) (Pouilles et al., 1999). To prevent contamination of the scanner, the excised specimen were sealed in plastic film using a 15" Cabela commercial grade vacuum sealer prior to scanning. The 1/3 region of the ulna was then measured and marked on the plastic as a reference point for specimen positioning during scanning. To mimic the presence—and density—of soft tissue surrounding the bone, the sealed specimens were submerged in a room temperature calcium-buffered saline solution, which has previously been demonstrated to be a useful soft tissue substitute when scanning excised bone (Rosen et al., 1994) (Mirzaali et al., 2018). Simulating soft tissue with saline was critical because DXA normally is utilized *in vivo* clinically, but could introduce potential variability if the bone floated, moved, or rotated in the saline. To combat this, the sealed ulna's movement in the saline was minimized by placing it into a clamp made entirely of polycarbonate. Polycarbonate plastic has low X ray attenuation as well as high near-infrared light penetration and thus does not interfere with imaging, making it optimal material for scanning (Michaelsen et al., 2012). The clamp not only kept the bone submerged, but also prevented rotation during testing and allowed the height and levelness of the ulna to be standardized between testing before and after immersion in either KOH or saline. To prevent the clamp from shifting or floating, the base of the clamp was held down with a ceramic cup outside the region of scanning. The height of the saline solution was standardized to 8cm. The clamp was positioned at the edge of the plastic tote in order to provide at least one inch of air, which the software needs as a baseline for assessment, as the software for measurement of the ulna bone expects to detect bone, tissue, or simulated bone tissue using saline and air.

The scans were performed and analyzed five times per ulna using the same analysis protocol as the baseline scans with the intact forearm. The scanning protocol with the Hologic software was performed in the same manner and orientation as the intact arm, with the exception of estimating where to start the scan due to the lack of carpal bones. As the regions of interest are determined standardized to the styloid process of the ulna and ulna length, this did not affect the size or positioning of the regions being assessed.

After DXA scanning, the bone was removed from the plastic sealing and tested using our lab's CBMT device. The ulna was supported at the proximal end by the humerus and was supported at the distal end with a platform that could be adjusted to level the ulna. The bone was positioned with the shaker probe of the device at the midpoint of the bone, with the bone as parallel to the probe as possible. A force of either 10, 15, or 20 Newtons was applied. Rubber strips were added below the probe to simulate soft tissue. Between transits, the bone was repeatedly sprayed with calcium-buffered saline solution to maintain moisture and prevent changes in bone stiffness due to drying, (Gustafson et al., 1996). Testing generated a frequency response function (FRF) as well as EI values.

After DXA and CBMT testing, each of the paired arms from the donor received one of two interventions: incubation by total submersion in either 1M KOH solution or calcium-buffered saline solution. KOH solution was obtained from Fisher Scientific and was prepared by LabChem (LC19350, Zelienople, PA); KOH is highly basic, and is believed to selectively denature organic tissue while leaving inorganic mineral intact (Wynnyckyj et al., 2010). Calcium-buffered 0.9% saline served as the control, as 10 days of immersion has previously been shown to not diminish EI or dissolve mineral content of bone (Gustafson et al., 1996). Incubation occurred at room temperature under a fume hood, and the duration of incubation was standardized to 39 hours. An incubation period of 39 hours was chosen based on prior trial data from four unpaired arms. A 39 hour immersion, based on this data, resulted in approximately a 30% decrease in EI, and thus was the standardized incubation time.

Incubation occurred within closed containers made of either polypropylene or polyethylene, both of which are resistant to exposure to strong bases, and were kept inside a second, high-walled container of the same materials for added safety (ThermoScientific). Additionally, to ensure homogeneity of exposure, the solutions were stirred, and pH was measured again during their respective incubations.

Neutralization of the KOH-treated specimen occurred by removing it from the KOH and immediately placing it into a bath of water for ten minutes, then assessed with pH test strips. The bone was then removed and placed into a second water bath with a continuous flow of water and assessed with pH test strips. All equipment coming into direct contact with KOH was immediately neutralized using a spray bottle of vinegar and rinsed thoroughly.

Due to the highly caustic nature of KOH, additional personal protection equipment (PPE) was utilized during handling during incubation and neutralization. Thick rubber boots, industrial chemical-resistant Tyvek suits, and protective goggles were worn at all time, as well as two pairs of chemical-resistant gloves (Dupont Chemical, Wilmington, DE). All work occurred with another lab member in PPE present as an added measure of precaution.

Results

The Hologic Discovery W 13.4.2 model scanner assesses three Regions of Interest (ROI): the ultradistal (UD), mid, and 1/3 regions. (FIG 1). Within each ROI, the software can assess the mineral parameters of the radius, ulna, or the radius and ulna together. For this project, the 1/3 region of the ulna was utilized, as the radius was removed prior to testing and the 1/3 region of the bone is farthest down the diaphysis of the bone and has the highest proportion of cortical bone. The results of this project supported the expected findings. As anticipated, incubation in KOH led to a decline of $20.6\% \pm 6.1\%$ ($p=0.01$) in EI as assessed by CBMT; DXA, however, did not detect a statistically significant change in either a BMD ($0.2\% \pm 0.8\%$) or area ($0.4\% \pm 0.3\%$). For the saline-treated control cohort, no statistically significant change in EI was assessed by CBMT ($-0.6\% \pm 2.3\%$) ($p=0.8$) and no statistically significant change was detected in aBMD ($-1.4\% \pm 0.9\%$) or area ($0.0\% \pm 0.4\%$) by DXA.



Figure 1. Regions of interest assessed by DXA.

Acknowledgements

Research described in this report was supported by the National Institute on Aging of the National Institutes of Health under Award Number R43AG058312. Thanks to Dr. Anne Loucks for guidance, and members of Dr. Loucks' lab for aid in carrying out the project and data analysis.

References

1. Viguet-Carrin, S., Garnero, P., & Delmas, P. D. (2006). The role of collagen in bone strength. *Osteoporosis International*, 319-336.
2. Fonseca, H., Moreira-Gonc,alves, D., Coriolano, H. A., & Duarte, J. A. (2014). Bone Quality: The Determinants of Bone Strength and Fragility. *Sports Medicine*, 37-53.
3. Turner, A., Mallinckrodt, C., Alvis, M., Bryant, H. (1995). Dual-Energy X-Ray Absorptiometry in Sheep: Experiences with In Vivo and Ex Vivo Studies. *Bone*, 381S-387S.
4. Poulles, J., Collard, P., Tremollieres, F., Frayssinet, P., Railhac, J., Cahuzac, J., Autefage, A., Ribot, C. (2000). Accuracy and Precision of *In Vivo* Bone Mineral Measurements in Sheep Using Dual-Energy X-Ray Absorptiometry. *Calcified Tissue International*, 70-73.
5. Rosen, H., Middlebrooks, V., Sullivan E., Rosenblatt, M., Maitland, L., Moses, A., Greenspan, S. (1994). Subregion Analysis of the Rat Femur: A Sensitive Indicator of Changes in Bone Density Following Treatment with Thyroid Hormone or Bisphosphonates. *Calcified Tissue International*, 173-175.
6. Mirzaali, M., Libonati, F., Ferrario, D., Rinaudo, L., Messina, C., Ulivieri, F., Cesana, B., Strano, M., Vergani, L. (2018). Determinants of Bone Damage: an Ex-Vivo Study on Porcine Vertebrae. *PLOS One*. 1-19.
7. Michaelsen, K., Krishnaswamy, V., Pogue, B., Brooks, K., Defreitas, K., Shaw, I., Poplack, S., Paulsen, K. (2012). Characterization of materials for optimal near-infrared and x-ray imaging of the breast, *Biomedical Optics Express*, 2078-2086.
8. Gustafson, M., Martin, R., Gibson, V., Storms, D., Stover, S., Gibeling, J., Grififn, L. (1996). Calcium Buffering is Required to Maintain Bone Stiffness in Saline Solution. *Journal of Biomechanics*, 1191-1194.
9. Wynnyckyj, C., Willett, T. L., Omelon, S., Wang, J., Wang, Z., & Grynepas, M. D. (2010, August 27). Changes in Bone Fatigue Resistance due to Collagen Degradation. *Journal of Orthopaedic Research*, 29(2), 197-203.

Mass Timber as a Sustainable Alternative for the Construction Industry

Student Researcher: Barbara L. Watkins

Advisor: Dean M. Bortz, MA, CSI, CDT, CCPR

Columbus State Community College

Design, Construction and Trades Department

Abstract

Materials used to construct modern buildings, roads and bridges are mined, harvested, or extracted from the earth. Concrete and steel have been the primary materials used to build mid and high-rise building for many decades. There have been improvements in the manufacturing of concrete and steel, but it remains a source of both high energy consumption and emissions.

An alternative building material that is starting to be used for mid-rise buildings is mass timber. Mass timber construction offers a more environmentally friendly approach to meeting the growing demands on the building industry. Unlike concrete and steel, wood is a renewable resource that can be sustainably grown and harvested. Wood products also serve as carbon reservoirs, sequestering carbon for the life of the wood product. This project will focus on how mass timber could be a viable alternative for building midrise, and hopefully soon, high-rise buildings in a more environmentally-friendly way.

Project Objective

The purpose of this project is to research environmental impacts of current construction practices and commonly used materials to then better understand how mass timber could be a more sustainable alternative. The research will also focus on different types of mass timber products, their primary uses, strength and load requirements, sustainability, fire resistance, and potential challenges.

Methodology Used

This project focuses on current industry research and examples of built projects involving the use of mass timber as a primary construction material.

Results Obtained

Mass timber is a viable material to be used for mid-rise building construction. The International Code Council recently endorsed updates to building codes for mass timber construction. The current research and testing indicate that mass timber is safe from a fire resistance perspective, can shorten construction timelines, and offers environmental benefits as a renewable resource.

Significance and Interpretation of Results

From a construction standpoint, mass timber offers quicker construction timeframes, prefabrication options, and requires fewer people to construct. The industry is experiencing a significant labor shortage; the use of a material that can shorten time and require fewer people will benefit the industry. Environmentally, mass timber is a remarkable alternative. Wood is a renewable resource that can be sustainably grown and harvested. Trees also sequesters carbon while growing in the forest and then contain the carbon for the life of the built structure as a wood product. Concrete and steel are and will continue to be important construction materials, but by increasing the use of mass timber or mass timber/concrete hybrid materials, the construction industry can improve its carbon footprint.

References:

1. American Wood Council. (2017, July 13). *Fire testing completed on full-scale mass timber building*. (AMC). Retrieved from: www.awc.org/news/2017/07/13/fire-testing-completed-on-full-scale-mass-timber-building
2. The Economist (2018, February 1). *Wooden skyscrapers could be the future for cities*. Retrieved from: www.youtube.com/watch?v=2DPp2NcnTb0&vl=en
3. McKee, Mik. (2016, March 23). *The Hidden Carbon Benefits of Cross Laminated Timber*. The Climate Trust. Retrieved from: www.triplepundit.com/2016/03/hidden-carbon-benefits-cross-laminated-timber/
4. Mehta, M., Scarborough, W., & Armpriest, D. (2018). *Building Construction: Principles, Materials, and systems*. (3rd Edition). New York, NY. Pearson
5. ReThink Wood. (PDF, no date given). *Mass Timber in North America: Expanding the possibilities of wood building design*. Retrieved from: www.awc.org/pdf/education/des/ReThinkMag-DES610A-MassTimberinNorthAmerica-161031.pdf
6. Rodgers, Lucy. (2018, December 17). *Climate change: the massive CO2 emitter you may not know about*. British Broadcasting Corporation. Retrieved from: www.bbc.com/news/science-environment-46455844
7. Science for Environment Policy. (2011, March). *Reducing the environmental impacts of building materials*. European Commission. Retrieved from website: http://ec.europa.eu/environment/integration/research/newsalert/pdf/232na1_en.pdf
8. U.S. Energy Information Administration. (2018, May 3). *How much energy is consumed in U.S. residential and commercial buildings?* (EIA). Retrieved from: www.eia.gov/tools/faqs/faq.php?id=86&t=1

Observing the Effects of Airfoil Alteration on Flight Parameters

Student Researcher: Carly G. Waugh

Advisor: Dr. Jed E. Marquart, P.E.

Ohio Northern University
College of Engineering

Abstract

Airfoils are the curved cross sections of aircraft wings that are designed to produce lift and give the aircraft the most favorable lift to drag ratio. The subject of this paper is to explore the effects of altering geometric characteristics of modified NACA 4-digit airfoils on various flight parameters. The airfoil computer models were “built” using the DesignFOIL® software, and then the maximum thickness and maximum thickness location were altered. Calculations were performed within DesignFOIL® on the modified airfoil shapes to determine the effects of these alterations on the maximum coefficient of lift, zero-lift drag coefficient, and the maximum lift to drag ratio. Comparisons were made between the various configurations and conclusions were drawn.

Nomenclature

α	=	angle of attack
b	=	wingspan
c	=	chord (length of airfoil)
S	=	planform area
E	=	Oswald’s Efficiency Factor
C_{D0}	=	zero lift drag coefficient
C_{LMax}	=	maximum coefficient of lift
AR	=	aspect ratio
K	=	proportionality factor
$(L/D)_{Max}$	=	maximum lift/drag ratio

Introduction

The study of airfoils dates back to before the Wright brothers attempted to be the first in flight. After their success, the need for better airfoils was essential. In 1915, The National Advisory Committee for Aeronautics (NACA) was formed with the goal of coordinating research efforts in aeronautics ^[1]. Most notably, their goal was to develop airfoils with more favorable lift and drag characteristics. Airfoils are the cross sections of aircraft wings that are designed to have the most effective curvature for the most favorable lift to drag ratio ^[2]. The earliest NACA airfoil series were produced using analytical equations to describe their curvature (camber) and maximum thickness. Research on airfoils continued into the 1930s, and beyond, with NACA publishing a report titled The Characteristics of 78 Related Airfoil Sections from Tests in the Variable Density Wind Tunnel ^[2]. This was a significant report because it

stated that the most important airfoil characteristics that affect its shape are the camber and the thickness distribution. NACA airfoils are separated into categories based on their shapes. These categories include the NACA Four-Digit Series, Five-Digit Series, Modified Four- and Five-Digit Series, 1-Series, 6-Series, 7-Series, and 8-Series. Each NACA Series was developed with differing areas of flight and conditions in mind ^[2]. Since this paper explores varying properties of the modified NACA Four-Digit Series, the denotation will be explained further.

Modified NACA Four-Digit Series airfoils contain 6 numbers. For example, take the NACA 0012-63. This airfoil will be the first one analyzed in this paper. The first digit in the series specifies the maximum camber as a percentage of the chord (length of the airfoil). In this example, the maximum camber is the 0% of the chord. The second number is the location of the maximum camber in tenths of a chord. With the second number being 0, the location of the maximum camber is located at 0% of the chord. Since the first two numbers of the airfoil are both 0, it can be said that the airfoil is symmetric (no camber). The last two numbers before the hyphen indicate what the maximum thickness of the airfoil is as a percentage of chord. This means that the NACA 0012-63 has a maximum thickness of 12% of the chord. The first number after the hyphen is the leading edge roundness factor. The second number after the hyphen indicates the location of the maximum thickness in tenths of chord ^[3]. This means that the NACA 0012-63 airfoil has a roundness factor of 6 and a maximum thickness location of 30% of the chord.

Problem Description

As previously stated, the objective of this research was to analyze the impact of altering the characteristics of airfoils on its flight parameters. Two airfoils were selected to be analyzed, one symmetric and the other with camber (asymmetric). The symmetric airfoil is the NACA 0012-63 airfoil and the asymmetric is the NACA 2412-63. The characteristics that were altered on both airfoils were the maximum thickness and the location of the maximum thickness. These two characteristics were chosen because of their noted impact in the aforementioned NACA report The Characteristics of 78 Related Airfoil Sections from Tests in the Variable Density Wind Tunnel ^[2]. It is also worth noting that one symmetric and one asymmetric airfoil were chosen to observe the impact that the variations in thickness had on airfoils of both these types. Another note is that once the thickness characteristics are changed on the airfoils, they are no longer the same airfoil in their respective series. The NACA 0012-63 and the NACA 2412-63 were chosen to be starting points since they are both common airfoil shapes. The DesignFOIL [®] software was used to “build” both airfoils and determine the characteristics of the test cases ^[4].

Assumptions

Before the airfoils could be built and analyzed in DesignFOIL[®], some airplane parameters had to be assumed. The following assumptions were made based on known parameters and needed flight conditions of the Legend Cub light sport aircraft ^[5].

- A wingspan of 35 feet
- A chord length of 6 feet
- An altitude of 500 feet
- Flight speed of 202.4 feet per second
- Oswald Efficiency Factor of 0.8
- An angle of attack of 3°

Modeling and Analysis

Both airfoils were then constructed in DesignFOIL®. Figure 1 shows the NACA 0012-63 airfoil after construction.

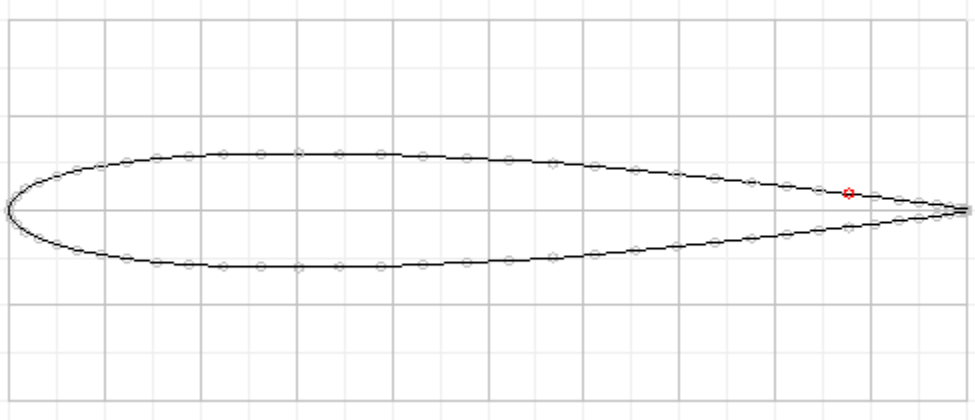


Figure 1. NACA 0012-63 Airfoil.

The airfoil was then placed into the “virtual wind tunnel” and ran under the conditions in the Assumptions section of this paper. The first case that was ran of this symmetric airfoil was adjusting the maximum thickness of the airfoil. The airfoil was adjusted from a max thickness of 12% to 30% of the chord by an interval of 2%. The NACA drag-polar plots for this case can be seen in Appendix A. The C_{D0} and the C_{LMax} data used in the calculations were obtained from these plots. Once they were recorded for the this case, the maximum lift to drag $((L/D)_{Max})$ ratio was to be determined. In order to calculate the $(L/D)_{Max}$ ratio, variables such as the planform area (S), the aspect ratio (AR), and the proportionality factor (K) needed to be calculated. The planform area refers to the top surface area of the entire wing. In this case, the assumed wingspan (b) was 35ft and the chord length (c) was assumed to be 6 ft. Equation 1 shows the planform area calculation [6].

$$S = b * c \quad (1)$$

The aspect ratio refers to the ratio of the wingspan squared (b^2) to the planform area [6]. This relationship can be seen in Equation 2.

$$AR = \left(\frac{b^2}{S}\right) \quad (2)$$

The proportionality factor relates the aspect ratio to the Oswald Efficiency Factor (e). Equation 3 shows the calculation for the proportionality factor [7]. Here, the Oswald Efficiency Factor (e) is 0.8.

$$K = \left(\frac{1}{\pi \cdot e \cdot AR}\right) \quad (3)$$

With the planform area, aspect ratio, and the proportionality factor calculated, the $(L/D)_{Max}$ ratio could now be calculated. Equation 4 shows the calculation for $(L/D)_{Max}$ [6]. The value for the zero lift drag coefficient was obtained from the drag-polar plot that was generated in DesignFOIL for each alteration. An example of the drag-polar plot can be seen in Appendix A.

$$\left(\frac{L}{D}\right)_{Max} = \sqrt{\frac{1}{4 \cdot K \cdot C_{D0}}} \quad (4)$$

The $(L/D)_{\text{Max}}$ ratio was the final flight parameter whose behavior as it related to the varying airfoil thickness (in this case maximum thickness) was to be analyzed. The Engineering Equation Solver (EES) code that contained Equations 1-4 can be seen in Appendix B [8]. The results for the maximum thickness variation as it impacted the C_{D0} , $C_{L\text{Max}}$, $(L/D)_{\text{Max}}$, will be discussed in the following section.

The same analysis was done again for the symmetric airfoil but with the location of the maximum thickness altered and the maximum thickness itself staying constant. The analysis was then performed again, with both the maximum thickness being altered and then the maximum thickness location being altered, but for the asymmetric airfoil. The base asymmetric airfoil that was chosen was the NACA 2412-63. Figure 2 shows the NACA 2412-63 airfoil after it was constructed in DesignFOIL®.

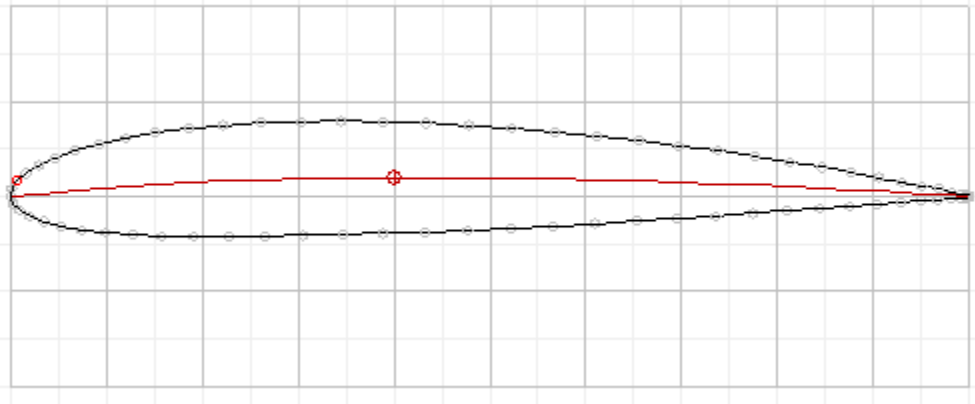


Figure 2. NACA 2412-63 Airfoil.

Results and Discussion

The goal of this research was to analyze the effects of altering the thickness and its location on three different characteristics of the airfoil's performance. The relationship between the zero lift drag coefficient and the maximum thickness of each airfoil type was the first performance parameter to be analyzed. As previously stated, the researcher obtained the C_{D0} value from the drag-polar plots that were generated by DesignFOIL®. For the symmetric case, C_{D0} was found to have a positive relationship with the maximum airfoil thickness. This means that as the thickness was increased, the C_{D0} value also increased. The correlation coefficient (R^2) value of the graphical relationship was also determined to be 0.9407. This indicates a strong correlation between the two the thickness and the C_{D0} value. Figure 3 shows the relationship between the C_{D0} and the maximum airfoil thickness value.

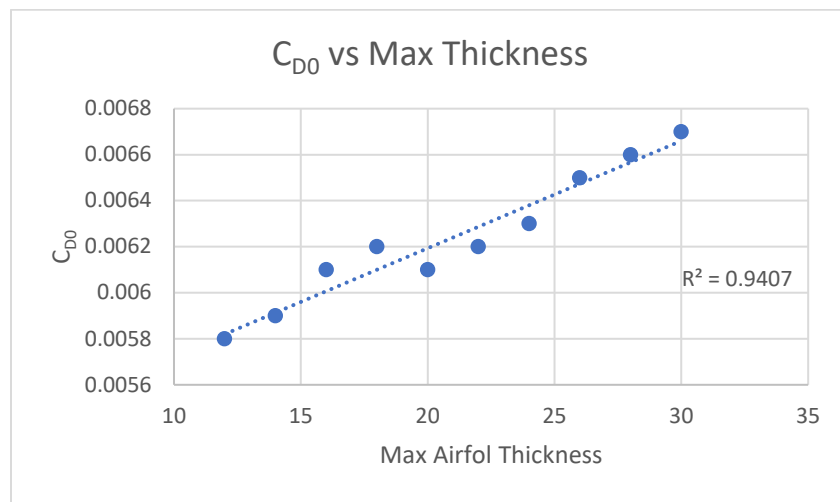


Figure 3. C_{D0} vs Maximum Airfoil Thickness (Symmetric).

The relationship between the maximum lift coefficient C_{LMax} and the maximum airfoil thickness was then analyzed. The graph of the data (Appendix C) shows that the variables had a negative relationship, meaning that as the thickness increased, the C_{LMax} decreased. The R^2 value (0.996) of the data also showed a high correlation between the two variables. Figure 4 shows this relationship graphically.

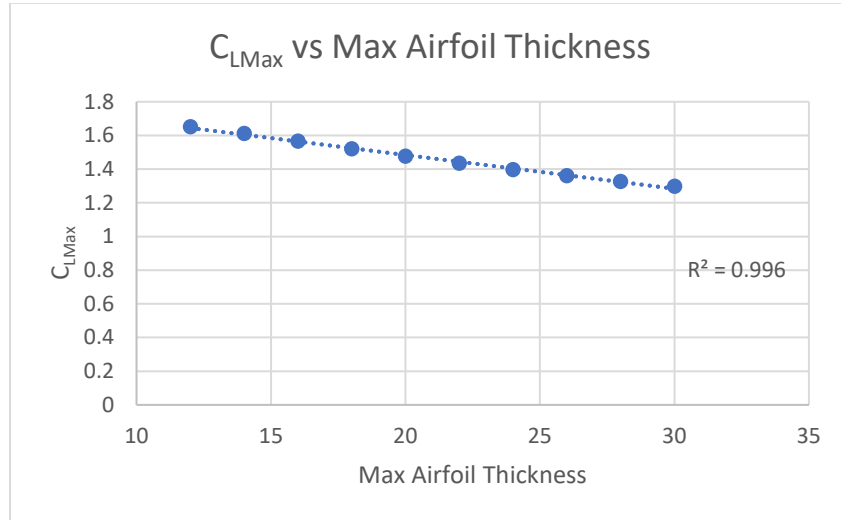


Figure 4. C_{LMax} vs Maximum Airfoil Thickness (Symmetric).

The final relationship that was studied for the maximum thickness increase was how it related to the Lift-to- Drag Ratio $(L/D)_{Max}$. From the graph in Figure 5, it can be seen that as the maximum thickness is increased, the $(L/D)_{Max}$ decreased. The data points also have a R^2 value of 0.9416, indicating a strong correlation.

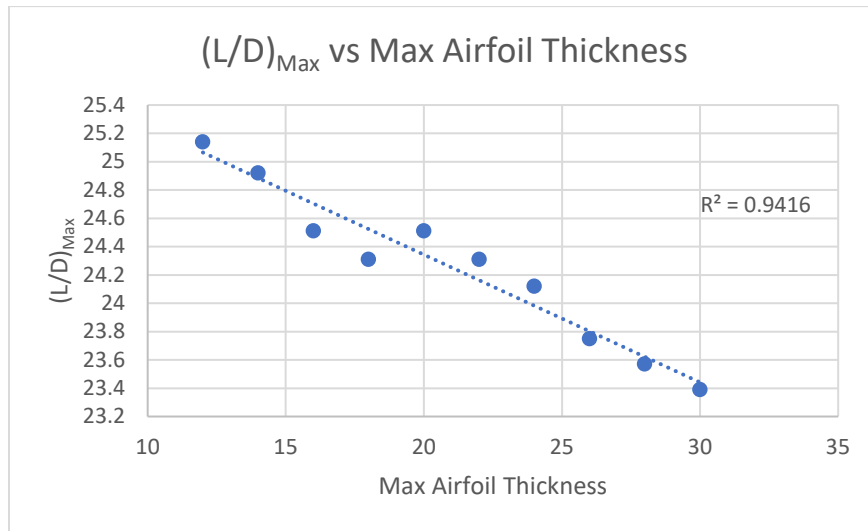


Figure 5. $(L/D)_{Max}$ vs Maximum Airfoil Thickness (Symmetric).

Once the effect of altering the maximum thickness value on the three studied flight parameters was analyzed, the parameters were analyzed again with the maximum thickness held constant and its location altered. Comparing the thickness location to the final values of the C_{D0} , C_{LMax} , and $(L/D)_{Max}$ parameters yielded results that showed no strong relationship. The R^2 values for each relationship were all well below the highest possible value of 1. The graphs of these relationships can be seen in Appendix C.

After analyzing the behavior of the C_{D0} , C_{LMax} , and $(L/D)_{Max}$ when looking at a symmetric airfoil, the same analysis was performed on the asymmetric airfoil. When comparing its maximum thickness value to the value of C_{D0} , it showed a positive correlation. Figure 6 shows that as the thickness increased, the value of C_{D0} also increased. The R^2 of 0.976 can also be seen on the graph along with the trendline.

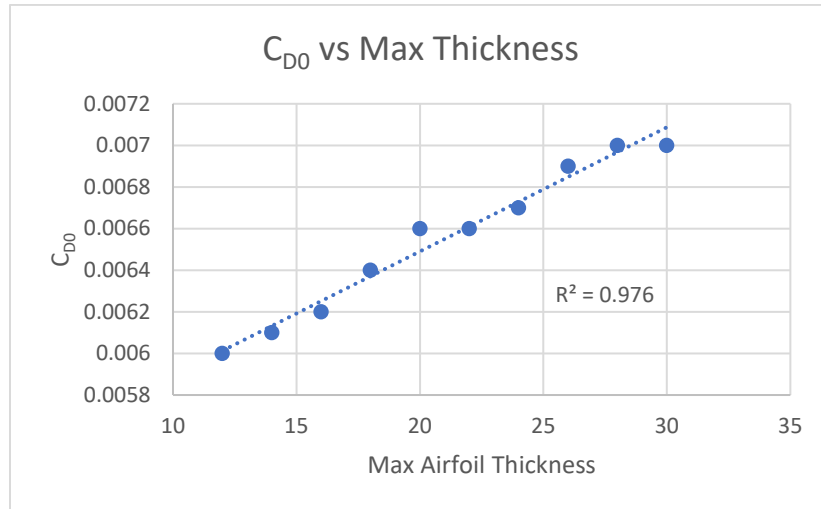


Figure 6. C_{D0} vs Maximum Airfoil Thickness (Asymmetric).

The behavior of the C_{LMax} variable as it compared to the maximum airfoil thickness can be seen in Figure 7. Here, it was observed that the C_{LMax} decreased as the maximum thickness increased. It was also found to have a high correlation since the R^2 value was high at 0.9918.

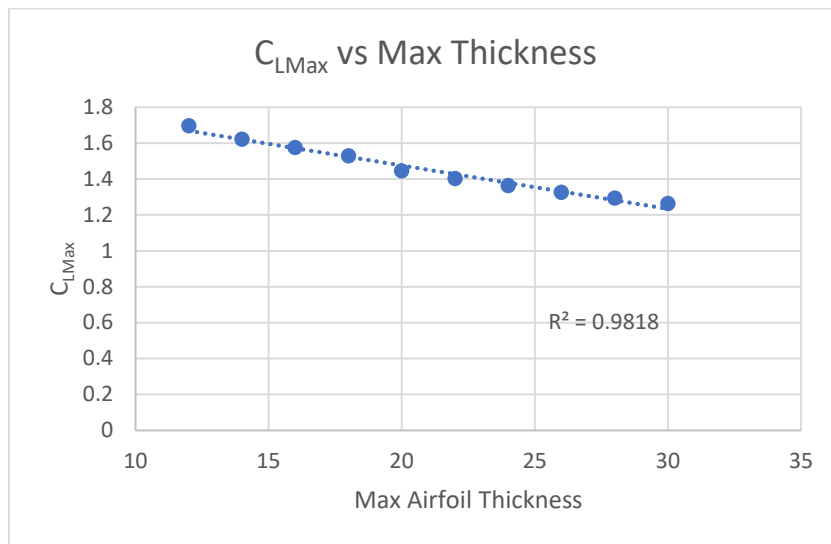


Figure 7. C_{LMax} vs Maximum Airfoil Thickness (Asymmetric).

The $(L/D)_{Max}$ parameter was then analyzed to see how it behaved as related to the maximum thickness. It was found that as the maximum thickness increased, the $(L/D)_{Max}$ parameter decreased. This relationship, along with the R^2 value of 0.9722 can be seen in Figure 8. As seen in the graph, there is a strong correlation.

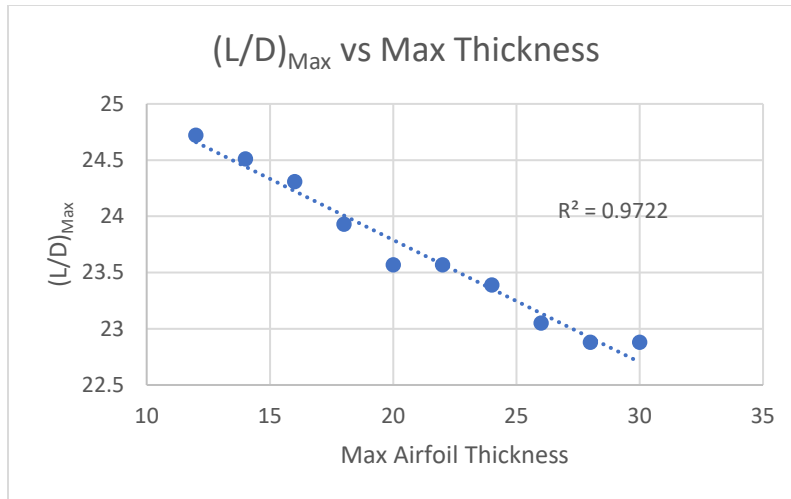


Figure 8. $(L/D)_{Max}$ vs Maximum Airfoil Thickness (Asymmetric).

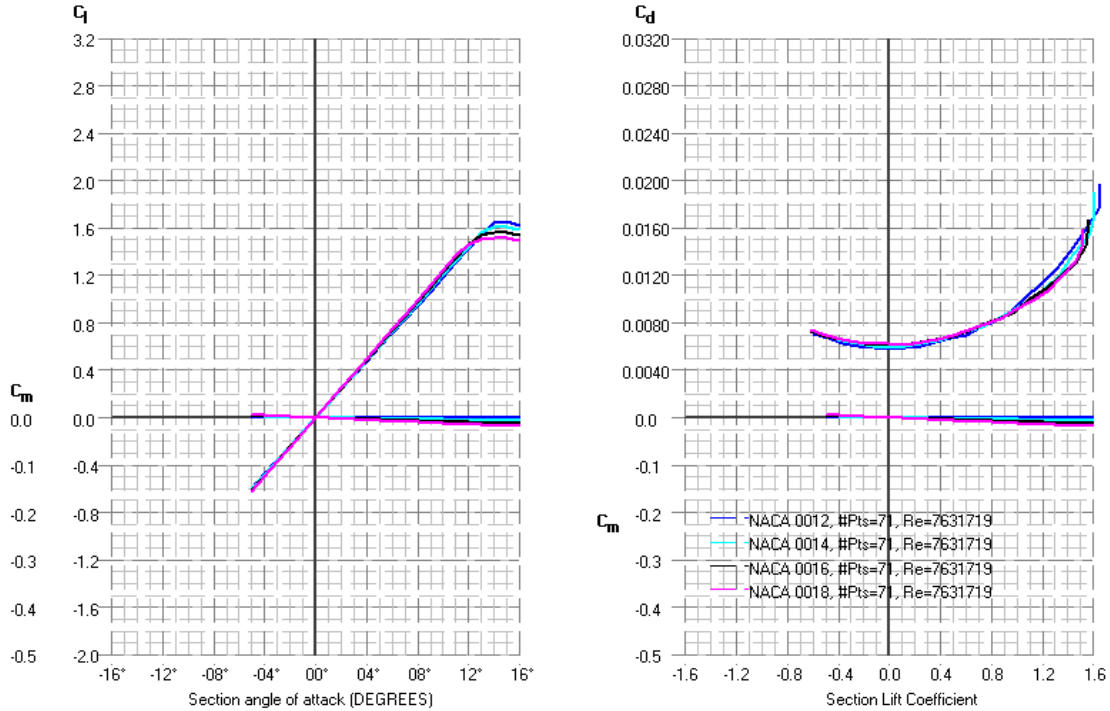
The location of the maximum airfoil thickness was then altered for each analysis with each parameter. Similar to the symmetric airfoil analysis, when comparing the thickness location to the final values of the C_{D0} , C_{LMax} , and $(L/D)_{Max}$ parameters yielded results that showed no strong relationship. The R^2 values for each relationship were all well below the highest possible value of 1. The graphs of these relationships can be seen in Appendix D along with their respective R^2 value.

Conclusions

While this research yielded no groundbreaking results, it did provide evidence that the maximum thickness of an airfoil has a direct impact on the flight parameters that were studied (C_{D0} , C_{LMax} , and $(L/D)_{Max}$). It also provided evidence that points to there being very little correlation between the location of the airfoil's maximum thickness and the aforementioned flight parameters. These results were found to be true for both the symmetric and airfoil analyses.

Appendices

Appendix A: Example of a Drag-Polar-Plot for Symmetric Airfoil



Appendix B: EES Code

"Known values for plane: Legend Cub (LSA)"

alpha= 3 {angle of attack}

b= 35 [ft] {Wingspan}

c= 6 [ft] {Chord Length}

S= (b*c) [ft^2] {Planform area}

e=0.8 {Oswald's Efficiency Factor}

"Values Obtained from Drag Polar"

C_D_0= {Zero Lift Drag Coefficient}

C_L_Max= {Max Coefficient of Lift}

"Equations"

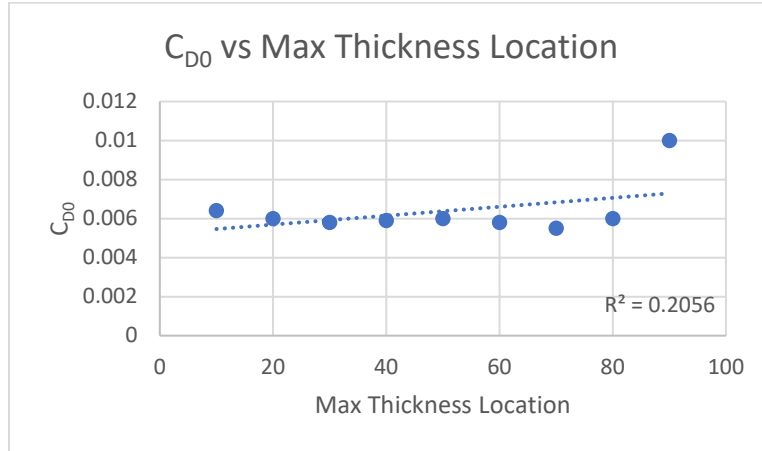
AR=(b^2)/S {Aspect Ratio}

K=(1/(pi*e*AR)) {Proportionality Factor}

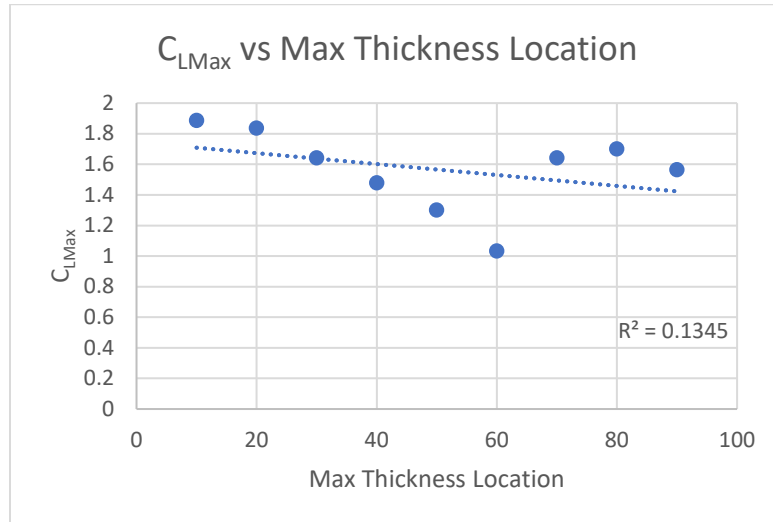
LD_Max= sqrt(1/(4*K*C_D_0)) {Max Lift/Drag ratio}

Appendix C: Relationship of Maximum Thickness Location and Flight Parameters (Symmetric)

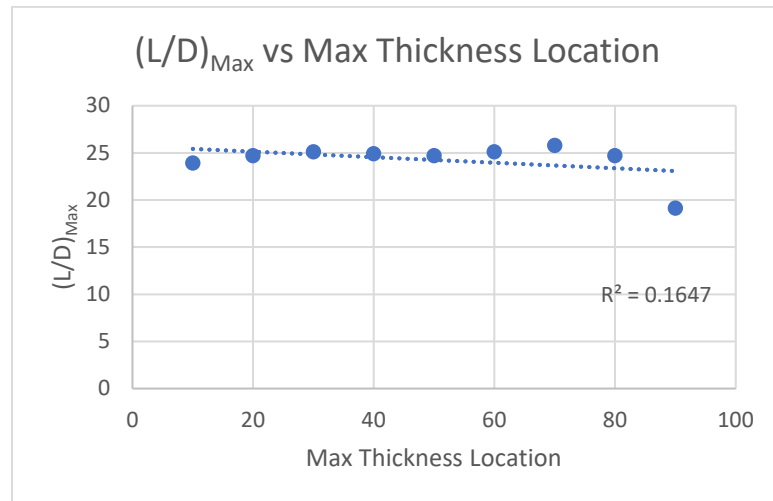
1. C_{D0} vs Maximum Thickness Location



2. C_{LMax} vs Maximum Thickness Location

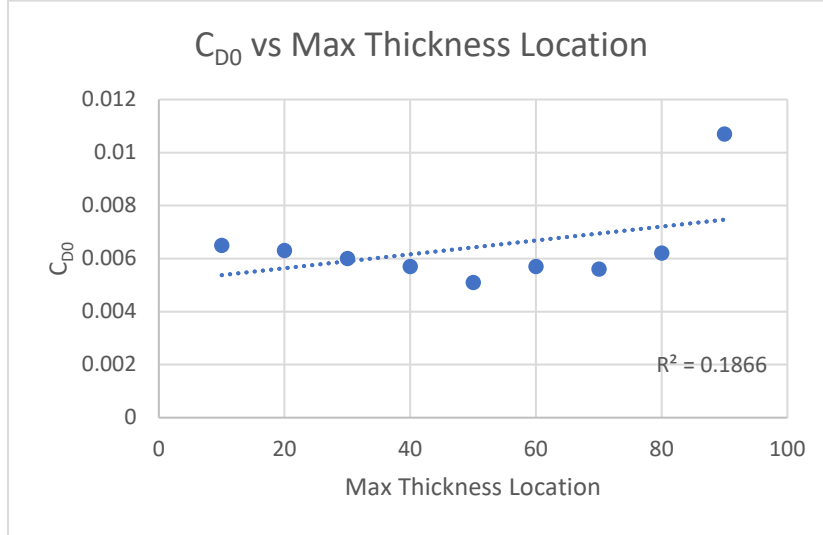


3. $(L/D)_{Max}$ vs Maximum Thickness Location

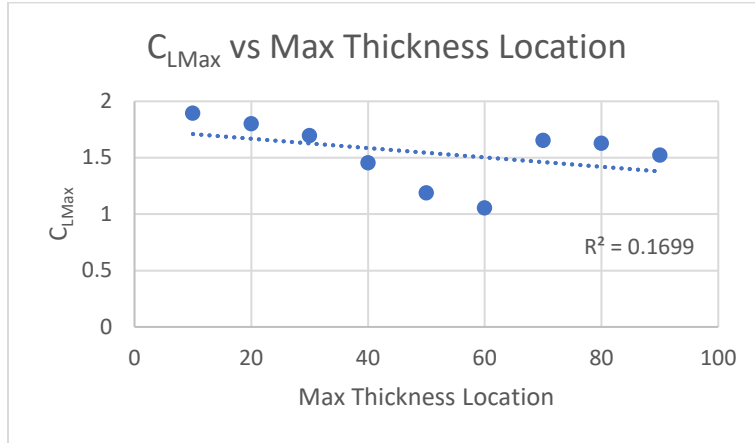


Appendix D: Relationship of Maximum Thickness Location and Flight Parameters (Asymmetric)

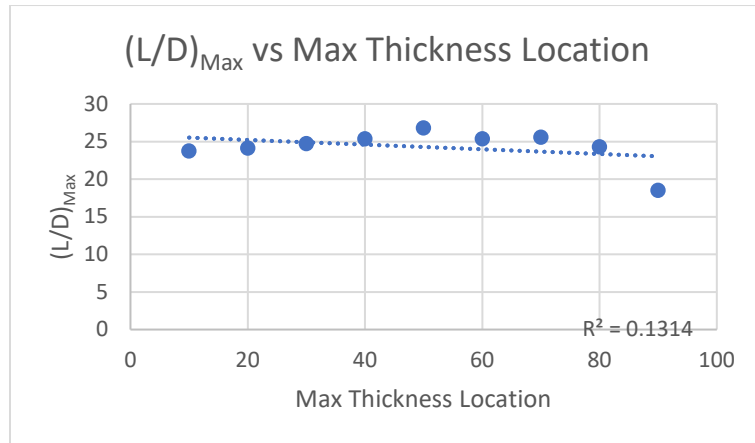
1. C_{D0} vs Maximum Thickness Location



2. C_{LMax} vs Maximum Thickness Location



3. $(L/D)_{Max}$ vs Maximum Thickness Location



References

1. Suckow, Elizabeth. "National Advisory Committee for Aeronautics." *NASA*, NASA, 21 Apr. 2009, history.nasa.gov/naca/index.html.
2. "Development of Aviation Technology." *Century of Flight*, [www.century-of-flight.net/Aviation history/evolution of technology/Airfoils.htm#r](http://www.century-of-flight.net/Aviation%20history/evolution%20of%20technology/Airfoils.htm#r).
3. Loftin, Laurence K, and Kenneth S Cohen. "Aerodynamic Characteristics of a Number of Modified NACA Four Digit Series Airfoil Sections." June 1948.
4. Drees, John. "DesignFOIL NACA Airfoil Coordinates and Airfoil Design Software." *DesignFOIL NACA Airfoil Coordinates and Airfoil Design Software*, www.dreesecode.com/.
5. "American Legend AL3 The Classic Cub." *Legend Aircraft*, legend.aero/american-legend-al3-the-classic-cub/.
6. Anderson, John D. *Aircraft Performance and Design*. McGraw-Hill Higher Education, 2012.
7. Abbott, Ira Herbert., and Albert E Von Doenhoff. *Theory of Wing Sections*. Dover Pubns.
8. Resources, e-Media. *Chart Software: Engineering Software*. www.fchart.com/ees/.

Controllable Stiffness “Smart” Skins Based on Magneto-Rheological Elastomers: Characterization and Application

Student Researcher: Kyle A. Weaver

Advisor: Dr. Jeong-Hoi Koo

Miami University

Department of Mechanical and Manufacturing Engineering

Abstract

Modeling skin is a difficult process due to the complexity of its structure. This research has two major components: 1) the development of a magnetorheological elastomer (MRE) skin model capable of replicating the age-dependent material behavior of human skin and 2) the development of a relatively transfer function able to account for the dissipative effect of skin to arterial pressure. For the first research objective, various indentation tests were done on MRE samples ranging from 0 to 80% iron by weight in order to note the hysteric effects and modulus trends of the model to compare against that of *in-vivo* skin. The ultimate goal of this research is to create a single skin model capable of behaving as each age group based on the applied magnetic fields. The second research objective involves more complex skin models and a cam system to generate human pulse waveforms. The pressure of the waveforms is then recorded using an air pressure sensor connected directly to the pressure generator and the pressure felt by an indenter pressing on a skin model. The differences in the noted pressures is representative of the dissipative effects of the skin, quantified by the augmentation index and other parameters. This research hopes to create a model capable of measuring blood pressure based solely on the pressure experienced by a small indenter pressing on skin above a vein. This model could then be integrated into wearables to take consistent and accurate blood pressure measurements without requiring constriction.

Introduction

The role of skin is vital; responsible for acting as a barrier between the external world and the carefully balanced systems within each human. The skin works to protect this balance while being exposed to a wide range of temperatures, injury, liquids, and literally everything that people touch. Aging is another factor that wears down the skin, leading to a loss of elasticity and overall stiffness. The literature shows that aging degrades the elasticity of skin, older skin showing a decreased ability to retake its shape after being deformed and higher viscoelasticity [1-3].

Skin deforms elastically and plastically, and is able to distribute stresses through the whole skin matrix. This is due mostly to the interconnecting matrices of collagen and elastin within the dermis of skin (see Figure 1). The collagen provides primarily mechanical strength to the skin, while the elastin provides flexibility. The combination of these two create the viscoelasticity of skin that makes it an effective and flexible barrier. The matrix begins to breakdown as humans age, making skin modeling even more difficult as the structure changes over time [1-3]. Older skin shows a decreased ability to “bounce back.”

In this study, magnetorheological (MR) materials were investigated due to their changing properties based on externally applied magnetic fields. MR elastomers (MREs) have ferromagnetic particles dispersed throughout an elastomeric matrix in order to create magnet-induced mechanical property variability [5]. Typically, the iron particles are mixed into a polymer during its curing period. The MRE effect is dependent on a number of factors relating to the dispersed particles, such as size, magnetic

saturation, and the type of particles included [4-5]. The stiffness of the MRE increases proportionally to the applied magnetic field, as the magnetic particles form chains within the molecule. These cross-linked chains increase its rigidity, the effect shown in Figure 2.

This research is bringing together two fields of research in a new application that will be useful in a number of industries. The tribology of human skin is being combined with the material science behind MREs to create new skin models capable of simulating the whole range of human skin stiffness based on age dependence. Additionally, these MRE samples are being tested for their viability as cardiovascular models by embedding MRE samples with a silicone vein and passing through known pulsatile waveforms in order to note the dissipating effects of the passing pulse. The data presented is a preliminary study of MREs functioning as variable stiffness artificial skins with and without pulsatile testing.

Project Objectives

The overarching goal of the proposed research is to develop a versatile artificial skin sample that can capture age-dependent human skin properties. The specific, determined objectives for this project are:

- To fabricate various MREs made of different base elastomers with varying iron content
- To use indentation testing to compare these artificial samples against *in vivo* properties.
- To determine the damping effect and other characteristics of MREs with embedded veins.

Methodology

Different samples will be fabricated and mechanically tested under various fields. These results will be compared against *in vivo* biomechanical properties reported in the literature, and the data will be used to refine the artificial skin.

Fabricate artificial skin for testing: Artificial skin samples will be created using commercially available polymer resins with added filler particles. The base material will be mixed with magnetic filler powders in order to function as an MRE. In order to identify the best possible composition of the MRE, multiple samples will be constructed using different (1) particle types, (2) concentrations of particle volume content, and (3) different substrate base materials. Depending on the testing conducted, a silicone vein may be embedded within the MRE layers.

Indentation Testing: With skin samples produced with varying MRE percentage levels, indentation testing will occur in order to determine the elasticity of the sample. For this specific testing, the sample will be loaded into an indentation testing machine with a plastic indenter, in order to minimize the magnetic field's influence on the mechanical properties. An electromagnet will be placed underneath the skin sample which will supply a direct current magnetic field. The machine will then lower onto the sample and record penetration depth and the corresponding force. This test will be run multiple times in order to collect stress and strain data for varying magnetic field and MRE content.

Vein-Inserted Sample Testing: Certain MRE samples include silicone tubing designed to simulate a vein through which model pulse waveforms can be passed through. The waveform is generated using a cam system (see Figure 3) with pulse patterns based on *in-vivo* data gathered. The cam system includes an air pressure sensor in order to monitor the actual pressure and this is compared to the pressure observed by an indenter through the skin (observing the damping effects of the skin).

Significant Results Obtained

Comparison of MRE & *In-Vivo* Data for Indentation MRE Samples

Comparing the MRE samples versus the *in-vivo* data [6] was the main test to see whether the experimental samples were capable of capturing human skin behavior. Figure 4 shows that MRE samples can replicate the loading behaviors of human skin. This graph represents a proof-of-concept, showing that MRE samples are capable of replicating the stress-strain behavior of *in-vivo* data. One problem that must be mentioned is the difference in hysteric effects. As discussed in the introduction, aging human skin loses its natural elasticity, leading to a greater energy loss as it does not “spring back” as fast as younger skin. This should correspond to greater hysteresis in older skin, but the MRE sample shows the reverse trend, an increase in iron content produces a higher hysteric effect.

Pulse Pressure Measurements

The pressure measured by the air sensor was compared against that of the skin pressure while the skin is indented. The air sensor is a direct measurement of the pressure versus the indirect skin pressure (due to the dissipation effects of the viscoelastic MRE samples). The results in Figure 5 show that the air sensor reports a pressure about twice as large as that of the indenter. This result is typical across all of the experiments conducted on the vein-inserted MRE samples.

The vein-inserted MRE samples show a significant increase in peak pressure in response to magnetic fields. Figure 5 shows that the E10-40% under a strong magnetic field presented a 21% increase in peak pressure, a significant change that demonstrates the ability of MREs to replicate multiple skin types using one sample. The MR effect increases the stiffness of a given sample as fields are applied, but this should correspond with a decreased peak pressure (as stiffer materials are not deflected as much by the passed air pressure). However, it is predicted that the MR effect is overpowered by shearing effects as the sample is deformed by the strong field being applied to it. This shearing may enhance the pressure being passed through the MRE sample as it is a thinner media to pass through.

Figures

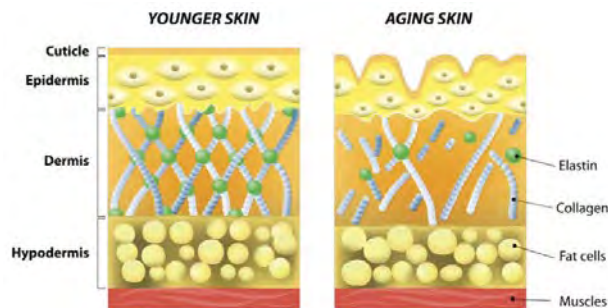


Figure 1. The Collagen-Elastin matrix responsible for the strength and flexibility of human skin.

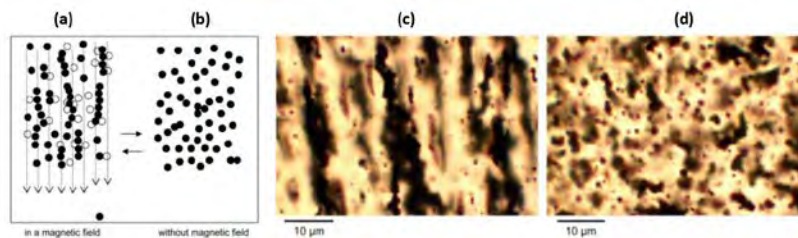


Figure 2. Diagrams demonstrating magnetic particle alignment (a) with an external magnetic field, (b) without field. Optical microscopy photos (c) in a 0.02 T field, (d) without field [8].

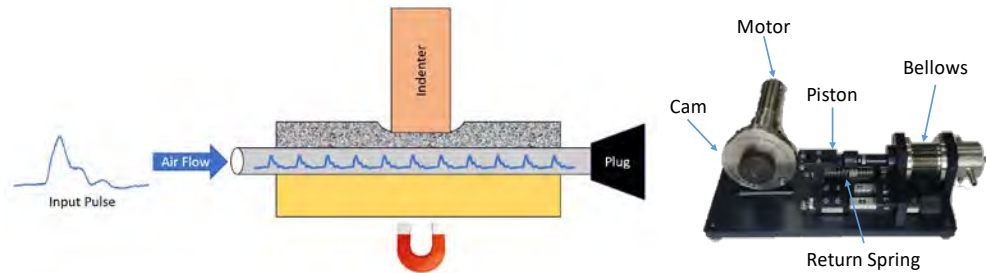


Figure 3. Left- Schematic of the pulsatile testing set-up. Right- Cam system used to generate waveforms.

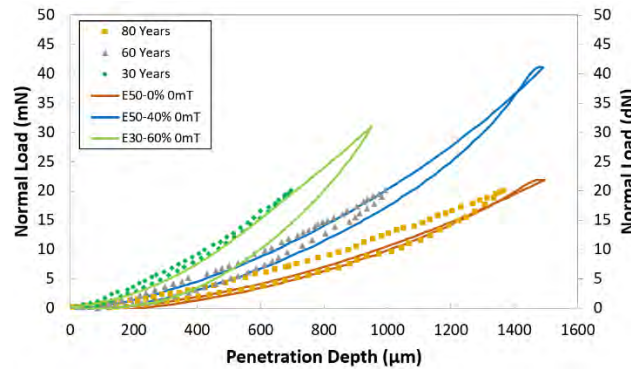


Figure 4. MRE vs. In-Vivo Data for indented samples.

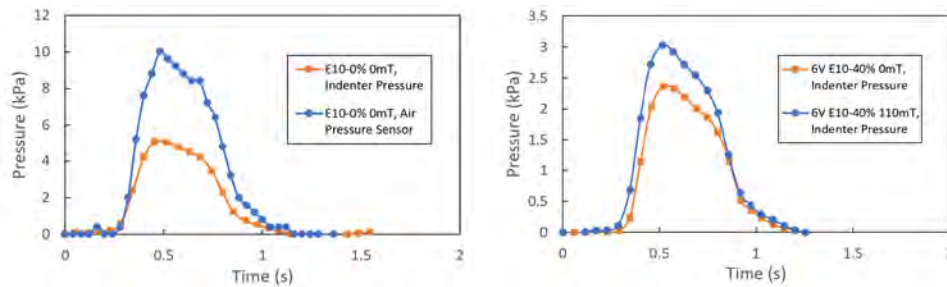


Figure 5. Left- Graph comparing direct and indirect pulse pressures. Right- Graph comparing the indenter pressure based on magnetic field.

References

1. Cua, A., Wilhelm, K., & Maibach, H. "Elastic properties of human skin: relation to age, sex, and anatomical region." *Archives of Dermatological Research* Vol. 282 No. 5 (1990): pp. 283-288.
2. Daly, C., & Odland, G. "Age-related Changes in the Mechanical Properties of Human Skin." *Journal of Investigative Dermatology* Vol. 73 No. 1 (1979): pp. 84-87.
3. Leveque, J., de Rigal, J., Agache, P., & Monneur, C. "Influence of ageing on the in vivo extensibility of human skin at a low stress." *Archives of Dermatological Research* Vol. 269 No. 2 (1980): pp. 127-135.
4. Stepanov, G., Abramchuk, S., Grishin, D., Nikitin, L., Kramarenko, E., & Khokhlov, A. "Effect of a homogeneous magnetic field on the viscoelastic behavior of magnetic elastomers." *Polymer*, Vol. 48 No. 2 (2007): 488-495.
5. Böse, H., & Röder, R. "Magnetorheological elastomers and use thereof." (2009).
6. Zahouani, H., Paillet-Mattei, C., Sohm, B., Vargiolu, R., Cenizo, V., & Debret, R. "Characterization of the mechanical properties of a dermal equivalent compared with human skin in vivo by indentation and static friction tests." *Skin Research and Technology* Vol. 15 No. 1 (2009): pp. 68-76.

Biomimicry of *Manduca sexta* Hawkmoth Wings for Use in a Flapping Wing Micro Air Vehicle

Student Researcher: Matthias S. Weisfeld

Advisor: Dr. Roger D. Quinn

Case Western Reserve University
Mechanical Engineering Department

Abstract

This work presents a morphological study of the wings of over 20 *Manduca sexta* hawkmoths, resulting in data for their overall mass, venation structure mass, and flexural stiffness. This data is then used in the creation of nine different artificial wings, based directly upon the wing geometry of these moths. These manufactured wings were made with three different materials, Icarex Ripstop Polyester, Mylar film, and Kapton film. These materials were selected through a careful study based on a number of factors. Likewise, these wings were based on different templates, each from a different moth wing. The manufactured wings were then compared with the extracted wings. This resulted in a number of conclusions. Both Icarex and Kapton were slightly heavier than desired, but certainly still acceptable. Mylar was far too lightweight and therefore unacceptable. Kapton is the most ideal material found so far for replicating the mass of the wings. Flexural stiffness was also assessed and none of the materials were deemed acceptable. They were all roughly an order of magnitude higher than desired, although Mylar proved the best among them. From this it can be concluded that if one is looking to create an accurately massed wing, a Kapton film is a good choice. However, if one is looking to create an accurately stiff wing, alternative materials must be selected.

Project Objectives

This project seeks to replicate the flight characteristics of the wings of the *Manduca sexta* hawkmoth using multiple different templates created from extracted wings. Likewise, these templates are made using different materials for the membrane. This work assess the similarity between a number of extracted wings and manufactured artificial wings in both mass properties and flexural stiffness.

Methodology Used

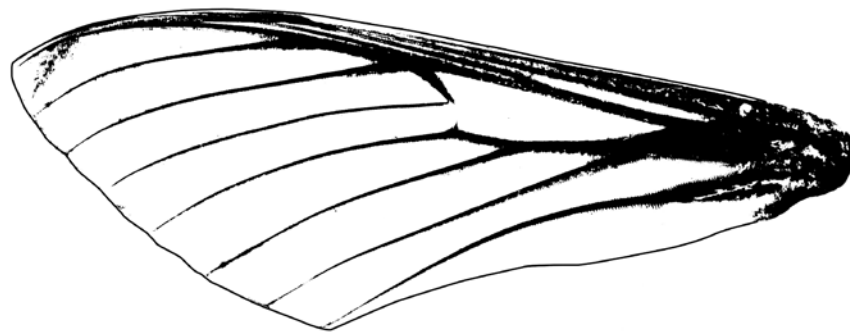
Initially wings were extracted from over 20 different *M. sexta* moths incubated on campus. These wings were extracted using a scalpel or dissection scissors. As the wings were liberated, they were weighed and their mass was recorded. Following the liberation of all four wings, each one was descaled in the same order they were extracted. This process involves in essence removing the outermost layer of the wings simply by rubbing a gloved finger of Q-tip across its surface. These were then weighed again. As wings begin to decay quite quickly after euthanization, most likely due to dehydration, the first wings descaled had to be measured multiple times. In order to establish consistency, the left forewing was always extracted first, followed by the left hindwing, then both the right wings. This meant that the left forewings were measured more times than any other wing type.

These extracted wings were then scanned using a standard flatbed scanner. These scans were taken as 12800 DPI. With a known DPI, these images can be used to measure specific features of the wings. Such things as the average thickness or length of specific veins of the venation structure could now be found. Perhaps more importantly, area could also be easily assessed. Area, in the absence of a better testing

method, serves as a decent metric for lift production. If two objects have similar areas and similar shape, it stands to reason that they would produce a similar amount of lift.

After scans had been taken, two avenues opened. First flexural stiffness data needed to be taken. In order to do this, wings were clamped into a jig that was then placed on a scale. This setup was then put into a CNC machine which could position a long one eighth inch steel rod precisely over the wing. By creating a small displacement at a known position along the wing, and measuring the force this produced, one could easily calculate the flexural stiffness.

The other avenue is more manufacturing related. In order to accurately create manufactured wings, one first must have templates that accurately show the venation pattern position of a wing. For this work, three different templates were created. These templates are purely black and white images that show the outline of the overall wing and the venation structure. The below image is one of the templates used in this study.



A number of different wings, that seemed to be particularly undamaged, were dissected further. In order to find more specific venation masses, the membrane structure was cut away. This allowed a measurement of the overall venation structure mass. From here, each individual vein was separated so that they could all be measured. This meant an average vein mass could now be found. Overall, five left and five right forewings underwent this process.

After templates have been created, manufacturing is ready to begin. This begins by printing both the left and right template for a given wing set onto a standard sheet of 8.5 x 11 copy paper. Following this, a membrane material is selected; either Icarex Ripstop Polyester, Mylar Film, or Kapton Film. The selected material is then taped on top of the section where the template was printed and it is re-run through the printer, such that the ink prints directly on the membrane. This is then removed from the paper and attached onto some hard surface, normally just a wooden board.

At this point the replica venation structure is ready to be constructed. In order to do this, thin strips of unidirectional carbon fiber is cut and laid in the correct position on the template. Each individual strip of carbon fiber serves to replicate one individual vein. As these strips are cut, they are checked to ensure they have a similar mass to the found average. Likewise, both the left and right wings are constructed at the same time, so left and right corresponding veins are checked for similarity. These veins are then attached to the surface of the membrane material with the use of a standard spray adhesive, M3 Super 77 specifically. This is then attached to a specially designed mold and placed in a vacuum bag. The setup is then put into an oven at 100 degrees Celsius for three hours. Once the wings cool, they are trimmed and they wings are completed. These are made with three different materials, as previously stated, likewise, each material is made with three different templates, resulting in nine total wing sets.

As the mass of each vein is recorded during the manufacturing process, it is easy to compare venation accuracy. Additionally, once the wings are completed, they can be weighed and the overall mass can be compared. Flexural stiffness testing is carried out in much the same way as it is for the extracted wings, although the step size of the displacement was normally altered. High quality scans are also taken, such that area can be found and verified.

Results Obtained

The average extracted mass of a forewing was found to be 41.03 mg ± 6.45 mg.

Template	Icarex Set 1		Icarex Set 2		Icarex Set 3	
	11/09/2017		02/21/2019a		02/21/2019b	
vein	left(mg)	right(mg)	left(mg)	right(mg)	left(mg)	right(mg)
A1	2.7	1.9	1.17	1.13	1.22	1.1
A2	0.3	0.5	0.29	0.38	0.5	0.58
Cu	2.1	3.1	1.5	1.25	1.79	1.8
Cu2	2	1.8	1.05	1.27	1.32	1.34
M3	1.2	1.1	0.76	0.6	0.69	0.76
M2	0.9	0.7	0.39	0.44	0.41	0.36
M1	1	1.2	0.46	0.48	0.68	0.5
R5	1	0.7	0.32	0.47	0.26	0.34
R+R4	3.1	3.6	3.04	2.96	3.53	3.55
R3	0.9	0.6	1.07	1.05	0.92	0.98
R2	1.1	1.2	0.81	0.85	0.99	1.05
R1	0.8	0.8	2.86	2.73	1.37	1.3
Re	1	0.8	1.53	1.73	2.25	2.32
Total	18.1	18	15.25	15.34	15.93	15.98
Total with membrane	47.5	47.3	49.78	49.74	52.55	51.82

Template	Mylar Set 1		Mylar Set 2		Mylar Set 3	
	11/09/2017		02/21/2019a		02/21/2019b	
vein	left(mg)	right(mg)	left(mg)	right(mg)	left(mg)	right(mg)
A1	1.52	1.44	1.42	1.26	1.46	1.48
A2	0.51	0.61	0.31	0.42	0.20	0.17
Cu	1.99	1.87	1.28	1.32	1.17	1.38
Cu2	1.03	1.18	1.35	1.37	1.03	0.83
M3	0.79	0.76	0.77	0.71	0.75	0.75
M2	0.69	0.52	0.39	0.48	0.37	0.42
M1	0.66	0.72	0.69	0.69	0.69	0.61
R5	0.41	0.60	0.48	0.47	0.39	0.45
R+R4	2.40	1.77	2.99	2.77	3.84	3.56
R3	0.70	0.76	0.48	0.53	0.96	1.00
R2	0.95	1.11	0.84	0.99	1.13	1.22
R1	1.46	1.84	2.57	2.51	3.59	3.71
Re	2.05	2.31	1.99	2.06	1.88	1.89
Total	15.16	15.49	15.56	15.58	17.46	17.47
Total with membrane	23.50	24.10	26.59	26.08	29.30	27.52

Template	Kapton Set 1		Kapton Set 2		Kapton Set 3	
	11/09/2017		02/21/2019a		02/21/2019b	
vein	left(mg)	right(mg)	left(mg)	right(mg)	left(mg)	right(mg)
A1	1.25	1.24	1.43	1.42	1.3	1.45
A2	0.29	0.44	0.54	0.54	0.39	0.38
Cu	1.92	1.54	2.14	2.22	2.01	1.94
Cu2	0.9	1.37	1.53	1.38	1.06	1.05
M3	1.02	0.8	0.87	0.9	0.74	0.65
M2	0.51	0.49	0.48	0.51	0.48	0.57
M1	0.37	0.39	0.63	0.65	0.73	0.68
R5	0.56	0.54	0.46	0.46	0.31	0.3
R+R4	1.48	1.76	3.6	3.46	3.57	3.57
R3	0.9	0.81	0.69	0.75	0.78	0.85
R2	1.43	1.37	0.9	0.94	0.89	0.83
R1	3.03	2.92	3.18	3.27	3.4	3.34
Re	2.07	2.05	2.51	2.29	2.29	2.4
Total	15.73	15.72	18.96	18.79	17.95	18.01
Total with membrane	45.88	45.43	51.14	50.16	49.55	50.56

Extracted Flexural Stiffness (N-m²)

Overall Average	0.0002148 +/-	0.0000711
Dorsal Average	0.0001963 +/-	0.0000565
Ventral Average	0.0002332 +/-	0.0000795
Set A Average	0.0001776 +/-	0.0000858
Left	0.0002310 +/-	0.0001100
Right	0.0001919 +/-	0.0000461
Set B Average	0.0002181 +/-	0.0000532
Left	0.0002363 +/-	0.0000607
Right	0.0002000 +/-	0.0000376

November Average	0.001681 +/-	0.000977
Left	0.001395 +/-	0.000767
Dorsal	0.000780 +/-	0.000254
Ventral	0.002010 +/-	0.000586
Right	0.001967 +/-	0.001088
Dorsal	0.001169 +/-	0.000453
Ventral	0.002765 +/-	0.000940
Set A Average	0.001962 +/-	0.000903
Left	0.001826 +/-	0.000363
Dorsal	0.001597 +/-	0.000190
Ventral	0.002055 +/-	0.000353
Right	0.002097 +/-	0.001221
Dorsal	0.002048 +/-	0.001738
Ventral	0.002147 +/-	0.000250
Set B Average	0.003091 +/-	0.001018
Left	0.003795 +/-	0.000916
Dorsal	0.003072 +/-	0.000389
Ventral	0.004517 +/-	0.000685
Right	0.002386 +/-	0.000492
Dorsal	0.002036 +/-	0.000339
Ventral	0.002737 +/-	0.000352

November Average	0.000664 +/-	0.000122
Left	0.000632 +/-	0.000101
Dorsal	0.000649 +/-	0.000107
Ventral	0.000615 +/-	0.000096
Right	0.000697 +/-	0.000134
Dorsal	0.000629 +/-	0.000124
Ventral	0.000764 +/-	0.000112
Set A Average	0.001694 +/-	0.000447
Left	0.001635 +/-	0.000466
Dorsal	0.001447 +/-	0.000249
Ventral	0.001824 +/-	0.000558
Right	0.001753 +/-	0.000427
Dorsal	0.001493 +/-	0.000452
Ventral	0.002014 +/-	0.000169
Set B Average	0.001581 +/-	0.000555
Left	0.001705 +/-	0.000652
Dorsal	0.001253 +/-	0.000523
Ventral	0.002157 +/-	0.000411
Right	0.001457 +/-	0.000412
Dorsal	0.001126 +/-	0.000323
Ventral	0.001788 +/-	0.000110

November Average	0.003132 +/-	0.000759
Left	0.003251 +/-	0.000358
Dorsal	0.003396 +/-	0.000318
Ventral	0.003106 +/-	0.000345
Right	0.003013 +/-	0.001007
Dorsal	0.002794 +/-	0.000874
Ventral	0.003232 +/-	0.001111
Set A Average	0.006180 +/-	0.000800
Left	0.006726 +/-	0.000589
Dorsal	0.006428 +/-	0.000203
Ventral	0.007023 +/-	0.000699
Right	0.005635 +/-	0.000583
Dorsal	0.005199 +/-	0.000317
Ventral	0.006070 +/-	0.000444
Set B Average	0.004779 +/-	0.001123
Left	0.004347 +/-	0.001277
Dorsal	0.003114 +/-	0.000219
Ventral	0.005579 +/-	0.000276
Right	0.005212 +/-	0.000740
Dorsal	0.005140 +/-	0.000491
Ventral	0.005284 +/-	0.000939

Wing	Area (in ²)
11-07-2019 Icarex Left	1.15164
11-07-2019 Icarex Right	1.17291
02-21-2019a Icarex Left	1.27138
02-21-2019a Icarex Right	1.30322
02-21-2019b Icarex Left	1.26568
02-21-2019b Icarex Right	1.30368
11-07-2019 Kapton Left	1.15396
11-07-2019 Kapton Right	1.19324
02-21-2019a Kapton Left	1.23212
02-21-2019a Kapton Right	1.25534
02-21-2019b Kapton Left	1.22848
02-21-2019b Kapton Right	1.25741
11-07-2019 Mylar Left	1.10451
11-07-2019 Mylar Right	1.10582
02-21-2019a Mylar Left	1.22600
02-21-2019a Mylar Right	1.25669
02-21-2019b Mylar Left	1.22562
02-21-2019b Mylar Right	1.26470
11-07-2019 Extracted Wing	1.12606
02-21-2019a Extracted Wing	1.21186
02-21-2019b Extracted Wing	1.20940

Significance and Interpretation

As can be seen, in terms of mass, both Icarex and Kapton are relatively acceptable, Mylar, however is far too low. In terms of flexural stiffness, all of these produce exceptionally poor results, however, among them, Mylar is the best. This is still not particularly promising as it is nearly an order of magnitude higher than desired. Fortunately, all wings did result in similar areas and therefore it can be assumed that they would produce a similar amount of lift. In short, provided one is looking to purely replicate the mass characteristics of the *Manduca sexta* hawkmoth's wings, then either Kapton film or Icarex Ripstop Polyester are both acceptable choices. If one is looking to include flexural characteristics, then none of these are acceptable by any means and further materials must be evaluated.

References

1. W. Shyy, M. Berg, and D. Ljungqvist, "Flapping and flexible wings for biological and micro air vehicles," *Progress in Aerospace Sciences*, vol. 35, no. 5, pp. 455–505, Jul. 1999.
2. G. Bunget and S. Seelecke, "BATMAV: a biologically inspired micro air vehicle for flapping flight: kinematic modeling," in *SPIE Smart Structures and Materials Nondestructive Evaluation and Health Monitoring*, vol. 6928.
3. T. N. Pornsin-sirirak, Y. C. Tai, H. Nassef, and C. M. Ho, "Titanium-alloy MEMS wing technology for a micro aerial vehicle application," *Sensors and Actuators A: Physical*, vol. 89, no. 1-2, pp. 95–103, Mar. 2001.
4. W. Herkewitz, "Behold Bat Bot, the First Flying Robot Bat," *Popular Mechanics*, 01-Feb-2017.
- A. Ramezani, S.-J. Chung, and S. Hutchinson, "A biomimetic robotic platform to study flight specializations of bats," *Science Robotics*, vol. 2, no. 3, Feb. 2017.
5. M. Keennon, K. Klingebiel, and H. Won, "50th AIAA Aerospace Sciences Meeting Including the New Horizons Forum and Aerospace Exposition," in *Development of the Nano Hummingbird: A Tailless Flapping Wing Micro Air Vehicle*.
6. R. P. O'Hara and A. N. Palazotto, "The morphological characterization of the forewing of the *Manduca sexta* species for the application of biomimetic flapping wing micro air vehicles," *Bioinspiration & Biomimetics*, vol. 7, no. 4, Oct. 2012.
7. Q. V. Nguyen, H. C. Park, N. S. Goo, and D. Byun, "Characteristics of a Beetle's Free Flight and a Flapping-Wing System that Mimics Beetle Flight," *Journal of Bionic Engineering*, vol. 7, no. 1, pp. 77–86, Mar. 2010.
8. R. Zbikowski, C. Galinski, and C. B. Pedersen, "Four-Bar Linkage Mechanism for Insectlike Flapping Wings in Hover: Concept and an Outline of Its Realization," *Journal of Mechanical Design*, vol. 127, no. 4, Jun. 2005.
9. R. Dudley, *The Biomechanics of Insect Flight: Form, Function, Evolution*. Princeton, NJ: Princeton University Press, 2000.
10. R. P. O'Hara, "The Characterization of Material Properties and Structural Dynamics of the *Manduca Sexta* Forewing for Application to Flapping Wing Micro Air Vehicle Design," thesis, 2012.
- A. P. Tobias, "Experimental Methods to Characterize Nonlinear Vibration of Flapping Wing Micro Air Vehicles," thesis, 2007.
11. T. W. Sims, "A Structural Dynamic Analysis of a *Manduca Sexta* Forewing," thesis, 2010.
12. K. C. Moses, S. C. Michaels, M. Willis, and R. D. Quinn, "Artificial *Manduca sexta* forewings for flapping-wing micro aerial vehicles: how wing structure affects performance," *Bioinspiration & Biomimetics*, vol. 12, no. 5, Sep. 2017.
13. S. K. H. Win, C. H. Tan, D. S. bin Shaiful, and J. E. Low, "2017 IEEE International Conference on Advanced Intelligent Mechatronics," in *The effects of chordwise wing optimization of single-winged samara in autorotation*.

14. R. C. Stillwell and G. Davidowitz, "Proceedings of the Royal Society B Biological Sciences," in A developmental perspective on the evolution of sexual size dimorphism of a moth.
15. S. A. Combes and T. L. Daniel, "Into thin air: contributions of aerodynamic and inertial-elastic forces to wing bending in the hawkmoth *Manduca sexta*," *Journal of Experimental Biology*.
16. S. C. Michaels, K. C. Moses, R. J. Bachmann, R. Hamilton, A. Pena-Francesch, A. Lanba, M. C. Demirel, and R. D. Quinn, "Living Machines 2015: Biomimetic and Biohybrid Systems," in *Biomimicry of the Manduca Sexta Forewing Using SRT Protein Complex for FWMAV Development*, pp. 86–91.
17. T. A. Ward, M. Rezadad, and C. J. Fearday, "A Review of Biomimetic Air Vehicle Research: 1984-2014," *International Journal of Micro Air Vehicles*, Sep. 2015.

VertiCat: Custom VTOL Platform

Student Researcher: Austin M. Wessels

Advisor: Dr. Kelly Cohen

University of Cincinnati
Aerospace Engineering

The goal of this project is to design, build, and test a custom transitional vertical takeoff and landing (VTOL) small unmanned aerial system (sUAS). Multirotor sUAS are notoriously inefficient, while fixed-wing sUAS cannot operate in the same confined area as a multirotor. These vehicle limitations restrict the mission parameters of each individual platform. A transitional VTOL is intended to be a middle ground between a multirotor and a fixed-wing. There are a variety of transitional VTOL sUAS designs on the market with different methods for takeoff and landing. The quadplane style of transitional VTOL is the focus of this research and will show the advantages and disadvantages of a transitional VTOL compared to its multirotor and fixed-wing counterparts.

The objective of the project is to demonstrate the capabilities of a transitional VTOL platform. A custom platform will be developed for this project. The vehicle shall be capable of autonomous transition as well as waypoint navigation.

The vehicle's airframe is based on the mini-telemaster airframe. This airframe has been around for many years and has stood the test of time. VertiCat has a longer wingspan to lower the wing loading given it will have a higher gross takeoff weight. The additional weight can be attributed to the extra electronics necessary for the quadplane airframe seen in figure 1. Those electronics include autopilot and additional motors. Additional aircraft structure is required to mount the additional motors also increasing the weight. A weight breakdown can be seen in table 1. The wing structure requires attention as it now being loaded by four upward motors extended chordwise from leading and trailing edges. The wing structure was stiffened with two carbon fiber spars running parallel in the wing. These spars act as hard points to attach the longitudinal tubes for the lifting motors.

Balance is important for both fixed wing and multirotor type aircraft. With this in mind, the longitudinal carbon tubes are attached in such a way to allow them to slide fore and aft to match the center of gravity (cg) location of the quadcopter frame and wing. Now the cg of both frames is aligned, the vehicle must balance there. As the weight of components and vehicle materials might be difficult to predict, the battery was positioned in such a way to allow a large range of motion for adjusting the location of the cg seen in figure 2.

Autopilot location accessibility is also important. It should lie near the cg of the vehicle. This poses a problem for most fixed wing as the cg lies within the wing. VertiCat uses a unique wing mounting technique to solve these issues. As seen in figure 3, the wing attaches to a hollow structure allowing the wing to surround the flight controller. Furthermore, when the wing is removed, it allows easy access to the ports and connections on the autopilot.

VertiCat uses a Pixhawk autopilot for control. While the vehicle should be dynamically stable in forward flight, it is unstable in hover mode without the autopilot. The Pixhawk runs PX4 opensource firmware and supports the quadplane vehicle type out of the box. The Pixhawk will navigate waypoints as well as fly autonomous missions. PX4 can also control the transition of the vehicle whether it is commanded in mission mode or by transmitter switch.

Following a crawl, walk, run approach, the vehicle will be tested incrementally. First, the vehicle will be flown as a quadcopter to verify the autopilot is able to control the vehicle with additional mass and aerodynamic surfaces on the vehicle. Initial quadcopter flight tests will be conducted indoors to minimize the effect of the aerodynamic surfaces in the wind. Next the vehicle will be flown outdoors in fixed wing mode in forward flight. Only when both flight configurations have been tuned will a transition be attempted. All initial flights will be conducted manually by the safety pilot.

Current results from this vehicle are minimal, as the vehicle is under construction. The aircraft is nearly ready to fly as a multirotor and begin initial flight testing.

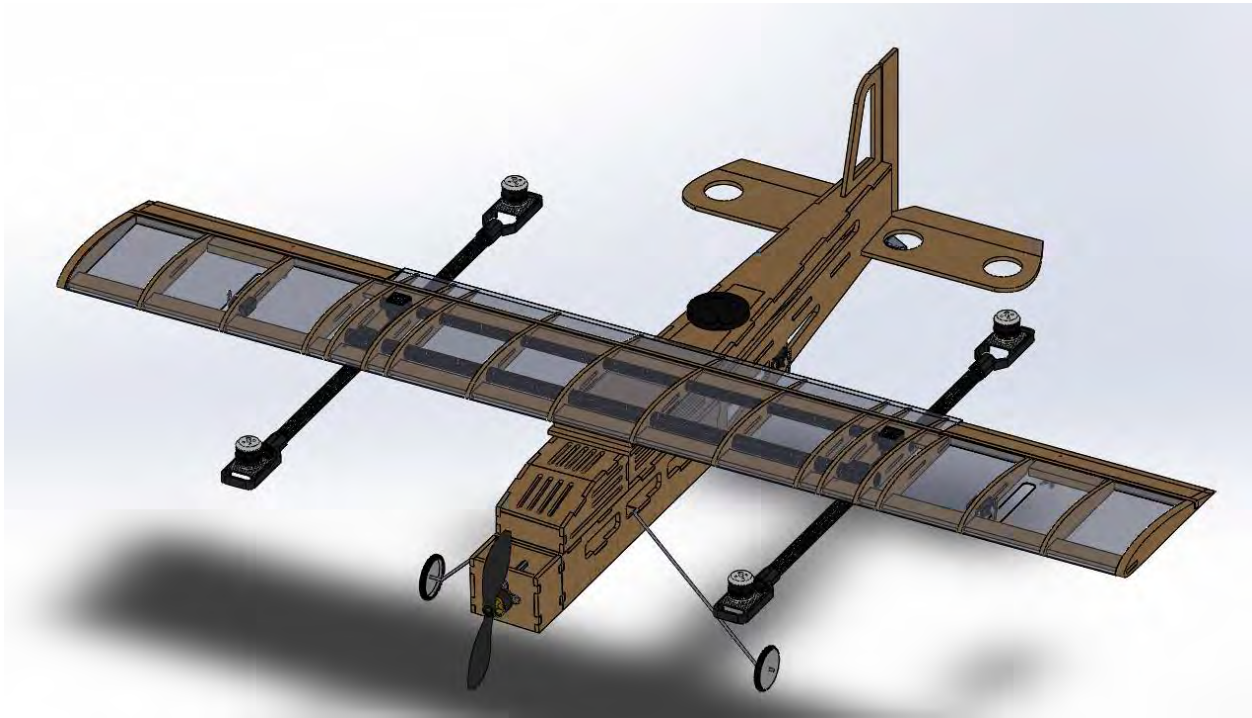


Figure 1. Isometric view.



Figure 2. The battery mount allows a wide range of mounting positions.



Figure 3. The wing mount gives easy access to the Pixhawk autopilot.

Table 1. Estimated weight breakdown of vehicle components. With 140% safety factor.

Electronics	Weight (grams)	Quantity	Total (grams)
Pixhawk	75	1	75
4s 5Ah LiPo	500	1	500
Quad Motor	75	4	300
Fixed Wing Motor	130	1	130
Servo	8	4	32
Quad ESC	27.8	4	111.2
Hardware			
Fuselage	300	1	300
Wing	150	1	150
16mm Carbon	150	1	150
12mm Carbon	50	1	50
Motor Mount	25	4	100
Arm Mounts	25	4	100
		Gross	1998.2
		140%	2797.48

I would like to thank Dr. Kelly Cohen and everyone at the UAV MASTER Labs for their help and making this research possible.

Design of an Experimental Facility for Characterization of Dynamic Stall

Student Researcher: Nicole L. Whiting

Advisor: Dr. Mo Samimy

The Ohio State University

Department of Mechanical and Aerospace Engineering

Abstract

Dynamic stall occurs in applications where airfoils rapidly change angle of attack, like rotorcraft or wind turbines. When the change is fast enough, flow over a pitching airfoil remains attached beyond the static stall angle. This results in the formation of a dynamic stall vortex (DSV) on the leading edge of the airfoil, which eventually convects over the airfoil and sheds. During the cyclic DSV convection and shedding from the airfoil and the accompanying flow separation, unsteady aerodynamic loads are produced. These loads can lead to fatigue and eventually structural failure, making it essential to mitigate the effects of dynamic stall. In preliminary work, Nanosecond Dielectric Barrier Discharge plasma actuators have shown promise at mitigating dynamic stall and significantly reducing unsteady loads. This work aims to improve the lift and reduce the unsteady forces associated with dynamic stall as well as improve the understanding of the unsteady flow physics so the effects of it can be better mitigated. Mitigating the negative effects of dynamic stall has the potential to increase the lifespan of blades and increase lift, which will allow rotorcraft to fly higher, faster, or carry larger loads. Before attempting to control the flow, the effect of the experimental setup on dynamic stall must be fully understood by investigating the effect of the airfoil aspect ratio and endplates as well as the data filtering. NACA 0012 airfoils with aspect ratios of two and three with and without endplates were experimentally tested. Detailed load cell measurements were carried out to assess the effect of each setup on the static and dynamic stall characteristics. Different filter parameters were also explored to mitigate the effect of the natural frequency of the setup. It was determined that an airfoil with an aspect ratio of two utilizing endplates minimizes the wind-tunnel area blockage while producing results similar to an infinite wing. The reduction in weight (over the longer airfoil) helps to separate the natural frequency of the setup from the low-frequency harmonics of the oscillation frequency and the frequency associated with the convective time scale of the DSV which are both essential to preserve while filtering out the natural frequencies of the setup.

Introduction

Rotorcraft are extremely important because of their ability to take off and land without a runway and hover in place. This makes them essential in specialized tasks like national defense, fire and rescue, and medical transport. While these enhanced capabilities create a specialized niche, they also complicate the aerodynamics of the rotorcraft. In order to maintain lift symmetry in the rotor, the retreating blades need to be at a significantly higher angle of attack than the advancing blades [1]. Therefore, the blades need to continuously change angle of attack as they rotate around the rotor. After pitching a retreating blade to a higher angle of attack than the static stall angle, during pitch up, or eventual pitch down, the flow can no longer remain attached to the blades and a phenomenon called dynamic stall may occur. Dynamic stall can occur in any application where the airfoils are rapidly changing angle of attack. When the change is fast enough, flow over a pitching airfoil remains attached beyond the static stall angle. This results in the formation of a dynamic stall vortex (DSV) on the leading edge of the airfoil, which eventually convects over the airfoil and sheds. Unsteady aerodynamic loads are produced by the DSV

convection and the accompanying flow separation. These unsteady loads significantly increase cyclic blade torsion which can lead to fatigue and eventually structural failure. Due to these issues, dynamic stall is normally the limiting factor in the maximum flight speed of helicopters [1]. Therefore, in order to expand the operational envelope of rotorcraft, it is essential to mitigate the effects of dynamic stall.

Previous research done at the Gas Dynamics and Turbulence Laboratory at Ohio State [2], has shown promise mitigating dynamic stall and reattaching the flow over a NACA 0015 airfoil using a NS-DBD plasma actuator. A high-voltage nanosecond pulse, provided at a particular frequency, drives the actuator and creates rapid, localized heating that results in a thermal perturbation. The thermal perturbation then excites the flow's natural instabilities and generates coherent flow structures. These can, if properly organized, entrain high-momentum free stream air into the low-momentum region near the airfoil surface, energizing the flow and mitigating or eliminating separation [3]. The plasma actuators consist of two copper electrodes separated by a dielectric barrier; they require a relatively low power input as only perturbations are required, which allows them to remain effective at high speeds.

While the previous research showed promising results, there were issues related to the setup that increased the uncertainty in the data. In order to better understand dynamic stall, the facility has recently undergone upgrades. The airfoil was changed to a NACA 0012, it is oscillated using a direct-drive servomotor, and the forces on the airfoil are directly measured using a 6-axis force/torque transducer. The new setup is essential to obtain accurate dynamic-stall data but along with it comes a number of challenges. First, because a load cell is used to measure the forces the airfoil cannot be connected at both ends to the wind tunnel, significantly decreasing the resonant frequency of the system. If it were, the airfoil would not be able to accurately read the forces since the airfoil needs to be solely supported by the load cell. This is the general arrangement when using pressure taps to determine the airfoil loads. However, now the airfoil must be a vertical cantilever beam with the servomotor and load cell underneath it. To eliminate the influences of the boundary layer on the walls of the wind tunnel and to produce a more two-dimensional air flow around the airfoil, endplates are required. The resonant frequencies of the setup, as well as the inertial loads, must also be eliminated when extracting the aerodynamic loads from the raw data.

Experimental Methodology

The Ohio State University's 61x61 cm Recirculating Wind Tunnel is being used for this work. The test section is 122 cm in length and is made out of optically clear acrylic, which will allow for optical diagnostics of the flow. The facility has recently undergone upgrades to the force measurement system, servomotor, and control system. In order to oscillate the airfoil in the wind tunnel a new direct-drive servomotor was installed. This greatly improved the repeatability of the airfoil motion and allows full optical access to the test section. In the previous setup, 35 static pressure taps were located on the surface of the airfoil in order to calculate the phase-averaged pressure coefficient. From these pressure measurements the lift, drag, and moment were calculated which introduced a prospective error due to the potential three-dimensionality in the flow since the pressure taps are only located along the center of the airfoil chordwise. Phase averaging the pressure data also introduces another error; this is because when each cycle is plotted independently, there is a bifurcation in the data distribution and the average falls somewhere between them. This means the phase averaged data, from pressure taps, which is generally provided in literature has very little chance of ever naturally occurring [4]. Therefore, the new system directly measures the lift, drag, and moment forces using a 6-axis force/torque transducer.

A NACA 0012 airfoil is being used for this research, instead of the previous NACA 0015, because it is a typical airfoil for rotorcraft research and it is well characterized in literature. Its chord was reduced from 8 in. to 7 in. to reduce the effect of solid blockage. The main airfoil has an aspect ratio of three (AR3) and is made of stainless steel; it has a replaceable Delrin leading edge on which to install the plasma actuators. The stainless steel was chosen for its high stiffness and the Delrin will help to prevent arcing between the high-voltage plasma actuators and the metal airfoil. A prototype aluminum airfoil with an aspect ratio of two (AR2) was constructed to determine the effect of aspect ratio and solid blockage on baseline static and dynamic stall data. This airfoil cannot be used with an active plasma actuator but it can be used to determine if it would be beneficial to use a smaller aspect ratio airfoil moving forward.

To minimize the flow interaction between the test section wall boundary layer and the airfoil, as well as produce a more two-dimensional airflow around the testing body, endplates were designed, built, and tested for the airfoil. The endplate diameter was chosen such that it follows Kármán's theory of vortex streets. The larger the wake created during testing, the larger the endplates need to be as they prevent the flow from outside of the endplates from interfering with the wake of the airfoil. Based on this approach, the endplates need to be 8.5 times the airfoils body depth (normal to the approaching flow) [5]. The required diameter was determined to be 18.5 in. The test section solid blockage was considered when choosing the thickness of the endplates. It is important to keep the solid blockage as low as possible, generally below 10%, because solid blockage will alter the flow around the airfoil. With an aspect ratio of three and no endplates, the 10% solid blockage limit is reached at 14 degrees, well before dynamic stall generally occurs for a NACA 0012 (around 20 degrees). However, with the aspect ratio two airfoil and 0.25 in thick endplates the 10% solid blockage limit is surpassed at 20 degrees. For these reasons, the endplates have an 18.5 in diameter, are 0.25 in thick, and are constructed out of optically clear acrylic.

Static Stall Results

With the new facility in place, the first objective was to establish a static baseline of the airfoil based on the measured aerodynamic coefficients and compare it with literature. Endplates help to eliminate the influence of the boundary layer on the walls of the wind tunnel and help to produce a more two-dimensional airflow around the airfoil. In Figure 1, the aspect ratio two airfoil was tested with and without endplates at a Reynolds number of 500k. The results are compared to a case from literature also at a Reynolds number of 500k but with an aspect ratio of six, which is indicative of an infinite wing [6]. The lift coefficient increases and approaches the case from literature as the endplates are added due to a more two-dimensional flow around the airfoil. The static stall angle of attack decreases, better matching the case from literature as the endplates are added. This is also due to a more two-dimensional flow. Three-dimensional effects can reduce the apparent separation since the separation grows in from the ends rather than appearing all at once, which is done in a two-dimensional flow, delaying the static stall angle of attack. Overall, the results with the endplates compare well with the literature results with an aspect ratio of six and the same Reynolds number of 500k. Figure 2 shows the effect aspect ratio has on the lift coefficient when endplates are used by comparing the aspect ratio three airfoil and aspect ratio two airfoil (both with endplates) to the case from literature. As expected, the aspect ratio three airfoil matches the literature results better than the aspect ratio two case. The lift coefficient increased (i.e. was closer to literature) and the static stall angle of attack decreased (i.e. was closer to literature). Overall, both airfoils match literature well when endplates are used.

Dynamic Stall Results

The total forces measured by the load cell include the aerodynamic forces as well as the inertial forces from the acceleration and mass of the setup. To account for the inertial loads, two sets of data are taken for each dynamic stall case one with the wind on, capturing the total forces, and one with the wind off, capturing just the inertial forces. These sets of data are first phase averaged over a minimum of thirty cycles then subtracted to get the phase averaged pure aerodynamic forces. When comparing the raw inertial loads to the ideal inertial loads derived from the rotational inertia equations it is evident that there is an imposed oscillation due to the first mode of the setup's natural frequency. When pressure taps are used to obtain the aerodynamic forces the airfoil generally spans the entire test section and is secured on both ends, significantly increasing the natural frequency of the system. However when using a load cell one end has to be free. The setup essentially becomes a spring mass damper system and will oscillate at some relatively low frequency when moved. For dynamic stall data collected using a load cell, it is essential to filter out the natural frequency of the full setup while preserving a minimum of the first two harmonics of the oscillation frequency [7]. The frequency associated with the convective time scale of the DSV must also be preserved since the DSV adds lift as it convects over the airfoil during dynamic stall. The frequency is only a function of the freestream velocity and the airfoil chord, since the DSV convective velocity is only a function of the freestream velocity, shown in Eq. 1. In order to determine the natural frequency from the setup, a fast Fourier transform (FFT) was done using a Hann window. The ideal frequency spectrum, with no interference from the natural frequency of the setup, would include the oscillation frequency or two times the oscillation frequency, depending on which load component is being examined, as the largest peak. The harmonics of the oscillation frequency would then decay.

$$f_{c,DSV} = \frac{U_{DSV}}{c} = \frac{U_{\infty}}{c} \quad (1)$$

Both the inertial and total forces data must be filtered in a way such that the first couple harmonics of the oscillation frequency and the frequency of the convective time scale of the DSV are preserved while the range of frequencies affected by the natural frequency of the setup are eliminated. The higher natural frequency modes of the setup appear as high-frequency noise and must also be eliminated. To do this, a band-stop filter is used on the lower frequencies and a low-pass filter is used on the high frequency noise. A 3rd order Chebyshev Type 2 filter is being used. It is an elliptic filter that has stopband ripples but a faster roll off than the typical Butterworth filter, making it a better option in this application. The filter transfer functions are then run through a zero-phase digital filter and applied to the inertial and total force data before they are subtracted from one another to get the aerodynamic forces.

To ensure that low frequency peaks being seen in the frequency spectrum were due to the natural frequency of the setup, three different oscillation frequencies were tested: 1 Hz, 3 Hz, and 3.5 Hz. The range of low frequencies affected did not change, only the magnitudes of the frequencies increased, meaning the disturbance is independent of the oscillation frequency and likely due to the natural frequency of the setup, shown in Figure 3. While Figure 3 only shows the inertial force frequency spectrum, the total force frequency spectrum shows the same trends. The same range of frequencies are affected, the magnitudes are just further increased because the wind amplifies the effect of the natural frequency making it even more essential to filter out.

The effects of the endplates, aspect ratio, and weight of the system were also investigated by taking the FFT of the load cell data to get the frequency spectrum. The effect of the system's weight on the natural frequency is shown in Figure 4 for six cases: nothing on the load cell, just the airfoil adapters that connect the airfoil to the load cell, aspect ratio two airfoil with and without endplates, and aspect ratio three airfoil with and without endplates. In all six cases the frequency spectrums are for the inertial loads oscillated at a frequency of 1 Hz. As the weight of the setup increases, the peak frequency affected by the natural frequency of the setup decreases. It is important that this peak value is not in the same band as the first couple harmonics of the oscillation frequency or in the range of the frequency of the convective time scale of the DSV. This would make it difficult to filter out the natural frequency disturbances without affecting the aerodynamic forces associated with the dynamic stall. Therefore, the aspect ratio three airfoil with or without endplates may be too heavy.

The effect of endplates is shown in Figure 5 for the normal-force inertial data at an oscillation frequency of 1 Hz and an aspect ratio of two. Due to the effect of weight, discussed previously; the peak frequency, affected by the natural frequency of the setup, is decreased as the endplates are added. The endplates also seem to help damp out the effects of the natural frequency by reducing both the magnitude and range of frequencies affected. Therefore, adding endplates not only helps to make the flow more two-dimensional around the testing body, it also helps mitigate the effects of the natural frequency of the setup. The normal-force coefficient, which is directly related to the lift coefficient, was calculated for a case from literature that uses a similar airfoil with an aspect ratio of 1 [8]. The test was conducted with the aspect ratio two airfoil, a Reynolds number of 200k, and an oscillation frequency of 2.5 Hz with and without endplates. Based on the frequency spectrum of the unfiltered data, the cutoff frequencies for both cases were 7 Hz and 45 Hz for the band-stop filter and 100 Hz for the low-pass filter. At 7 Hz the natural frequency of the setup begins to interfere with the harmonics of the oscillation frequency. Forty-five Hz was chosen because the frequency from the convective time scale of the DSV is 48 Hz. In the case with endplates, 45 Hz is near where the natural frequency of the setup ends but in the case with no endplates the natural frequency of the setup does not end until 70 Hz. The results are shown in Figure 6. The same general trend is seen with and without endplates. However, without endplates the magnitude is significantly lower which was also seen in the static stall results in Figure 1. This is because the endplates are needed to make the flow more two-dimensional and behave more like an infinite wing. When no endplates were used, the natural frequency of the setup was interfering with the frequency from the convective time scale of the DSV. By increasing the Reynolds number to 300k the ideal cutoff frequency of 70 Hz could be applied, since the frequency from the convective time scale of the DSV would be increased to 73 Hz.

Conclusion

This work aims to improve the lift and reduce the unsteady forces associated with dynamic stall using NS-DBD plasma actuators. Mitigating the negative effects of dynamic stall has the potential to increase the lifespan of blades and increase lift, which will allow rotorcraft to fly higher, faster, or carry larger loads. Before attempting to control the flow, the effect of the experimental setup on dynamic stall must be fully understood. The most important parameters in the determination of what physical setup should be used in this case are aspect ratio, blockage ratio, and whether or not endplates should be used. Based on the static stall data it can be seen that using an aspect ratio three airfoil produces similar results to an aspect ratio of two when endplates are used, which both produce similar results to literature. Reducing the aspect ratio and adding endplates reduces the solid blockage significantly, which is important to the quality of data. When processing dynamic stall data it is essential to keep a minimum of the first two harmonics of the oscillation frequency as well as the frequency associated with the convective time scale of the DSV, while filtering out the natural frequency of the full setup. It is

important that the natural frequency of the full setup does not interfere with either so it can be filtered out without affecting the aerodynamic data. Therefore, two filters are needed when processing the dynamic stall data, first a band-stop filter to eliminate the natural frequency of the setup and second a low-pass filter to eliminate the high frequency noise associated with the higher modes of the setup. Decreasing the weight of the setup increases the natural frequency of the setup, which is beneficial since it moves it away from low frequency harmonics of the oscillation frequency and adding endplates help to dampen out the natural frequency of the setup. Increasing the Reynold's number of the test increases the freestream velocity, which increases the frequency associated with the convective time scale of the DSV. Based on this, for dynamic stall tests, the Reynold's number can be chosen such that the frequency associated with the convective time scale of the DSV does not interfere with the natural frequency of the setup.

Figures

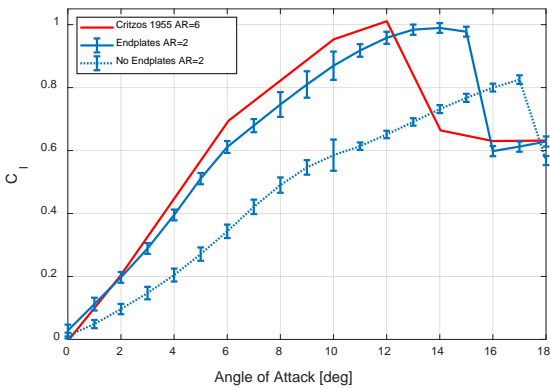


Figure 1. Effect of endplates on the lift coefficient.

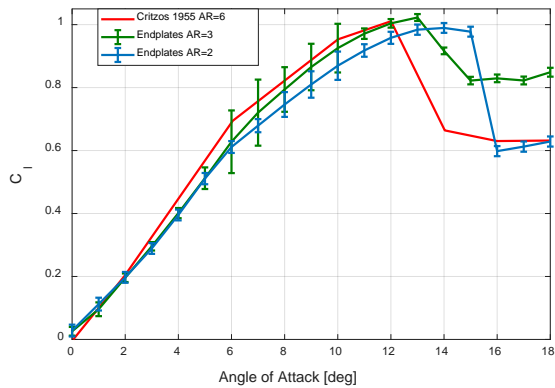


Figure 2. Effect of AR on the lift coefficient.

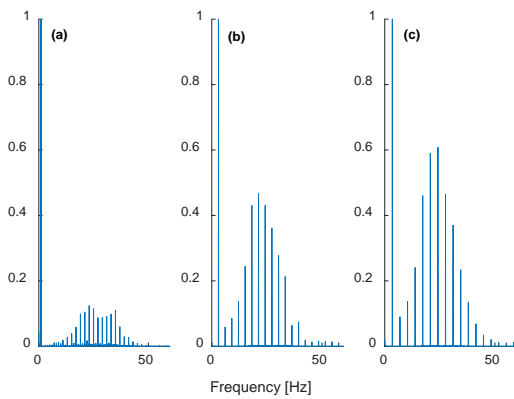


Figure 3. Frequency spectrum at varying oscillation frequencies: (a) 1 Hz, (b) 3 Hz, (c) 3.5 Hz.

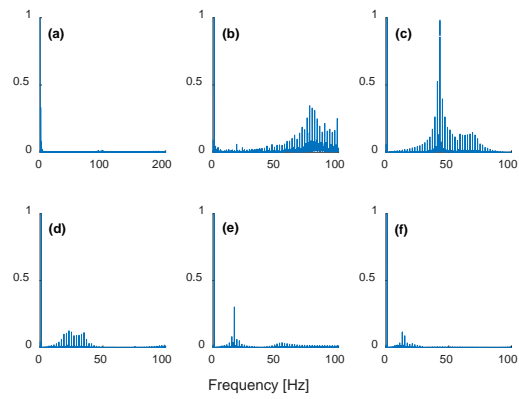


Figure 4. Varying setup weights: (a) 0 kg, (b) 2.40 kg, (c) 8.98 kg, (d) 10.85 kg, (e) 12.68 kg, (f) 14.55 kg.

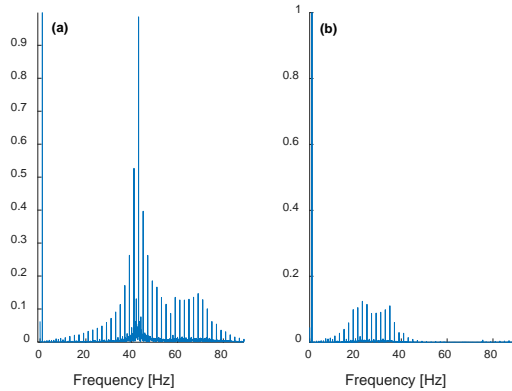


Figure 5. Inertial frequency spectrum:
(a) No Endplates (b) With Endplates.

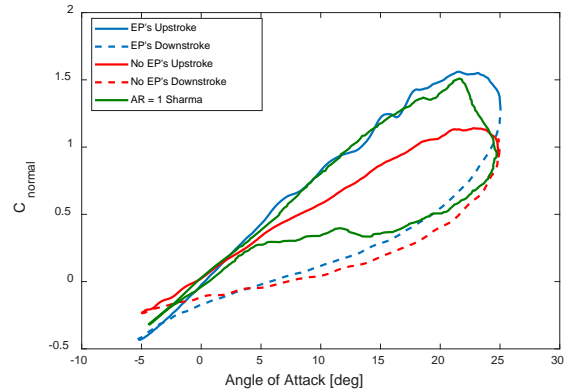


Figure 6. Effect of endplates on the filtered normal-force coefficient, compared to literature.

References

1. J. G. Leishman, Principles of Helicopter Aerodynamics, Cambridge: Cambridge University Press, 2000.
2. A. Singhal, D. Castaneda, N. Webb, and M. Samimy, "Control of Dynamic Stall over a NACA 0015 Airfoil using NS-DBD Plasma Actuators," AIAA Journal, Vol. 56, No. 1, pp. 78-89, 2018.
3. J. Little, K. Takashima, M. Nishihara, I. Adamovich, and M. Samimy, "Separation Control with Nanosecond Pulse Driven Dielectric Barrier Discharge Plasma Actuators," AIAA Journal, Vol. 50, pp. 350-365, 2012.
4. A. Sanayei, M. Ramasamy, J. Wilson, and P. Martin, "Development of Modal Analysis Based Clustering Technique Using Pitching Airfoil Measurements." AIAA Scitech 2019 Forum. 2019.
5. Kubo, Y., M. Miyazaki, and K. Kato, "Effects of end plates and blockage of structural members on drag forces." Journal of Wind Engineering and Industrial Aerodynamics, Vol. 32, No. 3, pp 329-342, 1989.
6. Rainbird, J. M., J. Peiró, and J. M. R. Graham, "Blockage-tolerant wind tunnel measurements for a NACA 0012 at high angles of attack." Journal of Wind Engineering and Industrial Aerodynamics, Vol. 145, pp. 209-218, 2015.
7. D. Yeo, E. Atkins, L. Bernal, W. Shyy, "Experimental Investigation of the Pressure, Force, and Torque Characteristics of a Rigid Flapping Wing." 50th AIAA Aerospace Sciences Meeting including the New Horizons Forum and Aerospace Exposition. 2012.
8. Sharma, Deepakkumar M., Experimental investigations of dynamic stall for an oscillating airfoil. Diss. PhD Thesis, IIT Kanpur, 2010.

Optimizing Terahertz Wave Emission for Photoconductive Switches

Student Researcher: Kweisi F. Wilson

Advisor: Dr. Nkorni Katte

Wilberforce University
Electrical Engineering

Introduction

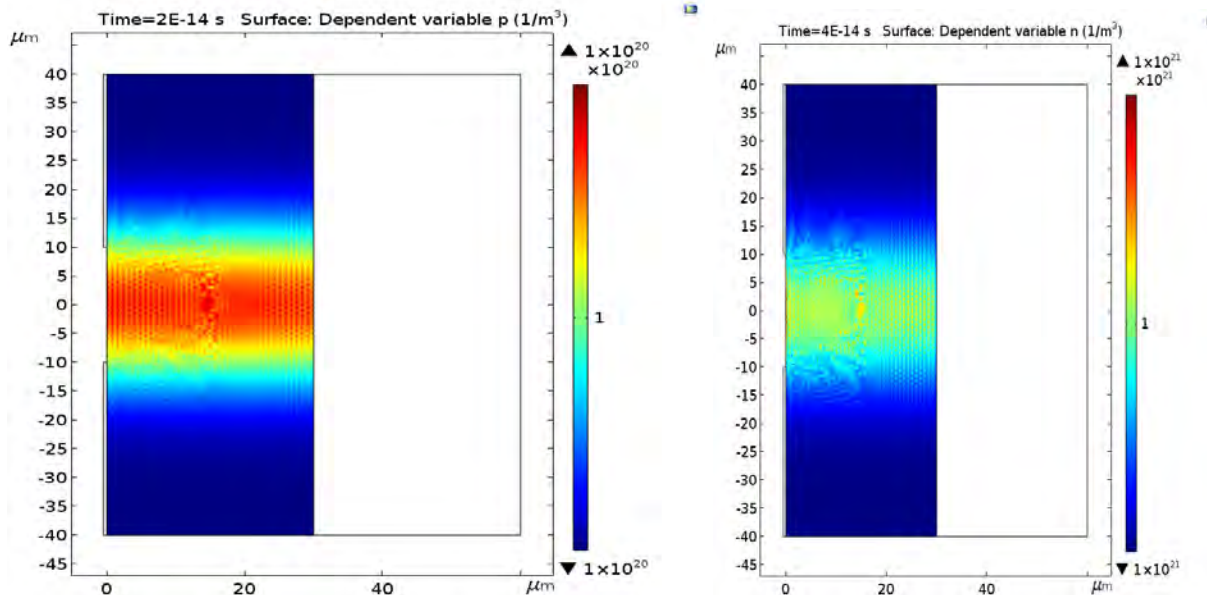
This Research revisits the problem of Terahertz generation with Photoconductive Switches and shows how the output power of Terahertz generation can be improved by carefully controlling, parameters which leads to a heat load within the material. Multiphysics simulations with COMSOL is used extensively to couple the various physical processes taking place, such as wave propagation, biased field and particle concentration. Terahertz technologies will provide new solutions in Medical Imaging, Security, Astronomy, Spectroscopy and Material Characterization.

Method

The challenge of the area of Research is to increase, the output power. Photoconductive antenna in general are the most efficient, yet its output power is still in the order of a few microwatts. We calculated the terahertz field using the theory based on the transient acceleration of charges in bulk semiconductor.

Results

We obtained the following results, in the design process.



(a) Figure 1(a).

Figure1 (b).

Figure 1. This Figure shows the distribution of holes and electrons after a femtosecond laser pulse is incident on a Semiconducting material (GaAs) Figure 1 (a) is the hole concentration , and Figure 1(b) is the electron concentration.

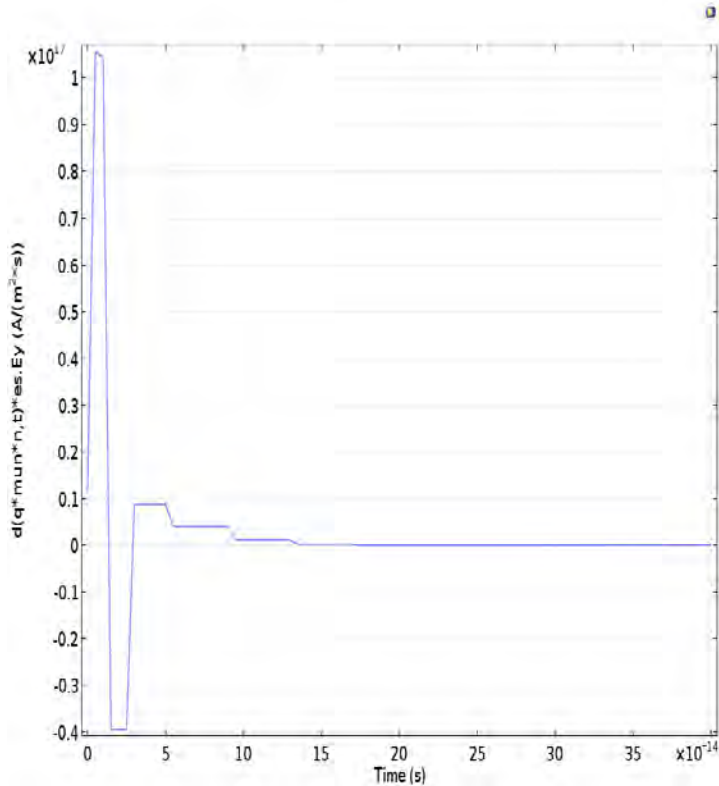


Figure 2(a).

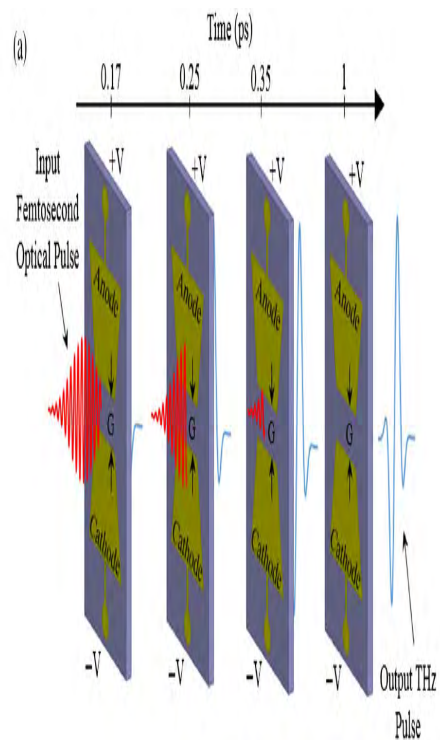


Figure 2(b).

Figure 2. Figure 2(a) Shows the field we have calculated, and Figure 2(b) shows a comparable result from [1].

Conclusion

We have shown how THz is generated by coupling several the physical processes involved. Increasing the DC bias voltage causes an increase in THz signal. (These devices usually have breakdown bias field at about $(5e7V/m)$). Reducing the gap between the metallic antenna does not change the THz signal very much. 3D simulations will be needed, especially to study the impact of the antenna design. Heating effects should be included (Joule heating, and laser heating). (PCA THz power generation will be greatly improved if the details about these physical processes are well understood) [2-5].

Acknowledgments

Special acknowledgment goes to Ohio Space Grant Consortium for the generous scholarship they provided for me and to Dr. Elliott Brown of Wright State University (Terahertz Sensors Labs) for contributing initial Ideas about the pathway for this research, who will also assist this work with experimental verification.

References

1. N. M. Burford and M. O. El-Shenawee, "Review of terahertz photoconductive antenna technology," *Opt. Eng.* 56(1), 10901 (2017).
2. Criollo, C., & Ávila, A. (2015). Simulation of photoconductive antennas for terahertz radiation. *Ingeniería e Investigación*, 35(1), 60-64. DOI: <http://dx.doi.org/10.15446/ing.investig.v35n1.45310>
3. O. A. Castañeda-Urbe, C. A. Criollo, S. Winnerl, M. Helm, and A. Avila, "Comparative study of equivalent circuit models for photoconductive antennas," *Opt. Express* 26, 29017-29031 (2018)
4. Collier, C. M. et al. Photoconductive terahertz generation from textured semiconductor materials. *Sci. Rep.* 6, 23185; doi: 10.1038/srep23185 (2016).
5. M. Khabiri, M. Neshat, and S. Safavi-Naeini, *Hybrid computational simulation and study of continuous wave terahertz photomixers*, IEEE Transactions on Therahertz and Science Technology 2 (2012), no. 6, 605–616.

Subsonic Wind Tunnel Development

Student Researcher: Robert R. Wilson

Advisor: D Blake Stringer Ph.D.

Kent State University

College of Aeronautics and Engineering

Abstract

The Aerospace Engineering program at Kent State University is a brand-new program breaking away from Aeronautics and focusing on traditional dynamics of engineering. With this new program the university is expanding its current facilities to benefit new students. A wind tunnel is an instrument used to measure aerodynamic forces and pressures applied to an object at a certain airspeed. The current wind tunnel is enough for basic analysis but, as the Aerospace program rapidly expands, a new and improved wind tunnel is needed for academic, public and private use. This wind tunnel will allow students to analysis data from test completed with larger testing equipment, at higher speeds, and in a more controlled environment. This project serves to determine factors needed for development of a closed loop wind tunnel for the university.

Introduction

A wind tunnel is an instrument used to measure aerodynamic forces and pressures applied to an object at a certain airspeed. There are generally two types: open and closed, both variations having their advantages and disadvantages. The wind tunnel at Kent State University is an open wind tunnel with a one-foot by one-foot test area. This wind tunnel serves as a sufficient academic tool for classroom work. However, as the aerospace program rapidly expands, a new and improved wind tunnel is needed for academic, public and private use. This project serves to determine factors needed for design and development of a larger wind tunnel for the university.

Background

An open wind tunnel is a device that uses the air in the laboratory as its base for the air flow of the test section. The air is sucked into the test section by a fan and pushed out back into the lab where it circulates back into the wind tunnel. Advantages to an open wind tunnel include a lower construction cost and overall size. The space that the wind tunnel is operated in must be large enough that the walls of the lab will not affect air flow. Another advantage due to overall room volume is low temperature fluctuation. Some disadvantages to an open circuit wind tunnel are higher energy output/cost and lower flow quality. Open wind tunnels are generally smaller than their counterparts but can be very large. One of the largest wind tunnels is an open wind tunnel at NASA Langley, which is capable of testing aircraft and spacecraft.

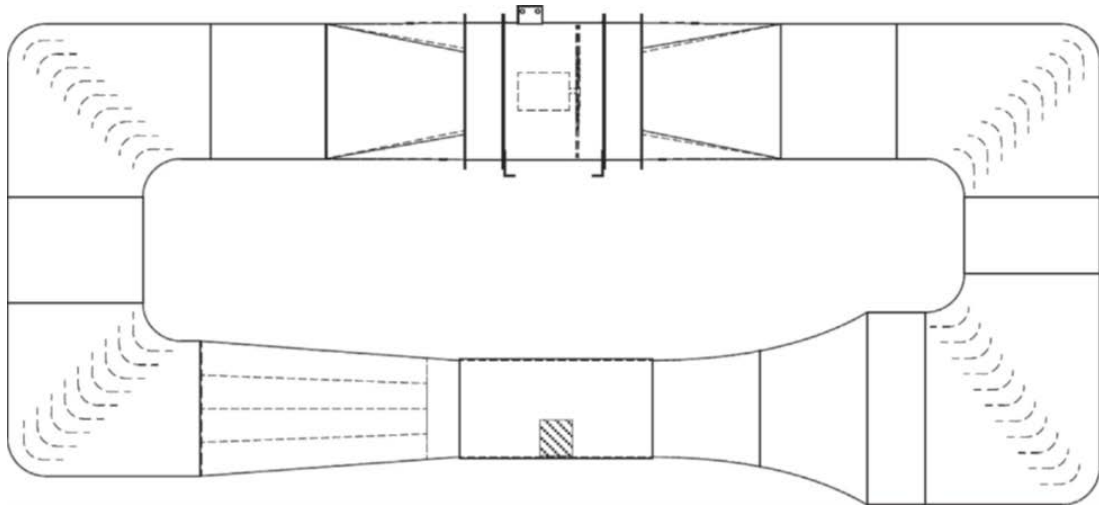


Figure 2.1. A closed-circuit wind tunnel. (John Calautit).

A closed wind tunnel differs from an open wind tunnel by enclosing the air used in the test section. The air is sent through the test section where it makes a 360-degree loop back to the starting point. The difference is that the air is enclosed in the wind tunnel as shown above. The advantages to a closed loop wind tunnel include: better flow quality, higher operating speeds, and lower operating costs. Some disadvantages are a higher construction cost and the overall size of the wind tunnel.

Wind Tunnel Section Identification

Test Section

The first area of the wind tunnel is the test section. This is the most crucial area inside the wind tunnel because it affects the flow quality. In general, the length of the test section should be maximized according to the cross-sectional area to maximize the flow quality. One factor to consider in design is the boundary layers of the test section and how these will interfere with the test data. "For a given cross section the length of the test section should not be made too large in order to avoid too much influence on the core flow from the wall boundary layers" (Lindgren).

Diffusers and Corners

The next area is the diffuser. The diffusers are found after the test section, in between the corners, and before and after the fan. These areas slow the air down as the diffuser expands. These areas use Bernoulli's Principle which states that area and velocity have an inverse relationship with fluids in a container. The air inside the wind tunnel is treated as fluid because it is a uniform gas. The air slows because the entrance area is smaller than the exiting area.

The area following are the corners. The corners are another crucial area for air flow quality. In traditional closed loop wind tunnels, the corners have a $\frac{1}{4}$ circle approach where the cross-sectional area of the opening is equivalent to the cross-sectional area of the exit. Inside these corners are guide vanes that guide the flow around the 90-degree corner, keeping the flow from transitioning from turbulent to laminar and decreasing build up or a blockage of air.

Another type of corner is an expanding corner. The difference is that the exit cross-sectional area is larger than the cross-sectional area of the opening. This combines the job of the corner and the diffuser in between the corners, optimizing spatial limits of the wind tunnel. The use of expanding corners shortens the total wind tunnel circuit length about 30% (Lindgren). In prior research, the use of

expanding corners was not popular due to poorly designed guide vanes. In more recent articles, newly designed airfoils that continued after the corner were used to decrease separation. This helped solve the flow quality issue.

Power Plant and Stagnation Chamber

The power plant is the area where the fan is kept. The layout changes the wind tunnel from a rectangular shape to a cylinder where the fan operates and then back to a rectangle. "The use of axial fans can, however, create some flow quality problems, if they are subjected to very high loads, but even with more moderate loads they can create a low frequency pulsating variation of the streamwise flow component" (Lindgren). Usually there are silencers that help convert the cross-section shape (Lindgren), while dampening the sound of the fan.

Finally, the stagnation chamber is an extremely important piece because its design directly impacts flow quality in the test section. The wind tunnel starting at the end of the test section, works as one diffuser. Its area slowly increases to a point at the stagnation chamber. The chamber, also known as a contraction chamber, contracts at first in a concave configuration and after in a convex configuration. The contraction is the same from all four sides which forms an almost rectangular funnel. This is another prime example of Bernoulli's Principle, and where velocity increases. The contraction must be done in a way to minimized turbulence so the length of the concave section should be maximized (Lindgren).

In the stagnation chamber, the air is turbulent due to the increased velocity and low area. To fix this turbulence, a honeycomb shaped screen is placed at the exit of the chamber. The honeycomb shape is effective in breaking cross stream flows, as well as fully straightening the flow. The honeycomb by itself can still leave turbulence. To ensure great flow quality, the honeycomb is usually paired with screens that form a rectangular pattern to straighten the flow completely.

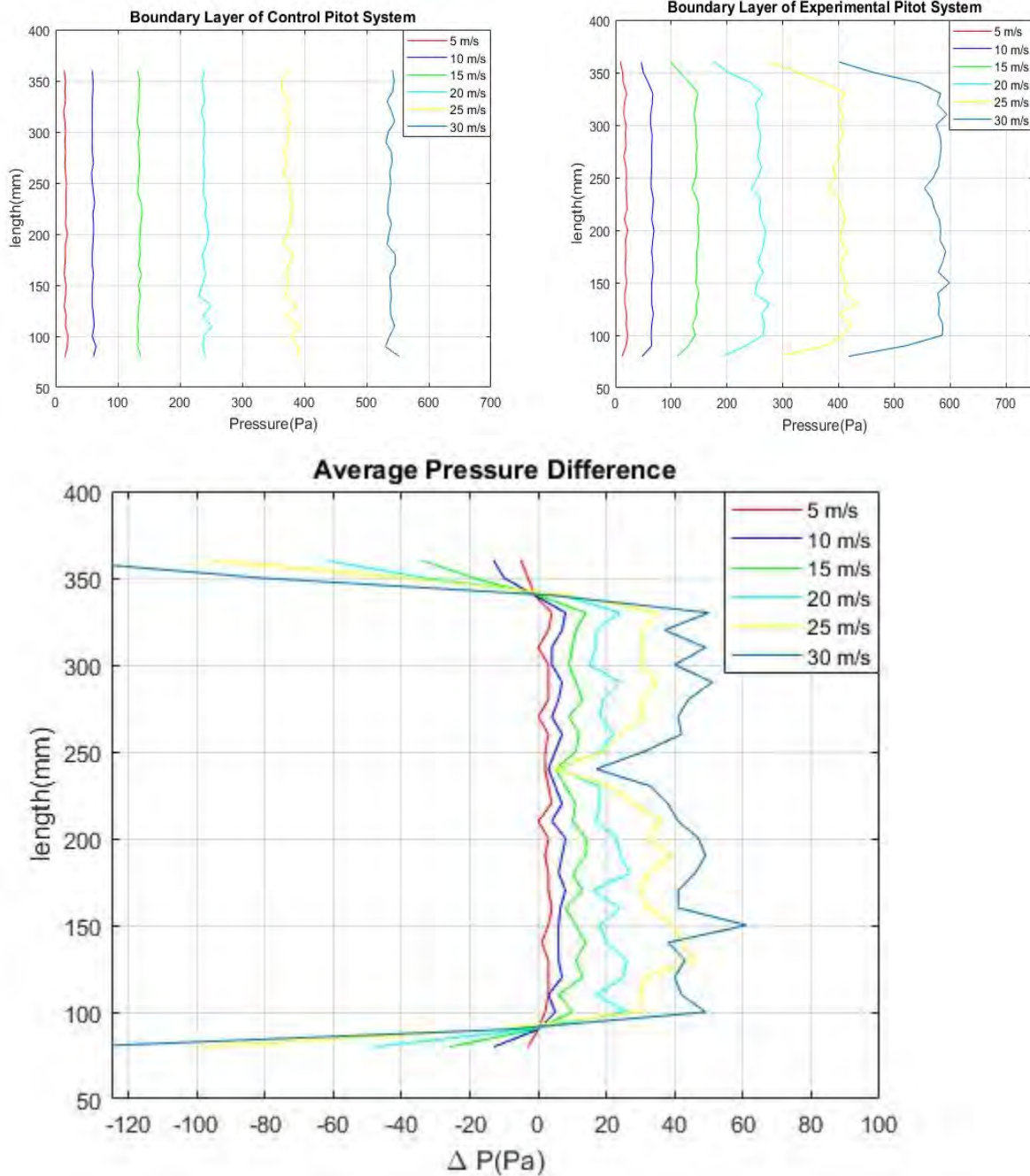
The contraction ratio also plays into the section. "The contraction ratio, CR, i.e. the ratio between the largest cross section area, (found in the stagnation chamber), and smallest cross section area, (found in the test section)" (Lindgren). The optimal contraction ratio is 9. Some smaller wind tunnels can have lower contraction ratios such as 6-8, but the optimal flow quality number is 9.

Flow quality defined by John Kaiser Calautit is the "uniformity of the velocity flow field, flow angularity and turbulence intensity" (Calautit). Ensuring excellent flow quality is essential in order to receive accurate results in taking data. At the test section, the turbulence needs to be minimized which is crucial in the corner before the test section and the stagnation chamber.

Kent State's Open Loop Wind Tunnel

An open wind tunnel contains a stagnation chamber, test section, diffuser, and a fan in that order. The open wind tunnel at Kent State (KSWT) sucks air into the stagnation chamber that contains a single honeycomb screen at the entrance of the test section. After the test section, there is a screen that leads into the diffuser that then leads to the fan. The fan blows the air out of the wind tunnel and back into the lab where it circulates in the lab back to the front of the lab and into the stagnation chamber. The KSWT has a test section with a cross sectional area of 305mm x 305mm (1 ft x 1 ft) and a length of 600mm (1.97 ft). The maximum velocity the wind tunnel can produce is 36 m/s (80.5 mph). The overall size of the KSWT is 3.7 m x 1.065m x 1.9 m (12.1 ft x 3.5 ft x 6.23 ft) and weighs 293 kg (646 lbf) (TECQUIPMENT).

The boundary layer in the KSWT extended from the top and bottom about 35 mm- 40mm. These boundary layers influence the flow quality and can cause an error in data. This is the wall effect and the testing material must be small enough that the flow over the testing material is not interfered by the wall effect. The pressure difference from the KSWT can be seen below:



The graphs above show the results of an experiment using the dual pitot tube system set up in the KSWT. Measurements were taken as one pitot tube was lowered, meanwhile the other pitot tube remained at the same distance from the wall during the experiment.

KSWT is designed with an academic purpose and is spatially optimized. This has made it affordable and small enough to fit into the current lab at Kent State. The negative effect is the wind tunnels flow quality is fair and the testing specimen needs to be rather small. The flow quality is only fair because the flow is sucked through the stagnation chamber which contains one honeycomb screen before being sent through the test section.

Closed Loop Wind Tunnel Research & Development

Guide Vanes

John Calautit states “wind tunnel flow quality can adversely affect experimental results; precise and steady flow quality measurements are essential...” (Calautit). The first area of improving the flow quality of the new wind tunnel will be implementing guide vanes into the corners of the wind tunnel. The testing that Calautit performed concluded that upstream and downstream guide vanes significantly reduces velocity variation in the test section as well as reduces pressure loss in the corners. The negative effect of the vanes is a velocity reduction of the airflow. This can be overcome by adding more power at the power plant to reach the velocity parameter. Though Reinke’s goal was to maximize the length of the test section without compromising the overall size of the wind tunnel, the research done on expanding the cross-sectional area of the flow in the corner can be used to minimize the overall size of the future wind tunnel. Reinke found that guide vanes of uniform thickness will expand the air flow without compromising flow quality. Reinke states that guide vanes that follow a circular arc pattern will provide the best expansion if the centers of the arc are slightly off set. On a cartesian plot, $(x_0, y_0) \approx (0, 0)$ and $(x_1, y_1) \approx (1, 2.3)$. The highest velocity tested was 12 m/s (Reinke) which is 55 m/s slower than the goal velocity for the Kent State wind tunnel. Lindgren and Johansson tested expanding corners up to a velocity of 40 m/s with a slightly different variation of guide vanes. The increased pressure loss that was associated with the guide vanes is expected; otherwise, guide vanes are suitable for implementation.

Power Plant

Literature covering the power plant of a closed loop wind tunnel provides different options for a power source. These mainly include centrifugal and axial fans as well as compressors. The most common fan used was an axial fan. The axial fan is more compatible for closed-loop wind tunnels because it completes the circuit without diminishing flow quality. Air compressors usually benefit high speed wind tunnels and are more useful at higher speeds, but the axial fan is more consistent and has a lower day to day cost. The literature mainly supported the rectangular-to-axial change as it allows for a more uniform flow as well as less separation and turbulence. The current Kent State wind tunnel uses a rectangular-to-axial diffuser that changes the cross-sectional area of the airflow as it flows through the power plant. A similar diffuser is needed for the closed loop wind tunnel as it passes through diffuser three. Hernandez offered a different solution, looking at saving costs by using commercial fans instead of specializing a single fan. It is unclear how the airflow would be affected by the rectangular multi-fan set up and more research needs to be done to validate that it will not cause a larger pressure increase than desired. The design would save money as it would allow for less powerful commercial fans to be built, as opposed to modifying or paying to modify a high-powered fan (Hernandez). Walker’s thesis modified the current Texas Tech closed loop wind tunnel fan to achieve a higher test section velocity. The changes made to the fan included a larger motor and the fan angle. These changes increased the test section velocity, but fell short of predicted parameters. Walker concluded the need for guide vanes after the fan to straighten the flow. In Towels-Moore’s Thesis, the motor of the fan is included in the airflow. To keep the flow uniform as well as avoid a drop-in flow quality, the cross-sectional area is expanded around the fan like in Figure 5.2.1. (Towels-Moore).

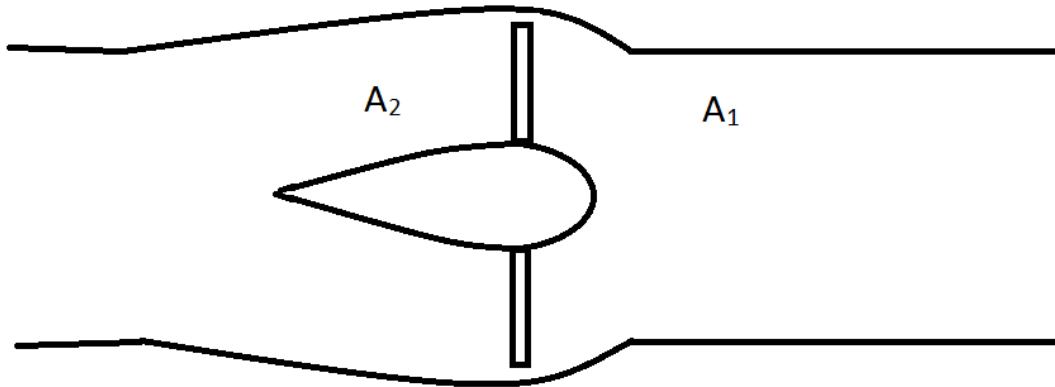


Figure 5.2.1. The cross-sectional area is expanded to maintain quality of flow (Towels-Moore).

Towels-Moore's thesis focused on a wind tunnel with a test section velocity of 450 mph and achieved a 4'x6' test section. The power output is stated for San Jose State's wind tunnel to be 12,000 HP (Towels-Moore). This is considerably larger than the current design parameters and the overall size and cost seems considerable. Also, this proves that one fan can produce the desired test section velocity. The estimated overall cost for the wind tunnel was \$740,904 with \$705,250 allotted for the fan and fan housing (Towels-Moore).

Design Plan and Future Study

Design Plan

Hernandez provided an Excel sheet that lays out the basics of a closed loop wind tunnel design. The excel sheet uses a list of preliminary design inputs and provides an output of a functioning closed loop wind tunnel. Examples of the inputs include test section parameters, contraction specifications, and testing speed. The excel sheet has some variations and warnings for excessive inputs but provides a very basic range for wind tunnel parameters. The wind tunnel also uses the multiple fan design as stated above. This will lead to some parameters being off, but overall the excel sheet is extremely useful for getting started. The parameters for the wind tunnel's test section are 2 feet wide by 2 feet tall by 4 feet long. This will allow larger objects to be tested and less effect from the flow straighteners. The contraction ratio was set at eight to allow for optimal flow quality while still maintaining spatial constraints. Finally, the determined test section velocity was set at 150 mph. This will allow more comprehensive testing to be done in future academic studies.

With these parameters, the wind tunnel's approximate length is 31.83 feet with a total width of 19 feet. The width and height at the stagnation chamber are 5.66 feet and the cross-sectional area is 31.97 ft². By completing a quick check, multiplying the cross-sectional area of the test section by eight (contraction ratio) will give a stagnation area of 32 feet. One thing to note in the figure below is the use of a non-linear contraction in the "nozzle" of the wind tunnel. This curve represents the x^3 curve and Hernandez speaks more about specifying the curve in his paper, "Design Methodology for a quick and Low-cost wind tunnel." The angles in which the curve uses cannot be too great. This would cause separation of the boundary layer, causing turbulence and greatly diminishing flow quality as it passes through the test section. Hernandez states, "... when both of the contraction semi-angles ... take the values in the order of 12°, the contraction has a reasonable length and [represents] a good fluid dynamic behavior" (Hernandez). The use of polynomial curve shortens the distance needed for contraction while maintain better flow quality.

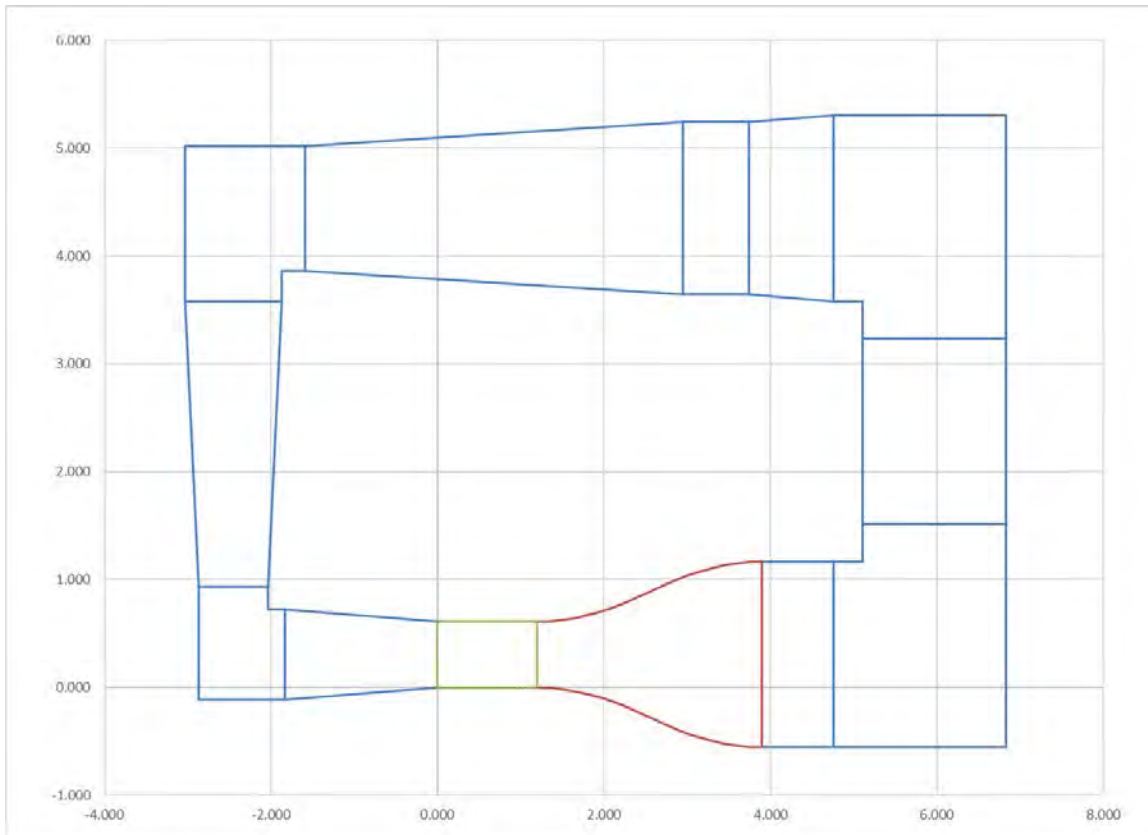


Figure 6.1. Hernandez’s excel sheet output with desired parameters for future wind tunnel.

This Excel sheet gives us a good idea of the spatial limitations. One thing to note is that the corners of Hernandez’s design use guide vanes that can be either circular or airfoil shaped. These guide vanes only focus on flow quality so that the use of expanding corners will shorten the overall length and width. The power plant layout will also change with the power plant specifications from other literature.

Future Study

Moving forward, the component needed for the power plant is whether to use Hernandez’s model of a fan matrix, or the model of a specialized fan with a pitch control device. The cost of specialized fan would be far greater than the matrix, but the flow quality of the fan matrix is unknown. The matrix can be tested as a 3D printed model using the current wind tunnel to measure pressure distributions and the parasite drag.

The following step is performing cost analysis on whether to build or purchase a wind tunnel. The cost of the power plant is going to be a major factor determining over all price. Other costs include; measurement systems, materials, fasteners, structure materials, screens and flow straighteners. The cost of building the wind tunnel should be determined in the coming months so that construction can begin over the summer.

Acknowledgments

I'd like to acknowledge Dr. Stringer for all his hard work in my personal journey at Kent State. I have him to thank for switching to aerospace engineering and finding my passion. He has been fundamental to re-energizing engineering at Kent State and our college is expanding mainly due to him.

I'd also like to acknowledge Kent State's College of Aeronautics and Engineering for allowing me to work on this project and the hard work the administrators do to further our education.

References

1. Bradshaw, P, and Pankhurst. R.C, "The design of Low-Speed Wind Tunnels." *National Physical Laboratory, Teddington*. 1964. pp 1-69.
2. Calautit, John Kaiser, et al. "A Validated Design Methodology for a Closed-Loop Subsonic Wind Tunnel." *Journal of Wind Engineering and Industrial Aerodynamics*, 21 Jan. 2014, pp. 180–194.
3. Cattafesta, Louis, et al. "Fundamentals of Wind-Tunnel Design." *Encyclopedia of Aerospace Engineering.*, Dec. 2010, pp. 1–11.
4. Hernandez, Miguel, et al. "Design Methodology for a quick and Low-cost wind tunnel." *Intech*. 2013. pp. 1-28.
5. Johansson, Arne V. "A Low Speed Wind-Tunnel with Extreme Flow Quality - Design and Tests." *Department of Mechanics, Royal Institute of Technology*, 1992, pp. 1603–1611.
6. Junca-Laplace, Jean-Philippe, "Design, Fabrication and Characterization of a New Wind Tunnel Facility – Linear Cascade with a Wake Simulator" (2011). *LSU Master's Theses*. 2773.
7. Lindgren, Bjorn, and Arne V Johansson. "Design and Evaluation of a Low-Speed Wind-Tunnel with Expanding Corners." *Technical Reports from Royal Institute of Technology*, Oct. 2002, pp. 1–47.
8. Reinke, Nico. "A Spatially Optimized Wind Tunnel." *Institute of Physics, University of Oldenburg*, 6 Mar. 2017, pp. 1–18.
9. "Subsonic Wind Tunnel AF1300 | Aerodynamics." *TecQuipment*, www.tecquipment.com/subsonic-wind-tunnel.
10. Towels-Moore, Jordan. "High Speed Subsonic Wind Tunnel Design." *Master's Thesis, Department of Aerospace Engineering, San Jose State University*. (May 2014). pp. 1-62
11. Walker, Todd. "Re-Design of A Drive System for A Low-Speed Wind Tunnel." *Master's Thesis, Institutional Research, Texas Technical University*. (May 1998). pp. 1-40.

Detection of Hazardous Gases

Student Researcher: Reis L. Zandier

Advisors: Dr. Pedro Cortes / Dr. Eric MacDonald

Youngstown State University
Chemical Engineering

Abstract

Carbon nanotubes offer a positive outlook on the development of accurate and durable sensing technologies. Their exceptional chemical, mechanical, electrical, and optoelectronic properties allow for easy manipulation and customization of nanotube devices that target specific stimuli. Certainly, much attention for carbon nanotubes continues to emerge from a diverse range of fields including chemistry, physics, materials science, and engineering. The development of quick and reliable methods of manufacturing carbon nanotube sensing devices will improve the platform of detection technologies available in the market.

Project Objectives

In the present work, a variety of different types of sensing substrates were used to lay down the technological platform for manufacturing 3D printed wearable sensors. Here, a water based polyetherimide solution was used to wrap the CNTs and induce selectivity and sensitivity features towards nitrogen dioxide. Different concentrations were tested to see which produced the best detection.

Methodology Used

Three main types of sensors were used in the testing. The 3D printed rectangles were embedded with either aluminum or copper wire. Another sensor was tested with aluminum tape on a zarconia. Different concentrations of solutions containing CNT and water were used in the testing as well. Using CNT's for detection has been done in previous work and compares to the findings made by Elsevier *Talanta* in 2008. However, this research has yet to be performed on 3D printed material.

Results Obtained

There was distinct detection among all four biological solutions tested. The best display of detection was with the aluminum on Zarconia. The graph below shows the change in resistance with the presence of NO_x which was detected by the sensor. The lower concentration of PEI proved better detection. The copper used in some of the original sensor designs oxidized during the NO_x test, so the aluminum was then used instead. Future work with this project will be with other hazardous gases and different explosives. Also solutions will be prepared with single wall carbon nanotubes and tested on flexible 3D printed sensors.

References

1. "Carbon Nanotube Networks as Gas Sensors for NO₂ Detection." *Talanta*, Elsevier, 23 July 2008, www.sciencedirect.com/science/article/pii/S0039914008005523.

